Measurement of the Branching Fraction of the Decay $B^0 \to \psi(2S)\pi^0$ and Studies of the Luminosity-dependent Background for the Belle II Experiment at the Future Accelerator SuperKEKB

Dissertation
an der Fakultät für Physik
der Ludwigs Maximilians Universität
München

vorgelegt von
Elena Nedelkovska

November 8, 2013

Measurement of the Branching Fraction of the Decay $B^0 \to \psi(2S)\pi^0$ and Studies of the Luminosity-dependent Background for the Belle II Experiment at the Future Accelerator SuperKEKB

Zur Erlangung des akademischen Grades eines

Doktors der Naturwissenschaften

von der Fakultät für Physik
der Ludwigs Maximilians Universität
München

genehmigte

Dissertation

von

ELENA NEDELKOVSKA

Tag der mündlichen Prüfung: 24.01.2014

Erstgutachter: Prof. Dr. Christian Kiesling

Zweitgutachter: Prof. Dr. Otmar Biebel

Datum der mündlichen Prüfung: 24.01.2014

Zusammenfassung

Diese Doktorarbeit umfasst zwei getrennte Analysen: zum einen die Messung des Verzweigungsverhältnisses $B^0 \to \Psi(2S)\pi^0$ aus den Daten des Belle Experimentes, zum anderen die Abschätzung der Rate von QED Untergrundereignissen bei kleinen Impulsen für das Detektorupgrade Belle II und deren Einfluss auf das Leistungsverhalten des neuen Pixeldetektors.
In der ersten Analyse wurde der Zerfallskanal $B^0 \to \Psi(2S)\pi^0$ untersucht und zum ersten Mal das zugehörige Verzweigungsverhältnis bestimmt. Die Analyse beruht auf Daten des asymmetrischen e^+e^- KEKB Beschleunigers, die mit dem Belle Detektor aufgezeichnet wurden. Verwendet werden die gesamten Belle Daten, die 772 Millionen $B\bar{B}$ Paare enthalten. Die Analyse liefert folgendes Ergebnis für das Verzweigungsverhältnis:

$$\mathcal{B}(B^0 \to \Psi(2S)\pi^0) = (1.07 \pm 0.23 \pm 0.08) \times 10^{-5}.$$

Die zweite Studie beschäftigt sich mit dem Leistungsverhalten des Belle II Detektors. Viele Detektorkomponenten des Belle Experimentes werden im Ramen des Upgrades ersetzt oder verbessert. Wichtigste Veränderung dabei ist der neue Pixeldetektor zur Messung des Wechselwirkungspunktes der kollidierenden Teilchen, der in unmittelbarer Nähe zum Strahlrohr eingebaut wird. Aufgrund seines geringen Radius wird er am stärksten von Untergrundereignissen beeinflusst. Es wird erwartet, dass zwei Photon QED Prozesse $e^+e^- \to e^+e^-e^+e^-$ dabei die wichtigste Rolle spielen. Da die Luminosität des neuen SuperKEKB Collider voraussichtlich 40-mal höher als die von KEKB sein wird, wird erwartet, dass die Rate von Untergrundereignissen entsprechend steigt. Um zwei Photon QED Prozesse zu analysieren, wurden Ereignisse verwendet, die nach dem Zufallsprinzip selektiert wurden (random trigger). Die bei diesen Ereignissen entstehenden Elektronen und Positronen haben eine sehr niedrige Energie und erreichen daher nur die innerste Lage des Pixeldetektors, die dadurch besonders belastet wird.
Die Messungen zeigt, dass die Okkupanz der innersten Lage durch zwei Photon QED Ereignisse 0.7% ist, was unterhalb der maximalen Okkupanz von 3% liegt, bei der der Detektor noch fehlerfrei funktioniert.

Abstract

This thesis encloses two separate studies: measurement of the branching fraction of $B^0 \to \psi(2S)\pi^0$ using Belle data and estimation of the low momentum QED background at the future experiment Belle II.
The first study refers to the analysis of the decay channel $B^0 \to \psi(2S)\pi^0$ and the measurement of its branching fraction. It is noteworthy to mention that this is the first measurement of the $B^0 \to \psi(2S)\pi^0$ branching fraction.
For this measurement, the complete data set of 772 million $B\bar{B}$ pairs, collected by the Belle detector at the asymmetric e^+e^- KEKB collider was used. The value obtained for the branching ratio is

$$\mathcal{B}(B^0 \to \psi(2S)\pi^0) = (1.07 \pm 0.23 \pm 0.08) \times 10^{-5}.$$

The second study regards the quality performance of the upgraded Belle detector, named Belle II. Many sub-components of the detector will be replaced or upgraded, but the major change will be the new pixel vertex detector, placed at extreme proximity to the beam-pipe. Due to its small radius it will be the most affected by background. In particular it is expected to suffer mostly from the low energy electrons and positrons coming from the QED process $e^+e^- \to e^+e^-e^+e^-$. Since the luminosity delivered by the new SuperKEKB collider is expected to be 40 times higher than the one delivered by KEKB, the background level of Belle II is expected to increase accordingly.
We particularly studied this QED process with a special random trigger, where the emitted very low energy secondary electrons and positrons reach only the innermost layers of the pixel detector. So far the cross section in this phase space was never measured and there may be therefore large uncertainties in the theoretical predictions.
The obtained measurements gave an occupancy in the innermost layer of 0.7 %, which is below the maximal occupancy of 3% that the pixel detector can handle to work properly.

Contents

Introduction

The main task of elementary particle physics is to answer the questions: what is the matter made of and what kind of interactions occur between its constituents.
In our present knowledge the most fundamental building blocks of matter are the two types of spin 1/2 fermions, namely leptons and quarks. There are three families of leptons and three families of quarks.
These particles interact with each other by the exchange of force carriers with integer spin. In Nature, four fundamental forces govern the interactions between particles: gravitational, electromagnetic, weak and strong. Gravitation is much too weak to have an influence on the interactions between elementary particles, and therefore has no significance in subatomic physics. The electromagnetic force is responsible for all atomic properties and is mediated by the exchange of a virtual photon. The weak force is the source of quark and lepton transformations and is mediated by the $W^{\pm}$. Electromagnetic and weak force are unified to a common description known as electroweak force entailing a neutral weak boson Z^0. The lepton and quark families as well as the fundamental forces that govern the interactions between the particles are shown in Figure 1.
The unified theory of the electroweak force and strong interactions constitutes the Standard Model of elementary particles. This model emerged from experimental discoveries and theoretical calculations in the 1960s and 1970s, being enormously successful in describing empirical foundations of particle interactions for many years. Until today, the Standard Model has been confirmed by many precise experimental data and all predictions made by this model turned out to be correct within the experimental uncertainties.
Nevertheless, there are several reasons why the Standard Model is not a completely satisfying theory. One of the reasons is the existence of too many parameters, namely the masses and mixing of the quarks and leptons, all of which are a priori unknown. The hierarchy of the quark and lepton masses and the quark mixing matrices suggest that some hidden mechanism occurring at higher energy scale governs their pattern.
Furthermore in 1964, the world of particle physics was struck by an exciting discovery: the violation of a symmetry between the matter and anti-matter, the so-called charge-parity violation (CP) in the decay of neutral K mesons [1]. CP violation is incorporated in the Standard Model as an irreducible complex phase in the Cabbibo-Kobayashi-Maskawa (CKM) [2] quark-mixing matrix. The CP violation is

very important, especially from the cosmological point of view, for the explanation of the excess of matter over anti-matter in the Universe [3]. But the Standard Model turned out to be imperfect, as the amount of CP violation predicted by the model is insufficient to account for the observed asymmetry.

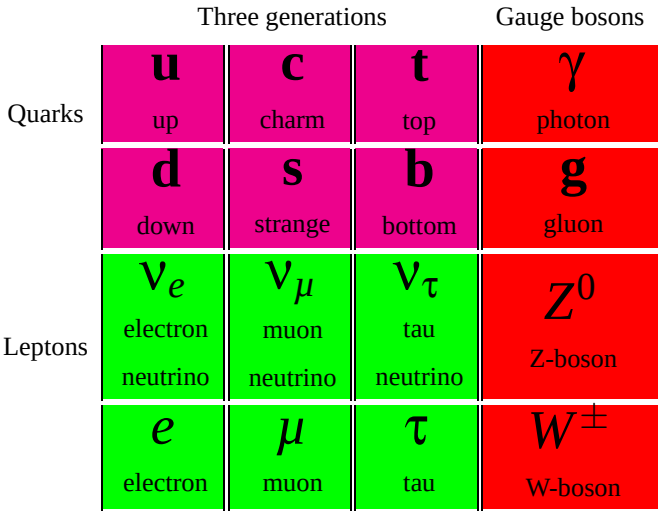

Figure 1: The three generations of quarks and leptons and the three fundamental forces in nature (excluding gravity).

The prediction of the Standard Model of large CP violating effects in certain B meson decays, led to a development of the B factories PEP II [4] and KEKB [5], where the BaBar [6] and Belle [7] detectors are located, respectively. These machines began operating in 1999, and have accumulated huge amounts of $B\overline{B}$ data at the $\Upsilon(4S)$ resonance. Before its shutdown in 2010, Belle had accumulated world record of data, exceeding $1040\,\text{fb}^{-1}$ that corresponds to 772×10^6 B meson pairs, while the BaBar detector had accumulated $557\,\text{fb}^{-1}$ of data. These samples provided sufficient data to test the Standard Model predictions.
Both Belle [8][9][10][11] and BaBar [12][13] measured CP violation in the neutral B meson system. CP violation was established through measurements of the time-dependent asymmetry in $B^0\to J/\psi K_S^0$ and $\overline{B}^0\to J/\psi K_S^0$ decays, which are $b\to c\overline{c}s$ transitions.
The Belle experiment provided the ability to measure a large number of B meson decay modes and to extract CKM matrix elements and other observables. It thus enabled measurement of the three angles of the unitarity triangle, ϕ_1, ϕ_2 and ϕ_3.
Apart from the decay $B^0\to J/\psi K_S^0$ the angle ϕ_1 of the unitarity triangle is also accessible via $b\to c\overline{c}d$ transitions. Such a decay is e.g. the channel that will be discussed in detail in this thesis, $B^0\to\psi(2S)\pi^0$.
In fact, $B^0\to\psi(2S)\pi^0$ decay channel has never been measured before. Although

from the experimental point of view, $B^0 \to \psi(2S)\pi^0$ is relatively easy to access, due to its clean signal signature, yet we are limited in statistics. An additional motivation to study this particular channel is the possibility to estimate the penguin pollution in $B^0 \to \psi(2S)K_S^0$. The possible penguin contribution from $b \to c\bar{c}d$ interactions, which contain different CKM phases, can bias the measured quantity of $\sin 2\phi_1$. Any discrepancy that can be observed would emerge either as a consequence of the penguin contribution effect or due to new physics. Therefore, measurements of CP asymmetries in $b \to c\bar{c}d$ interactions have huge importance in identifying whether or not the Standard Model provides a complete description of the CP violation in the B meson system. With this observation, but also by collecting many such observations from other decay modes, there is a chance to probe new physics and once it is established we can determine its properties. The possibility to probe new physics lies in the upgrade of the luminosity of KEKB by a substantial amount. A factor of 40 improvement will greatly emphasize the prospect to discover new physics.

Currently, the Belle detector and the KEKB accelerator are being upgraded. In the forthcoming KEKB upgrade, SuperKEKB [14], the instantaneous luminosity will reach a design value of $0.8 \times 10^{36}\,\mathrm{cm}^{-2}\mathrm{s}^{-1}$. The upgraded detector Belle II [14] involves change of most of the existent sub-detectors, but the main change in the design is the completely new pixel vertex detector (PXD).

The reason for having a pixel detector in the region closest to the beam-pipe instead of a silicon strip vertex detector (SVD) close to the beam-pipe is the increased amount of background at Belle II. At large luminosities, experiments are faced with extremely high background, thus the innermost layer of the silicon detector can no longer be realized with strips due to large occupancy that makes the reconstruction of B decay vertices impossible. The silicon vertex detector cannot handle the hostile background environment at Belle II so close to the beam-pipe, because it has much smaller number of channels. The background in fact increases roughly with the inverse square of the distance to the interaction point, which means the closer to the interaction point, the higher the background and therefore the higher the occupancy.

The precise knowledge of the expected background is then an important condition for the successful operation of the silicon pixel vertex detector. A realistic estimation of the expected background level is important for the new detector design. By estimating occupancy, radiation damage and dead time for each sub-detector, the impact of the background on physics analyses can be evaluated.

Generally, the background can be divided into two classes: background from the machine, such as beam-gas and beam-wall interactions and background from high cross section QED processes, such as the production of low momentum e^+e^- pairs from the process $e^+e^- \to e^+e^-e^+e^-$. The emitted low energy electrons and positrons, being of the order of $O(5\,\mathrm{MeV})$, influence the pixel detector the most. These particles only reach the innermost layers of the PXD. So far the cross section of this process ("no-tag" with low momentum secondary leptons) was never measured and there may be therefore large uncertainties in the theoretical predictions.

In order to determine the size of this contribution, we performed a set of dedicated

experiments at KEK just before it was closed down. We compared the measurements to several Monte-Carlo simulations which turn out to agree with the measurements. Based on these favorable findings, we were able to reliably determine the two-photon QED background and therefore the expected occupancy in the two PXD layers.

Chapter 1

Physics Motivation

1.1 The Standard Model

Our current knowledge and understanding of the interactions between the elementary particles and the forces they are governed by, are covered in one fundamental chapter of the particle physics, namely the Standard Model. Although the Standard Model has survived for many years it certainly is not the end of the story. There are many important issues that are not accounted for, the masses of the neutrinos and the matter-antimatter asymmetry in the Universe. The physics of B-mesons provides a rich ground for studying CP violation and therefore leading either to the confirmation of the Standard Model or setting the scene for an extension of the well-known theory and possibly look towards the New Physics. Regarding the B meson system, the Standard Model makes precise predictions of CP violation. If experimentally obtained results compared to the CP violation predictions of the Standard Model diverge, then this might be a hint for New Physics.

1.2 C, P and T-Symmetry

Symmetries play an important role in elementary particle physics, first because they are related to conservation laws (Noether's theorem). In the following several discrete symmetries will be described: Charge Conjugation **C**, Parity **P**, Time reversal **T** and combinations like **CP** or **CPT**.

1.2.1 Charge Conjugation

Charge Conjugation (C) transforms the particle into its antiparticle, by changing all internal quantum numbers like charge, baryon number, lepton number, strangeness, charm, beauty and truth, but leaving mass, energy, momentum and spin invariant.

$$C|p>=|\bar{p}> \tag{1.1}$$

If $|p>$ is an eigenstate of *C*, the application of *C*-symmetry gives

$$C|p>=\pm|p>=|\bar{p}> \tag{1.2}$$

thus $|p>$ and $|\bar{p}>$ differ only by a phase, which means that they represent the same physical state. Therefore only particles that are their own antiparticles such as e.g. the photon, π^0, η, η', J/ψ, ϕ, ρ^0 and ω and so on, can be eigenstates of C.

1.2.2 Parity

P transformation (*P*) can be represented as a system viewed in a mirror. Indeed Parity transformation inverts the coordinate system, thus transforming a right-handed coordinate system into a left-handed one. If the mirror reflection has the same physical properties as the original, then the system is invariant under parity transformation. Accordingly, the space coordinate $\vec{x}$, the momentum $\vec{p}$ and the angular momentum $\vec{l} \equiv \vec{x} \times \vec{p}$ under parity are transformed as follows

$$\vec{x} \xrightarrow{P} -\vec{x}, \quad \vec{p} \xrightarrow{P} -\vec{p}, \quad \vec{l} \xrightarrow{P} \vec{l} \tag{1.3}$$

Equation (1.3) shows that one can distinguish two different types of vectors: polar vectors that change their sign under parity transformation, $\vec{V} \xrightarrow{P} -\vec{V}$ and axial vectors that remain unchanged under parity transformation, $\vec{A} \xrightarrow{P} \vec{A}$. Likewise, for scalars *S* - like $\vec{p_1} \cdot \vec{p_2}$ and pseudo-scalars *P* - like $\vec{p} \cdot \vec{l}$ parity transformation yields $S \xrightarrow{P} S$ and $P \xrightarrow{P} -P$, respectively.

1.2.3 Time reversal

Time reversal *T* reflects *t* into -*t*, while leaving the space coordinate $\vec{x}$ unchanged, thus having

$$\vec{p} \xrightarrow{T} -\vec{p}, \quad \vec{l} \xrightarrow{T} -\vec{l} \tag{1.4}$$

Therefore *T* symmetry represents a reversal of motion.

1.2.4 CPT

All experimental data point to the fact that C, P and T are conserved separately in strong and electromagnetic interactions and the present theories of these interactions, namely QED and QCD are constructed such that these symmetries are preserved.

But, on the other hand, both C and P parities were found to be violated in weak interactions. Essentially, no left-handed neutrinos have been observed, while P invariance violation was first observed in β decay [15] and other nuclear decays. Furthermore, Kaon decays violate conservation of CP, thus weak interactions also violate the symmetry under the combination of C and P transformations (CP parity).
However, any given theory incorporating Lorentz invariance may violate C, P and T separately, but the combined CPT operation must stay conserved. Based only on the most general assumptions: Lorentz invariance, quantum mechanics and the idea that the interactions are represented by fields, the CPT theorem [16] states that the combined operation of the time reversal, charge conjugation and parity (in any order) is an exact symmetry of any interaction.

1.3 Basics of CP-Violation

The CP transformation is a combination of the two separate symmetries: Charge Conjugation C and parity P. If CP was an exact symmetry of Nature matter and antimatter would behave the same. However, it has been observed that C and P are conserved in two of the three fundamental forces: strong and electromagnetic, but in weak interactions there is maximal violation of C and P. On the other hand CP seemed conserved in weak processes. The charged W boson couples to left-handed electrons, e_L^- or to the CP conjugate right-handed positron, e_R^+, but it would never couple to a C conjugate left-handed positron, e_L^+ nor to a P conjugate right-handed electron, e_R^-. Still in rare weak processes such as neutral K meson decays and neutral and charged B meson decays CP is violated. CP violation was observed first in $K^0 \to \pi\pi$ decays [17] and later in various neutral B meson decays. Also, evidence of CP violation has been measured in neutral decays of D [18][19] and B_s [20].

1.4 The origin of CP violation in the Standard Model

The Standard Model describes the fundamental components of matter, quarks and leptons and their interactions under the strong, electromagnetic and weak forces. The governing symmetry of the Standard Model is the $SU(3)_{color} \times SU(2)_L \times U(1)_Y$ gauge symmetry, incorporating the quantum chromodynamics (QCD) and the electroweak theories. The $SU(3)_{color}$ symmetry determines the interactions governed by the strong force, while $SU(2)_L \times U(1)_Y$ controls the electroweak interactions. The Lagrangian of the Standard Model is given by

$$\mathcal{L}_{SM} = \mathcal{L}_{EW} + \mathcal{L}_{QCD}. \tag{1.5}$$

The electroweak part of the Standard Model is modeled as a spontaneously broken Yang-Mills theory based on $SU(2)_L \times U(1)_Y$ [21], [22]. The electroweak Lagrangian

is composed of four components: the Lagrangian of the fermion fields, the Lagrangian of the gauge fields, which gives rise to the bosons in the electroweak theory, the Lagrangian of the spontaneously broken symmetry (SSB) describing the Higgs sector, and the gauge invariant Yukawa couplings, which generate the masses to the fermions:

$$\mathcal{L}_{EW} = \mathcal{L}_{EW}^{fermion} + \mathcal{L}_{EW}^{gauge} + \mathcal{L}_{EW}^{SSB} + \mathcal{L}_{EW}^{Yukawa}. \tag{1.6}$$

The left-handed and right-handed particles behave differently under $SU(2)_L$ transformations. Namely, the quarks and leptons form doublets of left-handed and singlets of right-handed fields,

$$\Psi_L = \frac{1}{2}(1-\gamma^5)\Psi \quad \text{and} \quad \Psi_R = \frac{1}{2}(1+\gamma^5)\Psi. \tag{1.7}$$

The Lagrangian invariant under gauge transformations involves dynamical terms for the quark fields and kinetic terms for the gauge fields,

$$\mathcal{L} = \overline{\Psi}_L i\gamma^\mu \mathcal{D}_\mu \Psi_L + \overline{\Psi}_R i\gamma^\mu \mathcal{D}_\mu \Psi_R - \frac{1}{4}B_{\mu\nu}B^{\mu\nu} - \frac{1}{4}W^i_{\mu\nu}W_i^{\mu\nu} \tag{1.8}$$

where the covariant derivative $\mathcal{D}_\mu$ introduces couplings of the gauge fields B_μ and W^i_μ (i = 1,2,3 for the three generations) to the quark fields that can be expressed as

$$\mathcal{D}_\mu = \partial - \frac{1}{2}ig'YB_\mu - igT^aW^a_\mu \tag{1.9}$$

where g' and g are the electroweak coupling constants, while T^a and Y are the generators of the $SU(2)_L$ and the $U(1)_Y$ symmetry groups that introduce the weak isospin and hypercharge, respectively.
In $U(1)_Y$ the field strength tensor $B_{\mu\nu}$ is related to the gauge field by

$$B_{\mu\nu} = \partial_\mu B_\nu - \partial_\nu B_\mu \tag{1.10}$$

whereas in $SU(2)_L$, the field strength tensors $W^i_{\mu\nu}$ are related to the gauge fields by

$$W^i_{\mu\nu} = \partial_\mu W^i_\nu - \partial_\nu W^i_\mu - g\varepsilon^{ijk}W^j_\mu W^k_\nu, \text{ for } i \in 1,2,3. \tag{1.11}$$

The electric charge is related to the weak isospin and the weak hypercharge by

$$Q = T^3 + \frac{Y}{2}. \tag{1.12}$$

Since, the left-handed and right-handed fermion components have different properties

under the gauge group, behaving as doublets and singlets respectively, in the symmetric limit the two chiral components cannot interact with each other. Thereby, the mass term for fermions is forbidden. To give mass to fermions and gauge bosons, the electroweak theory is supplemented by the Higgs mechanism [22],[21] that provides masses by spontaneously breaking the $SU(2)_L \times U(1)_Y$ symmetry (SSB). Therefore, a complex scalar doublet of $SU(2)_L$ with hypercharge $Y = \frac{1}{2}$ is introduced

$$\phi = \begin{pmatrix} \phi^+ \\ \phi^0 \end{pmatrix}. \tag{1.13}$$

The Lagrangian for a scalar particle interaction is defined as follows:

$$\mathcal{L}_{EW}^{SSB} = (\mathcal{D}^\mu \phi)^\dagger \mathcal{D}_\mu \phi - \mu^2 \phi^\dagger \phi - \lambda(\phi^\dagger \phi)^2. \tag{1.14}$$

It is invariant under local $SU(2)_L \times U(1)_Y$ transformations. The covariant derivative $\mathcal{D}_\mu$ has the same form as in Equation (1.9) and introduces the scalar hypercharge in a way that the ϕ^0 does not couple to a photon.
If the scalar field acquires a non-vanishing vacuum expectation value, according to [22], in order to spontaneously break the $SU(2)_L \times U(1)_Y$ symmetry, the following is chosen

$$< 0|\phi|0 >= \frac{1}{\sqrt{2}} \begin{pmatrix} 0 \\ \nu \end{pmatrix}, \tag{1.15}$$

where

$$\phi = e^{i\tau\theta(x)/\nu} \begin{pmatrix} 0 \\ \frac{\nu + h(x)}{\sqrt{2}} \end{pmatrix} \quad \text{and} \quad \nu = \sqrt{-\frac{\mu^2}{\lambda}}, \tag{1.16}$$

with θ and $h(x)$ (Higgs field), being the four real fields. Consequently, the $SU(2)_L \times U(1)_Y$ gets spontaneously broken down to $U(1)_{em}$ sub-group that remains symmetric with respect to the vacuum.
To eliminate the massless scalar expectations, identified as Goldstone bosons, we make the Lagrangian from Equation (1.14), $SU(2)_L$ invariant and therefore remove the dependence on θ^i by rotations. Hence, the kinetic term of the Lagrangian in Equation (1.14) adopts the form

$$(\mathcal{D}_\mu \phi)^\dagger \mathcal{D}_\mu \phi = \frac{1}{2}(\partial_\mu h)(\partial^\mu h) + \frac{1}{8}[(g' B_\mu - g W_\mu^3)^2 + g^2 (W_\mu^1)^2 + g^2 (W_\mu^2)^2](h + \nu)^2. \tag{1.17}$$

From the Lagrangian that describes the Higgs mechanism, we obtain the following fields of the three massive vector bosons, constructed as combinations of the gauge fields B_μ and W_μ^i:

$$\begin{aligned} W_\mu^+ &= \frac{1}{\sqrt{2}}(W_\mu^1 - iW_\mu^2), \\ W_\mu^- &= \frac{1}{\sqrt{2}}(W_\mu^1 + iW_\mu^2), \\ Z_\mu &= \frac{1}{\sqrt{g^2+g'^2}}(gW_\mu^3 - g'B_\mu), \\ A_\mu &= \frac{1}{\sqrt{g^2+g'^2}}(g'W_\mu^3 + gB_\mu). \end{aligned} \tag{1.18}$$

The fields $W_\mu^\pm$ and Z_μ are identified as the heavy vector bosons $W^\pm$ and Z^0 mediating the weak interactions. The Lagrangian of the weak interaction can be written in two terms: one containing the charged current term and the other one the neutral current part, $\mathcal{L}_{weak} = \mathcal{L}_{CC} + \mathcal{L}_{NC}$, with $W_\mu^\pm$ being the mediators of the charged currents and Z_μ the mediator of the neutral currents. The field A_μ accounts for the massless photon. The fundamental coupling constants in Equation 1.18 can be represented in terms of the so-called Weinberg angle yielding the relations [16]

$$\begin{aligned} \tan\theta_W &= g'/g, \\ \cos\theta_W &= g/\sqrt{(g^2+g'^2)}, \\ \sin\theta_W &= g'/\sqrt{(g^2+g'^2)}. \end{aligned} \tag{1.19}$$

Using these definitions the relation between the W and Z mass is obtained to be

$$M_Z = \frac{1}{2}\nu\sqrt{(g^2+g'^2)} = M_w/\cos\theta_W. \tag{1.20}$$

In the Glashow-Weinberg-Salam theory [23], weak neutral current processes are mediated by Z^0 exchange. The associated weak current transition amplitudes, describing the coupling of leptons and quarks to Z^0, can be deduced from the field Z_μ, while the weak charged current part and the electromagnetic part can be extracted from the $W_\mu^\pm$ and A_μ fields. Correspondingly, the fermionic currents are given by

$$J_\mu^0 = \overline{\Psi}(i)\gamma_\mu(\frac{1}{2}T_3\frac{1-\gamma_5}{2} - Q\sin^2\theta_W)\Psi(i) \tag{1.21}$$

$$J_\mu^\pm = \bar{\Psi}(i)\gamma_\mu\frac{1-\gamma_5}{2}\Psi(i) \tag{1.22}$$

$$J_{EM} = \bar{\Psi}(i)\gamma_\mu Q\Psi(i) \tag{1.23}$$

where $\Psi(i)$ represents the isospin doublet for the fermion fields, with i acting as a family index, $1-\gamma_5$ is the left-handed chiral projector, $T^{\pm}$ are the isospin generators associated to the $W_{\mu}^{\pm}$ fields. The charged current describes interactions by which the electric charge is changed, while the remaining two produce transitions that are charge conserving.
Now, the Lagrangian from Equation (1.8) will be written containing two terms: one including interactions between the neutral current and the A_{μ} and Z_{μ} vector bosons, and another describing the interactions between the $W_{\mu}^{\pm}$ bosons with the charged current

$$\mathcal{L}_{EW} = \underbrace{eJ_{EM}A_{\mu} + \frac{g}{\cos\theta_W}(J_{\mu}^{0} - \sin^2\theta_W J_{EM})Z_{\mu}}_{\text{neutral current interaction (NC)}} - \underbrace{\frac{1}{\sqrt{2}}g(J_{+}^{\mu}W_{\mu}^{-} + J_{-}^{\mu}W_{\mu}^{+})}_{\text{charged current interaction (CC)}} \tag{1.24}$$

where e is defined as $e = g\sin\theta_W$.
The quark masses arise from their Yukawa interactions with the Higgs field. The Lagrangian of the Yukawa interaction involves the coupling of the right-handed quark singlets via the scalar field ϕ to left-handed quark field doublets and can be written as

$$\mathcal{L}_{EW}^{Yukawa} = -\bar{\Psi}_L\Gamma_{\mu}\Psi_R\phi - \bar{\Psi}_R\Gamma_{\mu}\Psi_L\bar{\phi} + h.c. \quad \text{where} \quad \phi = i\sigma^2\phi^{\dagger}. \tag{1.25}$$

In order to obtain fermion mass terms that are invariant under $SU(2)_L$ transformations, the Higgs field is required to have isospin equal to 1/2. The Γ_{μ} matrices contain the Yukawa constants, which determine the strength of the fermion couplings to the Higgs fields.
Upon symmetry breaking, the fermion masses are extracted from the mass matrix

$$\mathcal{M} = \frac{\Gamma_{\mu}\nu}{\sqrt{2}} \tag{1.26}$$

with its diagonalization, using unitary transformations U_L and U_R according to

$$\Psi_L' = U_L\Psi_L, \quad \Psi_R' = U_R\Psi_R \tag{1.27}$$

and consequently

$$\mathcal{M} \to \mathcal{M}' = (U_L)^{\dagger}\mathcal{M}U_R. \tag{1.28}$$

The matrices U_L^u, U_R^u, U_L^d and U_R^d transform the left-handed and right-handed quark fields from the weak eigenstate basis, denoted by u and d, to the mass eigenstate basis, denoted by u^m and d^m. Therefore, the Lagrangian describing the interactions

of quarks with the gauge fields in Equation (1.24), can be written in terms of the quark mass eigenstates. The expressions for the neutral currents retain their form when applying the above transformations. This invariance of the neutral currents with respect to the transformations from the weak to mass eigenstates is the reason that no flavor changing neutral currents occur at the tree level. This aspect of the neutral currents is described by the Glashow-Iliopolus-Maiani (GIM) mechanism [21].
The charged current component in the Equation (1.24), in terms of mass eigenstates, takes the form

$$\mathcal{L}_{CC} = \frac{g}{\sqrt{2}}\bar{u}_L[(U_L)^\dagger U_R]\gamma^\mu d_L + h.c. \tag{1.29}$$

where the charged currents J_μ^+ and J_μ^- are described by

$$\begin{aligned} J_\mu^+ &= \bar{u}_L\gamma^\mu d_L = \bar{u}_L^m\gamma^\mu U_L^u U_L^{d\dagger} d_L^m = \bar{u}_L^m\gamma^\mu V_{CKM} d_L^\mu \\ J_\mu^- &= \bar{d}_L\gamma^\mu u_L = \bar{d}_L^m\gamma^\mu U_L^d U_L^{u\dagger} u_L^m = \bar{d}_L^m\gamma^\mu V_{CKM}^\dagger u_L^\mu. \end{aligned} \tag{1.30}$$

The $V_{CKM} = U_L^u U_L^{d\dagger}$ is the 3×3 unitary Cabibbo-Kobayashi-Maskawa (CKM) matrix. The CKM matrix defines the couplings of the $W^\pm$ bosons to the quarks with definite masses in charged current interactions.

1.4.1 CKM Mechanism

In the Standard Model the (Cabibbo-Kobayashi-Maskawa) CKM matrix plays an essential role in understanding of the CP violation. The matrix introduces three generations of quarks, hence becoming an extension of the GIM mechanism [24], [21], which incorporates only two quark generations. The CKM mechanism is given by

$$\begin{pmatrix} d' \\ s' \\ b' \end{pmatrix}_{flavor} = V_{CKM} \begin{pmatrix} d \\ s \\ b \end{pmatrix}_{mass}, \tag{1.31}$$

thus transforming the mass eigenstates into flavor eigenstates. In Equation (1.31) V_{CKM} is the CKM matrix which is explicitly written as

$$V_{CKM} = \begin{pmatrix} V_{ud} & V_{us} & V_{ub} \\ V_{cd} & V_{cs} & V_{cb} \\ V_{td} & V_{ts} & V_{tb} \end{pmatrix} \tag{1.32}$$

where the V_{ij} are the quark mixing transitions from an up-type quark $i = u,c,t$ to

a down-type quark $j = d,s,b$. The CKM matrix is a generalization of the Cabibbo matrix depicted with the highlighted entries in the Equation (1.31).
In general, an arbitrary $n \times n$ matrix of complex elements contains $2n^2$ real parameters. Since, in the Standard Model the CKM matrix is unitary by construction

$$\sum_i (V_{CKM})_{ij}(V_{CKM})^*_{ik} = \delta_{jk} \quad \text{and} \quad \sum_j (V_{CKM})_{ij}(V_{CKM})^*_{kj} = \delta_{ik}, \tag{1.33}$$

the number of the independent parameters is reduced to n^2.
Additional $2n-1$ parameters may be removed by redefinition of the relative quark phases, that can be arbitrarily rotated according to the transformations, e.g:

$$u \to e^{i\phi}u, \quad d \to e^{i\phi}d. \tag{1.34}$$

When these transformations are applied to the CKM matrix elements, we are left with $(n-1)^2$ independent quantities in case of n families. In principle an $n \times n$ unitary matrix consists of $n(n-1)/2$ real rotation angles and $(n-1)(n-2)/2$ complex phases. Consequently, the CKM matrix can be build of

$$\underbrace{\frac{1}{2}n(n-1)}_{angles} + \underbrace{\frac{1}{2}(n-1)(n-2)}_{phases} = \underbrace{(n-1)^2}_{parameters}. \tag{1.35}$$

For $n = 2$, the matrix is real. In this case, CP violation cannot occur, since no complex phase is present. But, for three families of quarks, $n = 3$, the matrix contains three rotation angles and one complex phase. A non-vanishing complex phase is the unique evidence of CP violation in the Standard Model.
Indeed the CKM matrix has nine entries, but not all of them are independent. Therefore, the matrix can be reduced to a certain "canonical" form which is one of the conventions to represent the 3×3 CKM matrix imposing unitarity. This matrix configuration contains 4 free parameters (θ_{12}, θ_{23}, θ_{13} and δ) and its parametrization is given by [25]

$$V_{CKM} = \begin{pmatrix} c_{12}c_{13} & s_{12}c_{13} & s_{13}e^{-i\delta} \\ -s_{12}c_{23} - c_{12}s_{23}s_{13}e^{i\delta} & c_{12}c_{23} - s_{12}s_{23}s_{13}e^{i\delta} & s_{23}c_{13} \\ s_{12}s_{23} - c_{12}c_{23}s_{13}e^{i\delta} & -c_{12}s_{23} - s_{12}c_{23}s_{13}e^{i\delta} & c_{23}c_{13} \end{pmatrix} \tag{1.36}$$

where $s_{ij} = \sin\theta_{ij}$, $c_{ij} = \cos\theta_{ij}$, while δ is the CP violating KM phase that is responsible for all the CP violating phenomena in flavor changing processes in the SM. The angles θ_{ij} can be chosen to belong in the first quadrant, so that s_{ij} and

c_{ij} are taken to be positive. If $\theta_{23} = \theta_{13} = 0$, no mixing occurs between the third generation with the other two and the original Cabibbo-GIM picture is revealed where $\sin\theta_{12} = \lambda \equiv \sin\theta_C$, and θ_C is the Cabibbo angle.
Experimentally it is obtained that $s_{13} \ll s_{23} \ll s_{12} \ll 1$, hence it is very convenient to use the Wolfenstein parametrization [26] of the matrix. For this the following definitions are used

$$\begin{aligned} s_{12} = \lambda &= \frac{|V_{us}|}{\sqrt{|V_{ud}|^2 + |V_{us}|^2}}, \\ s_{23} = A\lambda^2 &= \lambda\left|\frac{V_{cb}}{V_{us}}\right|, \\ s_{13}e^{i\delta} = V_{ub}^* = A\lambda^3(\rho + i\eta) &= \frac{A\lambda^3(\bar{\rho} + i\bar{\eta})\sqrt{1 - A^2\lambda^4}}{\sqrt{1-\lambda^2}[1 - A^2\lambda^4(\bar{\rho} + i\bar{\eta})]}, \end{aligned} \tag{1.37}$$

where

$$\bar{\rho} \equiv (1 - \frac{\lambda^2}{2})\rho, \qquad \bar{\eta} \equiv (1 - \frac{\lambda^2}{2})\eta. \tag{1.38}$$

The diagonal CKM matrix elements are close to unity, while the off-diagonal elements are very small, with the hierarchy $V_{ud} \gg V_{us} \gg V_{ub}$. In terms of Wolfenstein parametrization taking the above definitions from Equation (1.37) the matrix is explicitly written as

$$V_{CKM} \approx \begin{pmatrix} 1 - \lambda^2/2 & \lambda & A\lambda^3(\bar{\rho} - i\bar{\eta}) \\ -\lambda & 1 - \lambda^2/2 & A\lambda^2 \\ A\lambda^3(1 - \bar{\rho} - i\bar{\eta}) & -A\lambda^2 & 1 \end{pmatrix} + O(\lambda^5) \tag{1.39}$$

which can be understood as an expansion in $\lambda = |V_{us}|$ up to the order of λ^3. In Equation (1.39) $\lambda \approx 0.23$, the sine of the Cabibbo angle plays the role of an expansion parameter. The parameters A, ρ and η turn out to be of the order one. From the Equation (1.39) it is obvious that matrix elements V_{ub} and V_{td} contain an irreducible complex phase which is responsible for the CP violation.

1.4.2 Unitarity Triangle

The unitarity relations of the CKM matrix lead to six independent relations that can be drawn as triangles in the complex plane and are given by

$$
\begin{aligned}
&\underbrace{V_{ud}^* V_{us}}_{\lambda} + \underbrace{V_{cd}^* V_{cs}}_{\lambda} + \underbrace{V_{td}^* V_{ts}}_{\lambda^5} = 0 \\
&\underbrace{V_{ud}^* V_{ub}}_{\lambda^3} + \underbrace{V_{cd}^* V_{cb}}_{\lambda^3} + \underbrace{V_{td}^* V_{tb}}_{\lambda^3} = 0 \\
&\underbrace{V_{us}^* V_{ub}}_{\lambda^4} + \underbrace{V_{cs}^* V_{cb}}_{\lambda^2} + \underbrace{V_{ts}^* V_{tb}}_{\lambda^2} = 0 \\
&\underbrace{V_{ud} V_{cd}^*}_{\lambda} + \underbrace{V_{us} V_{cs}^*}_{\lambda} + \underbrace{V_{ub} V_{cb}^*}_{\lambda^5} = 0 \\
&\underbrace{V_{ud} V_{td}^*}_{\lambda^3} + \underbrace{V_{us} V_{ts}^*}_{\lambda^3} + \underbrace{V_{ub} V_{tb}^*}_{\lambda^3} = 0 \\
&\underbrace{V_{cd} V_{td}^*}_{\lambda^4} + \underbrace{V_{cs} V_{ts}^*}_{\lambda^2} + \underbrace{V_{cb} V_{tb}^*}_{\lambda^2} = 0.
\end{aligned}
\tag{1.40}
$$

Four of these six triangles are almost degenerate, meaning that one side of the triangle is much shorter than the remaining two. Only two of these relations are triangles which sides are of similar length, which means that they are of the same order in terms of Wolfenstein parameter λ. These relations are

$$
\underbrace{V_{ud} V_{ub}^*}_{\lambda^3} + \underbrace{V_{cd} V_{cb}^*}_{\lambda^3} + \underbrace{V_{td} V_{tb}^*}_{\lambda^3} = 0 \tag{1.41}
$$

and

$$
\underbrace{V_{ud} V_{td}^*}_{\lambda^3} + \underbrace{V_{us} V_{ts}^*}_{\lambda^3} + \underbrace{V_{ub} V_{tb}^*}_{\lambda^3} = 0. \tag{1.42}
$$

These two non-degenerate triangles almost coincide. From the CKM matrix one can obtain $V_{ud} \approx V_{tb} = 1$, which is why the sides of these triangles have about equal lengths. Also, this is the reason of coinciding and the same size of the third side $V_{cd}^* V_{cb} = V_{us} V_{ts}^*$. Since, V_{us} and $-V_{cd}$ are of the order λ according to the CKM matrix, the following is obtained

$$
V_{ts}^* = -V_{cb}. \tag{1.43}
$$

Therefore, only one non-degenerate unitarity triangle is derived and described as a complex conjugate of the corresponding relation in Equation 1.40

$$
V_{ud} V_{ub}^* + V_{cd} V_{cb}^* + V_{td} V_{tb}^* = 0. \tag{1.44}
$$

It is very convenient to normalize this triangle by $V_{cd} V_{cb}^*$ that in the standard

parametrization is almost real, which results in this side being exactly from (0, 0) to (1, 0) in the complex plane. The apex of the triangle has coordinates $(\bar{\rho},\bar{\eta})$ given by Equation (1.38). This triangle is shown in Figure 1.1.

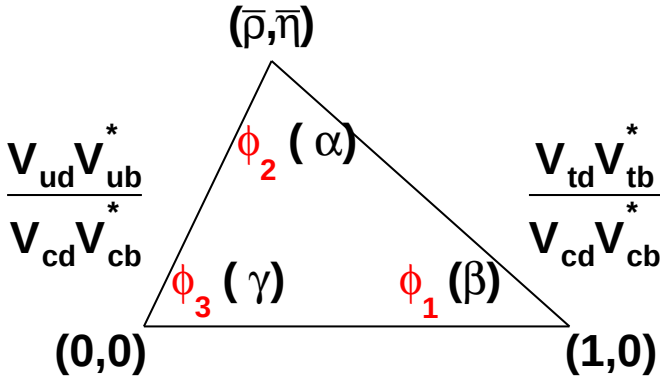

Figure 1.1: Graphical representation of the unitarity constraint $V_{ud}V_{ub}^* + V_{cd}V_{cb}^* + V_{td}V_{tb}^* = 0$ as a triangle in a complex plane.

Due to the sizable angles, a large CP asymmetry in B decays in the SM are expected. Therefore, the B meson system is perfect for testing the CKM formalism and thus the SM itself.
The unitarity triangle angles for the B meson system are defined as

$$\phi_1 = \beta \equiv arg[-V_{cd}V_{cb}^*/V_{td}V_{tb}^*] \tag{1.45}$$

$$\phi_2 = \alpha \equiv arg[-V_{td}V_{tb}^*/V_{ud}V_{ub}^*] \tag{1.46}$$

$$\phi_3 = \gamma \equiv arg[-V_{ud}V_{ub}^*/V_{cd}V_{cb}^*]. \tag{1.47}$$

Equations (1.45), (1.46) and (1.47) show that the phase of the matrix element V_{td} plays a fundamental role in generating a CP violation, thus enabling measurements of the angles ϕ_1, ϕ_2 and ϕ_3. There are two notations of the angles, one according to the BaBar collaboration (β,α,γ) and the second notation coming from Belle experiment (ϕ_1,ϕ_2,ϕ_3).
The Standard Model allows to construct the unitarity triangle using the sides, the angles or the combination of both. Any discrepancy that appears between the observed and the predicted value indicates a certain dynamics beyond the Standard Model. If any of the unitarity triangles does not close exactly, the unitarity of the CKM matrix would be broken, thus leading to incompleteness of the SM and therefore new physics beyond the SM. The current results of these measurements are shown in Figure 1.2.

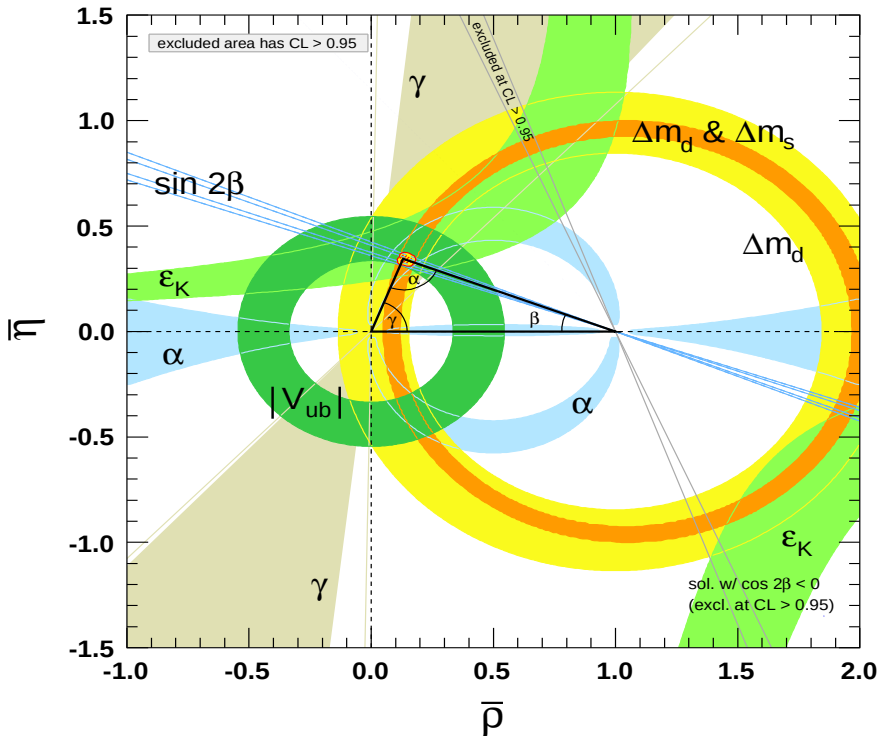

Figure 1.2: Current constraints on the unitarity CKM triangle in the $\bar{\rho}$, $\bar{\eta}$ plane.

Up to now, the obtained measurements [27] are in agreement with the CKM SM predictions, yet discrepancies may appear once the constraints are tightened up furthermore [28]. To achieve these high precision measurements very high statistics are needed. In addition it is also necessary to have good control of both, experimental and theoretical uncertainties in CP sensitive as in the insensitive rates.

1.5 CP-Violation in the B meson system

Two kinds of B mesons exist in Nature: neutral and charged. Neutral B mesons are composed of bottom anti-quark and either down quark ($B^0 = (\bar{b}d)$) or strange quark ($B_s^0 = (\bar{b}s)$). Charged B mesons contain bottom anti-quark and an up quark ($B^+ = (\bar{b}u)$). B mesons are produced by the strong interactions but they decay weakly. Their mass $m_B \sim 5.279\,\mathrm{GeV}/c^2$ [29] is large due to the large b mass which is $m_b \approx 4.3\,\mathrm{GeV}/c^2$.

B mesons provide a very rich field for investigating CP violation, mainly due to two reasons. CP violation expected in the B meson system is quite large due to the large angles in the unitarity triangle (see Equation 1.41). The second plus that goes in favor of studying CP violation in B mesons is the lifetime of these particles. Namely, B

mesons are also characterized by a relatively long lifetime

$$\tau_{B^0} = (1.519 \pm 0.007) \times 10^{-12}, \tag{1.48}$$

due to the small value of the coupling constant $|V_{cb}| = \lambda^2$ (see Equations (1.32), (1.37)), which defines the strength of the dominant decay of the b quark, $b \to c$.
This situation offers very good conditions for study of $B^0 - \overline{B^0}$ oscillation and the B meson lifetime itself. The dominant decays occur through $b \to c$ transitions, whereas those that undergo via $b \to u, d, s$ (such as $B^0 \to \psi(2S)\pi^0$) are considered rare because they are smaller, compared to the dominant one. In the CKM matrix this is described by their small corresponding matrix elements.

1.5.1 B meson mixing

The neutral B mesons, B^0 and B_S^0 can oscillate between their particle and antiparticle states due to the flavor-changing weak interactions. This oscillation from matter to anti-matter can be used to measure fundamental parameters of the standard model and in addition to have even more striking effects, such as breaking the matter-antimatter symmetry in the Universe.
The only hadrons that can undergo these oscillations are the following mesons: K^0, D^0, B^0 and B_S^0. The π^0 is its own antiparticle, the top quark is extremely heavy thus decays before forming stable hadrons, whereas exited meson states decay strongly or electromagnetically before any mixing can occur.
Regarding the B meson system, an arbitrary linear combination of the two neutral B meson flavor eigenstates is given by

$$\Psi(t) = \Psi_1(t)|B^0> + \Psi_2(t)|\overline{B^0}> \equiv \begin{pmatrix} \Psi_1(t) \\ \Psi_2(t) \end{pmatrix}. \tag{1.49}$$

Applying the free Schrödinger equation for the $\Psi(t)$ it is obtained

$$i\hbar\frac{\partial}{\partial t}\Psi = H\Psi \equiv (M - \frac{i}{2}\Gamma)\Psi, \tag{1.50}$$

where H is the Hamiltonian operator, consisting of mass and decay 2×2 Hermitian matrices, M and Γ [30],[31]. Since, the off-diagonal elements of the Hamiltonian H are associated with flavor changing transitions $B^0 \leftrightarrow \overline{B^0}$, in order for CP to be conserved, the term $H_{12} = H_{21}^*$ must be satisfied. If B^0 couples to itself the same way as the $\overline{B^0}$, the diagonal elements of the Hamiltonian H must be equal, $H_{11} = H_{22}$, assuming the invariance of CPT symmetry.

By diagonalizing the Hamiltonian we obtain two eigenvalues:

$$\mu_{1,2} = M - \frac{i}{2}\Gamma \pm \sqrt{(M_{12} - \frac{i}{2}\Gamma_{12})(M_{12}^* - \frac{i}{2}\Gamma_{12}^*)} \quad . \tag{1.51}$$

Their corresponding mass eigenstates are given as

$$|B_L >= p|B^0 > +q|\overline{B^0} >), \quad \text{for } \mu_1, \tag{1.52}$$

$$|B_H >= p|B^0 > -q|\overline{B^0} >), \quad \text{for } \mu_2 \ . \tag{1.53}$$

The ratio between p and q is defined as

$$\frac{p}{q} = \sqrt{\frac{M_{12}^* - \frac{i}{2}\Gamma_{12}^*}{M_{12} - \frac{i}{2}\Gamma_{12}}} \equiv \frac{1-\varepsilon}{1+\varepsilon}, \tag{1.54}$$

with

$$p = \frac{1+\varepsilon}{\sqrt{2(1+|\varepsilon|^2)}} \quad \text{and} \quad q = \frac{1-\varepsilon}{\sqrt{2(1+|\varepsilon|^2)}}, \tag{1.55}$$

where the complex coefficients, p and q satisfy the normalization condition $\sqrt{p^2+q^2} = 1$.
In case of CP invariance, the probability of one flavor being transformed into the opposite flavor is the same for both, the neutral meson B^0 and its antiparticle $\overline{B^0}$. This means that $M_{12} = M_{12}^*$ and $\Gamma_{12} = \Gamma_{12}^*$ and therefore $\varepsilon = 0$ and $p = q$. Those eigenstates, which represent the mass eigenstates, are also CP eigenstates.
The masses and lifetime values that correspond to these mass-eigenstates can be extracted from the eigenvalues

$$m_{1,2} = \mathcal{R}e(\mu_{1,2}) \qquad \Gamma_{1,2} = -2\Im(\mu_{1,2}). \tag{1.56}$$

The B mesons show some basic differences when compared to the neutral K meson system [32], [1]. Similarly as for the Kaon case, in addition to the two states with definite masses and lifetimes, the heavy B_H and light B_L state also exist. However, unlike the two kaon CP eigenstates K_S^0 and K_L^0, the eigenstates of the B meson B_H and B_L have almost identical lifetimes $\Gamma_H \sim \Gamma_L \equiv \Gamma\,(\Delta\Gamma = \Gamma_H - \Gamma_L,\ \Delta\Gamma/\Gamma \sim O(10^{-3}))$.
Additional important difference between the B and the K meson system is that the box diagram in Figure 1.3 showing $B^0 - \overline{B^0}$ oscillations, is dominated by virtual t-quark exchange because according to the CKM matrix $V_{tb} \sim 1$ is a dominant element. The decay rate contributing terms $(m_q/m_b)^2$ are much smaller for light quarks than for the

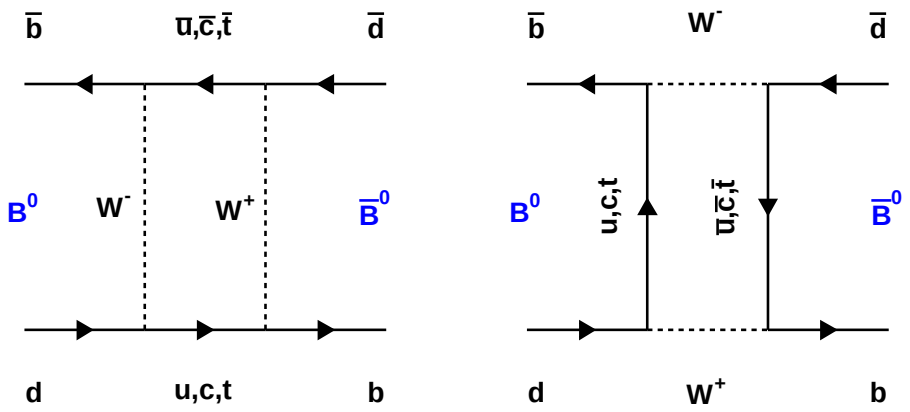

Figure 1.3: Example of leading order contribution to neutral meson mixing.

heavy t quark.
Furthermore, the mass eigenstates states B_H and B_L can be considered as pure CP states, since $\frac{q}{p} \sim 1$ is a good approximation. By using Equation (1.54) and the corresponding CKM matrix elements this approximation is obtained

$$\begin{aligned} \frac{q}{p} = \sqrt{\frac{M_{12}^*}{M_{12}}} + O(\frac{\Gamma_{12}}{M_{12}}) \simeq \frac{V_{tb}^* V_{td}}{V_{tb} V_{td}^*} \\ |\frac{q}{p}| \sim 1. \end{aligned} \tag{1.57}$$

The term depending on $\frac{\Gamma_{12}}{M_{12}} \sim (\frac{m_b}{m_t})^2 \approx 10^{-2}$ can be neglected.
B_H and B_L are very convenient for describing the evolution of particles in time. In the SM the interaction shown in Figure 1.3 results in a transition $B^0 \leftrightarrow \overline{B^0}$ and hence the mass eigenstates are not flavor eigenstates.

1.5.2 Time Evolution of Neutral B Mesons

The time evolution of neutral B mesons is given by

$$|B^0(t)> = g_+(t)|B^0> + \frac{q}{p} g_-(t)|\overline{B}^0>, \tag{1.58}$$

$$|\overline{B}^0(t)> = g_+(t)|\overline{B}^0> + \frac{p}{q} g_-(t)|B^0>, \tag{1.59}$$

where

$$g_{\pm}(t) \equiv \frac{1}{2}(e^{-im_H t-\frac{1}{2}\Gamma_H t} \pm e^{-im_L t-\frac{1}{2}\Gamma_L t}). \tag{1.60}$$

With the average mass $\overline{m} = (m_H + m_L)/2$ and average decay width $\overline{\Gamma} = (\Gamma_H + \Gamma_L)/2$ Equation (1.60) can be written as

$$g_{\pm} = \frac{1}{2}e^{-i\overline{m}t}e^{-\frac{1}{2}\overline{\Gamma}t}(e^{i\Delta mt/2}e^{-\Delta\Gamma t/4} \pm e^{-i\Delta mt/2}e^{\Delta\Gamma t/4}). \tag{1.61}$$

Since, for neutral B mesons the lifetime difference between the two mass eigenstates can be ignored, $\Delta\Gamma = 0$, the Equation (1.61) becomes

$$g_{\pm} = e^{-\Gamma t/2}\frac{e^{i\Delta mt/2} \pm e^{-i\Delta mt/2}}{2} \tag{1.62}$$

where $e^{-i\overline{m}t}$ is removed by convention.
By inserting Equation (1.62) in Equations (1.58) and (1.59), the time evolution of neutral B mesons takes the form

$$\begin{aligned} |B^0(t)> &= \frac{1}{2}e^{-\Gamma t/2}[(1+e^{-i\Delta mt})|B^0> + \frac{q}{p}(1-e^{-i\Delta mt})|\overline{B}^0>] \\ |\overline{B}^0(t)> &= \frac{1}{2}e^{-\Gamma t/2}[\frac{p}{q}(1-e^{-i\Delta mt})|B^0> + (1+e^{-i\Delta mt})|\overline{B}^0>], \end{aligned} \tag{1.63}$$

or the form

$$\begin{aligned} |B^0(t)> &= e^{-\Gamma t/2}[\cos(\frac{\Delta mt}{2})|B^0> + i\frac{q}{p}\sin(\frac{\Delta mt}{2})|\overline{B}^0>] \\ |\overline{B}^0(t)> &= e^{-\Gamma t/2}[i\frac{p}{q}\sin(\frac{\Delta mt}{2})|B^0> + \cos(\frac{\Delta mt}{2})|\overline{B}^0>]. \end{aligned} \tag{1.64}$$

The probability ratio of mixing through box diagrams as given in Figure 1.3 is $\Delta m/\Gamma = 0.770 \pm 0.008$ [29] for the B meson system. Therefore, the matrix element for the decay is more prominent than that for the mixing, which means that most B mesons decay before changing flavor.

1.5.3 Time-dependent CP-Violation

Because both B^0 and $\overline{B}^0$ can decay into the same final state, with definite CP parity, the corresponding decay amplitudes are defined by

$$A_{CP} =< f_{CP}|B^0 >, \quad \bar{A}_{CP} =< f_{CP}|\overline{B}^0 > . \tag{1.65}$$

Using the time evolution from Equation (1.64), the time-dependent decay amplitudes

are given by

$$\begin{aligned} |A_{CP}(t)> &= A_{CP}e^{-\Gamma t/2}(\cos(\frac{\Delta mt}{2})|B^0> + i\lambda_{CP}\sin(\frac{\Delta mt}{2})|\bar{B}^0>) \\ |\bar{A}_{CP}(t)> &= \bar{A}_{CP}e^{-\Gamma t/2}(\frac{i}{\lambda_{CP}}\sin(\frac{\Delta mt}{2})|B^0> + \cos(\frac{\Delta mt}{2})|\bar{B}^0>) \end{aligned} \tag{1.66}$$

where λ_{CP} is defined as

$$\lambda_{CP} = \frac{q}{p}\frac{\bar{A}_{CP}}{A_{CP}} \ . \tag{1.67}$$

The time-dependent decay rates are given by the squares of the decay amplitudes

$$\begin{aligned} \Gamma(B^0 \to f_{CP}) &= |< f_{CP}|B^0(t)>|^2, \\ \Gamma(\bar{B}^0 \to f_{CP}) &= |< f_{CP}|\bar{B}^0(t)>|^2. \end{aligned} \tag{1.68}$$

The time dependent CP asymmetry rate is defined as

$$\begin{aligned} a_{CP}(t) &\equiv \frac{\Gamma(\bar{B}^0 \to f_{CP}) - \Gamma(B^0 \to f_{CP})}{\Gamma(B^0 \to f_{CP}) + \Gamma(B^0 \to f_{CP})} \\ &= \frac{(|\lambda_{CP}|^2 - 1)\cos(\Delta mt) + 2\Im(\lambda_{CP})\sin(\Delta mt)}{1 + |\lambda_{CP}|^2} \\ &= \mathcal{A}_{CP}\cos(\Delta mt) + \mathcal{S}_{CP}\sin(\Delta mt), \end{aligned} \tag{1.69}$$

where

$$\mathcal{A}_{CP} \equiv \frac{|\lambda_{CP}|^2 - 1}{|\lambda_{CP}|^2 + 1}, \ \ \mathcal{S}_{CP} \equiv \frac{2\Im(\lambda_{CP})}{|\lambda_{CP}|^2 + 1}. \tag{1.70}$$

$\mathcal{A}_{CP}$ is a parameter that measures the direct CP violation, while $\mathcal{S}_{CP}$ is responsible for the mixing-induced CP violation.
In order to access these parameters, one needs to measure the time-dependent decay rates of B^0 and $\bar{B}^0$ decaying into a common CP final state. When rare decays are in question then this measurement is experimentally challenging.

1.5.4 Types of CP Violation

The decay amplitudes A_f, $A_{\bar{f}}$, $\bar{A}_f$ and $\bar{A}_{\bar{f}}$ of a given meson and its antiparticle, decaying respectively into a final state f or $\bar{f}$ are denoted by

$$\begin{aligned} A_f &= < f|H|M >, \\ A_{\bar{f}} &= < \bar{f}|H|M >, \\ \bar{A}_f &= < f|H|\bar{M} >, \\ \bar{A}_{\bar{f}} &= < \bar{f}|H|\bar{M} >, \end{aligned} \tag{1.71}$$

where H is the Hamiltonian.
The CP violation parameter then is represented as a combination of the ratio between the decay amplitudes A_f and $\bar{A}_f$ and the ratio of the two mixing coefficients p and q as given in Equation 1.67.
Depending on the λ_{CP}, three types of CP violation can be distinguished: CP violation in decay, CP violation in mixing and CP violation that arises from the interference between decay and mixing.
Furthermore, CP violation in charged meson decays can depend only on the combination $|\bar{A}_{\bar{f}}/A_f|$. In the case of neutral mesons the situation is more complicated, since the violation of CP depends on meson oscillations, $|q/p|$ and on $(\frac{q}{p})(\frac{\bar{A}_f}{A_f})$.

1.5.5 CP-Violation in Decay

In the case when CP violation in decay occurs, the decay amplitudes for a particle and its antiparticle in a certain final state or conjugated final state differ from one another. An example of this type of CP violation, also known as direct CP violation, is shown in Figure 1.4 and is defined by

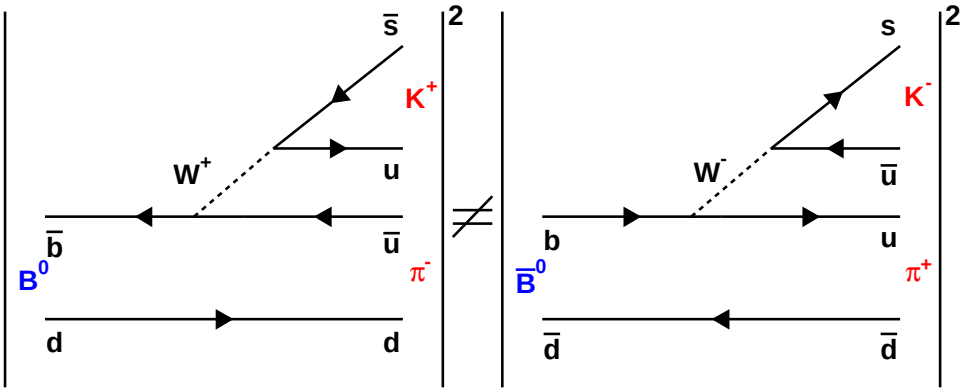

Figure 1.4: CP violation in decay in the B meson system.

$$|\bar{A}_{\bar{f}}/A_f| \neq 1 \tag{1.72}$$

This means that the two CP conjugate states have different absolute values for their decay amplitudes. This kind of process is possible for charged and for neutral mesons. In charged meson decays where no mixing effects are involved, this type of CP violation is the only possible source of CP asymmetries and is defined as:

$$\mathcal{A}_f \equiv \frac{\Gamma(M^- \to \bar{f}) - \Gamma(M^+ \to f)}{\Gamma(M^- \to \bar{f}) + \Gamma(M^+ \to f)} = \frac{|\bar{A}_{\bar{f}}/A_f|^2 - 1}{|\bar{A}_{\bar{f}}/A_f|^2 + 1}. \tag{1.73}$$

1.5.6 CP-Violation in Mixing

In the case of neutral mesons, flavor specific final states can reveal CP violation via $M^0 - \bar{M}^0$ oscillations. Flavor specific decays are those that can come either from the neutral meson or from its antiparticle, but not from both:

$$M^0 \to f \nleftarrow \bar{M}^0 \quad \text{or} \quad M^0 \nrightarrow f \leftarrow \bar{M}^0 \tag{1.74}$$

The violation of CP in $B^0 - \bar{B}^0$ mixing is depicted in Figure 1.5 and is described by

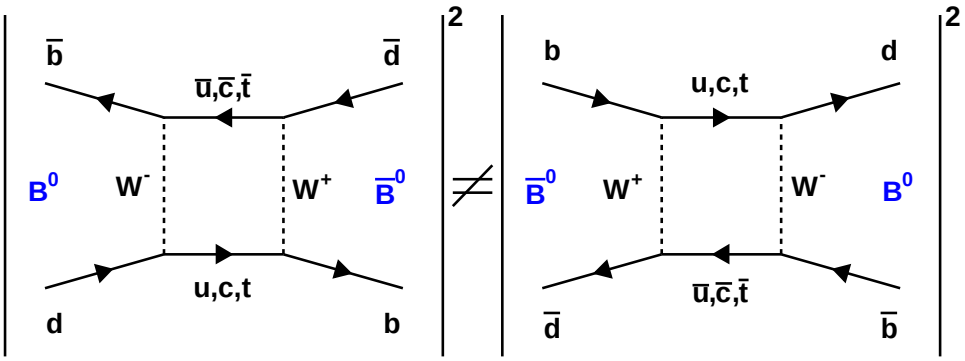

Figure 1.5: CP violation in $B^0 - \bar{B}^0$ mixing.

$$|q/p| \neq 1 \tag{1.75}$$

This kind of CP violation is only observable for neutral mesons. It originates from the fact that no such choice of phase convention exist in order to make the mass eigenstates identical to the CP eigenstates. Regarding the charged mesons, mixing between charged particles is not allowed due to charge conservation.

A typical example of a CP violation in mixing is seen in the decays of K mesons. In particular, prominent flavor specific channels for neutral mesons like K^0, D^0 or B^0 are provided by semileptonic decays. When charged current semileptonic neutral meson decays ($M^0, \bar{M}^0 \to l^{\pm} X$) are considered, then the CP violation in mixing is the only possible source of CP asymmetry. In such case $|A_{l^+X}| = |\bar{A}_{l^-X}|$ and $A_{l^-X} = \bar{A}_{l^+X} = 0$, thus the asymmetry is given by

$$\mathcal{A}_{SL} \equiv \frac{d\Gamma/dt[\overline{M}^0(t) \to l^+X] - d\Gamma/dt[M^0 \to l^-X]}{d\Gamma/dt[\overline{M}^0(t) \to l^+X] + d\Gamma/dt[M^0 \to l^-X]} = \frac{1-|q/p|^4}{1+|q/p|^4}. \tag{1.76}$$

1.5.7 CP-Violation in Interference between Decay and Mixing

CP violation can also appear when the particle and the antiparticle decay into a common final state, $M^0 \to f$ and $\bar{M}^0 \to f$. In order for this to happen the final state must be a CP eigenstate, $f = f_{CP}$. Hence, the CP violation in interference between decay ($M^0 \to f_{CP}$) and mixing ($M^0 \to \overline{M}^0 \to f_{CP}$) where different states decay to a common final CP eigenstate is defined by

$$\Im(\lambda_f) \neq 0, \tag{1.77}$$

where λ_f is given by the Equation 1.67.
This type of CP violation obviously depends on the neutral meson mixing and therefore is time-dependent. This is the reason why it sometimes bears the name time-dependent CP asymmetry.
The effect of CP violation that occurs due to the interference between the decays to a common final state with and without mixing is proportional to the imaginary part of λ_f as shown in Equation (1.77) and thus can be non-zero even when the absolute value of $|A_f/\bar{A}_f| = |q/p| = 1$. Decays where this condition is fulfilled are particularly interesting. If this is the case then the observed asymmetry can be interpreted as a direct measurement of certain differences of phases of the CKM matrix elements, with no theoretical uncertainties.
CP violation as a result of interference between decay and mixing is observed for example in the decays of neutral mesons such as

$$K^0 \to \pi\pi \leftarrow \bar{K}^0 \tag{1.78}$$

$$D^0 \to K\bar{K}, \pi\pi, K\pi, \bar{K}\pi \leftarrow \bar{D}^0 \tag{1.79}$$

$$B^0 \to \psi K_S, D\bar{D}, \pi\pi \leftarrow \bar{B}^0. \tag{1.80}$$

The situation of CP violation in interference considered in the B meson system is shown in Figure 1.6.

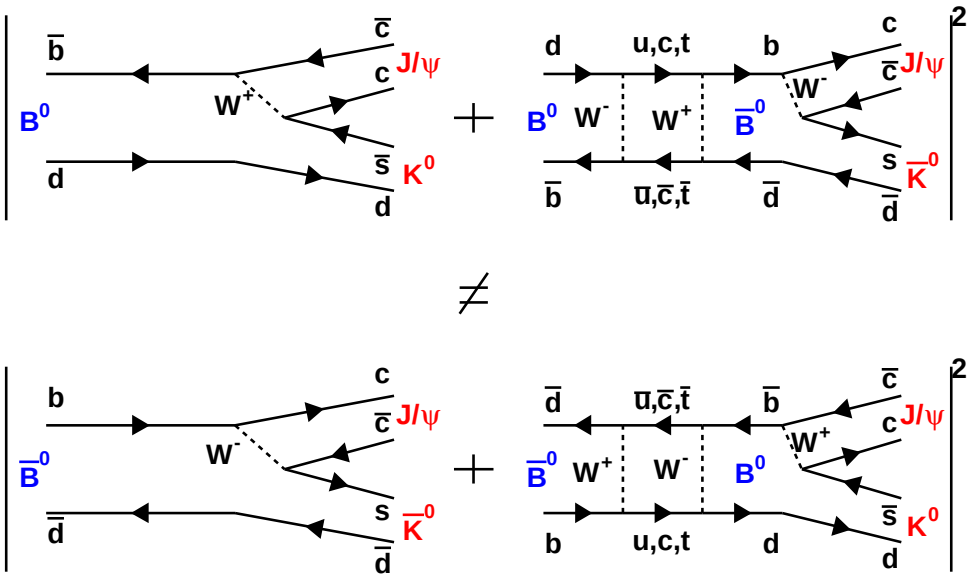

Figure 1.6: CP violation via mixing and decay regarding the B meson system.

Considering decays of neutral mesons into common CP eigenstate, the CP violation is described by the following time-dependent asymmetry:

$$A_{CP}(t) \equiv \frac{d\Gamma/dt[\overline{M}^0(t) \to f_{CP}] - d\Gamma/dt[M^0 \to f_{CP}]}{d\Gamma/dt[\overline{M}^0(t) \to f_{CP}] + d\Gamma/dt[M^0 \to f_{CP}]}. \tag{1.81}$$

The asymmetry calculated by the time-dependent decay rates from Equation (1.68) can be given as

$$A_{CP}(t) = \frac{\mathcal{S}_{CP}\sin(\Delta m t) - \mathcal{A}_{CP}\cos(\Delta m t)}{\cosh(\Delta\Gamma t/2) - \mathcal{A}_{\Delta\Gamma}\sinh(\Delta\Gamma t/2)}, \tag{1.82}$$

where $\mathcal{S}_{CP}$ and $\mathcal{A}_{CP}$ are described by Equation 1.70, while $\mathcal{A}_{\Delta\Gamma}$ is given by

$$\mathcal{A}_{\Delta\Gamma} = \frac{2\mathcal{R}e(\lambda_{CP})}{1+|\lambda_{CP}|^2} \tag{1.83}$$

The Equation representing the relation between the CP parameters is given by

$$|\mathcal{S}_{CP}|^2 + |\mathcal{A}_{CP}|^2 + |\mathcal{A}_{\Delta\Gamma}|^2 = 1. \tag{1.84}$$

It shows explicitly that the observed CP asymmetry in this case consists of two sources, which can be clearly separated by the time dependence. The corresponding parameters $\mathcal{S}_{CP}$ and $\mathcal{A}_{CP}$ measure mixing-induced and direct CP violation, respectively. The

parameter $\mathcal{A}_{\Delta\Gamma}$ provides additional observable in neutral meson decays with sizable decay width difference $\Delta\Gamma$.

1.5.8 Measurement of CP-Violation

Since, B mesons are so heavy a high variety of decay modes are available and the branching fractions for the modes usable for CP violation are generally small. Therefore, huge amount of B meson of the order of $O(10^8)$ is necessary to obtain significant measurements of CP violation. Such high precision measurements are provided by machines like PEP II at SLAC [4] and the KEKB accelerator at KEK. These machines enable the required conditions for performing an experimental determination of the angles and sides of the unitarity triangle using B meson decays.
These B factories produce $B\bar{B}$ pairs at the $\Upsilon(4S)$ resonance, at $10.579\,\mathrm{GeV}$, being the lowest energy at which B mesons can be produced in an e^+e^- collider. Furthermore, the produced B mesons at the $\Upsilon(4S)$ resonance are essentially at rest in the center-of-mass system (CMS). $\Upsilon(4S)$ decays to more than 95 % into $B\bar{B}$ pairs. The fractions of produced charged and neutral pairs is almost identical, namely B^+B^- $(51.3\pm0.6)\%$ and $B^0\bar{B^0}$ $(48.7\pm0.6)\%$, respectively [29].
The $\Upsilon(4S)$ has the quantum numbers $J^{PC}=1^{--}$. Since, C and P are conserved in strong interactions, their values must be the same for the $B\bar{B}$ pair. The B mesons are pseudo-scalars ($J^P=0^-$), produced in a coherent state $B^0\bar{B^0}$, with the relative orbital momentum $l=1$. The two pseudo scalar B mesons must be produced in p-wave state to conserve angular momentum. The parity of the system is $P=(-1)^l=-1$ and requires the spatial part of the wave function of the $B^0\bar{B^0}$ state to be anti-symmetric. Therefore, the only possibility to achieve this is that the $B^0\bar{B^0}$ pair oscillates coherently. The quantum mechanically entangled state is given by

$$|\Psi(t_1,t_2)>=\frac{1}{\sqrt{2}}(|B_1^0(t_1)>|\bar{B_2^0}(t_2)>-|\bar{B_1^0}(t_1)>|B_2^0(t_2)>. \tag{1.85}$$

The coherence of $B^0\bar{B^0}$ pair is preserved until one in the particle pair decays. After the decay of one of the B mesons, the flavor of the remaining meson is tagged and continues evolving in time. Because of the $B^0\bar{B^0}$ mixing effect one can observe events with both particles decaying as B^0 or $\bar{B^0}$, but only if these decays occur at different times.
Substituting the quantum mechanical state in Equation 1.64, the following time evolution is obtained

$$|\Psi(t_1,t_2)>=\frac{1}{\sqrt{2}}e^{-\Gamma(t_1+t_2)/2}[\cos\frac{\Delta m_d\Delta t}{2}|B_1^0>|\bar{B_2^0}>+i\frac{q}{p}\sin\frac{\Delta m_d\Delta t}{2}|\bar{B_1^0}>|B_2^0>], \tag{1.86}$$

where $\Delta t=t_2-t_1$. If we can determine Δt and the flavor of one B meson, then the

flavor and the time evolution of the other B meson is known.
For the time-dependent CP violation measurements, one of the B mesons is reconstructed in a CP eigenstate, e.g. $B^0 \to J/\psi K_S^0$. From the remaining particles in the event, the vertex of the other B meson is reconstructed and depending on its daughter particles its flavor is identified. The procedure of flavor identification of the other B meson is called tagging. For example, the tag side reveals its flavor by the sign of the produced lepton: If the produced lepton on the tag side carries negative charge (signaling a $\overline{B}^0$) then the B meson reconstructed from a CP eigenstate is B^0. If the tag side has a positively charged lepton, then the reconstructed B meson on the CP side is $\overline{B}^0$.
Despite the fact that B mesons have a long lifetime, yet it is very difficult to measure its value as precise as needed for the study of CP violation. Experimentally, a lifetime measurement in order of a pico second is impossible with current technology. This is why B-factories are constructed with asymmetric beam energies: B mesons at a B-factory are produced with a Lorentz boost along the electron beam, z-direction making it possible to measure the distance Δz between the two decay vertices of the B mesons. Since, the produced B^0 and $\overline{B}^0$ are approximately at rest in the $\Upsilon(4S)$ center-of-mass system, the measurements of the displaced decay vertices of the produced B mesons allow to translate the flight length difference Δz into a proper decay time difference Δt: $\Delta t \simeq \Delta z/(\beta\gamma c)$. The vertex position of the f_{CP} decay is reconstructed using charged tracks (for example, lepton tracks from J/ψ in $B^0 \to J/\psi K_S^0$ decays), while that of the f_{tag} decay is reconstructed using well-reconstructed tracks that are not assigned to f_{CP}. In Figure 1.7 the production of the two coherent B meson pairs and their corresponding decays is explicitly depicted.

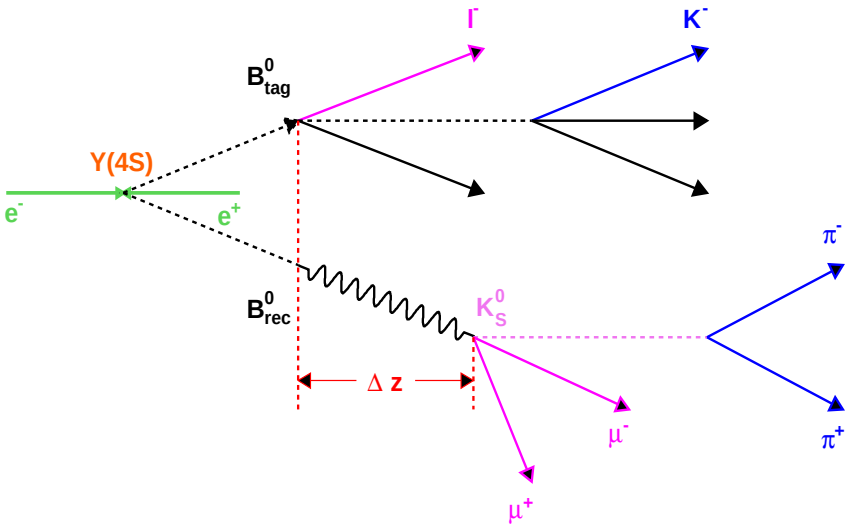

Figure 1.7: The decay of $B^0\overline{B}^0$ into the golden mode $J/\psi K_S^0$.

Therefore, the combination of the flavor obtained from the second B meson and the time difference measurement, provides convenient conditions to measure the time-dependent CP violating asymmetry.
Considering the decay chain $\Upsilon(4S) \to B^0\bar{B^0} \to f_{CP}\, f_{tag}$, where one B meson decays at time t_{CP} into CP final state f_{CP}, while the other B meson at time t_{tag} decays to a final state f_{tag} that distinguishes between the B^0 and $\bar{B^0}$, the decay rate is time-dependent and is given by

$$\mathcal{P}(\Delta t) = \frac{e^{-|\Delta t|/\tau_{B^0}}}{4\tau_{B^0}}(1 + q[\mathcal{S}_{CP}\sin(\Delta m_d \Delta t) + \mathcal{A}_{CP}\cos(\Delta m_d \Delta t)]). \tag{1.87}$$

Here $\mathcal{S}_{CP}$ and $\mathcal{A}_{CP}$ are the CP violating parameters already introduced in Equation 1.70, τ_{B^0} is the life time of the B^0, Δm_d is the mass difference between the two neutral B mass eigenstates, $\Delta t = t_{CP} - t_{tag}$ and $q \pm 1$ is the b flavor charge, depending whether the B meson is a B^0 or a $\bar{B^0}$.

1.5.9 $B^0 \to \psi(2S)\pi^0$ and the decay angle ϕ_1

Depending on the chosen CP eigenstate, any of the three angles ϕ_1, ϕ_2 or ϕ_3 of the B triangle can be measured. These over-constraint measurements are used to improve the determination of the elements of the CKM matrix or to discover new physics beyond the SM.
One angle of this triangle ϕ_1 (β) is measured via the first asymmetry observation in B meson decays using the decay $J/\psi K^0_S$ and related decay channels. In absence of direct CP violation the time dependent CP asymmetry is given by

$$\frac{N(\bar{B} \to X) - N(B \to X)}{N(\bar{B} \to X) + N(B \to X)}|_t = \sin 2\phi_1 \sin \Delta m \Delta t \tag{1.88}$$

where Δt is the difference between the decay times of the two neutral B mesons coming from the $\Upsilon(4S)$ decay.
CP violation in the neutral B meson system has been established by performing measurements of the CP violating parameter $\sin 2\phi_1$, where ϕ_1 is $arg[-V_{cd}V^*_{cb}/V_{td}V^*_{tb}]$ and V_{ij} are the CKM parameters, involving $b \to c\bar{c}s$ transitions e.g. $B^0 \to J/\psi K^0_S$. These measurements have been performed by Belle [33] and BaBar [34] collaborations. The SM in this case predicts $\mathcal{S}_{f_{CP}} = -\xi_f \sin 2\phi_1$, where $\xi_f = \pm 1$, corresponding to a CP even or CP odd final state, respectively and $\mathcal{A}_{f_{CP}} = 0$.
In the Standard Model the decay $B^0 \to \psi(2S)\pi^0$ occurs either through a tree diagram with internal W emission ($b \to d$), or a penguin which includes an intermediate loop diagram ($b \to d$). The amplitudes of both diagrams are of the same order, but the penguin diagram is highly color suppressed due to the three gluons introduced to conserve color. The corresponding Feynman diagrams are shown in Figure 1.8.
For $f_{CP} = \psi(2S)\pi^0$ final state, which is a CP-even final state, the mixing -induced CP

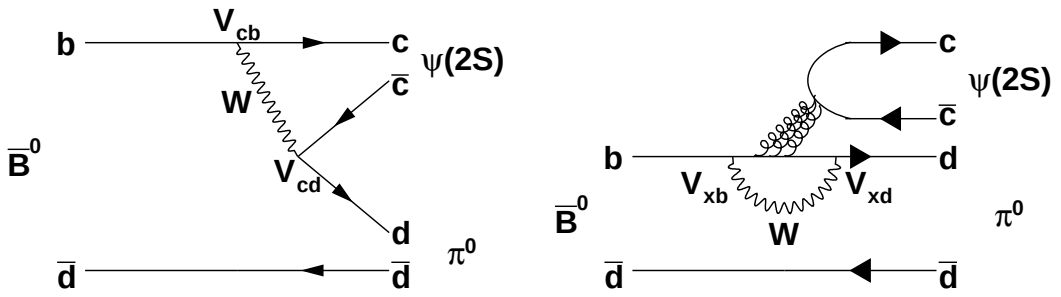

Figure 1.8: Feynman diagrams of the $B^0 \to \psi(2s)\pi^0$ decay that can occur either through a tree diagram (left) or a penguin diagram (right).

parameter $S_{\psi(2s)\pi^0}$ becomes $-\sin 2\phi_1$ if the tree diagram dominates.
However, if there is significant penguin contribution or other substantial contributions, precision measurements of time-dependent CP asymmetry in $b \to c\bar{c}d$ transitions e.g $B^0 \to \psi(2S)\pi^0$ or $B^0 \to J/\psi\pi^0$ may reveal values for the CP violating parameters $\mathcal{S}_{f_{CP}}$ and $\mathcal{A}_{f_{CP}}$ that are different from the SM predictions $-\sin 2\phi_1$ and 0, respectively. Thus, the possible penguin contribution of the $b \to c\bar{c}d$ transitions, which contain a different CKM phase, can alter the measured $\sin 2\phi_1$ value. Any discrepancy that can be observed would appear either as a consequence of the penguin contribution effect or due to new physics. Therefore, measurements of CP asymmetries in the $b \to c\bar{c}d$ transition B meson decays, play an important role in identifying whether or not the CKM model provides a complete description of the CP violation in the B meson system.
Additional motivation for this study involves a possibility to provide model-independent constraint on the penguin pollution within $B^0 \to \psi(2S)K^0_S$.

Chapter 2

The Belle experiment

The aim of the Belle Experiment [35], [7] is to study and measure with high precision the CKM matrix parameters using B meson decays. The KEKB accelerator [35], [5] is located at the High Energy Accelerator Research Center (KEK) in Tsukuba, Japan. This particle collider exceeded its design luminosity of $1 \times 10^{34}\,\mathrm{cm}^{-2}\mathrm{s}^{-1}$, achieving the world's largest luminosity of $2.11 \times 10^{34}\,\mathrm{cm}^{-2}\mathrm{s}^{-1}$ (Figure 2.1). Until its shutdown in 2010 the machine has accumulated integrated luminosity of about $1040\,\mathrm{fb}^{-1}$. Most of the data was taken at the center-of-mass of the $\Upsilon(4S)$ resonance and contains 772 million $B\overline{B}$ pairs.

2.1 KEKB Accelerator

The KEKB accelerator (Figure 2.2 (left)) is an asymmetric two ring e^+e^- collider operating at $\Upsilon(4S)$ resonance, designed to produce large numbers of $B\overline{B}$ pairs. The electrons circulate in the so-called high energy ring at 8 GeV, while the positrons are filled in the low energy ring at 3.5 GeV. Both rings are placed in a tunnel of about 3 km circumference. The beams are provided from a linear injection accelerator. They cross at two points but collide at only one. Figure 2.2 (right) shows the layout of the two rings. The different energies of the e^+ and e^- beam give the $\Upsilon(4S)$ a Lorentz boost of $\beta\gamma = 0.425$. Therefore, the produced B mesons are also boosted, which allows measurement of the decay flight length in the order of $100\,\mu$m. This enables the study of B meson decay time (see Section 1.5.8).
The total beam currents are $I_- = 1.35\,\mathrm{A}$ for the electron beam and $I_+ = 2.0\,\mathrm{A}$ for the positron beam. About 1600 bunches are stored in each beam.
In order to minimize the coupled bunch instabilities that occur due to the electromagnetic field induced by the beams, two different radio frequency acceleration systems were installed at Belle. One type are the normal conducting Accelerator Resonantly-coupled with Energy Storage (ARES) cavities, placed in the positron beam in order to handle the higher beam currents. Another type are the super-conducting cavities located in the electron beam to achieve higher voltage [36].

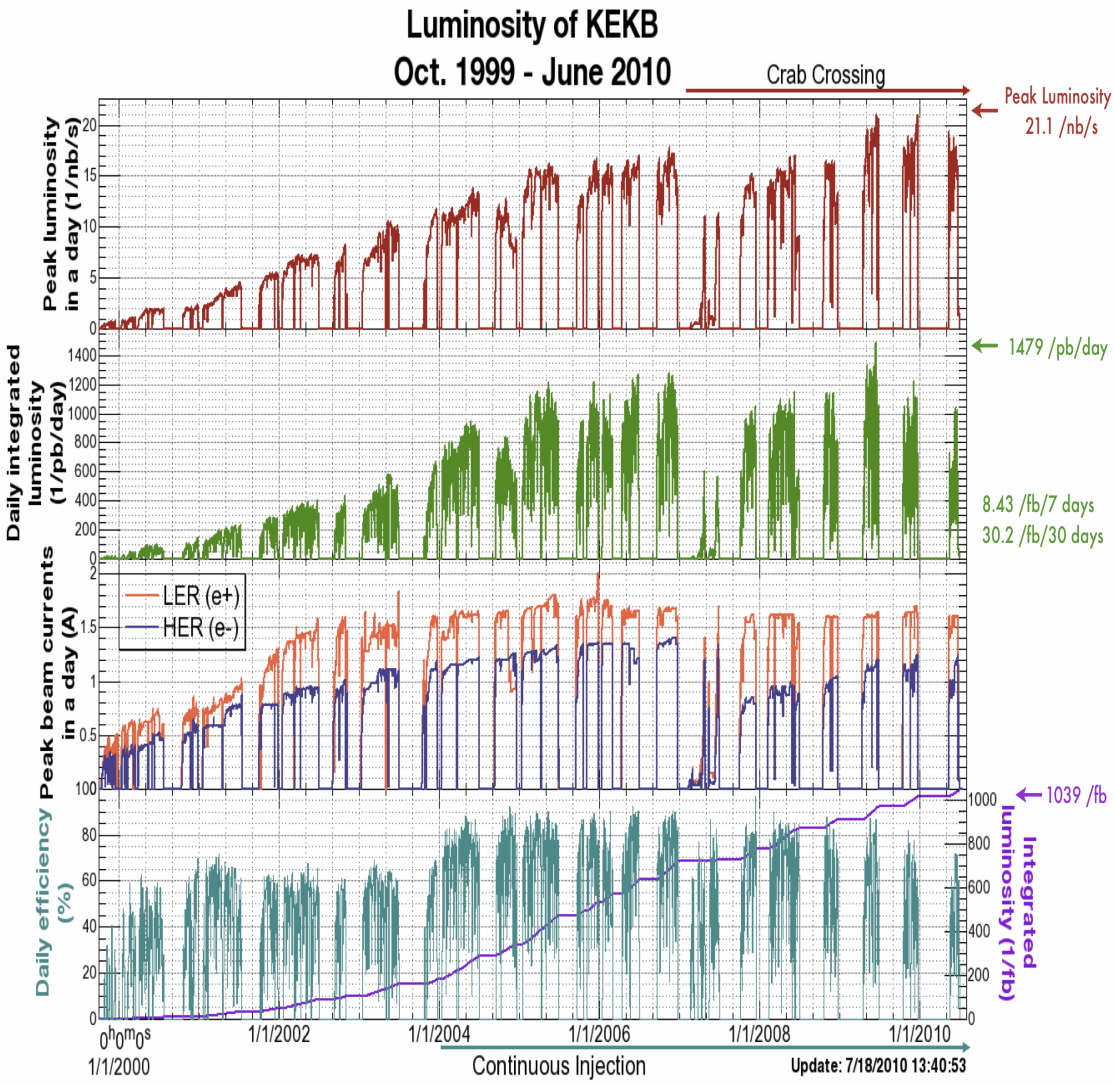

Figure 2.1: Total integrated luminosity at Belle.

In December 2006, two super-conducting crab cavities [37] were installed, one in the low energy ring and another in the high energy ring. These crab cavities tilt the bunches before colliding providing an increase in luminosity.
One of the most important features of the KEK B-factory accelerator is the crossing angle between the positron and the electron beam that is set to $\pm 11\,\mathrm{mrad}$ in order to avoid parasitic collisions. In this way there is no need for a bending magnet in order to separate the beams. As a result, the background due to synchrotron radiation is significantly reduced and a circular beam-pipe could be used.

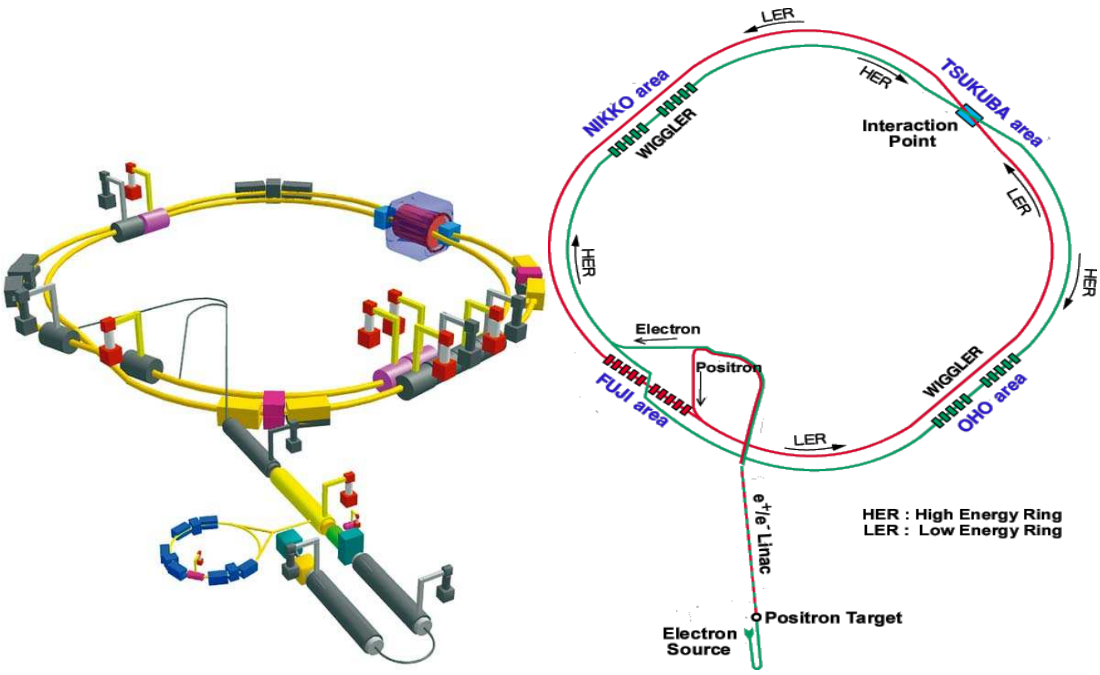

Figure 2.2: Schematic view of the KEKB accelerator system.

2.2 Belle Detector

The Belle detector was designed and constructed to carry out quantitative studies of B meson decays and especially rare B-decay modes with very small branching fractions. It is a large solid-angle magnetic spectrometer, constructed around 1.5 T superconducting solenoid and iron structure surrounding the KEKB beams at the interaction region. Its purpose was to detect visible final state particles that occur in the decays of B mesons. The detector was designed such that the angular acceptance for both charged and neutral particles is $17^\circ < \Theta < 150^\circ$. Belle detector was designed such that it could provide good vertex and momentum resolution, as well as particle identification for separating π, K and e in order to satisfy the requirement of an efficient B-flavor tagging. High efficiency and good resolution in particular, especially for low energy photons ($20\,\text{MeV} - 500\,\text{MeV}$), were also properties of the detector. For the detection of K_L and angular measurements, high detection efficiency and good resolution, as well as high detection efficiency and low fake rate for muons with momentum as low as $0.6\,\text{GeV}$, were also necessary for precise operation of the Belle detector. These criteria were satisfied in the separate sub-systems that constitute the Belle detector. The layout of the Belle detector with all its components is shown in Figure 2.3.

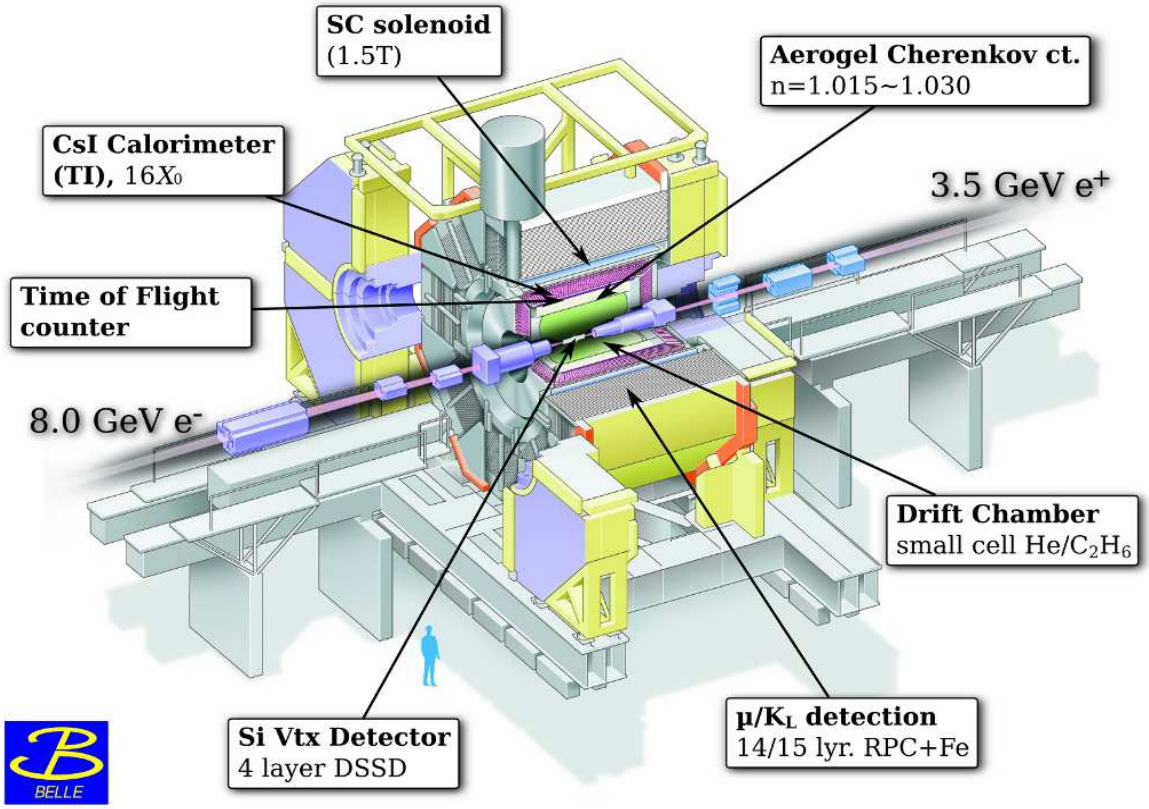

Figure 2.3: Belle detector.

2.2.1 Beam-pipe

The beam-pipe is the first piece of material surrounding the interaction point. Since, the interaction point is in a vacuum inside the beam-pipe, the beam-pipe itself has to withstand the pressure from the atmosphere in order to keep the vacuum.
On the other hand, the beam-pipe has constraints on the building material. One of the most important features of the Belle detector is the precise determination of decay vertices. However, z-vertex position resolution is limited by multiple Coulomb scattering in the beam-pipe wall and the first layer of the silicon vertex detector. Therefore, to reduce the impact of the beam-pipe on the trajectories of the particles a very thin beam-pipe material is chosen.
For the construction of the double-wall cylinder which is in fact the central part of the beam-pipe beryllium is used. The two beryllium cylinders are separated by a 0.5 mm gap filled with paraffine for cooling. The total material thickness of the central beryllium section is 0.3% [7] of a radiation length. The outer surface of the beam-pipe is covered by 20 μm thick gold foil to reduce the low energy X-ray background from the high energy ring. The total thickness of the outer coverage corresponds to 0.6% of radiation length [7].

2.2.2 Silicon Vertex Detector

The first detector sub-system just outside the beryllium beam-pipe is the silicon vertex detector (SVD), which provides vertex information of B meson decays. This is crucial for the observation of time-dependent CP asymmetries, which was one of the primary goals of the Belle experiment. Since, the vertex resolution is dominated by Coulomb scattering, the design of the detector has strict constraints. In particular, the innermost layer of the vertex detector must be placed as close as possible to the interaction region.
In the initial design the silicon vertex detector (SVD1) [38] was build out of three concentric cylindric layers with radii of 30 mm, 45.5 mm and 60.5 mm respectively and covers a solid angle $23^\circ < \theta < 139^\circ$, with θ being the angle from the beam axis. This corresponds to 86% of the full solid angle. However, due to the smaller acceptance and the insufficient radiation hardness, the SVD1 detector was replaced. The later design (SVD2) [39] included four detector layers instead of three, standing at radii of 20 mm for the innermost layer and 43.5 mm, 70 mm and 88.8 mm for the remaining three layers, respectively. In addition, in the upgraded silicon vertex detector design the geometry acceptance was increased to $17^\circ < \theta < 150^\circ$. Schematic view of the SVD2 along with the central drift chamber inner wires is shown in Figure 2.4. The distance between the first layer and the interaction point should be as short as possible, but since radiative background increases inversely with the distance, the layout of the inner layer is determined by the radiation tolerance of the electronics used and vertex precision needed.

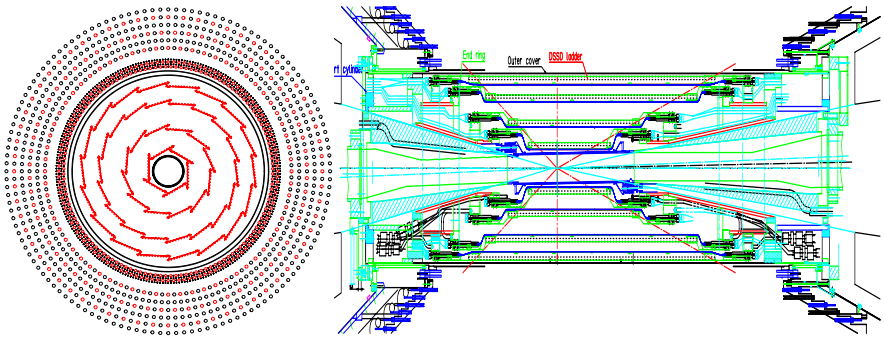

Figure 2.4: View of the SVD2 sub-detector structure along with the CDC inner wires.

On the other hand the distance of the layer most out is constrained by the radius of the next coming sub-detector.
On each layer, ladders consisting of double-sided silicon strip detectors (DSSD) are mounted. Each ladder is constructed of two half-ladders that are joined by support structure. The DSSD's have thickness of 300 μm and provide depleted pn-junctions. On the n-side of the pn-junction a 75 V voltage is applied, while the p-side is grounded. The DSSD is designed such that the large diode area is divided into

strips, each of which is read out by a separate electronic circuit. The n-strips are interleaved with p-implants to provide better separation. When a charged particle traverses through the n-bulk silicon electron-hole pairs are produced. These produced electrons and holes then drift towards the corresponding n or p strips on the surface of the DSSD. The p strips are along the beam axis and allow measurement of the $r\phi$ coordinate of a traversing charged particle, while the n strips are perpendicular to the beam axis and measure the z position. A charged particle will travel in the electrical bias field, producing a 2D signal indicating the position of the charged particle. The best way to estimate the performance of the SVD is through the impact parameter resolution. The impact parameter is defined as the point of closest approach to the interaction point. The resolution is determined from the distribution of two track parameters σ_z and $\sigma_{r\phi}$. The resolution in z and $r\phi$ depends on the momentum of a traversing particle p and the polar angle θ and can be expressed as [7]:

$$\begin{aligned} \text{SVD1:}\sigma_z &= (42.2 \oplus \frac{44.3}{p\beta\sin^{5/2}\theta})\,\mu\text{m}, \quad \sigma_{r\phi} = (19.2 \oplus \frac{54.0}{p\beta\sin^{3/2}\theta})\,\mu\text{m} \\ \text{SVD2:}\sigma_z &= (27.8 \oplus \frac{31.9}{p\beta\sin^{5/2}\theta})\,\mu\text{m}, \quad \sigma_{r\phi} = (21.9 \oplus \frac{35.5}{p\beta\sin^{3/2}\theta})\,\mu\text{m}. \end{aligned} \tag{2.1}$$

The term in the denominator is denoted as pseudo-momentum, while $\oplus$ denotes a quadratic sum. The momentum and angular dependence of the impact parameter resolution are shown in Figure 2.5.

2.2.3 Central Drift Chamber

The precise determination of particles' momentum and the efficient reconstruction of charged particle tracks are essential features of the measurements performed at the Belle experiment. These measurements are obtained using the Central Drift Chamber (CDC) as primary device for particle tracking. The CDC also plays an important role in measurements of charged particle energy loss in the chamber gas (dE/dx) used for particle identification and provides fast trigger signals [40].
The Central Drift Chamber of the Belle detector is located in a $1.5\,\text{T}$ magnetic field provided by a super-conducting solenoid. The chamber structure is shown in Figure 2.6. The CDC is asymmetric in the z-direction in order to provide an angular coverage within the detector acceptance and to accommodate the fact that the particles from $\Upsilon(4S)$ are boosted due to the asymmetric nature of the collider itself.
Belle's CDC is a cylindrical wire drift chamber. It is composed of axial drift cells, stereo drift cells and cathode image read-out. The CDC has in total 8400 drift cells distributed amongst the 3 layers of cathode strips and 50 anode layers that are organized in 11 super-layers. Each anode layer contains between three and six either axial or small-angle-stereo layers as indicated in Table 2.1. The individual cells of the chamber are almost square. Except for the inner three layers, the drift cells have maximum drift distance between $8\,\text{mm}$ and $10\,\text{mm}$, whereas the radial thickness ranges between

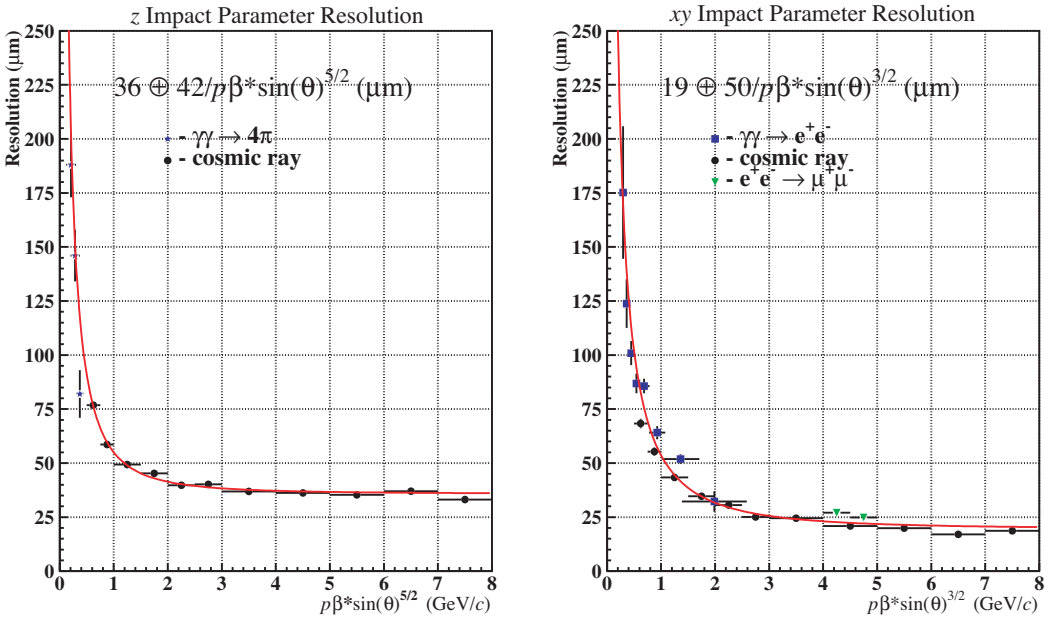

Figure 2.5: Impact parameter resolution in z and $r\phi$ dependent on the pseudo momentum $\bar{p}$ for muons from cosmic ray data [7]. The pseudo-momentum $\bar{p}$ is defined as $\bar{p} = p\beta\sin\theta^{5/2}$ in z (left) and $\bar{p} = p\beta\sin\theta^{3/2}$ in $r\phi$ (right), respectively.

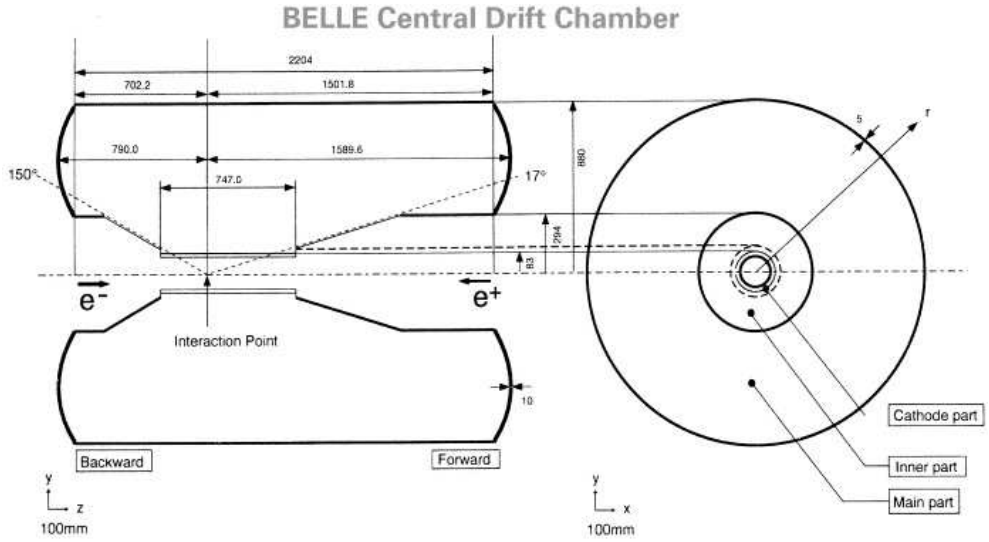

Figure 2.6: Schematic view of the Belle CDC structure.

15.5 mm and 17 mm. The cells of the inner three layers have smaller size, while their signal is read by the cathode strips on the cylinder walls. A 30 μm diameter gold-plated tungsten is used for the axial wires in order to maximize the drift electric field. On the other hand for the stereo wires aluminum is used with diameter of 126 μm providing

reduction of the material used in the tracking chamber volume. This diameter of the field wires was chosen in order to keep the electric field on the surface of the wires below $20\,\mathrm{KV/cm}$, which is the limit for avoiding the radiation damage. The length of the longest wires is $2400\,\mathrm{mm}$. The inner radius is set to $103.5\,\mathrm{mm}$ to achieve good tracking efficiency for low p_t-tracks, whereas the outer radius is $874\,\mathrm{mm}$.

Super layer type and no.	No. of layers	Signal channels per layer	Radius(mm)	Stereo angle (mrad) and strip pitch (mm)
Cathode	1	$64(z)\times 8(\phi)$	83.0	(8.2)
Axial 1	2	64	88.0-98.0	0
Cathode	1	$80(z)\times 8(\phi)$	103.0	(8.2)
Cathode	1	$80(z)\times 8(\phi)$	103.5	(8.2)
Axial 1	4	64	108.5-159.5	0
Stereo 2	3	80	178.5-209.5	$71.46\sim 73.75$
Axial 3	6	96	224.5-304.0	0
Stereo 4	3	128	322.5-353.5	$-42.28\sim -45.80$
Axial 5	5	144	368.5-431.5	0
Stereo 6	4	160	450.5-497.5	$45.11\sim 49.36$
Axial 7	5	192	512.5-575.5	0
Stereo 8	4	208	594.5-641.5	$-52.68\sim -57.01$
Axial 9	5	240	656.5-719.5	0
Stereo 10	4	256	738.5-785.5	$62.10\sim 67.09$
Axial 11	5	288	800.5-863.0	0

Table 2.1: The configurations of the CDC sense wires and cathode strips.

The total amount of wire tension was supported by aluminum end-plates and carbon-fiber-reinforced-plate cylinder structures that extend between the end-plates. The end-plates contain cathode, inner and main part. The properties of each of these parts are described elsewhere [41]. They are connected to each other by a stainless-steel bolts and are gas sealed with a silicon glue.

For the operation of the CDC in order to obtain a good momentum resolution, even for less than $1\,\mathrm{GeV}$, multiple Coulomb scattering should be reduced. For this purpose a low-Z gas was used because it has smaller photo-electric cross section than argon-based gases and in addition, it provides reduction of the background caused by synchrotron radiation and spent particles. For the CDC a gas mixture of $50\,\%$ helium and $50\,\%$ ethane was used. The mixture has a long radiation length of $640\,\mathrm{m}$ and drift velocity that saturates at $4\,\mathrm{cm}/\mu\mathrm{s}$ at low electric field, which allows for simpler calibration and reliable and stable performance of the CDC. The ethane component provides good dE/dx resolution [42].

Important feature of the Belle's drift chamber was the ability of performing particle identification. By using the dE/dx measurements from the chamber it is possible to distinguish between kaons and pions in the momentum region below $0.7\,\mathrm{GeV/c}$. The

separation between different particle species according to the different energy loss obtained from the CDC is shown Figure 2.7.

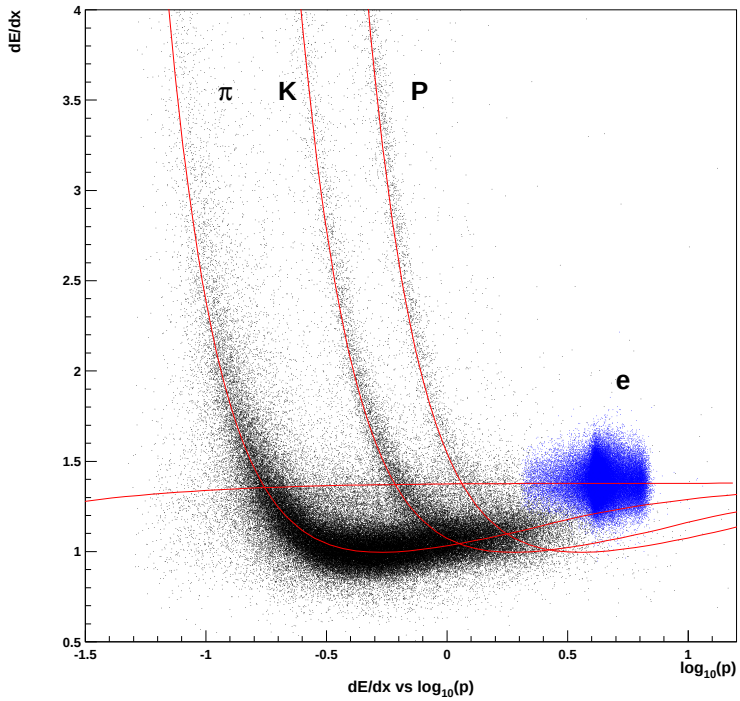

Figure 2.7: Energy depositions in the CDC for different particles as a function of momentum observed in collision data [7].

2.2.4 Aerogel Čerenkov Counter

Particle identification, in particular the identification of charged pions and kaons, plays an important role in two aspects of CP violation studies. One of these aspects is the flavor determination of the parent B mesons decaying into specific CP eigenstates, which can be obtained from the charge of the final state kaon in cascade decays. The other aspect is the reconstruction of exclusive B meson decays, such as two body decays.
The momentum distribution of the final state kaons from the cascade decays is in the range up to $1.5\,\mathrm{GeV/c}$, which is already covered by the dE/dx measurements in the CDC and time-of-flight (TOF) measurements. However, the π/K separation up to $\sim 4\,\mathrm{GeV/c}$ momentum range is important for unambiguous reconstruction of the two-body decays and therefore the Belle detector is equipped with a device based on Čerenkov techniques.
When a charged particle moves through a material medium faster than the speed of

light in that same medium, it radiates Čerenkov radiation. The speed of light in a medium c_{medium} is related with the refractive index n of the medium as

$$c_{medium} = \frac{c_{vacuum}}{n}. \tag{2.2}$$

Consequently, a charged particle with velocity β, mass m and momentum p, radiates Čerenkov light, if

$$n > \frac{1}{\beta} = \sqrt{1+(\frac{m}{p})^2}. \tag{2.3}$$

Due to the different masses the aerogel Čerenkov counter (ACC) [7], [43] is able to distinguish between pions and kaons. By selecting material with appropriate refractive index n pions with momenta larger than $1\,\mathrm{GeV/c}$ will emit Čerenkov radiation, while kaons with the same momenta are below the threshold velocity and therefore will not generate Čerenkov radiation. Thus, the ACC operates as a threshold counter system, used in the Belle experiment to extend the momentum range coverage for the π/K separation up to $3.5\,\mathrm{GeV/c}$.
The ACC is divided into two segments: a barrel ACC and forward end-cap ACC. The barrel component consists of 960 counter modules, arranged into 60 cells in ϕ direction. The end-cap part is composed of 228 counter modules, arranged in five concentric layers. The configuration of the ACC in the central part is shown in Figure 2.8.

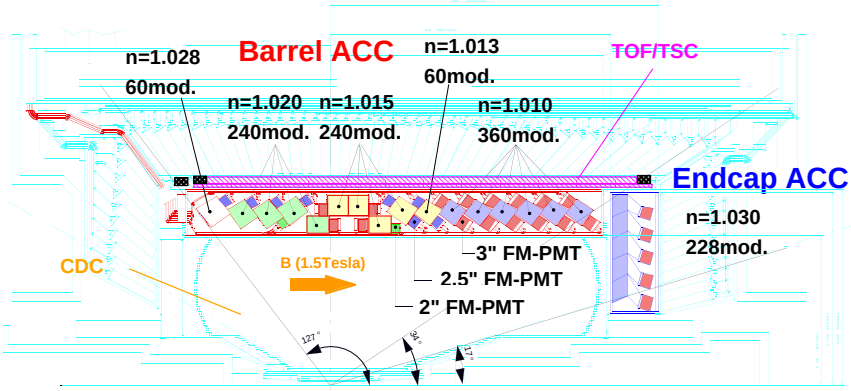

Figure 2.8: Arrangement of the ACC modules in the central region of the Belle detector.

The barrel ACC module, whose typical size is $12 \times 12 \times 12\,\mathrm{cm}^3$ is made of $0.2\,\mathrm{mm}$ thick aluminum. Five aerogel tiles are installed in each module and one or two fine-mesh photo multiplier tubes (FM-PMT) are attached directly to the aerogels at its sides.

The end-cap module has rather complicated shape and consists of five aerogel tiles. The inner surface of the module counter is coated with diffusive reflector sheets for better efficiency and uniformity of the light collection. The Čerenkov light is detected by the fine-mesh photo multipliers connected with the aluminum boxes.
The refractive index (n) of silica aerogels in the barrel part of the sub-detector device ranges between 1.010 and 1.028, depending on the polar angular regions to cover the momentum range from $1.2\,\mathrm{GeV/c}$ to $3.5\,\mathrm{GeV/c}$. On the other hand, areogels with $n = 1.030$ are used so that the device is suitable for flavor tagging.
Silica aerogels with low refractive indices are developed and produced in a two step fabrication method. The first step concerns the preparation of the alcogels and the second is related to the hydrophobic surface, which ensures long-term stability of the device. Details of the production method are described elsewhere [44], [45]. The maximal radiation damage on aerogels is set up to $\sim 10\,\mathrm{Mrad}$ equivalent dose [46], which corresponds to more than 10 years of running at the KEK B-factory.

2.2.5 Time of Flight Counter

In order to establish precise event timing and to enhance discrimination between different particle types, e.g. pions and kaons, in the momentum region below $1.2\,\mathrm{GeV/c}$, a Time-of-Flight counter (TOF) [47] is used at Belle. The time-of-flight sub-detector system is used to measure the time particles travel from the interaction point to the TOF module. Since TOF is sensitive in a track momentum region below $1.2\,\mathrm{GeV/c}$, it is complementary to the ACC. Combined with momentum measurements Belle's TOF system provides K/π separation and an effective B-flavor tagging. The TOF technique using plastic scintillators is very powerful, although conventional method for particle identification. The time resolution of the TOF system in order to provide clean K/π separation for particle momentum below $1.2\,\mathrm{GeV}$ is $100\,\mathrm{ps}$.
The basic principle of the TOF measurement provides determination of the mass m of the particle. The particle mass m is related to the measured time of flight T by

$$m = p\sqrt{\frac{1}{\beta^2} - 1} = p\sqrt{(\frac{cT}{L})^2 - 1}, \tag{2.4}$$

where p denotes the particle momentum measured by the CDC and SVD and L denotes the helical distance traveled by the particle from the interaction point to the TOF module.
To achieve the design time resolution goal, a few considerations were taken into account. For this a fast scintillator was used. The light guides were eliminated to minimize the time dispersion of scintillation photons propagating in the counter. And in addition, photo-tubes with large area photo-cathodes were used, to obtain maximal photon collection. These strategies led to a module configuration consisting of two plastic scintillators with a fine mesh photo-multiplier tube (FM-PMT) [47] mounted directly to the each end of the TOF module. The two scintillators are accompanied

with thin Trigger Scintillation Counter (TSC) and are located inside the 1.5 T magnetic field.
Each TOF module consists of two TOF counters with readout at both ends and one thin TSC with backward readout only. In total there are 64 TOF modules placed in the barrel region of the detector. The radial distance to the interaction point is 1.2 m. The TOF covers a polar angle of $34° < \theta < 121°$.
The photo multiplier tubes are attached to the ends of the TOF with an air gap of ~ 0.1 mm which provides earlier arrival photons to pass selectively, thus reducing the gain saturation effect of the tubes due to large pulses at high rate. On the other hand, the tubes are glued to the light guides at the backward ends of the TSC. Each PMT signal is split into two. One is used for charged measurement and the other is providing two output signals depending on the threshold level applied. The low level signal is providing time measurement, while the high level component provides a gate to the charge-to-time converter (QCT) [47]. The layout of the TOF counter is shown in Figure 2.9.

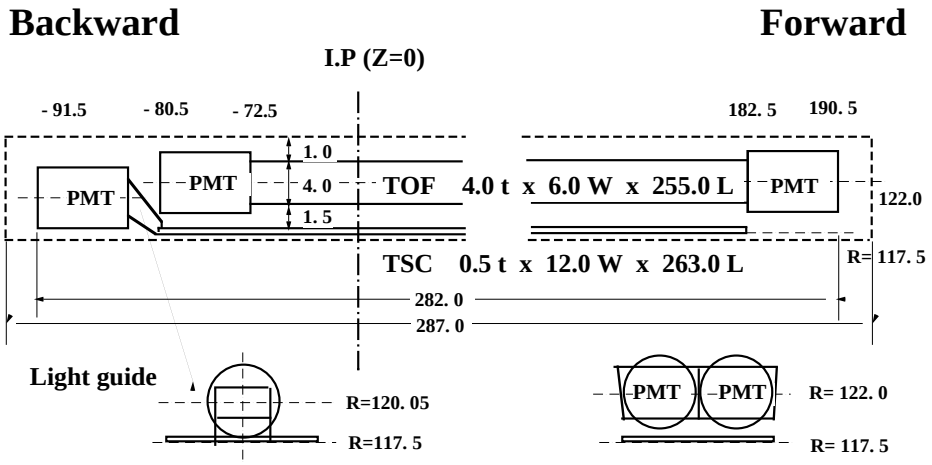

Figure 2.9: Layout of the time-of-flight counter.

2.2.6 Electromagnetic Calorimeter

The electromagnetic calorimeter (ECL) [7] measures the energy and the position of electromagnetic showers caused by photons and electrons. Since about one third of the hadron decay products are neutral pions, the ECL has to provide efficient π^0 reconstruction. It has to provide high energy resolution over a wide range of energies, from $20\,\mathrm{MeV}/c^2$ up to $8\,GeV/c^2$. Because most of the photons that appear as end products of cascade decays have very low energies, the ECL needs to ensure good performance in the energy region below 500 MeV. Moreover, the ECL should be also suitable for detection of high energy photons originating directly from B meson decays, for instance e.g. $B^0 \to K^{*0}\gamma$ and $B^0 \to \pi^0\pi^0$. The high resolution [7] is

therefore needed in order to reduce backgrounds for these modes. In addition, the electron identification in Belle relies primarily on a comparison of the charged particle momentum and the energy deposited in the ECL.
The ECL (Figure 2.10) is composed of segmented array of counters, containing 8736 thallium doped cesium iodide CsI(Tl) crystals and pairs of silicon photo-diodes with a cross-section of $1 \times 2\,\mathrm{cm}^2$ used for readout. The barrel component consists of 6624 crystal counters, while the forward and backward end-caps contain 1152 and 960 counters, respectively.
Each CsI(Tl) crystal has a tower structure shape, pointing towards the vicinity of the interaction point. The length of each crystal is 30 cm, corresponding to 16.2 radiation lengths (X_0). This length is chosen to prevent deterioration of the energy resolution from the shower leakage at high energy. The crystals have different transverse dimensions depending on the polar angle positions. Typical dimension of a barrel crystal is $55\,\mathrm{mm} \times 55\,\mathrm{mm}$ for the front face and $65\,\mathrm{mm} \times 65\,\mathrm{mm}$ for the rear face. The end-cap crystals have larger variations in dimension, ranging from 44.5 mm to 70.8 mm for the front surface and from 54 mm up to 82 mm for the rear area.

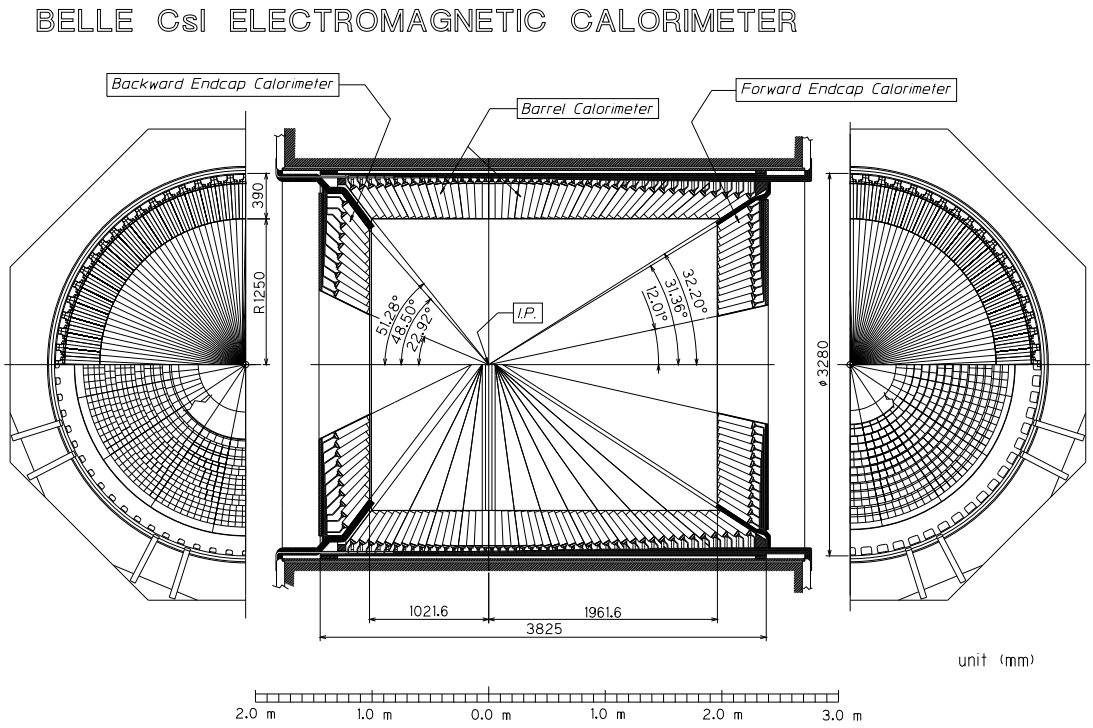

Figure 2.10: The ECL configuration.

The ECL covers 91% of the solid angle. 3% of the total angular acceptance is inefficient due to the gap between the barrel and the calorimeter end-caps. The energy resolution of the electromagnetic calorimeter is given by [7]

$$\frac{\sigma_E}{E} = (1.34 \oplus \frac{0.066}{E} \oplus \frac{0.81}{E^{1/4}})\%, \tag{2.5}$$

where E is the energy measured in units of GeV. The energy resolution is limited by the electronic noise, contributing to the first term and by shower leakage fluctuations, contributing to the second and third term.
The position resolution is given as [7]

$$\sigma_{position} = (0.27 + \frac{3.4}{E^{1/2}} + \frac{1.8}{E^{1/4}})\,\text{mm}. \tag{2.6}$$

Furthermore, the ECL plays an important role in the identification of electrons. Charged particles, such as pions and kaons, deposit less energy in the calorimeter than the electrons. These particles can be distinguished by the differences in the shower shapes. Electromagnetic shower and hadronic shower have different shape in both transverse and longitudinal direction, thus one can distinguish electrons from hadrons. The shower shape in transverse direction can be evaluated quantitatively by a "$E9/E25$" measurement, defined as the ratio between the energy summed in 3×3 crystals and the energy accumulated in the 5×5 crystals of the ECL. An additional feature that is used for electron identification is E/p, denoting the ratio of the energy measured by the calorimeter to the three momentum measured by the CDC [48].

2.2.7 Extreme Forward Calorimeter

The Extreme Forward Calorimeter (EFC) [7] is a multi-purpose device. One of its tasks is to provide online luminosity information using Bhabha scattering and tag information of the two-photon processes. It is also used as a beam mask to reduce the backgrounds for the central drift chamber. And in addition, in order to improve the experimental sensitivity to some physics processes, the EFC is utilized to extend the angular coverage beyond $17^\circ < \theta < 150^\circ$.
The extreme forward calorimeter is constructed of two parts, forward and backward, which are mounted on the front surfaces of the cryostats of the compensating solenoids of the KEK B-factory. The calorimeter covers from 6.4° to 11.5° in polar angle in the forward direction, while the angular coverage for the backward region ranges from 163.3° to 171.2°.
It is located near the interaction point in a very high radiation level area. Because the radiation hardness is an important issue for the calorimeter, for its construction radiation-hard bismuth germanium oxide $Bi_4Ge_3O_{12}$ (BGO) [49] crystals are used. The layout of the crystals is shown in Figure 2.11. Each of the two calorimeter parts consists of 160 such crystals, with 5 segments in θ and 32 segments in ϕ. Space limitation in the detector led to crystal sizes of 12 and 11 radiation lengths for the forward and backward part, respectively.

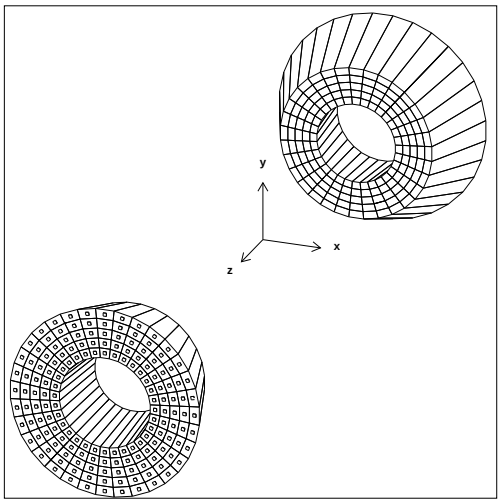

Figure 2.11: Arrangement of the BGO crystals in the forward and backward EFC detectors.

2.2.8 Solenoid

The super-conducting solenoid provides a magnetic field of 1.5 T parallel to the z-direction. Its cylinder volume is 3.4 m in diameter and 4.4 m in length. The coil consists of a single layer of niobium-titanium-copper alloy, embedded in a high purity aluminum stabilizer. Liquid helium circulates through a tube placed on the inner surface of the aluminum support cylinder and is used for cooling. The main coil parameters are presented elsewhere [50].

2.2.9 K_L and Muon Detector

The super-conducting coils is surrounded by a multi-layer structure consisting of iron plates and calorimeters, which is integrated into the magnetic return yoke: The K_L and μ detector (KLM) [7] is designed to identify long lived, highly penetrative particles, such as K_L and $\mu^{\pm}$, for instance from the semileptonic decays of B and D mesons or from $J/\psi \to \mu^+\mu^-$. For a particle to reach the KLM detector a momentum greater than 600 MeV/c is needed, therefore this device should ensure high efficiency over a broad momentum range, that exceeds this threshold.
The KLM sub-system consists of 15 alternating super-layers of charged particle detectors and 14 iron plates with thickness of 4.7 cm in the octagonal barrel region. There are also 14 detector super-layers in each of the two end-caps. Each super-layer contains resistive plate counters. The detection of charged particles is provided by these glass electrode resistive plate counters (RPCs) [51], [52], which have two parallel plate electrodes with high bulk resistivity, separated by a gap filled with gas (Figure 2.12). An ionizing particle traversing the gap initiates a streamer in the gas, thus resulting in a local discharge of the plates which is limited by the high resistivity of the plates

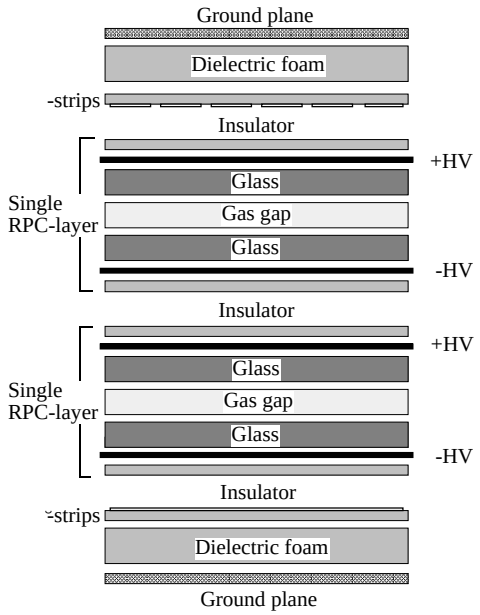

Figure 2.12: Cross-section of a KLM super-layer.

and the quenching characteristics of the gas between the plates. The location of the discharge is recorded electronically. In addition, the gas used to fill the gap between the plates is non-combustible mixture [53] of 62 % HFC-134a, 30 % argon and 8 % butane-silver in order to provide high detection efficiency and stable operation of the RPCs.

The iron plates provide a total of 3.9 interaction lengths of material for a particle traveling in the direction which is orthogonal to the detector planes.

The barrel-shaped region around the interaction point covers a range of $45^\circ < \theta < 125^\circ$ in polar angle, while in the forward and backward end-caps this coverage is extended to 22° and 155°, respectively.

The K_L particles which interact in the iron produce a shower of ionizing particles. Measuring the direction of these showers one can reconstruct decays such as, e.g. $B^0 \to J/\psi K_L$ using the kinematic constrains of energy and momentum conservation.

The discrimination between muons and charged hadrons is based on the distance they travel and the amount of scattering that occurs. In comparison with the strongly interacting hadrons, electromagnetically interacting muons on average travel significantly farther and with smaller deflections. The KLM is able to detect muons whose momentum is above $1.5\,\mathrm{Gev}/c$, with an efficiency greater than 90 % and a fake rate of about 3 %.

The detection of K_L is based upon the obtained cluster information in the KLM. The cluster information is fundamentally different for K_L and charged muons. Muons gen-

erate thin clusters which penetrate deep, while clusters produced by K_L are broader and will stop within the KLM.

2.2.10 Trigger and Data Acquisition

The trigger system at Belle is used to record physics events or discard background, using information from several sub-detectors. Since, at high luminosity the production of $B\bar{B}$ events occurs at very high rate, this is accompanied by high beam background due to the high beam currents. Therefore, the trigger system plays an essential role in the selection of useful events from the pool of many unwanted events. Another important feature regarding the operation of the trigger system is the data acquisition system (DAQ). The data acquisition system reads out and records the data selected by the trigger. Therefore, the trigger must be flexible, it has to keep the rate of accepted events at tolerable level for the data acquisition which stores the data, and it must be efficient by using information from many sub-detectors to keep the efficiency for the physics events high.
The trigger system at Belle is configured such that the data is selected in three steps. The first two triggers, the hardware trigger Level-1 and software trigger Level-3 operate in real time. The event reconstruction and classification is done off-line by the Level-4 trigger.

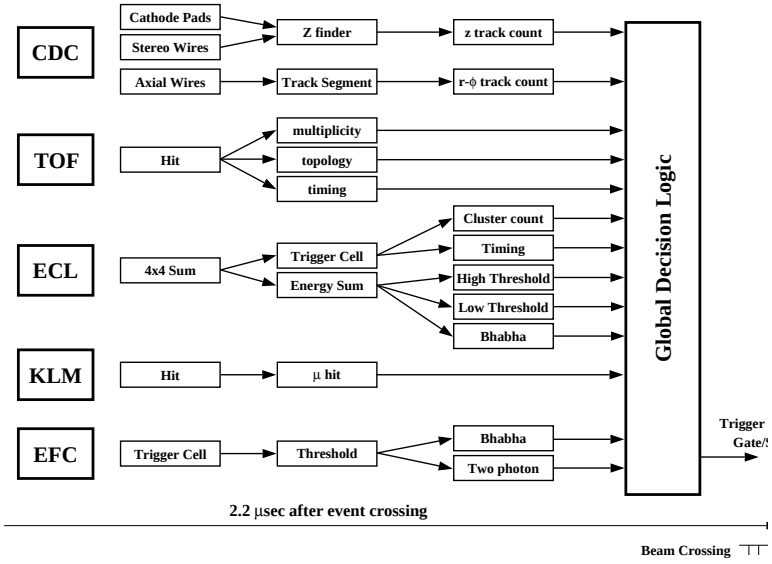

Figure 2.13: The Level-1 trigger system of the Belle detector.

The Level-1 trigger is consisting of a sub-trigger system and a central trigger system named Global Decision Logic (GDL). The trigger system of the sub-detectors can be divided into two categories: triggers based on selected tracks and triggers based on energy deposition measurements. CDC and TOF provide trigger signals for the charged

particles, while the energy deposition in the ECL provides signals from charged and neutral particles. The KLM trigger system gives additional information on muons and the EFC triggers are used for tagging two-photon events as well as Bhabha events. The GDL processes in parallel all information received from the separate sub-triggers and obtains an information about the decision whether an event is selected as signal or discarded as background. The processing of the information is done within $1.85\,\mu$s after the collision and the trigger decision is provided $2.2\,\mu$s after the event occurance. Figure 2.13 shows the schematic view of the Level-1 trigger system at Belle.
The purpose of the Level-3 trigger is to further reduce the number of triggered events to be stored. It reduces the event rate by about 50 % by selecting events with at least one track, with z impact parameter less than 5 cm and at least 3 GeV energy deposited in the ECL.
The Level-4 trigger works by the same principle as the Level-3 trigger but it has stricter track requirements: the distance from the interaction point in z direction should be less than 4 cm, the radial distance from the interaction point around the z axis should be less than 1 cm and the transverse momentum should satisfy the condition $p_t > 300\,\mathrm{MeV}/c$.
The Data Acquisition (DAQ) system collects information for events that passed the Level-1 trigger requirements. For these events, the DAQ system processes the data taken from the separate sub-detectors. Data from each sub-system are combined into a single event recorded by an event builder. The output of the event builder is then transferred to an online computer farm, the Level-3 trigger. The DAQ is designed for operation up to 500 Hz trigger rate, with dead time fraction less than 10 %. An overview of the DAQ system is shown in Figure 2.14.

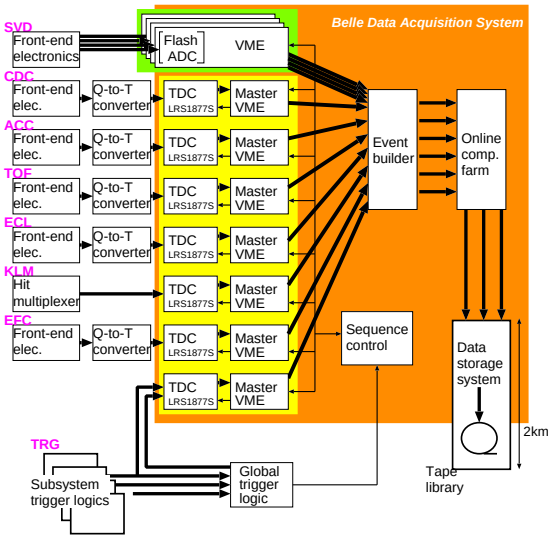

Figure 2.14: DAQ system at Belle.

Chapter 3

Analysis of the decay channel $B^0 \to \psi(2s)\pi^0$

In this chapter we present tools and eventually measure the branching fraction of $B^0 \to \psi(2S)\pi^0$, which would yield the first measurement of this value. The analysis itself is performed using the so-called "Blind Analysis" technique.

3.1 The Concept of "Blind Analysis"

According to this technique, in the development of the analysis it is important not to optimize the analysis procedure on the data that will be used for the measurement, known also as "tuning of the data". Instead, the measurement is performed without looking at the real data until almost all or eventually all analysis criteria are finalized. This means that we verify that the developed analysis procedure is properly working on Monte Carlo (MC) data samples. After these criteria are established we can look at the data. The purpose of this step is to avoid the possibility of biasing the result in a particular direction. After that the analysis may not be changed furthermore in order not to introduce a bias in our result.

3.2 Analysis procedure

At the KEKB collider positron and electron beam collide at the center-of-mass energy of the $\Upsilon(4S)$. At this energy, the $q\bar{q}$ cross section (see Figure 3.1) is consisting of three quarters of $q\bar{q}$ pairs (events called "continuum"), where $q = u,d,s,c$, while in the remaining quarter the $\Upsilon(4S)$ is produced. The $\Upsilon(4S)$ decays almost exclusively in $B\bar{B}$ pairs. From the total of 772×10^6 $B\bar{B}$ pairs collected with the Belle detector, we extract a lot less signal events compared to background. The first step to reduce the amount of background is to apply the event selection (see Section 3.5). We reconstruct one B meson by combining the four-momentum of final state daughter particles in or-

der to compose the parent B meson. The B meson in this analysis can be reconstructed in four modes, two leptonic and two hadronic modes: $B^0 \to \psi(2S)(\to e^+e^-)\pi^0(\to \gamma\gamma)$, $B^0 \to \psi(2S)(\to \mu^+\mu^-)\pi^0(\to \gamma\gamma)$, $B^0 \to \psi(2S)(\to J/\psi(\to e^+e^-)\pi^+\pi^-)\pi^0(\to \gamma\gamma)$ and $B^0 \to \psi(2S)(\to J/\psi(\to \mu^+\mu^-)\pi^+\pi^-)\pi^0(\to \gamma\gamma)$, respectively. We start the reconstruction from the "final" reconstructed particles, e.g. we combine two photons in order to obtain a neutral pion and we combine the four-momentum of two leptons, electrons or muons to reconstruct the $\psi(2S)$ meson or the J/ψ meson. Then, in the particular case where $B^0 \to \psi(2S)\pi^0$, $\psi(2S) \to l^+l^-$, we combine the four-momentum of the $\psi(2S)$ meson, accompanied by a neutral pion in order to form a B meson. In the case when the $\psi(2S)$ meson decays hadronically, then we combine the four-momentum of the J/ψ meson reconstructed from two leptons and the four-momenta of the two charged pions in order to reconstruct the parent B meson. Many selection criteria are applied to every event that is being recorded. Detailed description of the applied selection criteria are given in Section 3.5.

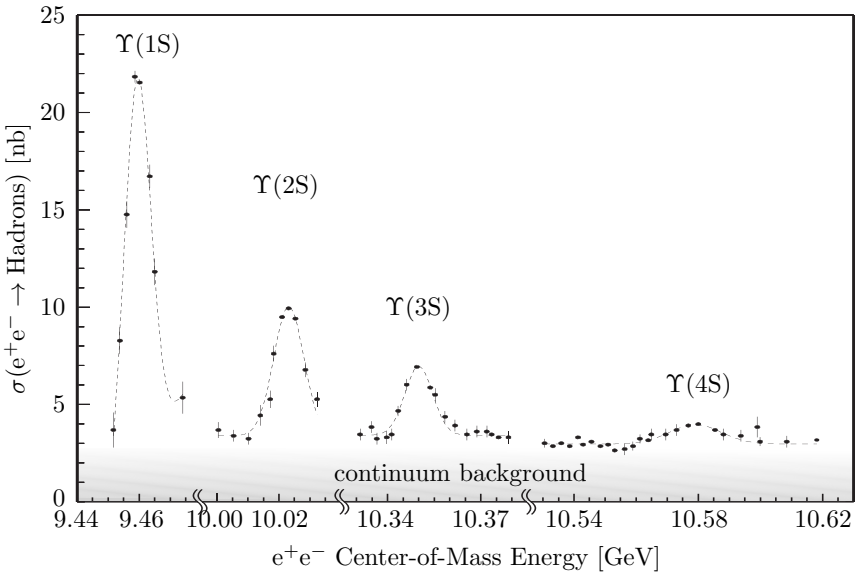

Figure 3.1: Hadronic cross sections around the center-of-mass energies of the Υ resonances [54].

After the reconstruction of the particles and the application of the selection criteria, the analysis continues by obtaining the probability density functions (PDFs) for signal and background events. We discriminate signal against various backgrounds using two kinematic variables: the mass of the reconstructed B meson, M_{BC}, and the energy difference between the reconstructed B energy and the beam energy in the center-of-mass system, ΔE (Section 3.5.6).
The signal component is $B^0 \to \psi(2S)\pi^0$. The different background contributions come from generic $B\bar{B}$ and continuum ($q\bar{q}$) events, misreconstructed B meson decays, which happen to occur in the same kinematic region and $B \to c\bar{c}X$ decays ("generic" decays).

We treat the generic $B\bar{B}$ decays that are not charmonium decays together with the continuum as one background component, named "combinatorial" background. The reason for this is that these generic B decays do not produce a peak in the signal region as it is the case for the $B \to c\bar{c}X$ decays. For all these four components we have to find the probability density functions through a fitting procedure.
Modeling of the separate components is done using a maximum likelihood approach. The branching fraction value is extracted with an extended maximum likelihood fit, later also referred as "final" fit described in Section 3.6.6.
The pure Monte Carlo sample, which is needed for obtaining the PDFs, is taken from full detector simulation for the signal component and the B decay backgrounds. The combinatorial background component is extracted directly from the data set.
To account for possible differences between data and MC, we use an additional decay mode (control sample), that is similar to the $B^0 \to \psi(2S)\pi^0$ decay. The correction factors (see Section 3.7.1) for the model parameters can be determined from the control sample and then applied to $B^0 \to \psi(2S)\pi^0$ real data. In this way we prevent biasing of the result.

3.3 Data Set

The measurement of the branching fraction of $B^0 \to \psi(2S)\pi^0$ is based on a data sample of $772 \times 10^6\, B\bar{B}$ pairs collected with the Belle detector at the KEKB asymmetric-energy e^+e^- (8 on 3.5 GeV) collider. This corresponds to a sample for a total of $\sim 1040\,\text{fb}^{-1}$.

3.4 Event Generation

For the Monte Carlo study, the Monte Carlo generator EvtGen [55] is used. Events generated by EvtGen are made to pass through the full detector simulation, performed using the GEANT [56] package. The GEANT package accommodates the geometry of each sub-detector device. Background coming from beam and electronic noise in each of the detector components is also added to the generated (simulated) events.

3.5 Event Selection

The event selection is the first step in the analysis chain. The aim of the event selection is to reduce the number of events that are going to be analyzed, from the total of $772 \times 10^6\, B\bar{B}$ pairs to a much smaller data set. The event selection is done in two steps: since, analyzing of the whole data set of Belle by one individual is inefficient and requires much time, smaller data subsets are prepared. These subsets of data in which a specific physics mode is enhanced are called "skims". The selection of this subset of events is based on loose criteria in the selection. The main purpose of this

is to keep all the interesting events, but at the same time not necessarily reject all the background events. In other words we do not want to obtain a very pure sample, but we want to keep the reconstruction efficiency high to avoid bias.
For the analysis of $B^0 \to \psi(2S)\pi^0$ decay, we use an official skim, that contains all $B \to J/\psi(\psi(2S))X$ candidates. The official skims are not optimized to a particular signal mode, but rather include other decay modes which can be removed safely by applying additional selection criteria.

3.5.1 Track selection

The quality of the reconstructed tracks is determined by the impact parameters, which denote the distance of closest approach to the interaction point along the beam direction, $|dz|$ and in the transverse $(r-\phi)$ plane, $|dr|$. For all selected tracks used to reconstruct $\psi(2S)$ and J/ψ mesons these impact parameters fulfill the following criteria:

- The impact parameter in the $r-\phi$ plane should satisfy: $|dr| < 1.5\,\mathrm{cm}$.
- The impact parameter in beam direction should satisfy: $|dz| < 5\,\mathrm{cm}$.

3.5.2 Continuum discrimination

One way to distinguish between a signal and a background is to use event shape variables. Signal events have spherical and uniform topology, while the continuum events are jet-like. In $q\bar{q}$ events the energy is distributed among the quark and the anti-quark. In the center-of-mass system the momentum of the quark and anti-quark is basically oriented in opposite direction from one another. Therefore, $q\bar{q}$ events emerge as jets collimated back to back. On the other hand, if the $\Upsilon(4S)$ resonance is created, the energy is distributed between the two produced B mesons, thus causing $B\bar{B}$ events to retain a spherical shape. Therefore, in order to distinguish between these two different event topologies we use so-called event-shape variables, which are the measures of sphericity or jet-likeness of a certain event.
In e^+e^- annihilation processes event shapes are usually characterized using Fox-Wolfram moments [57]. In our analysis the ratio of the second to zeroth Fox-Wolfram moment is used. It ranges between 0 and 1 and is expressed by [57]

$$R_2 = \frac{H_2}{H_0}, \quad \text{where} \quad H_k = \frac{\sum_{ij} |\vec{p}_i||\vec{p}_j| P_k(\cos\theta_{ij})}{(\sum_i E_i)^2}. \tag{3.1}$$

Here, P_k is the Legendre polynomial, θ_{ij} is the opening angle between the momentum p of the i-th and j-th particle, while $\sum_i E_i$ represents the visible energy of the particles in the event.
This quantity is indicative, meaning that values of R_2 closer to zero indicate a more spherical event, while the jet-likeness is described by R_2 value closer to 1. In order to suppress continuum we use the condition of R_2 being less than 0.5. Figure 3.2 shows this quantity for signal Monte Carlo (red) and continuum (blue). As one can see from this Figure, with the condition we apply we remove almost no signal, but we reduce the continuum by half.

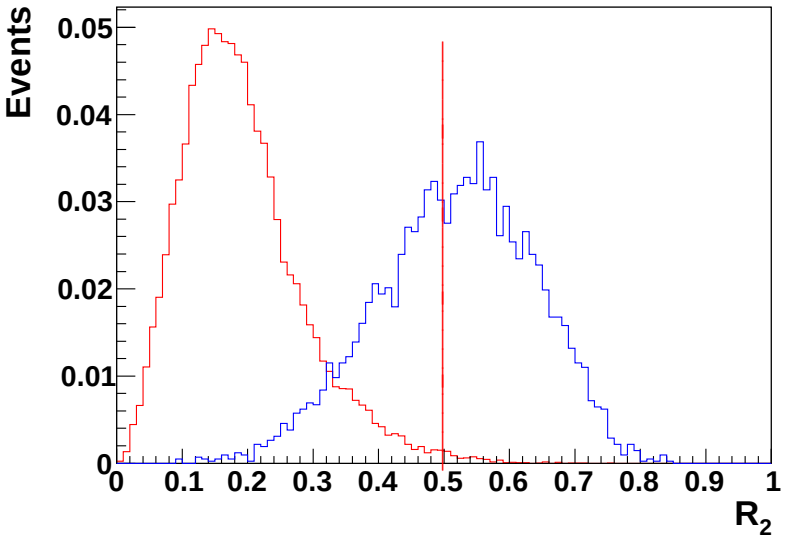

Figure 3.2: The second to zeroth Fox-Wolfram moment for signal MC (red) and continuum (blue).

3.5.3 Reconstruction of particles

The B^0 meson is reconstructed by selecting a $\psi(2S)$ meson, that decays either in two electrons or two muons, or it decays into a J/ψ ($J/\psi \to e^+e^-, \mu^+\mu^-$) accompanied by two charged pions. As a second daughter particle in the reconstruction chain of the B^0, the π^0 meson is selected, that decays into two photons.

3.5.4 Reconstruction of $\psi(2S)$ and J/ψ mesons

The $\psi(2S)$ candidates are obtained by combining either two oppositely charged leptons, $e^\pm$ or $\mu^\pm$, or J/ψ in addition with two charged pions, π^+ and π^-. The J/ψ is reconstructed using either its decay into two electrons or into two muons.

3.5.4.1 The $\psi(2S)(J/\psi) \to e^+e^-$ ("leptonic") decay mode

Electrons are identified on a basis of the electron likelihood $\mathcal{L}_e$ distributed on the interval [0,1]. For electron identification, the likelihood is calculated using the light yield in the aerogel Čerenkov information, the time-of-flight in the TOF counter and the ionization loss dE/dx in the central drift chamber. We reconstruct $\psi(2S)(J/\psi)$ candidates requiring that either both of the tracks are identified as electrons, satisfying the condition $\mathcal{L}_e > 0.01$ or one of the tracks fulfills the electron likelihood condition and for the other track we require either $E/p > 0.5$, where E/p is the ratio between the energy measured by the electromagnetic calorimeter and the momentum measured by the drift chamber, or $dE/dx > 0.5\,\mathrm{KeV/cm}$, where dE/dx is the energy deposition measured by the drift chamber.
Electrons from $\psi(2S)$ or J/ψ decays into e^+e^- may radiate photons, therefore lose part of their energy. Consequently, the four-momenta of the photons within 50 mrad of the e^+e^- tracks direction is added in the calculation of the invariant mass window to account for the energy loss due to the emission of bremstrahlung photons. Furthermore, because of the radiative tail in the $\psi(2S)(J/\psi) \to e^+e^-$ signal shape, an asymmetric invariant mass window of $-150\,\mathrm{MeV}/c^2 \leq M_{e^+e^-} - M_{J/\psi(\psi(2S))} \leq 36\,\mathrm{MeV}/c^2$ is chosen in order to select $\psi(2S)$ and J/ψ candidates. The $M_{J/\psi(\psi(2S))}$ mass is the PDG value. Figure 3.3 shows the mass distribution of the $\psi(2S) \to e^+e^-$ (left) and $J/\psi \to e^+e^-$ (right).

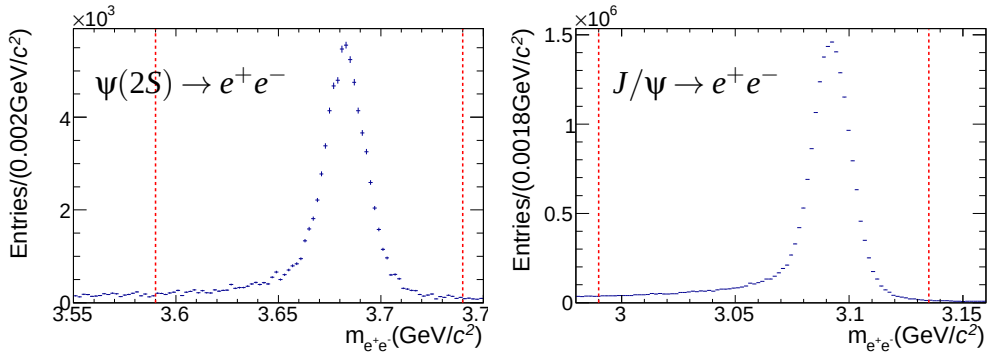

Figure 3.3: The invariant mass of $\psi(2S) \to e^+e^-$ (left) and $J/\psi \to e^+e^-$ (right) candidates. The red-dashed vertical lines indicate the invariant mass window selected in the case when the decays of $\psi(2S)$ and $J/\psi(2S)$ mesons into two electrons are considered.

3.5.4.2 The $\psi(2S)(J/\psi) \to \mu^+\mu^-$ ("leptonic") decay mode

Muons are identified on the basis of a track penetration depth and hit scatter pattern in the K_L-muon detector. Besides the K_L-muon detector information, the muon identification uses also the information from the inner tracking chambers, the central

drift chamber and the silicon vertex detector. The track is identified as a muon when it satisfies the muon identification condition $\mathcal{L}_\mu > 0.1$, where $\mathcal{L}_\mu$ is the muon likelihood, with distribution between 0 and 1. The cut $\mathcal{L}_\mu > 0.1$ is chosen in order to obtain higher muon detection efficiencies. We reconstruct $\psi(2S)$ and J/ψ mesons by requiring that both tracks are identified as muons according to the likelihood probability or one track is identified as muon using the $\mathcal{L}_\mu$ information and the other track is identified using the energy measured by the calorimeter, that ranges between $0.1\,\mathrm{GeV}$ and $0.3\,\mathrm{GeV}$. In addition, for the $\mu^+\mu^-$ decay mode we select the following mass window: $-60\,\mathrm{MeV}/c^2 \leq M_{\mu^+\mu^-} - M_{J/\psi(\psi(2S))} \leq 36\,\mathrm{MeV}/c^2$. In Figure 3.4 the mass distribution of the $\psi(2S) \to \mu^+\mu^-$ (left) and $J/\psi \to \mu^+\mu^-$ (right) is showed.

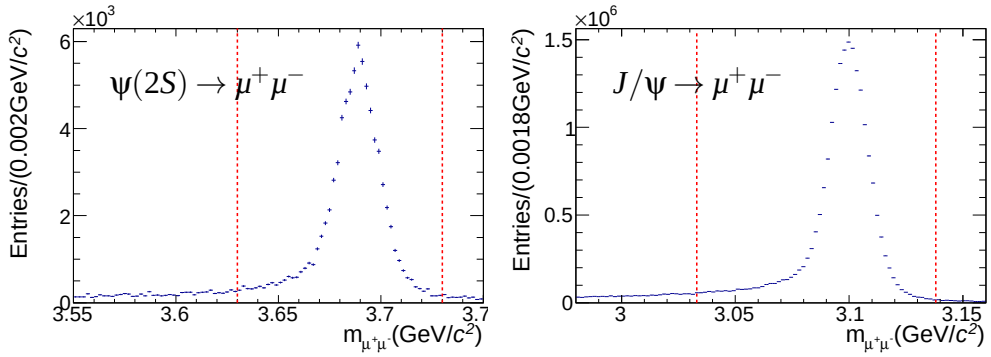

Figure 3.4: The invariant mass of $\psi(2S) \to \mu^+\mu^-$ (left) and $J/\psi \to \mu^+\mu^-$ (right) candidates. The red-dashed vertical lines indicate the invariant mass window selected in the case when the decays of the $\psi(2S)$ and $J/\psi(2S)$ mesons into two muons are considered.

3.5.4.3 The $\psi(2S) \to J/\psi\pi^+\pi^-$ ("hadronic") decay mode

For $\psi(2S) \to J/\psi\pi^+\pi^-$ decay, the reconstruction is done by combining two oppositely charged pions with the reconstructed J/ψ. For particle identification of the pion candidates we use three measurements: the number of photons from Čerenkov counter, time-of-flight from the TOF counter and the energy deposition dE/dx from the drift chamber. These three information are combined allowing particle identification in physics analyses over a range of momenta and polar angles. The pion/kaon identification is based upon the likelihood ratio, distributed on the interval [0,1] and is defined as:

$$Prob(K:\pi) = \frac{\mathcal{L}_K}{\mathcal{L}_K + \mathcal{L}_\pi} \tag{3.2}$$

In our analysis, $B^0 \to \psi(2S)\pi^0$, in case of $\psi(2S) \to J/\psi\pi^+\pi^-$, charged tracks

with $Prob(K:\pi) < 0.9$ are identified as pions. In this case we consider the following mass window: $0.58\,\mathrm{GeV}/c^2 \leq \Delta M \equiv (M_{J/\psi(l^+l^-)\pi^+\pi^-} - M_{J/\psi(l^+l^-)}) \leq 0.60\,\mathrm{GeV}/c^2$.

3.5.5 Reconstruction of π^0 from two photons

π^0 candidates are reconstructed using their decay into two photons. The photons from a B decay have a wide energy distribution from very low energies of a few tens of MeV to very high energies of a few GeV, most of which are low energies of about a few hundreds MeV. The detection of those photons is very important for the reconstruction of the B mesons. In the Belle detector the identification of photons is based on their electromagnetic interactions in the calorimeter. Photon candidates are selected from clusters in the electromagnetic calorimeter that are not matched to any charged particle track. Also the transverse cluster shape should be consistent with an electromagnetic shower. Each of the photon candidates should have an energy measured in the barrel of the calorimeter, $E_\gamma > 0.05\,\mathrm{GeV}$, whereas in the end-cap the photon candidate should exceed energy of $E_\gamma > 0.10\,\mathrm{GeV}$ in order to suppress combinatorial background.

3.5.6 Reconstruction of the neutral B mesons

The reconstruction of B meson is done by combining a $\psi(2S)$ candidate and a neutral pion. After we reconstruct B mesons we select events for which good discrimination between signal and background can be obtained. This is done by using two kinematic variables that describe the reconstructed B mesons: the beam constrained mass M_{BC} and the energy difference ΔE.
The reconstructed B meson mass, M_{BC}, is calculated using the momentum of the reconstructed B meson candidate and the beam energy in the center-of-mass system:

$$M_{BC} = \sqrt{E_{beam}^2 - p_B^{*2}}. \tag{3.3}$$

A very similar, but orthogonal observable used in this analysis is ΔE, given as the difference between the reconstructed B energy and the beam energy in the center-of-mass system:

$$\Delta E = E_B^* - E_{beam} \tag{3.4}$$

Here, E_B^* and p_B^* are the energy and the momentum of the reconstructed B candidate evaluated in the center-of-mass system, whereas E_{beam} is the beam energy also in the center-of-mass system. To obtain these quantities we use information from the precise particle tracking detectors. In this analysis, B candidates are reconstructed in the following analysis window: $5.22\,\mathrm{GeV}/c^2 \leq M_{BC} \leq 5.30\,\mathrm{GeV}/c^2$ and $-0.2\,\mathrm{GeV} \leq \Delta E \leq 0.1\,\mathrm{GeV}$.

3.5.6.1 Best B^0 selection

On average, 1.18 B^0 candidates are reconstructed per event from MC data, as shown in Figure 3.5. Because it is possible to have events with more than one reconstructed B meson, for those events the best candidate with smallest χ^2 is selected, where

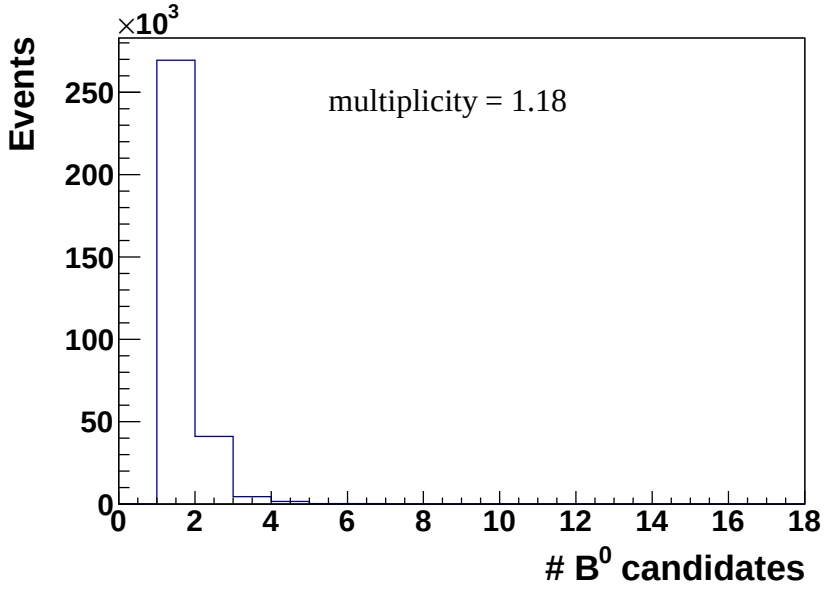

Figure 3.5: Multiplicity distribution of reconstructed $B^0 \to \psi(2S)\pi^0$ from MC data.

$$\chi^2 = \left(\frac{m_{l^+l^-} - m_{\psi(2S)}}{\sigma_{l^+l^-}}\right)^2 + \left(\frac{m_{\gamma\gamma} - m_{\pi}}{\sigma_{\gamma\gamma}}\right)^2, \tag{3.5}$$

when the $\psi(2S)$ decays leptonicaly, or

$$\chi^2 = \left(\frac{m_{\pi^+\pi^-} - (m_{\psi(2S)} - m_{J/\psi})}{\sigma_{\pi^+\pi^-}}\right)^2 + \left(\frac{m_{l^+l^-} - m_{J/\psi}}{\sigma_{l^+l^-}}\right)^2 + \left(\frac{m_{\gamma\gamma} - m_{\pi}}{\sigma_{\gamma\gamma}}\right)^2, \tag{3.6}$$

when the $\psi(2S)$ undergo the decay to $J/\psi\pi^+\pi^-$ ("hadronic" decay). Here, l^+l^- is either electron, e, or a muon, μ, while σ is obtained from the corresponding Gaussian fitted mass distributions from Figures 3.3 and 3.4, as listed in Table 3.1.

Decay Modes	Resolution [MeV/c^2]			
	SVD1		SVD2	
	$m_{\psi(2S)}$	$m_{J/\psi}$	$m_{\psi(2S)}$	$m_{J/\psi}$
$\psi(2S) \to e^+e^-$	9.2	-	9.8	-
$\psi(2S) \to \mu^+\mu^-$	6.6	-	6.0	-
$\psi(2S) \to J/\psi(\to e^+e^-)\pi^+\pi^-$	-	6.5	-	6.8
$\psi(2S) \to J/\psi(\to \mu^+\mu^-)\pi^+\pi^-$	-	6.7	-	6.0

Table 3.1: Typical resolution of mass distributions from signal Monte Carlo in both SVD1 and SVD2 for $B^0 \to \psi(2S)\pi^0$.

The obtained $m_{\gamma\gamma}$ resolution is $3.8\,\mathrm{MeV}/c^2$ and $3.7\,\mathrm{MeV}/c^2$ for SVD1 and SVD2, respectively.

3.5.7 Detection efficiencies

After the applied selection criteria, the detection efficiencies for the leptonic and hadronic mode correspondingly, are found to be as listed below.
Here the detection efficiencies are defined as a product between the raw efficiency and the PDG branching fraction value, where the raw efficiency is the ratio between the number of reconstructed and generated events calculated for each of the considered decay modes. The calculation is done for the two detector configurations SVD1 and SVD2, respectively.

$$
\begin{aligned}
&SVD1: \\
&\varepsilon(B^0 \to \psi(2S)(\to e^+e^-)\pi^0) = 0.00151 \pm 0.00005 \\
&\varepsilon(B^0 \to \psi(2S)(\to \mu^+\mu^-)\pi^0) = 0.00254 \pm 0.00026 \\
&\varepsilon(B^0 \to \psi(2S)(J/\psi(\to e^+e^-)\pi^+\pi^-)\pi^0) = 0.00187 \pm 0.00002 \\
&\varepsilon(B^0 \to \psi(2S)(J/\psi(\to \mu^+\mu^-)\pi^+\pi^-)\pi^0) = 0.00281 \pm 0.00004 \\
&SVD2: \\
&\varepsilon(B^0 \to \psi(2S)(\to e^+e^-)\pi^0) = 0.00175 \pm 0.00004 \\
&\varepsilon(B^0 \to \psi(2S)(\to \mu^+\mu^-)\pi^0) = 0.00279 \pm 0.00029 \\
&\varepsilon(B^0 \to \psi(2S)(J/\psi(\to e^+e^-)\pi^+\pi^-)\pi^0) = 0.00249 \pm 0.00003 \\
&\varepsilon(B^0 \to \psi(2S)(J/\psi(\to \mu^+\mu^-)\pi^+\pi^-)\pi^0) = 0.00356 \pm 0.00004
\end{aligned}
\tag{3.7}
$$

3.6 Data Models

The aim of this analysis is to obtain a measurement of the branching fraction for the signal channel $B^0 \to \psi(2S)\pi^0$. For this purpose we model the signal and background components, looking into two variables, M_{BC} and ΔE. We are describing the shape of each individual distribution for every component. Parameterizations used for modeling the shapes, the probability density functions (PDF), implying that they are normalized in the fit region. The determination of the yields of each individual component is performed using an extended unbinned maximum likelihood fit. Using the reconstruction efficiencies we can determine the branching fraction value from the yield measurement.
The fit is performed in two dimensions using as fitting variables the M_{BC} and ΔE. In the fitting procedure we fit simultaneously the leptonic and the hadronic mode in the two SVD configurations: During the lifetime of the Belle detector, the configuration of the silicon vertex detector (SVD) was changed, from a three layer vertex detector SVD1 to a four layer vertex detector SVD2. The complete Belle data set was recorded in two run periods with different tracking sub-systems. The run period from experiment 7 to 29 is recorded using the SVD1 configuration of the vertex detector, while from experiment 31 to 65, the SVD2. With the SVD1 configuration Belle collected 152 Million $B\bar{B}$ pairs, while with the SVD2 configuration the amount of collected data was 620 Million $B\bar{B}$ pairs. The PDFs for the signal and background are modeled as separate components. The description of how each PDF is built is given below.

3.6.1 Signal Model

The signal model shape is determined from correctly reconstructed signal MC events and is expressed as

$$\mathcal{P}(M_{BC}, \Delta E) = \mathcal{P}(M_{BC}|\Delta E) \cdot \mathcal{P}(\Delta E). \tag{3.8}$$

The M_{BC} distribution is modeled using two Bifurcated Gaussians (PDF with different widths on left and right side of the maximum value) and an ARGUS function [58]. The model is given by

$$\begin{aligned}\mathcal{P}_{Sig}(M_{BC}|\Delta E) = {} & f_1(\Delta E) G1(M_{BC}; \mu_1(\Delta E), \sigma_{R_1}(\Delta E), \sigma_{L_1}(\Delta E)) \\ & + f_2(\Delta E) G2(M_{BC}; \mu_2(\Delta E), \sigma_{R_2}(\Delta E), \sigma_{L_2}(\Delta E)) \\ & + (1 - f_1(\Delta E) - f_2(\Delta E)) ARGUS(M_{BC}; a, E_{beam}).\end{aligned} \tag{3.9}$$

As seen from Equation 3.9 the PDF is built such that M_{BC} depends on ΔE. We consider the following slices of ΔE :

- $-0.2\,\mathrm{GeV} \leq \Delta E < -0.15\,\mathrm{GeV}$,
- $-0.15\,\mathrm{GeV} \leq \Delta E < -0.1\,\mathrm{GeV}$,
- $-0.1\,\mathrm{GeV} \leq \Delta E < -0.05\,\mathrm{GeV}$,
- $-0.05\,\mathrm{GeV} \leq \Delta E < 0.\,\mathrm{GeV}$,
- $0.\,\mathrm{GeV} \leq \Delta E < 0.05\,\mathrm{GeV}$ and
- $0.05\,\mathrm{GeV} \leq \Delta E \leq 0.1\,\mathrm{GeV}$.

The M_{BC} fit projections in these intervals of ΔE are shown in the Appendix C in Figures C.1 and C.2.
With the exception of the ARGUS parameter a, all M_{BC} model parameters depend on ΔE. The dependence of each parameter is given in the Appendix B, while the signal model of the M_{BC} distribution fitted in the entire range of ΔE is shown in Figure 3.6.

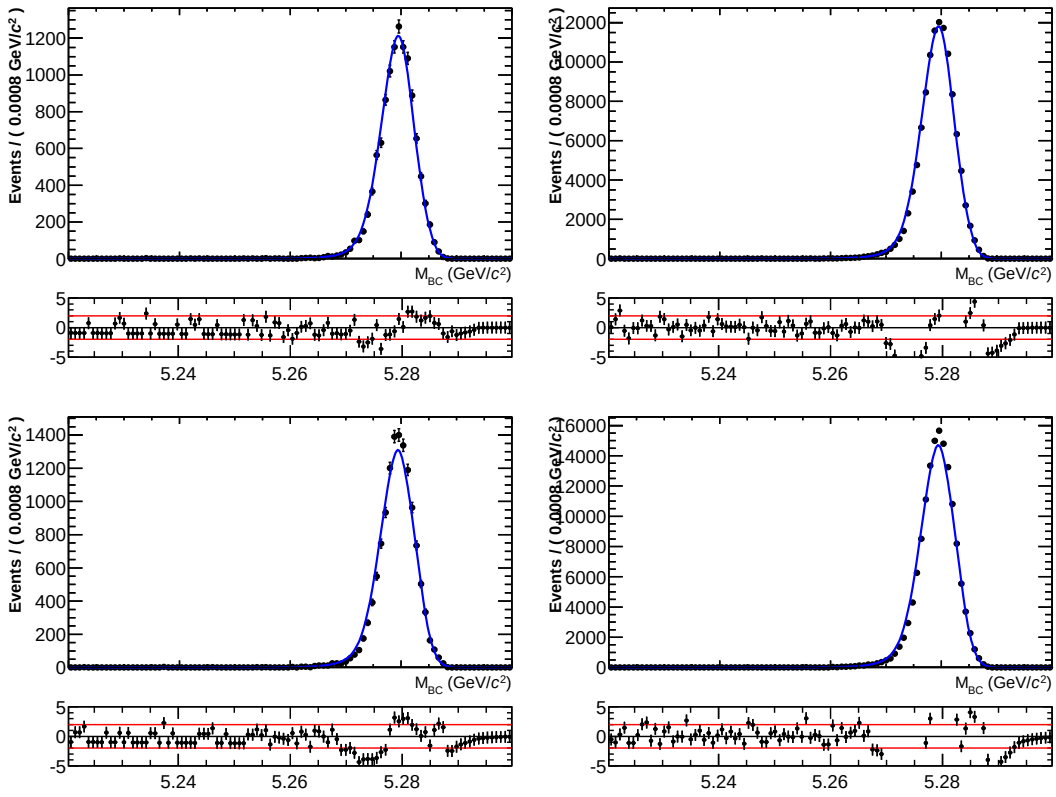

Figure 3.6: M_{BC} fit projections of correctly reconstructed signal MC for $B^0 \to \psi(2S)\pi^0$ for leptonic mode (left) and hadronic mode (right) for the two detector configurations SVD1 (top) and SVD2 (bottom).

The model used to fit the ΔE distribution contains triple a Gaussian and Bernstein Polynomial function of the second order (see Appendix A.3). It is given by

$$\begin{aligned}\mathcal{P}_{Sig}(\Delta E) = f_1 G1(\Delta E;\mu_1,\sigma_1) + f_2 G1(\Delta E;\mu_2,\sigma_2) \\ + f_3 G3(\Delta E;\mu_3,\sigma_3) + (1-f_1-f_2-f_3) BP(\Delta E;c_1,c_2).\end{aligned} \tag{3.10}$$

Figure 3.7 shows the fit projection of the signal model for ΔE distribution. The sub-plot of the normalized residuals in Figures 3.6 and 3.7 shows the difference between the data bin and the PDF, divided by the error of the data bin. Even though it seems that the signal model in some regions does not describe the data perfectly, we have estimated a systematic uncertainty coming from the imperfections of the signal model of 2.8% (see Section 3.10.9).

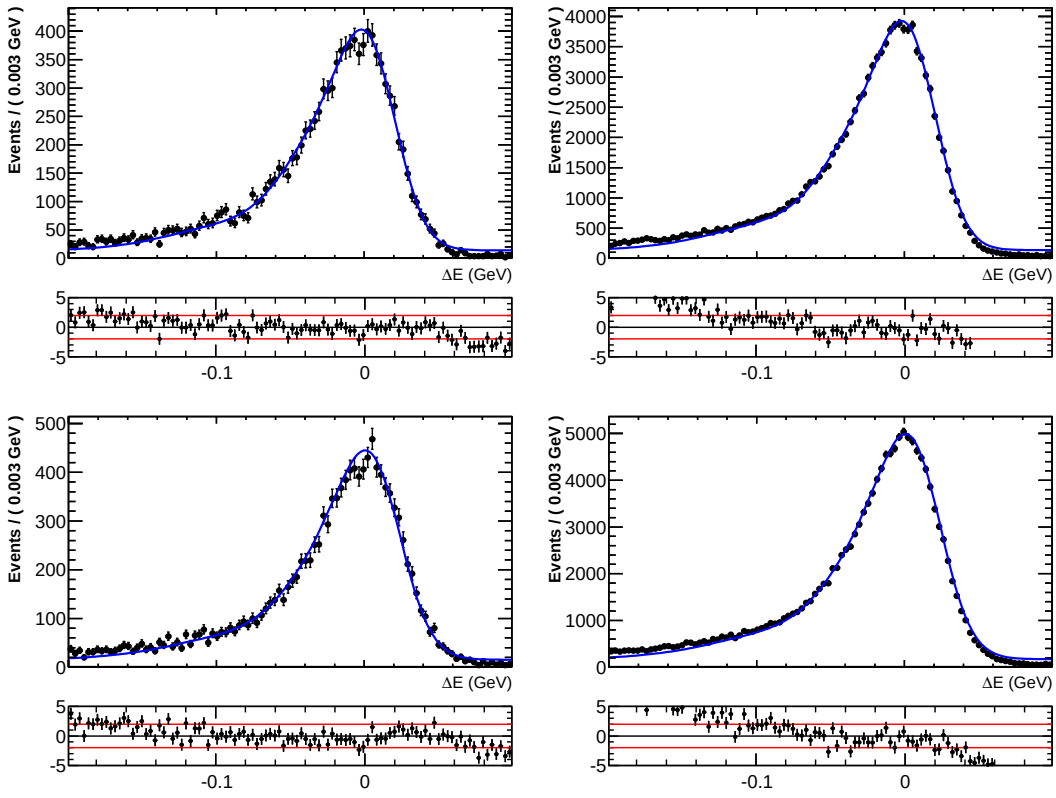

Figure 3.7: ΔE fit projections of correctly reconstructed signal MC for $B^0 \to \psi(2S)\pi^0$ for leptonic mode (left) and hadronic mode (right) for the two detector configurations SVD1 (top) and SVD2 (bottom).

3.6.2 Misreconstructed Model

The shape of the misreconstructed fraction of events for $B^0 \to \psi(2S)\pi^0$ is determined from incorrectly reconstructed MC events, identified using the MC truth information. As PDF model $\mathcal{P}(M_{BC}, \Delta E)$ for this component we use histogram PDFs in two dimensions. Projections of the two fit observables are shown in Figures 3.8 and 3.9.

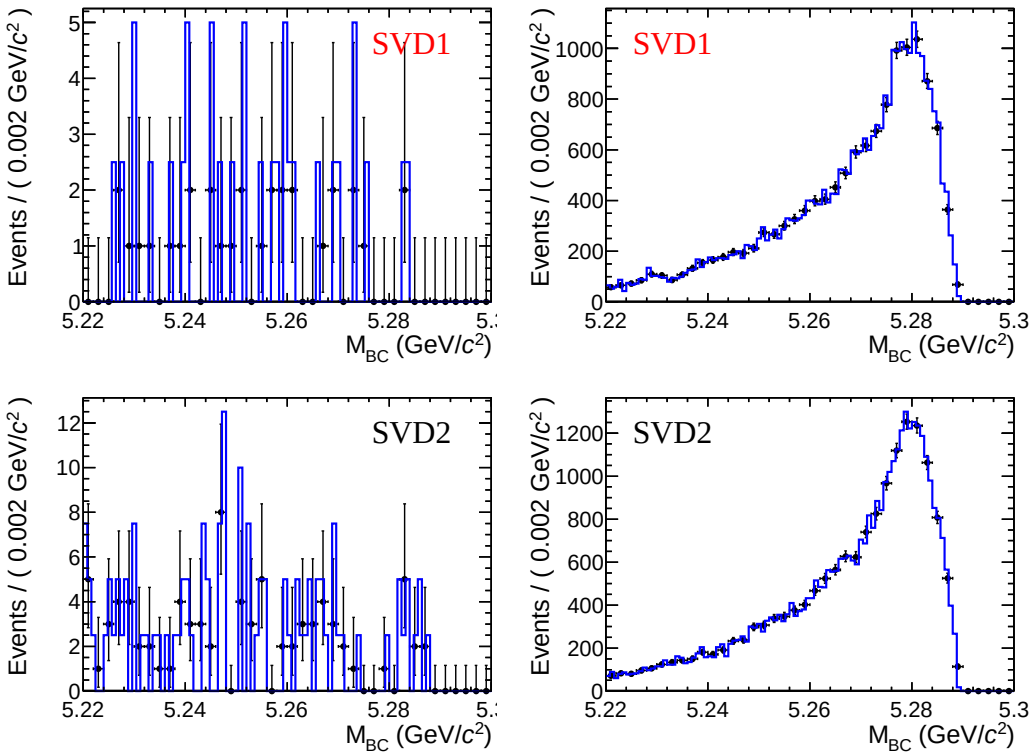

Figure 3.8: M_{BC} fit projections of misreconstructed $B^0 \to \psi(2S)\pi^0$ signal MC for the leptonic mode (left) and the hadronic mode (right) for the two detector configurations SVD1 (top) and SVD2 (bottom).

The extracted misreconstructed fractions corresponding to the leptonic or hadronic mode for both SVD1 and SVD2 are listed in the Table 3.2.
As it can be seen from the Table 3.2, the fraction of misreconstructed signal in the leptonic decays is of the order of 0.3% for SVD1 and 0.6% for SVD2, which is very small compared to the signal. Therefore, we do not include these components coming from the leptonic modes in the final fit elaborated in Section 3.6.6. Whereas the misreconctructed fraction in the case of hadronic decay of $\psi(2S)$ is 11% for SVD1 and 10% for SVD2, thus the misreconstructed hadronic components are included in the final fit.

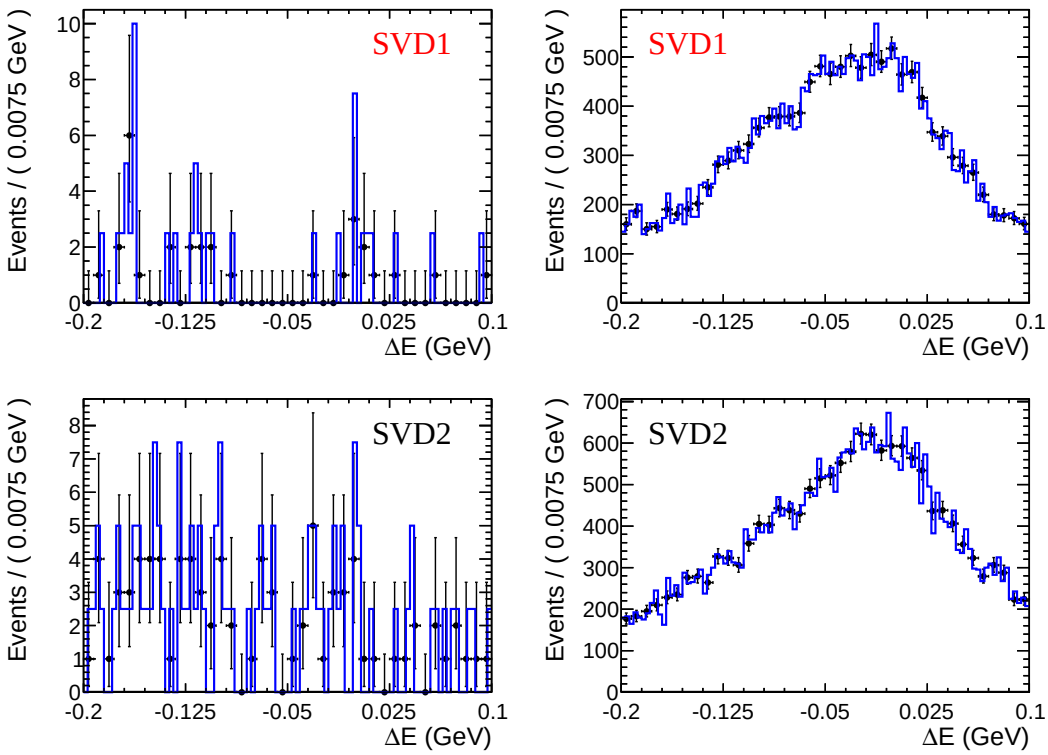

Figure 3.9: ΔE fit projections of misreconstructed $B^0 \to \psi(2S)\pi^0$ signal MC for the leptonic mode (left) and the hadronic mode (right) for the two detector configurations SVD1 (top) and SVD2 (bottom).

Decay Modes	Misreconstructed signal fraction	
	SVD1	SVD2
$B^0 \to \psi(2S)(\to l^+l^-)\pi^0$	0.003	0.006
$B^0 \to \psi(2S)(\to J/\psi\pi^+\pi^-)\pi^0$	0.11	0.10

Table 3.2: Fraction of the misreconstructed signal events in SVD1 and SVD2 for both decay modes, leptonic and hadronic.

3.6.3 $B^0 \to c\bar{c}X$ background model

The backgrounds having the same final state as the signal decay, peak in the $M_{BC} - \Delta E$ signal box, hence are named ”peaking backgrounds”. Therefore, these contributions cannot be discriminated from the signal decay. The possibility of having a peaking

background coming only from $B^0 \to \psi(2S)K_S$ decay, where $K_S \to \pi^0\pi^0$ and a $B^0 \to \psi(2S)K_L$ decay has been considered. This would lead to a separation of the peaking and non-peaking background.
However, the investigation of the leptonic and the hadronic contribution in the distributions of M_{BC} and ΔE showed that while the majority of the peaking background comes from $B^0 \to \psi(2S)K_S$ and $B^0 \to \psi(2S)K_L$ decays, which is about 2/3 of the total, an additional peaking background contribution appears in the charged B meson $(\psi(2S), J/\psi)$ decays to charmonium. The charged B meson decays from the $B \to c\bar{c}X$ MC data also include the $B^+ \to \psi(2S)K^{*+}$ decay, which is our control sample and will be discussed later in Section 3.7. The plots showing these effects are depicted in Figures 3.10 and 3.11.

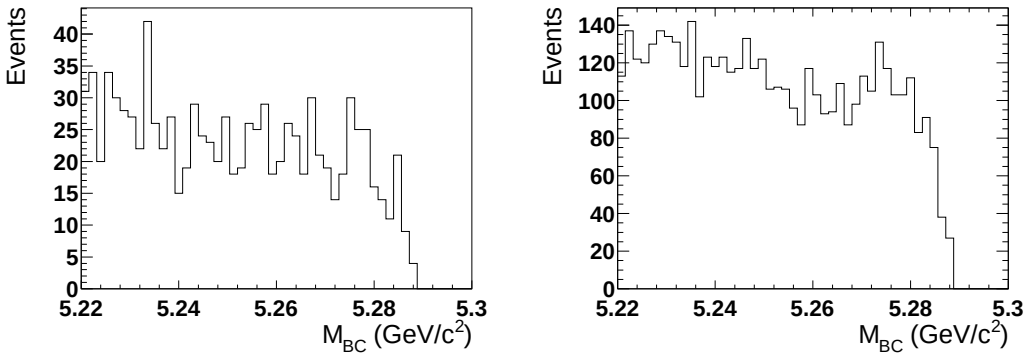

Figure 3.10: M_{BC} distribution of charged B meson decays, $B^+(B^-) \to \psi(2S)X$, $\psi(2S) \to l^+l^-$ for SVD1 (left) and SVD2 (right).

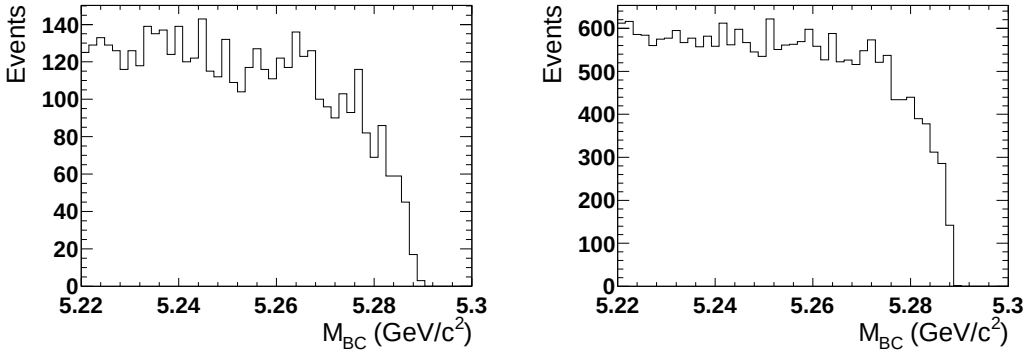

Figure 3.11: M_{BC} distribution of charged B meson decays, $B^+(B^-) \to J/\psi X$, $J/\psi \to l^+l^-$ (which includes $\psi(2S) \to J/\psi\pi^+\pi^-$ decay) for SVD1 (left) and SVD2 (right).

In the neutral B meson decays to charmonium this peaking background is also visible

and is much more pronounced than in the charged charmonium modes. The M_{BC} distribution in the neutral B meson charm decays can be seen in Figures 3.12 and 3.13.

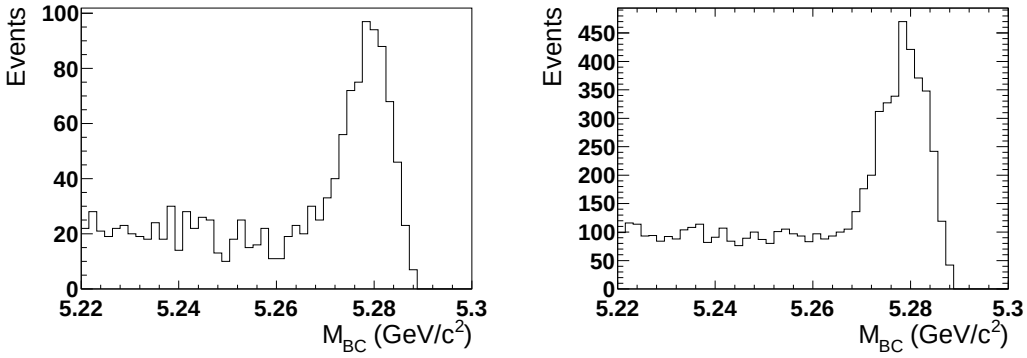

Figure 3.12: M_{BC} distribution of neutral B meson decays, $B^0(\bar{B}^0) \to \psi(2S)X$, $\psi(2S) \to l^+l^-$ for SVD1 (left) and SVD2 (right).

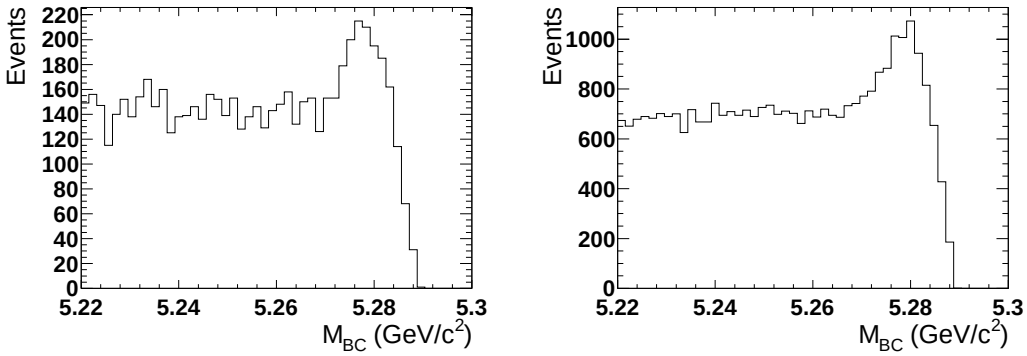

Figure 3.13: M_{BC} distribution of neutral B meson decays, $B^0(\bar{B}^0) \to J/\psi X$, $J/\psi \to l^+l^-$ (which includes $\psi(2S) \to J/\psi\pi^+\pi^-$ decay) for SVD1 (left) and SVD2 (right).

The ΔE distribution on the other hand, does not give a peaking background neither in the charged B meson decays into charmonium as shown in Figures 3.14 and 3.15, nor in the neutral B meson charmonium decays, as seen from Figures 3.16 and 3.17.
Therefore, we treat both leptonic and hadronic contributions for the charged and neutral B meson decays together using only one shape to model the $B^0 \to c\bar{c}X$ background component.

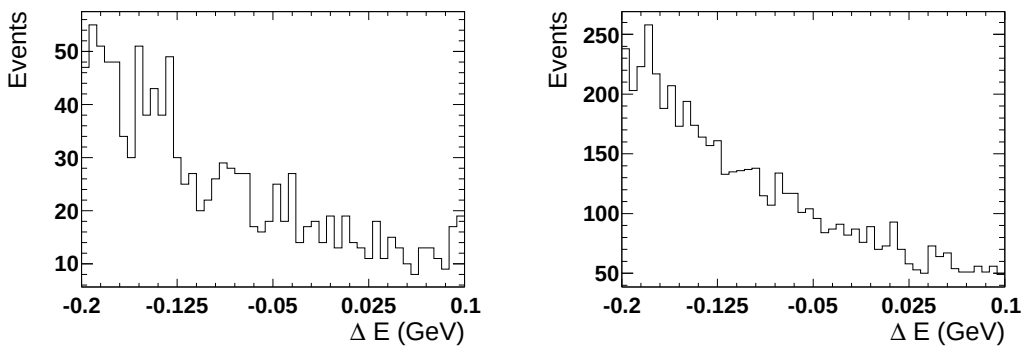

Figure 3.14: ΔE distribution of charged B meson decays, $B^+(B^-) \to \psi(2S)X$, $\psi(2S) \to l^+l^-$ for SVD1 (left) and SVD2 (right).

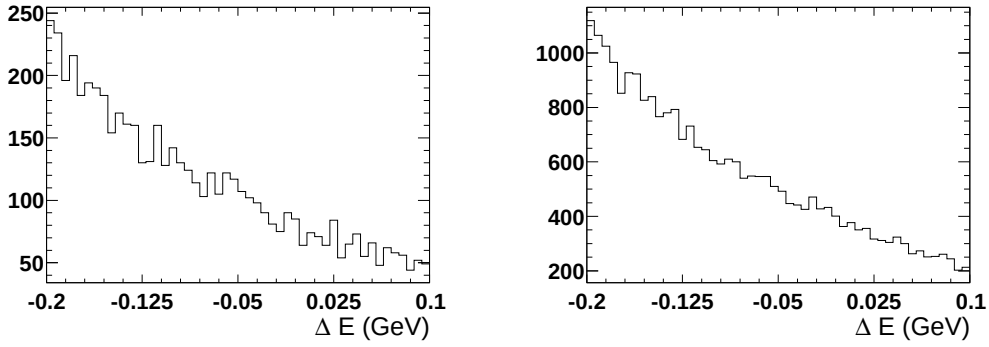

Figure 3.15: ΔE distribution of charged B meson decays, $B^+(B^-) \to J/\psi X$, $J/\psi \to l^+l^-$ (which includes $\psi(2S) \to J/\psi\pi^+\pi^-$ decay) for SVD1 (left) and SVD2 (right).

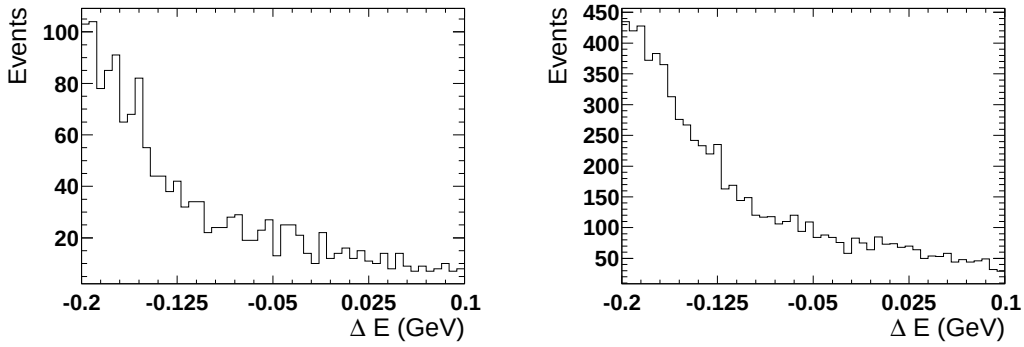

Figure 3.16: ΔE distribution of neutral B meson decays, $B^0(\bar{B^0}) \to \psi(2S)X$, $\psi(2S) \to l^+l^-$ for SVD1 (left) and SVD2 (right).

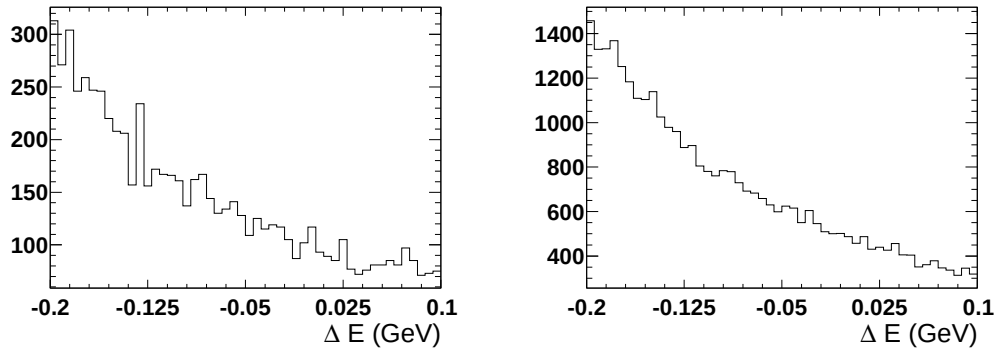

Figure 3.17: ΔE distribution of neutral B meson decays, $B^0(\bar{B^0}) \to J/\psi X$, $J/\psi \to l^+l^-$ (which includes $\psi(2S) \to J/\psi\pi^+\pi^-$ decay) for SVD1 (left) and SVD2 (right).

For the shape of the $B^0 \to c\bar{c}X$ background component a 2D histogram PDF is used. The fit projections of M_{BC} and ΔE distributions are shown in Figures 3.18 and 3.19, respectively.

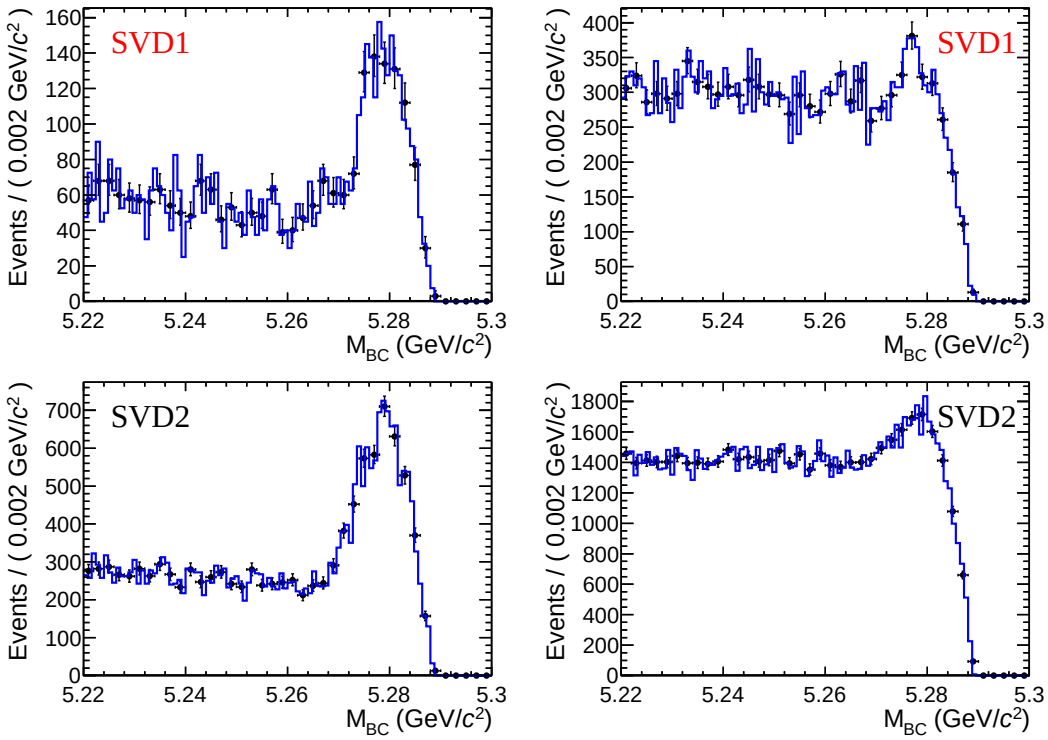

Figure 3.18: M_{BC} fit projections of $B \to c\bar{c}X$ MC for leptonic mode (left) and hadronic mode (right) for the two detector configurations SVD1 (top) and SVD2 (bottom).

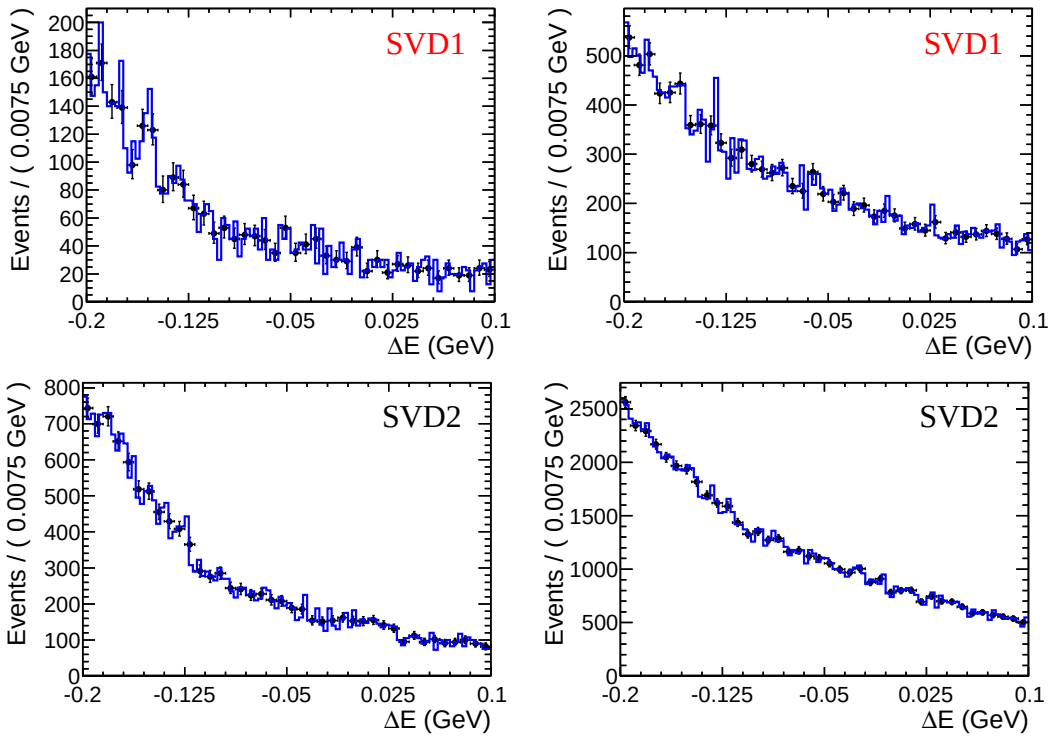

Figure 3.19: ΔE fit projections of $B \to c\bar{c}X$ MC for leptonic mode (left) and hadronic mode (right) for the two detector configurations SVD1 (top) and SVD2 (bottom).

3.6.4 Sideband Studies

We also considered the possibility of having peaking backgrounds coming from other B decays that are not B decays to charmonium states. In this particular case of estimating the peaking background coming from $B\bar{B}$ decays we look at real $B^0 \to \psi(2S)\pi^0$ data, which is different with respect to $B \to c\bar{c}X$ decays where MC was used.

The amount of peaking background is estimated looking at the sidebands from mass ($M_{\psi(2S)(J/\psi)}$) and mass difference ($M_{\psi(2S)} - M_{J/\psi}$). Depending on that in which of these three distributions we looked, we separated the data in three different subsets. This separation was done applying different mass selection criteria for the reconstructed $\psi(2S)$ and J/ψ mesons in the $B^0 \to \psi(2S)\pi^0$ decay.

For $\psi(2S) \to l^+l^-$ only events for which $3.45\,\mathrm{GeV}/c^2 < m_{ll} < 3.53\,\mathrm{GeV}/c^2$ (below the $\psi(2S)$) and $3.8\,\mathrm{GeV/c^2} < m_{ll} < 3.9\,\mathrm{GeV}/c^2$ (above the $\psi(2S)$) are considered. For $J/\psi \to l^+l^-$ the applied mass cuts are following: $2.6\,\mathrm{GeV}/c^2 <$

$m_{ll} < 2.8\,\mathrm{GeV}/c^2$ (below the J/ψ) and $3.2\,\mathrm{GeV}/c^2 < m_{ll} < 3.4\,\mathrm{GeV}/c^2$ (above the J/ψ). As for the third data subset the mass difference between $\psi(2S)$ and J/ψ is used and the following mass selection criteria are taken into account, $0.49\,\mathrm{GeV}/c^2 < m_{ll} < 0.53\,\mathrm{GeV}/c^2$ and $0.64\,\mathrm{GeV}/c^2 < m_{ll} < 0.68\,\mathrm{GeV}/c^2$. According to these three different mass cuts, the $B^0 \to \psi(2s)\pi^0$ sideband data was discriminated in three subsets with each of the data subset being checked separately. The investigation showed that in all three separate data subsets, no peaking background appeared. The plots showing this result are depicted in Figure 3.20. The sub-plot of the normalized residuals in Figure 3.20 shows the difference between the data bin and the PDF, divided by the error of the data bin.
The extracted SVD1 and SVD2 peaking background yields corresponding to the different decay modes are presented in Table 3.3. As it can be seen from this table, the amount of peaking background estimated using the sideband data is completely negligible.
Since, this kind of background is non-peaking cannot be separated from continuum and therefore we treat them as one, "combinatorial" background component.

Mass selection	$3.45 < m_{\psi(2S)} < 3.53$ $3.8 < m_{\psi(2S)} < 3.9$	$2.6 < m_{J\psi} < 2.8$ $3.2 < m_{J\psi} < 3.4$	$0.49 < m_{\psi(2S)} - m_{J\psi} < 0.53$ $0.64 < m_{\psi(2S)} - m_{J\psi} < 0.68$
SVD1	0.0 ± 4.4	1.3 ± 2.8	0.0 ± 4.3
SVD2	0.0 ± 21.7	6.7 ± 13.7	0.0 ± 0.0

Table 3.3: Peaking background yields from SVD1 and SVD2 using different sideband data set according to the separate decay modes of B^0.

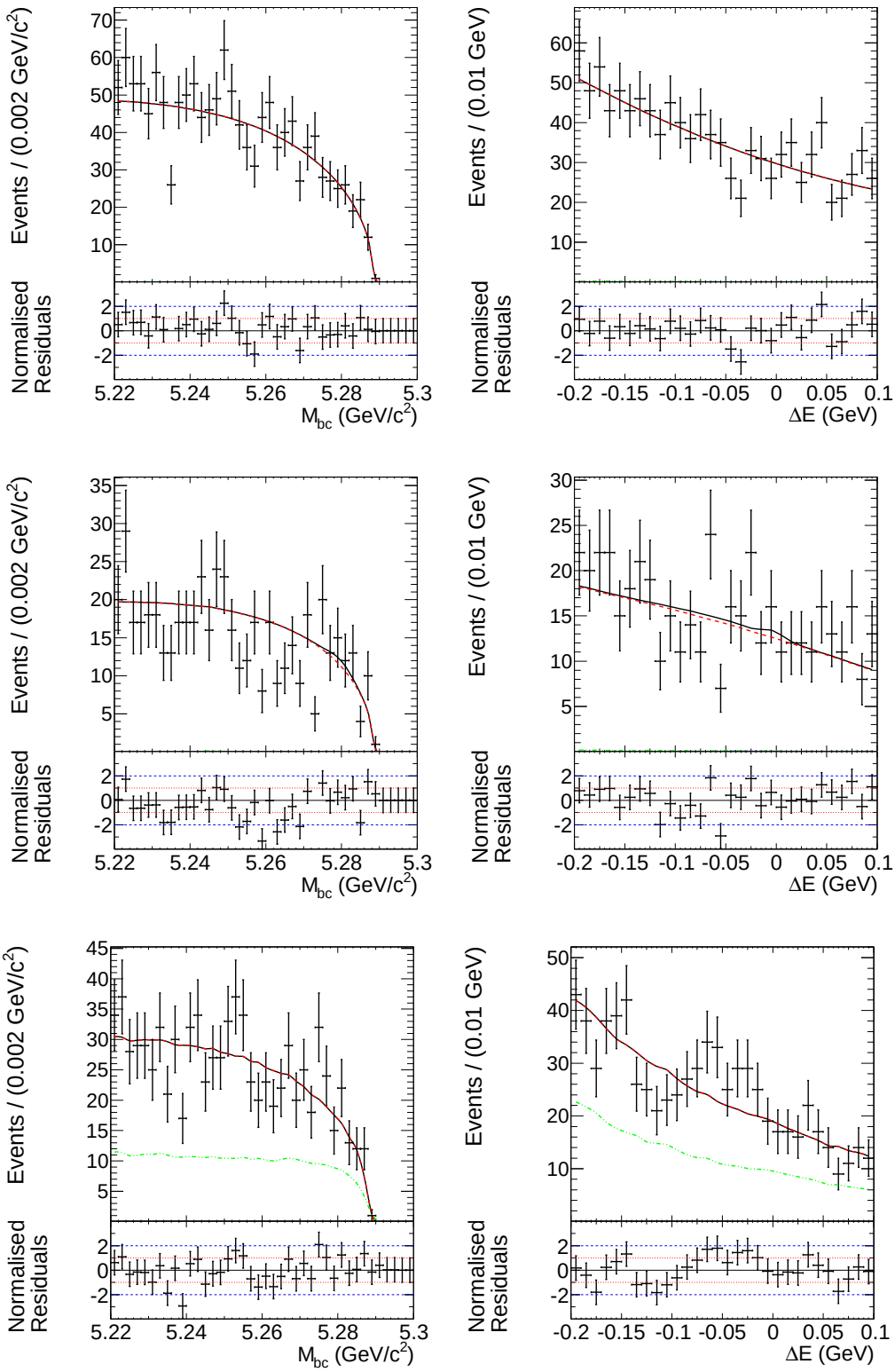

Figure 3.20: Separate $B^0 \to \psi(2S)\pi^0$ sideband data subsets. The M_{BC} (left) and ΔE (right) distributions using $M_{\psi(2S)}$ data sidebands (top), for cuts valid for the mass spectrum of the reconstructed J/ψ mesons (middle) and for the sideband data, chosen according to the applied cut on the mass difference between $\psi(2S)$ and J/ψ. Blue (dashed) line for the misreconstructed component, green (dotted dashed) line for the $B \to c\bar{c}X$, red (dashed) line for the PDF composed from all the background components and the black solid line for the total PDF.

3.6.5 $B\bar{B}$ and continuum Background Model

As explained in Section 3.5.2, continuum background is suppressed using the ratio of second to zeroth Fox-Wolfram moment, $R_2 < 0.5$ criteria. For the shape of the generic $B\bar{B}$ and continuum ($q\bar{q}$) background, an ARGUS function for M_{BC} and Chebyshev polynomials for ΔE are used. The corresponding PDFs are given by

$$\mathcal{P}_{B\bar{B},q\bar{q}}(M_{BC}) = ARGUS(M_{BC}; a, E_{beam}) \tag{3.11}$$

and

$$\mathcal{P}_{B\bar{B},q\bar{q}}(\Delta E) = c_1 C(\Delta E) \tag{3.12}$$

The corresponding $B\bar{B}$ and $q\bar{q}$ model parameters of M_{BC} and ΔE are freed in the final fit. The values of the free parameters (the yields of the combinatorial background for SVD1 and SVD2 and its shape) are determined, minimizing the $-log\mathcal{L}_{B^0\to\psi(2S)\pi^0}$, where $\mathcal{L}_{B^0\to\psi(2S)\pi^0}$ is the total likelihood for the $B^0 \to \psi(2S)\pi^0$, described explicitly in Section 3.6.6.

3.6.6 Complete parameterization containing all the components

The total likelihood for $B^0 \to \psi(2S)\pi^0$ is built incorporating the signal PDF, misreconstruction, $B \to c\bar{c}X$ and the common generic $B\bar{B}$-continuum ($q\bar{q}$) PDF. For the misreconstruction and $B \to c\bar{c}X$ component, 2D histogram PDFs are used. The PDFs for the signal and $B \to c\bar{c}X$ are obtained from Monte Carlo. The combinatorial background PDF is obtained from data. We determine the yields of each individual component using an extended unbinned maximum likelihood fit. The extended likelihood function is constructed from the probability density functions for the signal and background components and Poisson factors to estimate the signal and background yields. A minimization of the extended likelihood of a composite model with a signal and background term gives directly the estimates for the signal and background event yields. In the final fit the yields from $B \to c\bar{c}X$ are fixed to the values determined from MC (see Table 3.4). The combinatorial (generic $B\bar{B}$ and continuum) yield $N_{B\bar{B}-q\bar{q}}$ and its shape are treated as a free parameters.

	$B^0 \to \psi(2S)(\to l^+l^-)\pi^0$	$B^0 \to \psi(2S)(\to J/\psi(\to l^+l^-)\pi^+\pi^-))\pi^0$
SVD1	22.68	99.79
SVD2	108.89	482.85

Table 3.4: $B \to c\bar{c}X$ yields for the leptonic and hadronic mode in SVD1 and SVD2 extracted from MC.

The total likelihood for $B^0 \to \psi(2S)\pi^0$ is given by

$$\begin{aligned}\mathcal{L}_{B^0\to\psi(2S)\pi^0} = \frac{e^{-(N_{Sig}+N_{mis}+N_{c\bar{c}X}+N_{B\bar{B},q\bar{q}})}}{N!}\prod_{i=1}^{N}(&N_{Sig}\mathcal{P}_{Sig}(M_{BC},\Delta E)\\ &+N_{mis}\mathcal{P}_{mis}(M_{BC},\Delta E)\\ &+N_{c\bar{c}X}\mathcal{P}_{c\bar{c}X}(M_{BC},\Delta E)\\ &+N_{B\bar{B},q\bar{q}}\mathcal{P}_{B\bar{B},q\bar{q}}(M_{BC},\Delta E)).\end{aligned} \tag{3.13}$$

The final fit is performed in two dimensions, fitting simultaneously the SVD1 and SVD2 detector configurations for two separate decay modes: leptonic and hadronic. In the final fit, the signal yields for $B^0 \to \psi(2S)\pi^0$ are replaced by the branching fraction which is then chosen as a free parameter. The $N^i_{Sig,B^0\to\psi(2S)\pi^0}$ (yields of the simultaneous fit) and the branching fraction are related as

$$\begin{gathered}N^i_{Sig,B^0\to\psi(2S)\pi^0} = \mathcal{B}(B^0 \to \psi(2s)\pi^0)\cdot N_{B\bar{B}}\cdot\varepsilon^i_{Sig,B^0\to\psi(2S)\pi^0}\\ (i = \text{leptonic}, \text{hadronic}, \text{SVD1}, \text{SVD2})\end{gathered} \tag{3.14}$$

where $\varepsilon^i_{Sig,B^0\to\psi(2S)\pi^0}$ is the detection efficiency (see Section 3.5.7) and $N_{B\bar{B}}$ is the number of $B\bar{B}$ pairs.

3.7 Control sample

For estimating the systematic uncertainty due to the difference between the data and MC, we use the control sample $B^+ \to \psi(2S)K^{*(+)}, K^{*(+)} \to K^+\pi^0$, which is well established and has a similar event topology as $B^0 \to \psi(2S)\pi^0$. The reason of choosing this particular channel as a control sample is due to the fact that in order to test the model on real data it is necessary to have a sample which is as close as

possible to the decay in question.
The reconstruction of $\psi(2S)$ candidates follows the same procedure described in Section 3.5. The $K^{*(+)}$ candidates in the considered case disintegrate into K^+ and π^0. For the kaons particle ID criteria are applied, according to the kaon/pion separation method (see Section 3.5.4.3), thus requiring

$$Prob(K:\pi) = \frac{\mathcal{L}_K}{\mathcal{L}_K + \mathcal{L}_\pi} > 0.4 \ . \tag{3.15}$$

In addition, the π^0 helicity angle, which is the angle between the π^0 momentum in $K^{*(+)}$ rest frame and $K^{*(+)}$ momentum vector in the laboratory frame, is requested to be less than $1.5\,\mathrm{rad}$. This requirement is introduced in order to select high momentum π^0's that travel forward with respect to $K^{*(+)}$ momentum. The invariant mass window used for the selection of $K^{*(+)} \to K^+\pi^0$ candidates is $0.793\,\mathrm{Gev}/c^2 < M_{K^+\pi^0} < 0.990\,\mathrm{GeV}/c^2$.

3.7.1 Difference between Data and MC

Before applying the MC derived signal shape parameters for M_{BC} and ΔE to real data, we make some adjustments of the MC results by comparing to real data of the control sample. These adjustments are the so-called "offsets" and "fudge factors".
The difference between data and MC defined as "offset" given by

$$Offset_{mean} = (mean_{data} - mean_{MC}) \pm Err^{Offset_{mean}} \tag{3.16}$$

holds for the mean of the distribution. While the "fudge factor" described as

$$FudgeFactor_{width} = \frac{width_{data}}{width_{MC}} \pm Err^{FudgeFactor_{width}} \tag{3.17}$$

is valid for the width of the distribution.
These values are extracted from a simultaneous fit of the leptonic and the hadronic mode in both SVD1 and SVD2 detector configurations of the control sample data, obtained by fixing all the parameters of the fit according to the MC model described in Section 3.6.1, but leaving the offset which is the global mean and the fudge factor which is the ratio of all Gaussians as free parameters. The fitted distributions of the

control sample of both M_{BC} and ΔE are given in Figure 3.21 and in Figure 3.22, respectively.

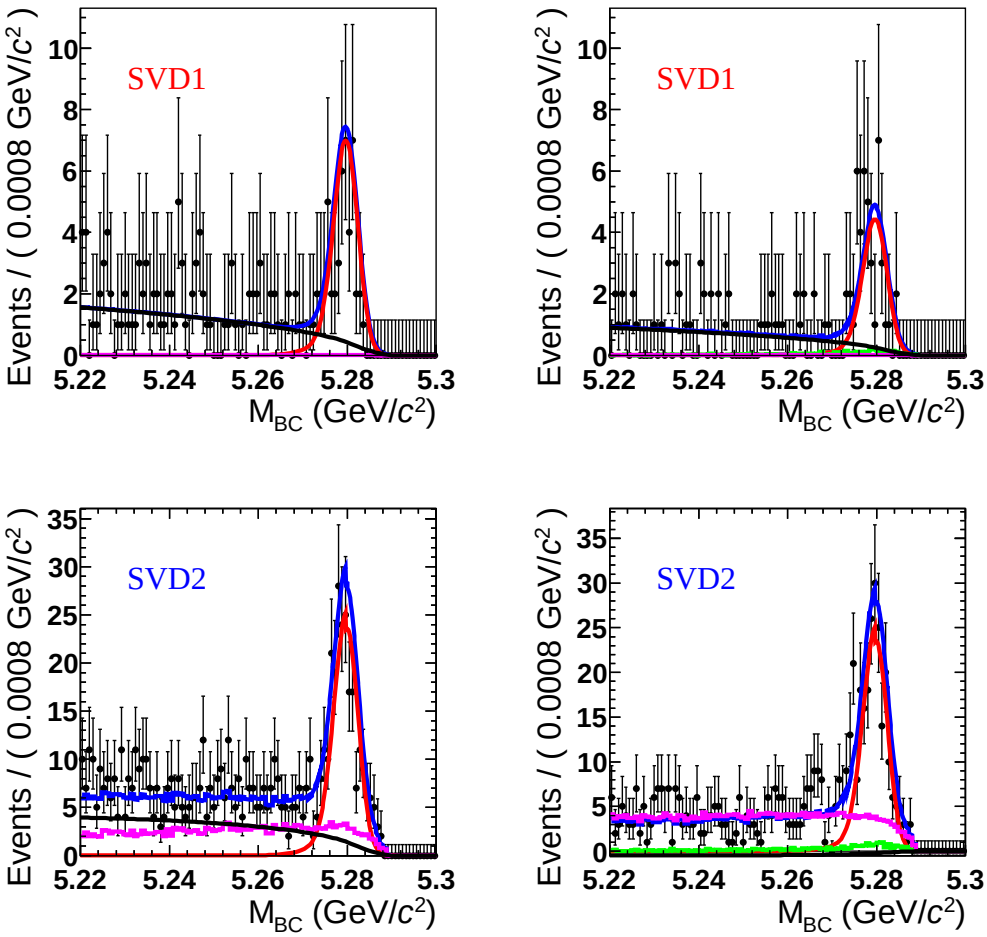

Figure 3.21: M_{BC} distribution of the data from the control sample fitted simultaneously for the leptonic mode (left), hadronic mode (right), SVD1 (top) and SVD2 (bottom). The red solid line shows the signal PDF, green solid line misreconstruction PDF, magenta solid line the PDF of $B \to c\bar{c}X$ component, the black solid line is the $B\bar{B}, q\bar{q}$ PDF and the blue solid line represents the total PDF.

The extracted corresponding differences between data and MC are shown in Table 3.5. As can be seen from the Table 3.5, obtained values of the global mean and the width from the fit of the control sample are consistent with 0 and 1, respectively. However, the error in ΔE distribution is found to be quite large, of the order of $\sim 40\%$. Unfortunately due to the limited statistics that is on disposal in this control sample

these values cannot be reduced anymore.

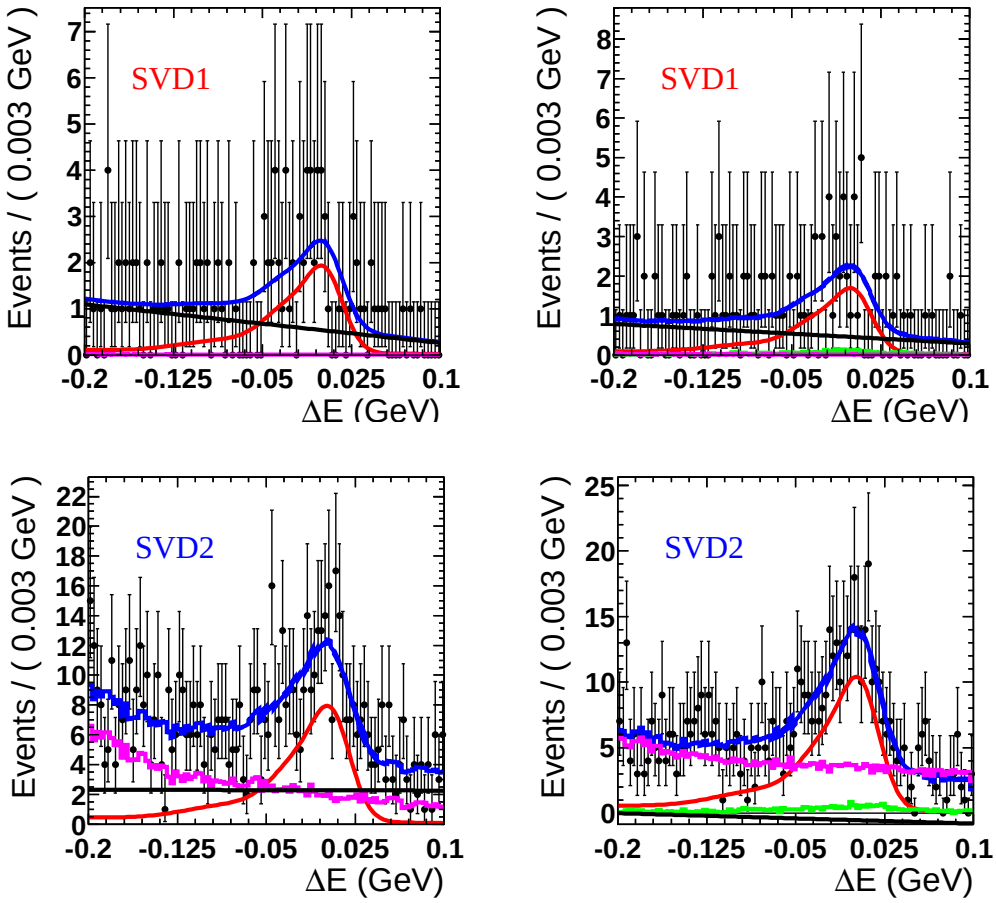

Figure 3.22: ΔE distribution of the data from the control sample fitted simultaneously for the leptonic mode (left), hadronic mode (right), SVD1 (top) and SVD2 (bottom). The red solid line shows the signal PDF, green solid line misreconstruction PDF, magenta solid line the PDF of $B \to c\bar{c}X$ component, the black solid line is the $B\bar{B}, q\bar{q}$ PDF and the blue solid line represents the total PDF.

	Offset (MeV)	Fudge Factor
M_{BC}	$(0.0 \pm 0.7) \times 10^{-4}$	0.96 ± 0.06
ΔE	$(-0.52 \pm 1.52) \times 10^{-3}$	0.80 ± 0.40

Table 3.5: Offset and width for both distributions M_{BC} and ΔE obtained from the control sample $B^+ \to \psi(2S)K^{*(+)}, K^{*(+)} \to K^+\pi^0$.

Since, ΔE resolution depends strongly on π^0, instead of $B^+ \to \psi(2S)K^{*(+)}, K^{*(+)} \to K^+\pi^0$ it is better to use $B^+ \to J/\psi K^{*(+)}, K^{*(+)} \to K^+\pi^0$ as a control sample. Therefore, we extract these values from the already performed analysis of $B^0 \to J/\psi\pi^0$ [59] where $B^+ \to J/\psi K^{*(+)}$ is used as a control sample. The corresponding extracted values are summarized in Table 3.6.

	Parameter	SVD1	SVD2 (Experiment 31-43)
M_{BC}	offset (MeV)	0.1 ± 0.1	0.3 ± 0.1
	fudge factor	0.92 ± 0.04	0.97 ± 0.03
ΔE	offset (MeV)	-4.1 ± 1.7	-7.1 ± 1.3
	fudge factor	1.03 ± 0.06	1.01 ± 0.04

Table 3.6: The obtained offset and fudge factor values from the fit result in the control sample $B^\pm \to J/\psi K^{*(\pm)}, K^{*(\pm)} \to K^\pm\pi^0$ (for more details see [59]).

Figure 3.22, also shows that in the ΔE distribution of the control sample $B^+ \to \psi(2S)K^{*(+)}, K^{*(+)} \to K^+\pi^0$ in the hadronic mode $\psi(2S) \to J/\psi\pi^+\pi^-$, the $B \to c\bar{c}X$ background component dominates the $B\bar{B}, q\bar{q}$, which is not the case in the leptonic mode $\psi(2S) \to l^+l^-$. In order to check if the same effect is present in real $B^0 \to \psi(2S)\pi^0$ data, a so-called blind fit is performed.

3.8 Blind Fit

A blind fit is actually a fit applied on the real $B^0 \to \psi(2S)\pi^0$ data, but masking the signal region of the M_{BC} and ΔE distributions. In this way the analysis of the data

is pointed only in the direction of the sideband regions of both distributions, without extracting the value of the branching fraction as an outcome of the fit. The signal yield in this fit is a random number. In Figures 3.23, 3.24, the likelihood projections of M_{BC} and ΔE distribution, respectively, are shown.
These plots indicate that the tension in the hadronic decay of $\psi(2S)$ at higher ΔE that has been seen in the control sample, $B^+ \to \psi(2S)K^{*+}$ (see Figure 3.22), where the $B \to c\bar{c}X$ background component dominates the combinatorial background and over shoots the total PDF curve is now resolved. Thus, in the real data the fit describes all the components quite well, and no further adjustments are needed.

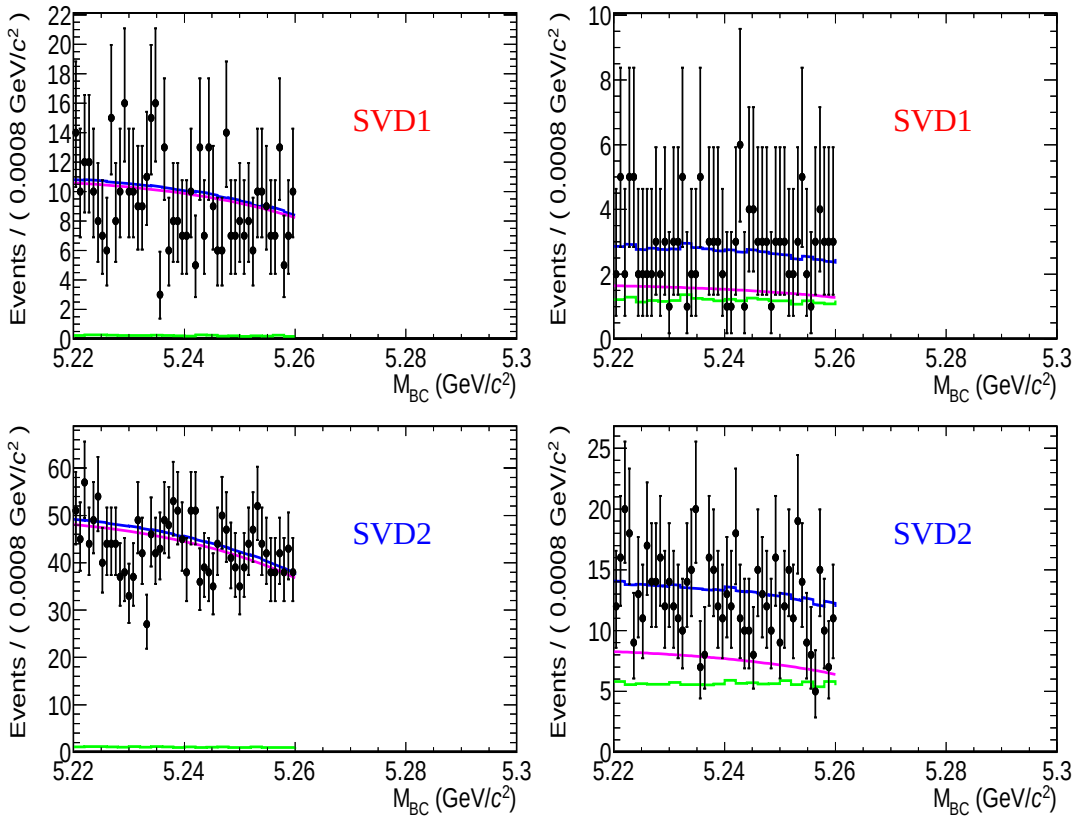

Figure 3.23: Blind fit performed on real $B^0 \to \psi(2S)\pi^0$ data, showing the M_{BC} fit projections, left: the leptonic decay and right: the hadronic decay in SVD1 and SVD2. Solid green line - $B \to c\bar{c}X$ component, solid magenta line - combinatorial background, and solid blue line - total PDF.

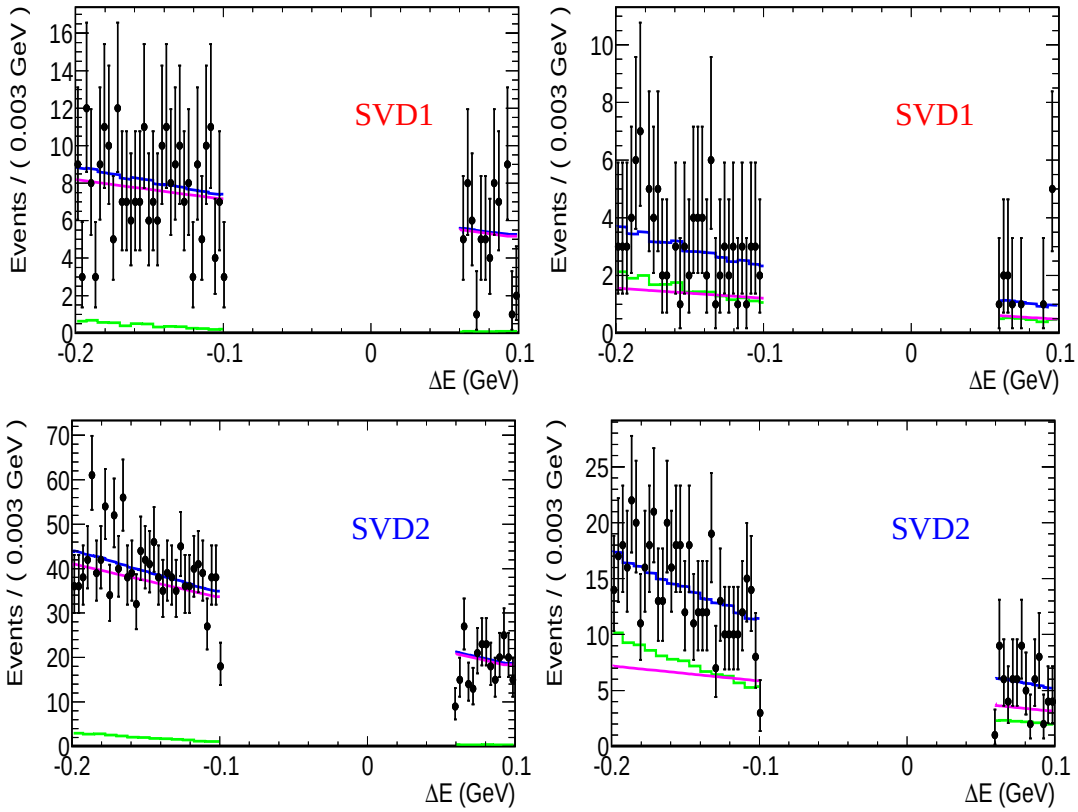

Figure 3.24: Blind fit performed on real $B^0 \to \psi(2S)\pi^0$ data, showing the ΔE fit projections: left: the leptonic and right: the hadronic decay of the $\psi(2S)$ in SVD1 and SVD2. Solid green line - $B \to c\bar{c}X$ component, solid magenta line - combinatorial background, and solid blue line - total PDF.

3.8.1 Fit Validation

Before looking at the signal region in data, the methodology used for the signal yield extraction must be verified. This is done by performing so-called toy MC ensemble tests. In this way we want to check if there are biases in the result as a consequence of the fit procedure. Therefore, we generate a number of pseudo-experiments and use the complete parameterization to extract the physics parameters.

3.8.1.1 Pseudo-experiment setup

For every pseudo-experiment we determine the number of events per component, which means the yield, with the following procedure. The expected event yields are determined assuming a certain branching fraction, looking at the number of events in the M_{BC}, ΔE sidebands and using the reconstruction efficiencies described in Section 3.5.7. The resulting yields are then distributed around their values according to Poisson statistics.
Essentially, there are two approaches of how to generate the events: We can either pick random events from a big set of events using the full detector simulation, or we can generate these events from the PDF. Here, fully simulated events are used, except for the combinatorial ($B\overline{B}$-$q\overline{q}$) background component which are generated only from PDFs.
For 11 branching fraction hypotheses a set of 250 pseudo-experiments is generated for both simulated and PDF events.
The results are shown as distributions of the pull quantity which is defined as

$$pull = \frac{X_{fit} - X_{generated}}{\sigma_{fit}} \tag{3.18}$$

where σ_{fit} is the error of the fit result.

3.8.1.2 Pull distributions using different branching fraction hypothesis

Since, the branching fraction of the decay $B^0 \to \psi(2S)\pi^0$ is unknown, the pseudo-experiments are performed using various assumed values of the branching fraction in the range between 10^{-6} and 10^{-4}. Figure 3.25 shows the pull distributions for simulated events, using different branching fraction hypothesis. The mean and the sigma of each pull distribution are indicated on each plot. In our toy Monte Carlo tests, as shown in Figure 3.25 we obtain the value we expect ($\sigma = 1$) for the width of the distribution within its errors. Concerning the mean which expectation value is zero, we obtain a result that gives us a bias in the range between 3 and 13% depending on the assumed value of the branching fraction.
In order to obtain more precise results we performed toy Monte Carlo tests with more statistics (16 000 pseudo experiments using the measured branching fraction). From these tests we obtained a systematic uncertainty due to the imperfections of the model in the order of 2.8% (see Section 3.10.4). We therefore treat this bias as tolerable and consider that our model is validated.

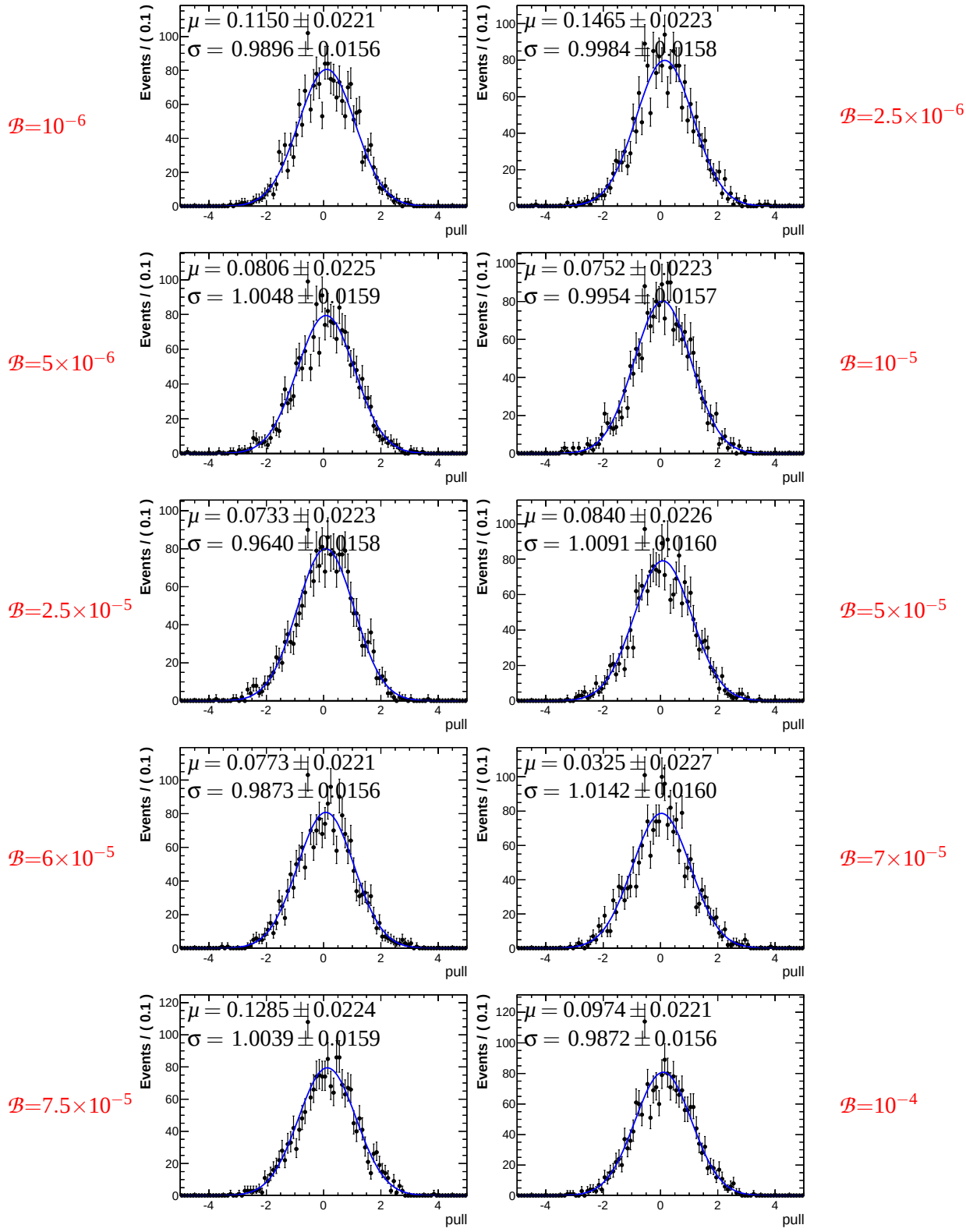

Figure 3.25: Pull distributions using different branching fraction hypothesis.

3.9 Measurement of the branching fraction using real $B^0 \to \psi(2s)\pi^0$ data

After the validation of the fitting procedure, we can look at real $B^0 \to \psi(2S)\pi^0$ data. The fit used to describe the data was elaborated in Section 3.6.6. Due to the differences between data and Monte Carlo coming from particle identification efficiencies, we need to account for these differences. This step is done by applying correction factors on the detection efficiencies extracted from Monte Carlo (see Section 3.5.7). The correction factors are obtained using PID information and by considering two tacks in the leptonic mode and four in the hadronic mode. They are indicated in Table 3.7.

Decay mode	SVD1	SVD2
$B^0 \to \psi(2S)(\to e^+e^-)\pi^0$	1.025 ± 0.149	1.023 ± 0.163
$B^0 \to \psi(2S)(\to \mu^+\mu^-)\pi^0$	0.976 ± 0.152	0.954 ± 0.135
$B^0 \to \psi(2S)(J/\psi(\to e^+e^-)\pi^+\pi^-)\pi^0$	1.024 ± 0.152	1.025 ± 0.173
$B^0 \to \psi(2S)(J/\psi(\to \mu^+\mu^-)\pi^+\pi^-)\pi^0$	0.975 ± 0.154	0.955 ± 0.148

Table 3.7: Particle identification correction factors.

The corrected efficiencies for the leptonic and hadronic mode are found to be:

$$
\begin{aligned}
&SVD1: \\
&\varepsilon(B^0 \to \psi(2S)(\to l^+l^-)\pi^0) = 0.00402 \pm 0.00052 \\
&\varepsilon(B^0 \to \psi(2S)(J/\psi(\to l^+l^-)\pi^+\pi^-)\pi^0) = 0.00465 \pm 0.00052 \\
&SVD2: \\
&\varepsilon(B^0 \to \psi(2S)(\to l^+l^-)\pi^0) = 0.00445 \pm 0.00055 \\
&\varepsilon(B^0 \to \psi(2S)(J/\psi(\to l^+l^-)\pi^+\pi^-)\pi^0) = 0.00595 \pm 0.00068
\end{aligned}
\tag{3.19}
$$

These corrected efficiencies are consequently included in our fit. The fit projections of M_{BC} distribution for the leptonic and hadronic are shown in Figures 3.26 and 3.27, respectively. These Figures compare the complete distribution on the left with the signal enhanced on the right. The signal enhancement for the M_{BC} is done in the following region of ΔE: $-0.04\,\text{GeV} < \Delta E < 0.04\,\text{GeV}$.

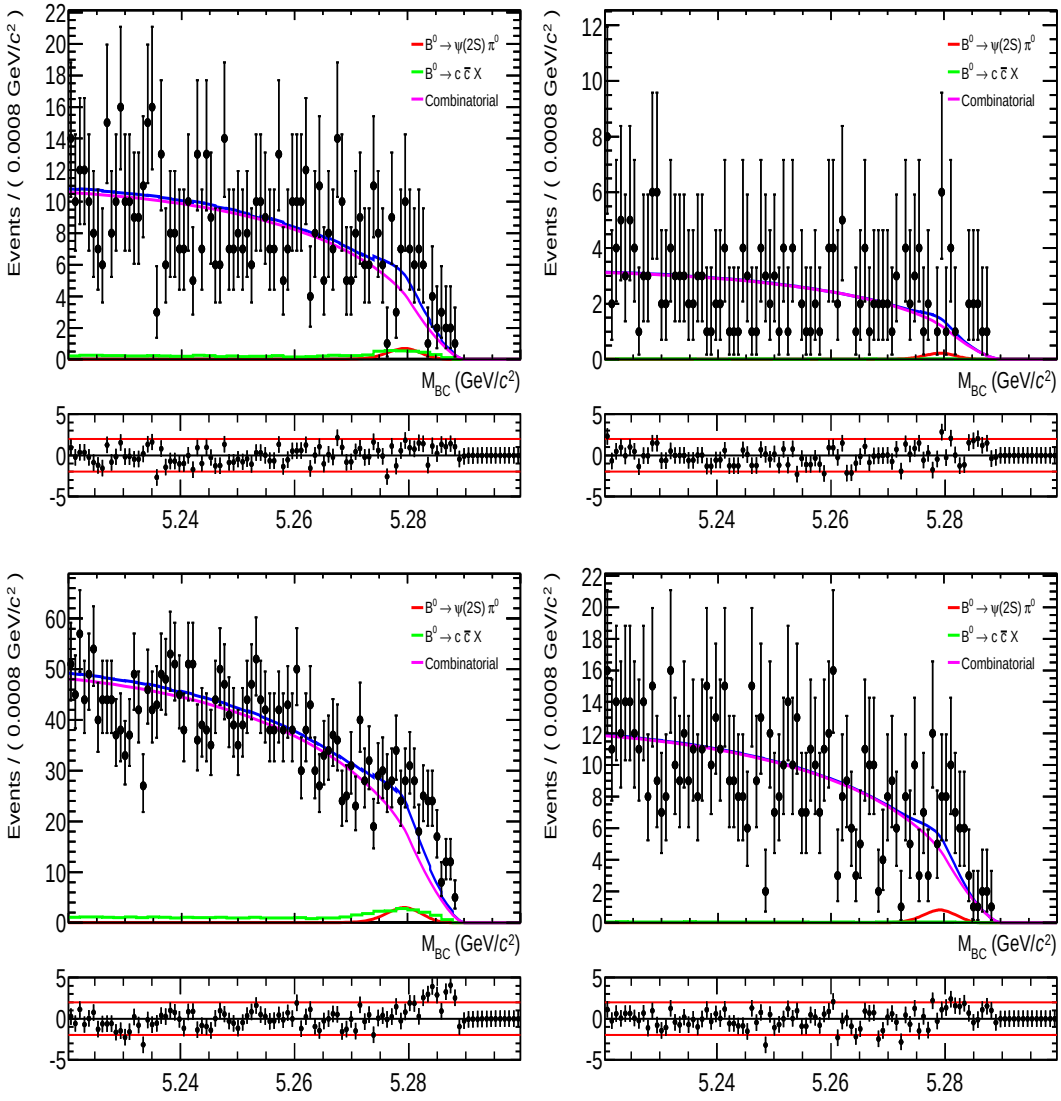

Figure 3.26: Fit projections of M_{BC} distribution for the leptonic decay mode for SVD1 (top) and SVD2 (bottom).

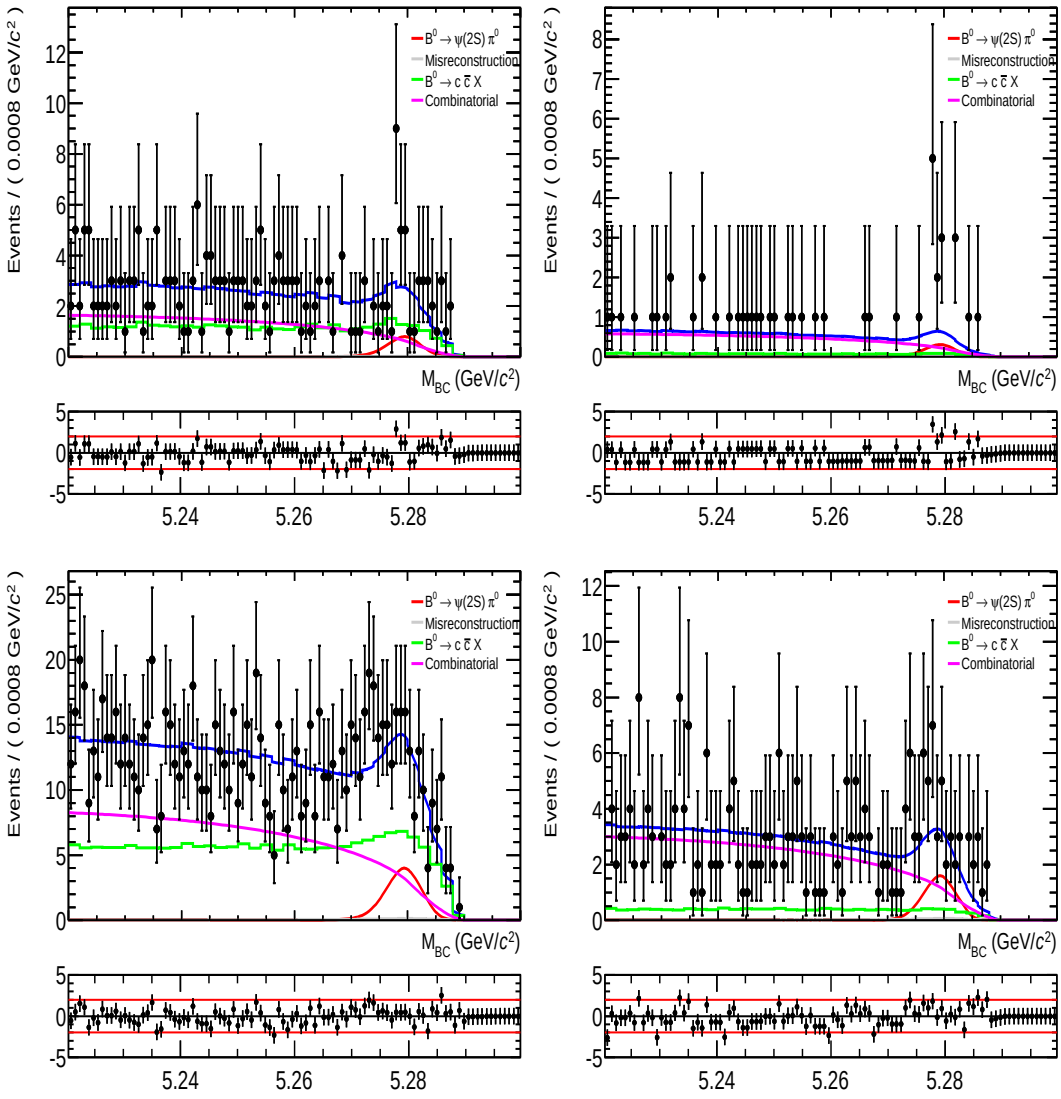

Figure 3.27: Fit projections of M_{BC} distribution for the hadronic decay mode for SVD1 (top) and SVD2 (bottom).

The fit projections of the ΔE distribution for the leptonic and hadronic decay of the $\psi(2S)$ meson are shown in Figures 3.28 and 3.29, respectively. These Figures also compare the complete distribution on the left with the signal enhanced on the right. The signal enhancement for the ΔE is done in the following region of M_{BC}: $27\,\mathrm{GeV}/c^2 < M_{BC} < 29\,\mathrm{GeV}/c^2$.
The corresponding signal yields, extracted for each of the relevant decay modes are presented in Table 3.8.

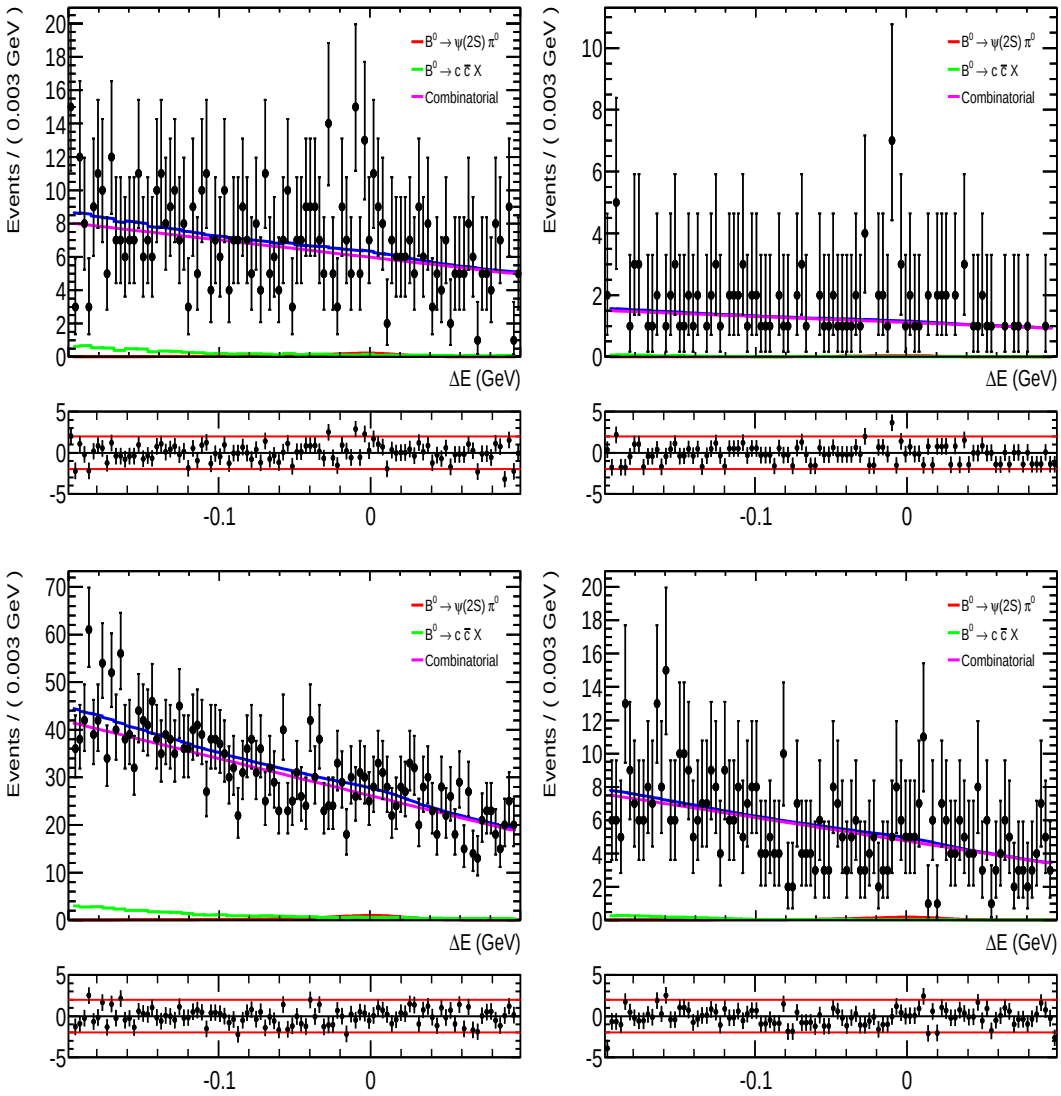

Figure 3.28: Fit projections of ΔE distribution for the leptonic decay mode for SVD1 (top) and SVD2 (bottom).

Decay mode	SVD1	SVD2
$B^0 \to \psi(2S)(\to l^+l^-)\pi^0$	6.5	29.5
$B^0 \to \psi(2S)(J/\psi(\to l^+l^-)\pi^+\pi^-)\pi^0$	7.6	39.5

Table 3.8: Signal yields extracted from real $B^0 \to \psi(2S)\pi^0$ data.

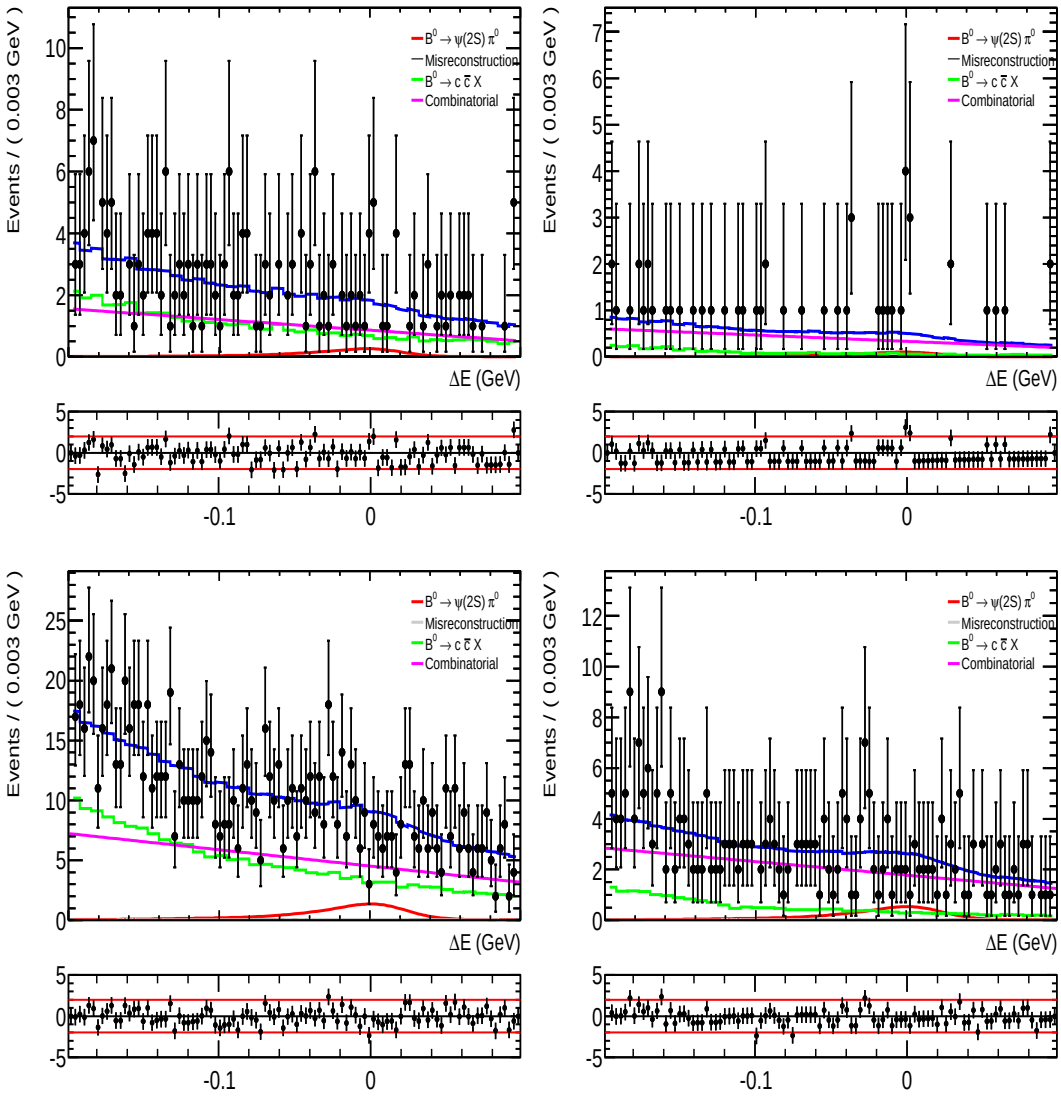

Figure 3.29: Fit projections of ΔE distribution for the hadronic decay mode for SVD1 (top) and SVD2 (bottom).

The fit projections combining the four decay modes, leptonic and hadronic in SVD1 and SVD2 are shown in Figure 3.30. In this Figure again the comparison between the full projections (left) and the signal enhanced ones (right) is shown.

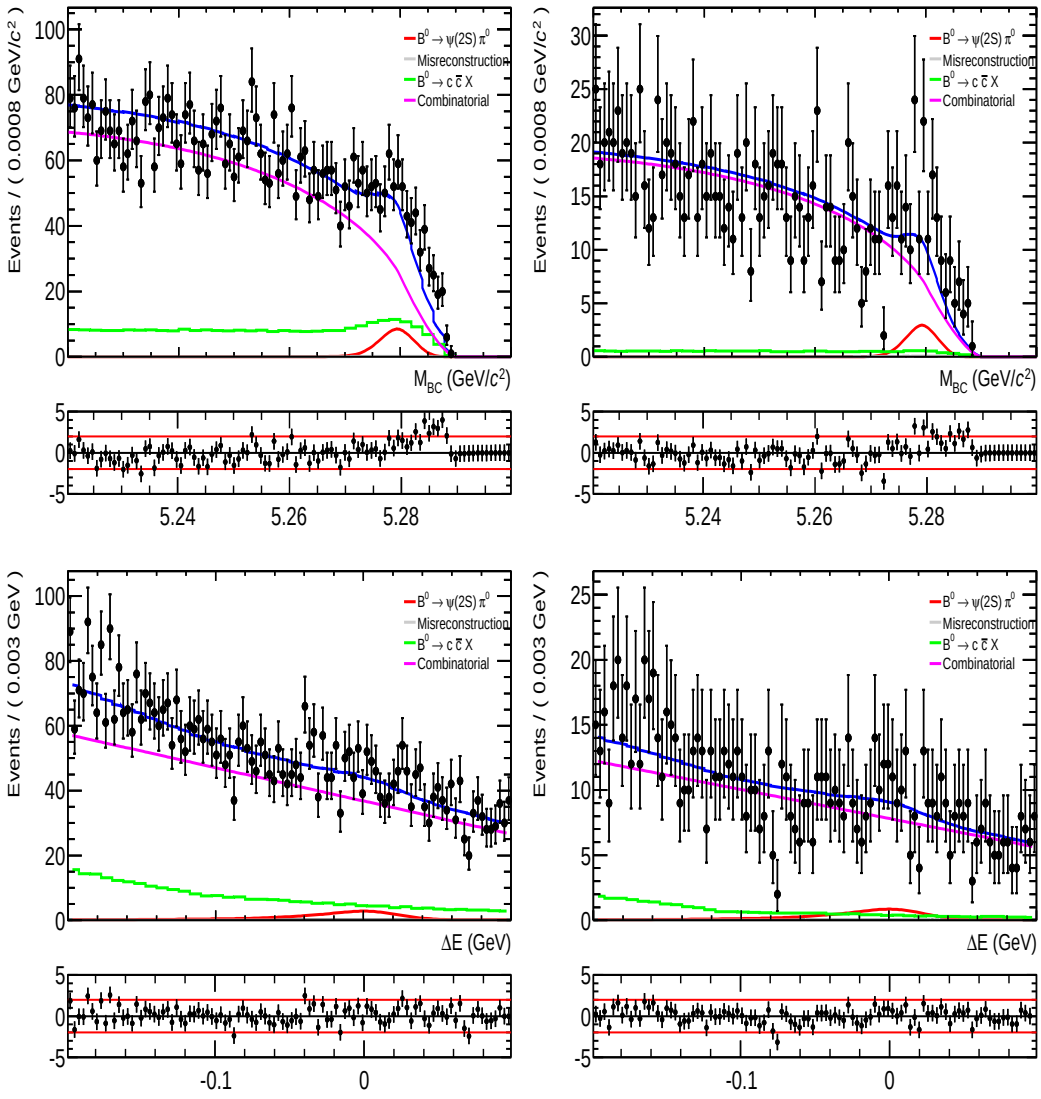

Figure 3.30: Fit results on data, top: M_{BC} ; bottom: ΔE , combining the leptonic decay and hadronic decay of $\psi(2S)$ in SVD1 and SVD2.

From the fit we extracted the following value for the branching fraction of the decay $B^0 \to \psi(2S)\pi^0$:

$$\mathcal{B}(B^0 \to \psi(2S)\pi^0) = (1.07 \pm 0.23) \times 10^{-5}$$

3.10 Estimation of the Systematic Uncertainties

For a careful estimation of the systematic errors, we follow a well established procedures in the Belle collaboration. Many of these procedures are standard procedures performed within the Belle experiment.
This section explains the contributions coming from various sources to the systematic error of the branching fraction. Such sources are, for example, the number of $B\bar{B}$ pairs in the data sample, and contributions to the uncertainty in the selection efficiency due to particle identification. Systematic uncertainties coming from tracking, and π^0 reconstruction are calculated by independent studies at Belle.

3.10.1 Number of $B\bar{B}$ pairs

The determination of the number of $B\bar{B}$ pairs is done directly with the Belle detector. The procedure is described elsewhere [60]. The estimated systematic uncertainty for the whole Belle data set is 1.37%.

3.10.2 π^0 reconstruction efficiency

As a systematic uncertainty due to the reconstruction of π^0 mesons, we assign a value of 4%. This estimation was determined in an internal study by the Belle Collaboration of the systematic uncertainties of π^0 mesons [61].

3.10.3 $\psi(2S)$ efficiency

Tracking systematics address the uncertainty of the track reconstruction. Depending on a momentum of a particle track, there is an uncertainty of a track being found or not. This uncertainty is 0.35% for a particle track with a momentum higher than $200\,\mathrm{MeV}$. This value has been determined in an internal study by the Belle Collaboration of the track finding efficiency using partially reconstructed D^* decays [62]. Since, we consider four different decay modes, which have either two or four charged tracks, the resulting track efficiency uncertainty is 0.7% and 1.4%, respectively. Accordingly, these systematic uncertainties are included in the estimation of the total $\psi(2S)$ efficiency.
Additional corrections to the $\psi(2S)$ efficiency are coming from the uncertainty on particle identification efficiency. We are considering lepton identification and K/π identification corrections.
The systematic uncertainty regarding the possible efficiency differences in the particle identification between Monte Carlo simulations and data with respect to the applied K/π selection is determined using information from [63].
Leptons are identified on the basis of likelihood cuts, which need to be corrected. For this corrections, the official lepton identification study [64], [65] is used for muon

identification. For the electron identification we use a different cut, than the cuts investigated by the official lepton identification group. Therefore, in order to determine the electron identification correction we use information from [66]. The corrections taking into account the tracking efficiency and the particle identification efficiency are weighted according to the number of signal events, thus resulting in estimated uncertainty of 4.3%.

3.10.4 Fit bias

In order to determine the fit bias of our model, we performed Toy Monte Carlo ensemble tests. The outcome of these test is shown in Figure 3.31.
Biases are expected due to some imperfections in the parameterization of the Monte Carlo data. These biases can in principle be determined with arbitrary precision. However, one cannot tell if the bias present in Monte Carlo will be the same in data.

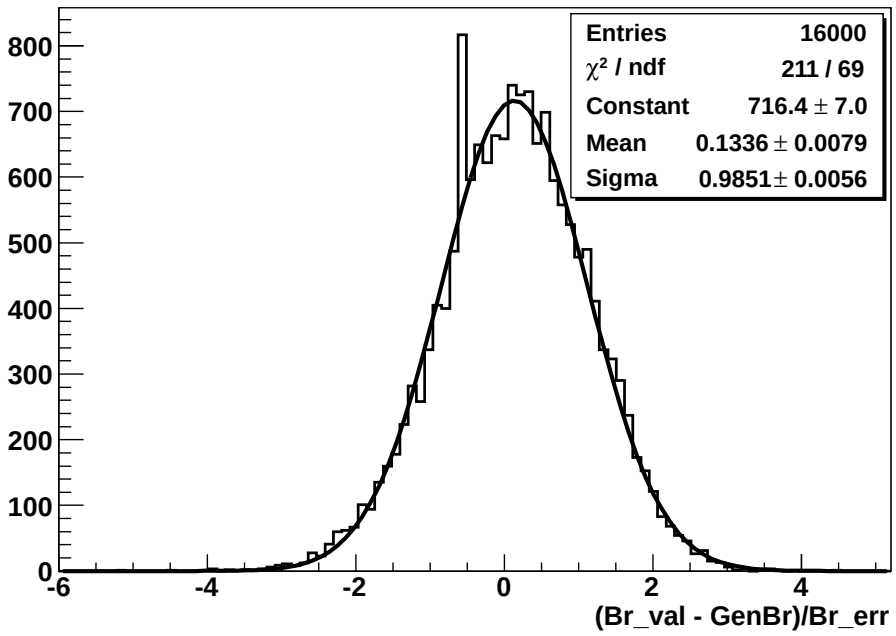

Figure 3.31: The result from the Toy MC tests.

Therefore, the following method is used to determine the systematic error of this fitting bias. We are confident in the fact that the small bias is due to the imperfect parametric description of the PDF and the neglection of some correlations. We do not correct the fit bias and assign the full fit bias as systematic uncertainty. We obtained systematic uncertainty resulting in 2.8%.

3.10.5 Parameters of the signal distribution

The systematic error for the signal component is determined due to the imperfections of the signal model. In our simultaneous fit we consider four different decay modes. This results in having many parameters, which are strongly correlated. In order to account for these correlations, we perform fits to the data, where the parameters are generated according to their correlations. The width obtained from the distribution shown in Figure 3.32 is taken as the systematic uncertainty, which is found to be 0.042%.

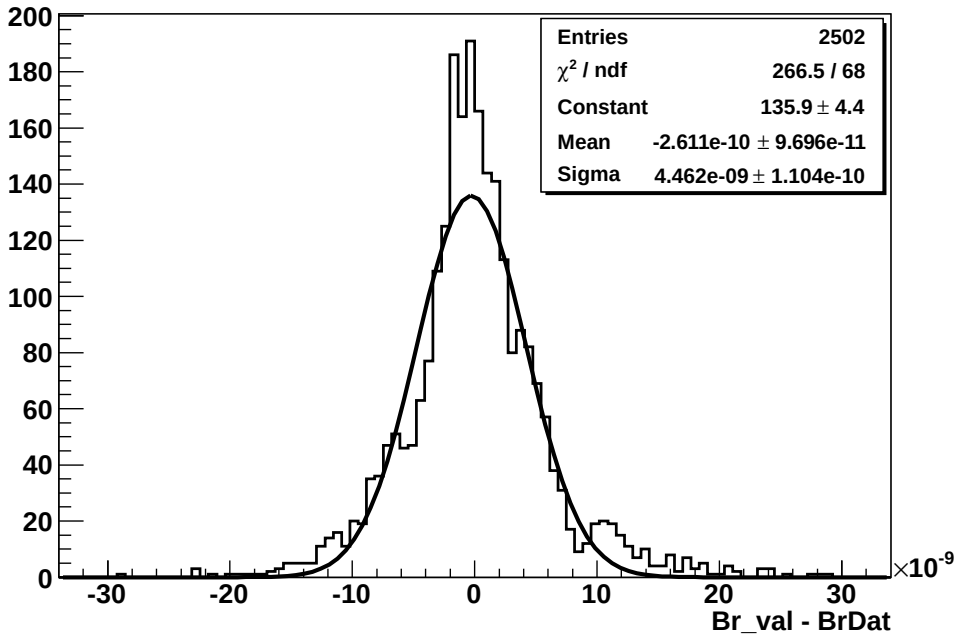

Figure 3.32: Signal distribution generated according to the parameters correlations.

3.10.6 Difference between data and Monte Carlo

In order to determine the systematic uncertainty due to the differences between data and Monte Carlo, we perform Monte Carlo ensemble tests. The Toy Monte Carlo experiments are generated according to the data corrected PDF, while the fit is performed according to our PDF parameterization. The shift from the resulting distribution shown in Figure 3.33 is taken as a systematic uncertainty. The estimated systematic uncertainty coming from this source is found to be 1.9%.

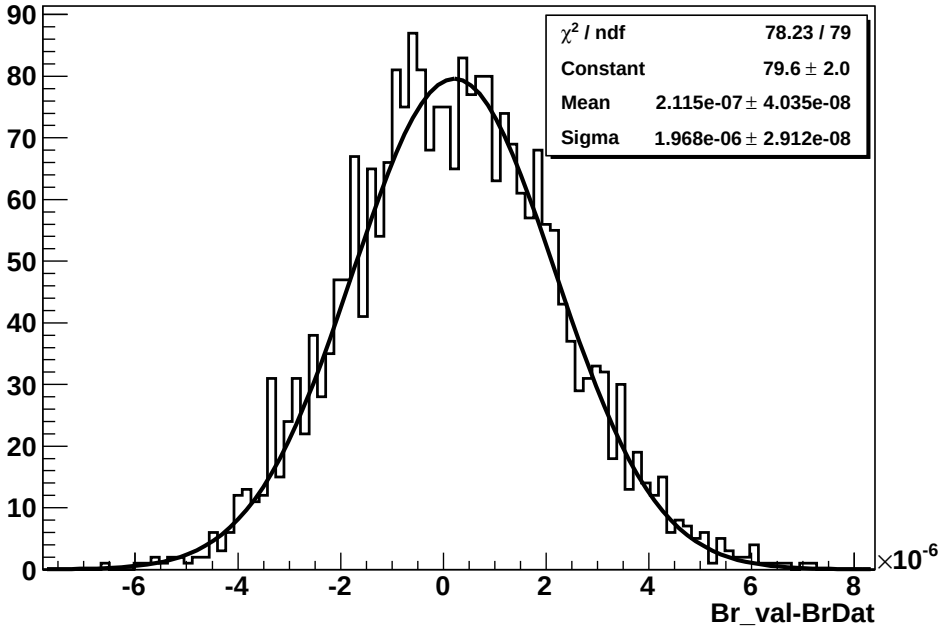

Figure 3.33: Toy MC distribution of the difference between data and Monte Carlo.

3.10.7 Fraction of the misreconstructed signal and $B \to c\bar{c}X$ background

Another source of systematic uncertainty comes from the way of treating the misreconstructed signal and the $B \to c\bar{c}X$ background component. The systematic uncertainty due to this is estimated by performing Monte Carlo pseudo experiments. These Monte Carlo experiments were done generating the fractions, within $\pm 50\,\%$ and $\pm 10\,\%$ for the misreconstructed and $B \to c\bar{c}$ component, respectively. This method was cross-checked by performing a fit where the fraction of the misreconstructed events and the $B \to c\bar{c}$ yield are Gaussian constrained. The resulting systematic uncertainties are 1.2 % coming from the misreconstructed fraction and 2.6 % coming from the $B \to c\bar{c}X$ background fraction.

3.10.8 Varying the binning of the histogram PDF

We used histogram PDFs to parameterize some background components, e.g. the $B \to c\bar{c}X$ and the misreconstructed component. These histograms are created by a Monte Carlo data set. As a result of the statistical Poissonian distribution of the events in our simulated Monte Carlo experiments, an uncertainty to every bin of the histogram can be assigned. The systematic uncertainty due to the change of the binning is included in the estimation of the total systematic error. The uncertainty as a result of this change

is estimated to be 2.6%.

3.10.9 Total systematic error on the branching ratio

Systematic errors calculated from different sources are summarized in Table 3.9. As one can see from this Table, the largest contribution to the systematic error is caused by the uncertainties on the efficiencies.

Source of Systematic Error	$\mathcal{B}(B^0 \to \psi(2S)\pi^0)[\%]$
π^0 efficiency	4.0
$\psi(2S)$ efficiency	4.3
Misreconstruction fraction	1.2
$B \to c\bar{c}X$ fraction	2.6
Fit bias	2.8
Parameters of the signal distribution	0.04
Histogram PDF binning	2.6
Difference between data and MC	1.9
$N_{B\bar{B}}$	1.37
Total	7.9

Table 3.9: Estimated systematic errors and the total systematic uncertainty of the branching fraction measurement for the decay $B^0 \to \psi(2S)\pi^0$ (in %).

The total systematic uncertainty on the branching fraction is calculated by the quadratic sum of the individual contributions. The branching fraction for the $B^0 \to \psi(2S)\pi^0$ decay therefore is:

$$\mathcal{B}(B^0 \to \psi(2S)\pi^0) = (1.07 \pm 0.23 \pm 0.08) \times 10^{-5},$$

where the first is the statistical error extracted from the fit (see Section 3.9), while the second is the systematic uncertainty.

3.10.10 Statistical significance

To obtain the statistical significance we performed a likelihood scan for the branching fraction (see Figure 3.34). The significance can be defined as

$$\#\sigma = \sqrt{2(\mathcal{L}_0 - \mathcal{L}_{fit})}, \tag{3.20}$$

where $\mathcal{L}_0$ and $\mathcal{L}_{fit}$ are the $-log$ likelihoods of the fits with branching fraction fixed to zero and from the fit, respectively.
In order to determine the significance we considered the uncertainties coming from the yields determination (misreconstructed fraction, $B \to c\bar{c}X$, fit bias and difference between data and MC). We neglected the parameters of the signal distribution (see Table 3.9). And we did not include the uncertainties coming from the efficiencies (π^0 and $\psi(2S)$) nor from the number of $B\bar{B}$ pairs, since they are multiplicative numbers (see Equation (3.14)) and they have no impact on the fact if we are going to see something or not.
We included the misreconstructed fraction and the $B \to c\bar{c}X$ fraction floating their yields according to a Gaussian constraint center to their mean value and we obtained statistical significance of 5.3σ.

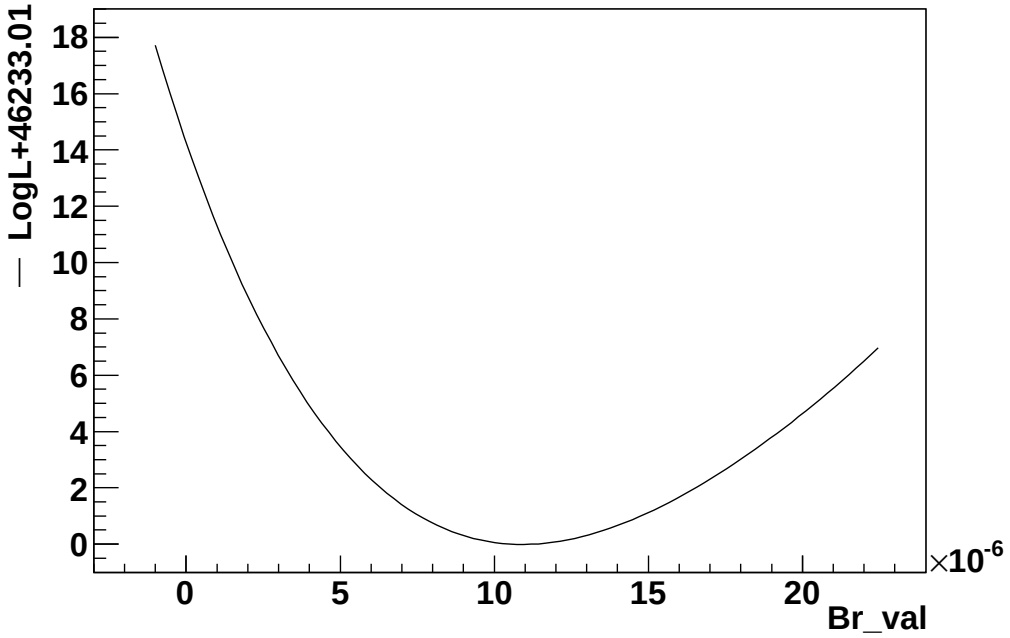

Figure 3.34: Likelihood scan of $\mathcal{B}(B^0 \to \psi(2S)\pi^0)$.

Since, the fit bias and the difference between data and MC are not distributed, we

considered their effect as a shift of the likelihood. This is equivalent to considering a "flat" region around the minimum of the $-log\mathcal{L}$.
Taking into account all these contributions we obtained a significance of 5.06σ.

Chapter 4

The Belle II experiment

The tremendous success that was achieved by the two B-factories, KEKB and PEP II, led to the confirmation of the Standard Model in the quark-flavor sector. In a decade of running, the data accumulated by the KEKB collider enabled measurements of invaluable importance for the flavor structure of elementary particles and especially the violation of CP symmetry in the quark sector.
With the planned upgrade of the KEKB collider and Belle detector, much larger data sample will become available, providing a new view in the heavy flavor physics research.

4.1 SuperKEKB Accelerator and Belle II Detector

The main goal of the SuperKEKB project is to increase the integrated luminosity for about a factor of 40 compared to KEKB. The design luminosity of SuperKEKB is $8 \times 10^{35}\,\mathrm{cm}^{-2}\mathrm{s}^{-1}$. This will allow to accumulate $50\,\mathrm{ab}^{-1}$ around 2021-2022, corresponding to approximately 50 billion $B\bar{B}$ pairs. The luminosity depends on several parameters as defined in [67]

$$L = \frac{\gamma_{\pm}}{2er_e}(1+\frac{\sigma_y^*}{\sigma_x^*})(\frac{I_{\pm}\xi_{\pm y}}{\beta_y^*})(\frac{R_L}{R_y}), \tag{4.1}$$

where $\gamma_{\pm}$ is the Lorentz factor, r_e is the classical electron radius, e is the electric charge, $\sigma_{x,y}^*$ are the beam sizes at the interaction point in x and y direction, $I_{\pm}$ denote the beam currents, $\xi_{\pm y}$ are the beam-beam parameters in x and y direction and β_y^* is beta function at the interaction point in x or y direction.
To achieve the design luminosity, the "nano-beam" scheme was chosen. In order to meet the criteria of this scheme major upgrades of the KEKB collider and the Belle detector are needed. For the upgraded machine the same tunnel KEKB will be used. In order to reach the target luminosity, beam energies from 3.5 GeV and 8.0 GeV will be changed to 4.0 GeV and 7.0 GeV, respectively. The half crossing angle ϕ is 41.5 mrad which is about 4 times larger than that at the KEKB. Accordingly, the

Lorentz boost factor of the center of mass system is $\beta\gamma = 0.28$, which is about 2/3 of that in the KEK B-factory. Additional change in the beam parameters is the increase by a factor of 2 in the beam currents. Thus the beam currents at SuperKEKB will be 3.60 A for the low energy ring and 2.62 A for the high energy ring. The machine parameters of the upgraded SuperKEKB machine compared with the previous KEKB machine are shown in Table 4.1.

Parameters	KEKB achieved	SuperKEKB
Energy (GeV) (LER/HER)	3.5/8.0	4.0/7.0
ξ_y	0.129/0.090	0.090/0.088
β_y^* (mm)	5.9/5.9	0.27/0.41
I(A)	1.64/1.19	3.60/2.62
Luminosity ($10^{34}\,\mathrm{cm}^{-2}\mathrm{s}^{-1}$)	2.11	80

Table 4.1: Fundamental parameters of SuperKEKB and KEKB [68].

The magnet system will also be subjected to several replacements. The main dipole magnets in the low and high energy ring will be changed with dipole magnets that are longer for the LER and shorter for the HER. Also, in order to achieve the design luminosity, the number of dipole, quadruple and sextuple magnets needed for the operation of the SuperKEKB will be increased with respect to KEKB.
As a result of focussing the beam-pipe radius will be decreased from 15.0 mm radius to a 10 mm radius.
The upgraded Belle detector will be called Belle II. The layout of the upgraded Belle II detector (above) in comparison with the Belle detector (below) is shown in Figure 4.1. One huge change in the upgrade of the Belle detector is introducing a completely new pixel detector that has to handle very harsh background environment due to the increase of background as a result of 40 times higher luminosity. The Pixel Vertex Detector (PXD) will be mounted directly on the beam-pipe, to be as close as possible to the interaction point. It is based on a Depleted Field-Effect Transistor (DEPFET) technology [69]. This technology allows for very thin ($50\,\mu$m) sensors. The PXD consists of two layers of pixel sensors, standing at radii of 14 mm and 22 mm for the inner and outer layer, respectively. Figure 4.2 shows the layout of the two PXD layers. The inner layer consists of 8 planar sensors ("ladders") each with a width of 15 mm and a sensitive length of 90 mm. The outer layer consists of 12 modules with a width of 15 mm and a length of 123 mm [14]. The angular acceptance of the pixel detector is $17^\circ < \theta < 150^\circ$ in polar angle. Outside this acceptance region the readout electronics which need an active cooling are located. The pixel sensors will consume very little power and therefore the air cooling is sufficient.

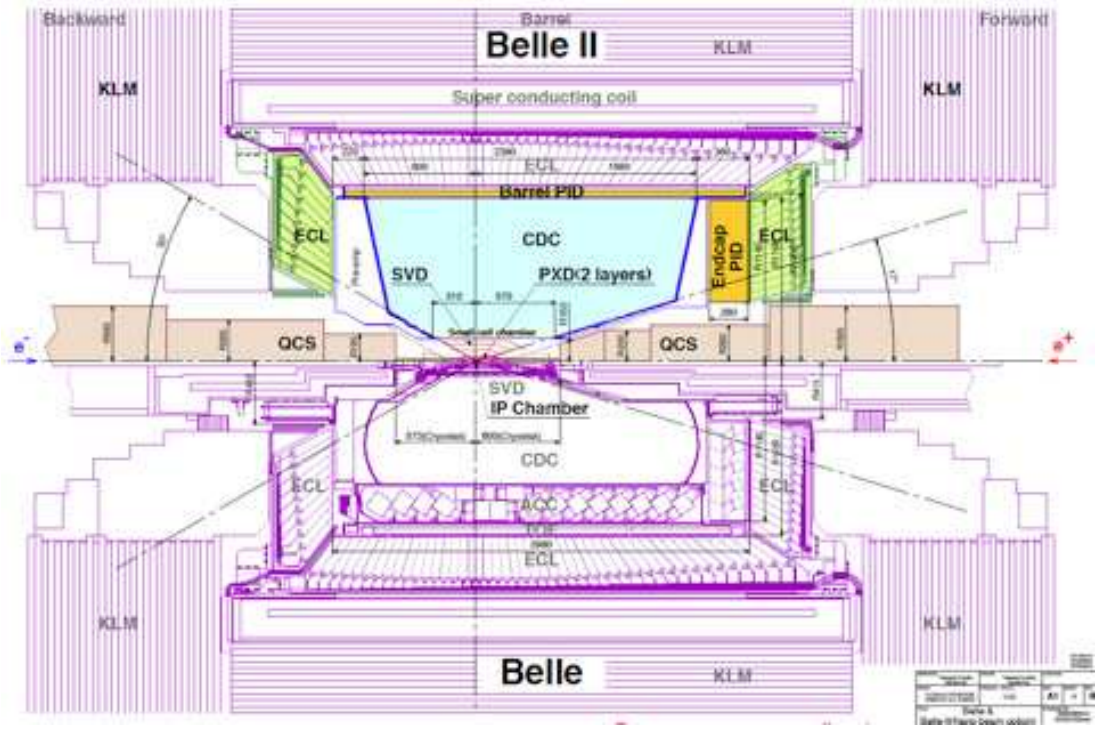

Figure 4.1: Belle II detector layout compared to Belle.

Figure 4.2: Schematic view of geometrical arrangement of the sensors for the PXD. The light gray surface are the sensitive DEPFET pixels, which are entirely covering the acceptance of the tracker system.

The SVD for the Belle II detector as a tracking device inherits the physics capability of the Belle SVD2 system, such as low mass, high precision, background resistivity, tolerance to radiation and long-term stability. In order to increase both robustness and precision of vertexing, the future silicon vertex detector will be composed of 4 layers as its predecessor (SVD2), but at increased radii to provide enough space for the PXD. The inner radius is 35 mm and the most distant layer will be placed at radius of 140 mm. The future SVD will be slanted in the forward region to reduce multiple scattering and give better precision in the forward direction. The main parameters of the Belle II SVD and the former SVD detector of Belle are presented in Table 4.2.

Parameters	Belle (SVD2)	Belle II
Layers	4	2 DEPFET; 4 DSSD
Radius of layer (mm)	20/43.5/70/88.8	14/22; 38/80/115/140
Ladders/layer	6/12/12/18	8/12; 8/10/14/17
Modules/ladder	2/3/5/6	1/1; 2/3/4/5
Modules	246	20; 187
Module width (mm)	25.6(33.28 layer 4)	12.5; 57.6(38.4 layer 1)
Module length (mm)	76.8(74.75 layer 4)	38.2/58.7; 115.2
Module thickness (μm)	300	50; 300
Pitch, Pixelsize $r\phi$ (μm)	50 (65 layer 4)	50/50; 75 (50 layer 1)
Pitch, Pixelsize z (μm)	75 (73 layer 4)	76/117; 113 (75 layer 1)
Angular coverage	$17^\circ < \theta < 150^\circ$	$17^\circ < \theta < 150^\circ$

Table 4.2: Parameters of the former SVD configuration and the current combined design of PXD and SVD [14].

In order to satisfy the requirements of the PXD and SVD in terms of space, the CDC will be moved farther away from the interaction region. The radius of the CDC will be increased to improve the momentum resolution, as well as the sense wire density, resulting in about 15000 sense wires. The main parameters of the future CDC are listed in Table 4.3 and are compared with the former chamber parameters.
The upgrade of the detector involves replacement of the TOF and ACC with a new particle identification system, consisting of a Time of Propagation Counter (TOP) in the barrel region and Aerogel Ring-Imaging Čerenkov (ARICH) detector device for the end-caps [70], [71]. TOP measures the time of propagation of the Čerenkov photons

Parameters	Belle	Belle II
Radius of inner cylinder (mm)	77	160
Radius of outer cylinder (mm)	880	1130
Radius of innermost sense wire (mm)	88	168
Radius of outermost sense wire (mm)	863	1111.4
Number of layers	50	56
Number of sense wires	8400	14336
Gas	$He-C_2H_6$	$He-C_2H_6$
Diameter of sense wire (μm)	30	30

Table 4.3: Main parameters of the Belle CDC and the future chamber of Belle II [14].

that are reflected internally inside a quartz radiator. The Čerenkov image is reconstructed from a 3 dimensional information provided by 2 coordinates (x, y) and precise timing. The time component is determined by micro-channel plate (MCP) photo multiplier tubes, located at the end surfaces of the quartz bar. An array of such quartz bars surrounds the outer wall of the CDC. The second component of the particle identification device, the ARICH consists of an aerogel radiator where Čerenkov photons are produced by charged particles, an expansion volume to allow Čerenkov photons to form rings on the photon detector surface, an array of position sensitive detectors that can detect single photons in a high magnetic field with high efficiency and with good resolution in two dimensions and a readout system for the photon detector.
Concerning the next following sub-detector, the ECL will have almost the same design as its former, except the end-cap parts which will be replaced with pure CsI crystals to improve the time resolution.
The solenoid and the barrel part of the KLM will remain unchanged. The Belle KLM was based on glass-electrode resistive plate counters, which had a long dead time during the recovery of the electric field after a discharge. The long dead time reduces significantly the detection efficiency under high background fluxes. Even though the estimated occupancy in the barrel region of the KLM at SuperKEKB will be increased with respect to KEKB, implying much higher background, the barrel resistive plate counters can still be operated successfully. However, in the end-caps the background will be much worse due to the limited shielding of the neutrons and other particles that are generated externally along the beam lines. Thus, for the forward region of the KLM the resistive plate counters will be replaced by silicon photo multipliers, because of the suffered radiation damage.

Chapter 5

Luminosity-dependent Background

One of the biggest challenges in high energy accelerators is to understand the backgrounds. If these effects are not carefully studied and controlled, they may create dangerous situations. Even if they are well studied and understood, they may significantly reduce the lifetime of the detector.
The Belle detector was dealing with several sources of background. These sources are divided in two main categories: machine background which depends on the particular beam settings and luminosity-related background induced by the increase in luminosity.
The machine background includes several background sources. One of this sources is the background due to beam-gas scattering [72][73][74]. In e^+e^- colliders, ideal vacuum conditions are never achieved, resulting in interactions between the charged particles with the residual gas molecules. This prompts deviation of the traveling charged particles from their original path. In e^+e^- storage ring such particles are called beam-scattered or spent electrons or positrons. The beam particles interact with the residual gas molecules via two kinds of interaction: Bremsstrahlung and Coulomb scattering. A considerable amount of these particles deviate quite a lot from their initial direction and finally hit the detector, thus causing background events.
Belle detector was also affected by synchrotron radiation [75], as background source that also depends on the machine parameters: the beam current, magnet position, bending radii and beam orbits. This type of background occurs when a charged particle is accelerated, therefore losing its energy and in addition is involved in circular motion. This severely limits the efficiency of storage rings for energetic electrons and positrons.
Another beam-induced background is the Touschek effect [76], which is in principle an intra-bunch scattering. Elastic scattering between two particles in a same beam bunch changes their energy, resulting in having one particle with too much energy, while the other is left with too little energy. The scattering rate of the Touschek effect depends proportionally on the bunch current and number of bunches, but it is inversely proportional to the beam size. Tosuchek scattered particles are lost by hitting the inner wall of the beam-pipe while they propagate around the ring. If their loss position is close to the detector, generated shower might reach the detector, producing fake detector hits.

This results in deterioration of the detector's physics resolution.
On the other hand, Belle also was coping with backgrounds that depend on luminosity: radiative Bhabha scattering and the $e^+e^- \to e^+e^-e^+e^-$ process.
The rate of the radiative Bhabha events is proportional to the luminosity. In the radiative Bhabha scattering process, the produced photons travel along the beam axis direction, during which they interact with the iron of the magnets. In these interactions, neutrons are copiously produced, which are the main source of background affecting the outer detector, K_L and μ detector.
The luminosity dependent background caused by the low momentum QED $e^+e^- \to e^+e^-e^+e^-$ process (see Figure 5.2 (d)), will be discussed in detail in this chapter. It will also be referred as a two-photon QED process.
The Belle experiment is now being upgraded to the Belle II experiment, designed to record instantaneous luminosity 40 times higher than the one recorded by the Belle experiment. Such a high luminosity will be realized by the SuperKEKB collider, where background rates due either to machine or to luminosity settings are expected to be much higher than those of KEKB. This means that the understanding of the backgrounds in the Belle detector is necessary in order to determine the expected background rates at Belle II.
At Belle II, the new pixel vertex detector will be placed very close to the interaction point, where the background levels are highest. Due to its small radius, the pixel detector will be affected from low energetic electrons and positrons emitted in the two-photon process. These secondary electrons and positrons are not able to penetrate too far into the detector.
Therefore, the estimation of the two-photon QED background is of great importance for the safe operation of the pixel detector.

5.1 Theory prediction for two-photon QED background

The forthcoming upgrade of the KEKB accelerator to SuperKEKB will bring a large increase of luminosity. This brings up the question of the behavior of the luminosity-dependent background. This background is generated mainly from QED processes.
In principle, there are two background processes that we need to consider. These are: Bhabha scattering, shown in Figure 5.1 and $e^+e^- \to e^+e^-e^+e^-$ process shown in Figure 5.2 (d).
Within the acceptance of the Belle II detector ($17^\circ < \theta < 150^\circ$), the estimated cross section for the t-channel Bhabha scattering is about 120 nb, whereas for the $\gamma\gamma$ process it is $\sigma \sim O(10^7)$ nb. Therefore, the concentration is put on the $\gamma\gamma$ process, because its cross section is so much larger compared to the other process.

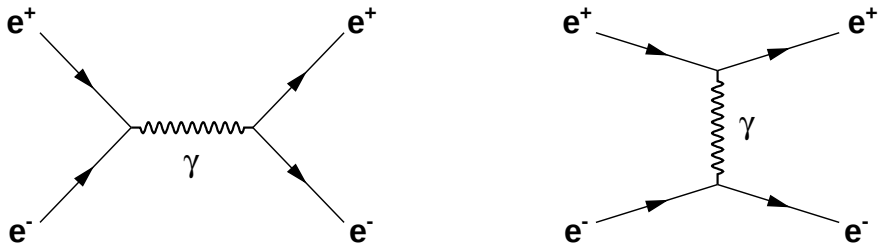

(a) s-channel (b) t-channel

Figure 5.1: Bhabha scattering.

5.1.1 Standard $\gamma\gamma$ Monte Carlo generators

In order to predict the $\gamma\gamma$ background situation at Belle II, Monte Carlo simulation is needed. However, the cross section in the phase-space expected for the low energy secondary e^+e^- pairs was never studied experimentally. We therefore analyzed three different Monte Carlo (MC) generators that are being used to simulate this process. Those were BDK [77], KoralW [78] and Grace [79].
The BDK generator only simulates the principle interaction of $e^+e^- \to 4f$. In leading order there are 36 diagrams where 4 fermions are produced in e^+e^- collision. These are classified into bremsstrahlung (Figure 5.2 (a)), conversion (Figure 5.2 (b)), annihilation (Figure 5.2 (c)) and the multi-peripheral process (Figure 5.2 (d)), The latter process is the dominant two-photon process that is being investigated in these studies. In BDK it is simulated by its own sub-generator.
KoralW is a more recent generator. In addition to the main interaction it also simulates initial and final state radiation and takes into account the interferences. It is therefore the most advanced generator so we expect that it gives us the best possible prediction for the $\gamma\gamma$ -background in Belle II.
To estimate the systematic uncertainty of the background estimation coming from this choice of the generator, the two generators BDK and KoralW were compared. In principle, we expect less particles in the simulation from BDK since the initial and final state radiation are not simulated by this particular Monte Carlo. This effect of initial and final state radiation, the largest systematic uncertainty of the prediction, can then be seen in the difference between the BDK and the KoralW prediction.
In addition, we looked as well at Grace, which is a generator that simulates also initial state radiation together with the multi-peripheral graph. The resulting simulation showed that Monte Carlo prediction extracted from Grace is consistent with the one obtained from BDK.

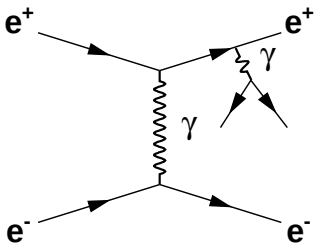

(a) Bremsstrahlung

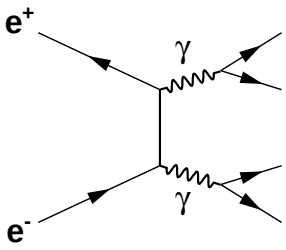

(b) Conversion

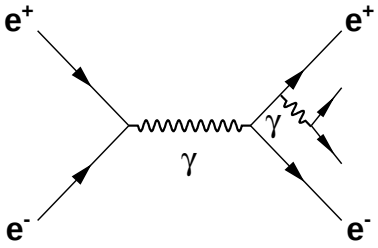

(c) Annihilation

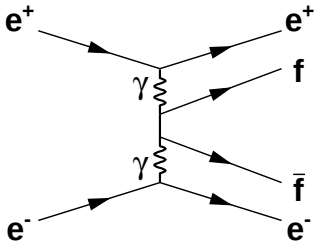

(d) Multiperipheral

Figure 5.2: QED processes.

The energy spectrum of the electron simulated using the KoralW simulation is shown in Figure 5.3 (a). After the Lorentz boost in the laboratory system, the electron spectrum is different, as shown in Figure 5.3 (b).

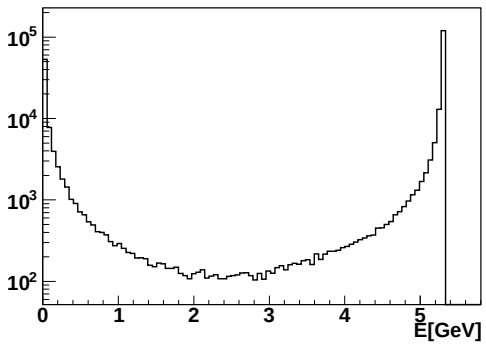

(a)

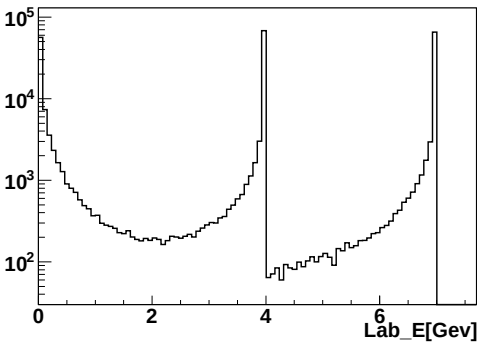

(b)

Figure 5.3: Energy spectrum of the electron in the CMS (left) and after the Lorentz boost (right) extracted using the KoralW Monte Carlo generator.

These spectra simulated using the BDK generator show the similar trend (see Figure D.1 in Appendix D.0.1).
Comparing the event kinematics of the two generators, it can be seen, as shown in Figure 5.4, that the generated energy spectra using the two separate Monte Carlo generators are in a good agreement. One can also see that particles produced in this process have an extremely soft spectrum. Due to the magnetic field of the Belle II, only very small amount of $\gamma\gamma$ QED background particles will reach the inner detectors. To reach the pixel detector a minimum transverse momentum of 3.5 MeV is needed. Thus, only a small fraction of the tracks has enough energy to produce a hit in the pixel detector. This is also taken into account in these studies. In addition, only a few hits are expected in the larger tracking detectors, e.g. central drift chamber.

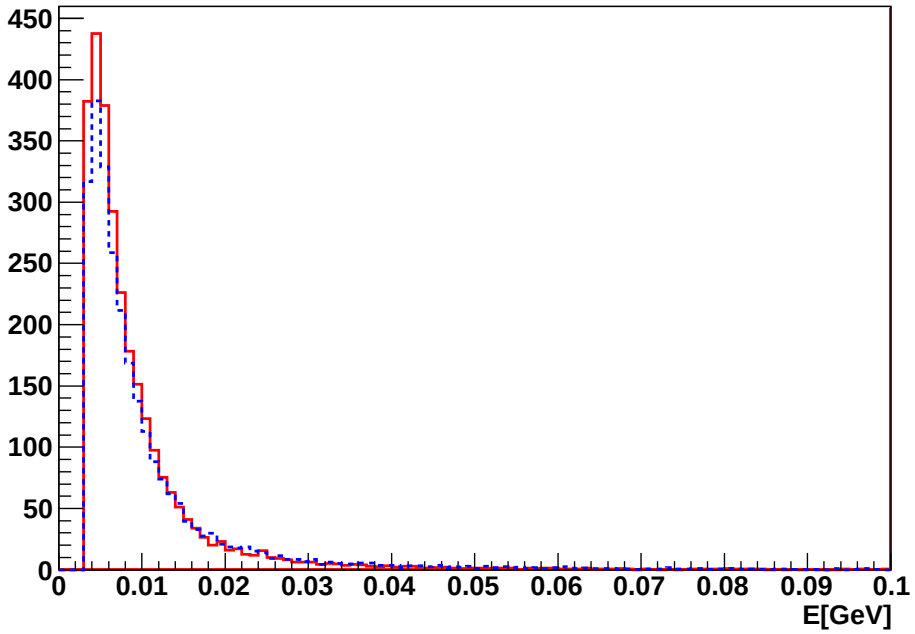

Figure 5.4: KoralW (dashed blue) and BDK (solid red) simulation.

For a first estimation of the occupancy, we looked at the produced particles at the generator level. To these particles we applied the acceptance cut, satisfying the $17° < \theta < 150°$ condition and the requirement of minimum transverse momentum for a charged particle to reach the inner layer of the pixel detector. We obtained about 2500 tracks using the KoralW simulation and roughly 2600 tracks using the BDK. From the number of tracks obtained in the acceptance of the pixel detector, the expected occupancy coming from the $\gamma\gamma$-process is calculated. For this we assumed that each track produces at most three hits in the PXD, which is a reasonable upper limit. The occupancy is calculated as the ratio between the number of fired pixels (number of hits) and the total amount of pixels in the innermost layer, which is

3.2×10^6. The results of this estimation are shown in Table 5.1.

MC generator	KoralW	BDK	SuperB(BDK)
Tracks	2500	2600	13800
Occupancy	0.25%	0.26%	1.3%

Table 5.1: First estimation of the occupancy in the PXD using a simple assumption of 3 hits per track.

As one can see both, KoralW and BDK predict a similar amount of tracks. This good agreement makes us confident that the systematic uncertainty of our estimation is small. The deduced occupancies are in the order of 0.3%, which is far below the operational limit of the pixel detector which is 3%.
This investigation was triggered by a statement from the SuperB [80] collaboration, saying that they expect a rate for the 2γ-process of $10\,\mathrm{MHz/cm^2}$ in their vertex detector. They obtained their prediction using the BDK generator. In the following we will refer to it as the SuperB (BDK) prediction. Already at first sight, this prediction was far bigger than the numbers we have extracted. For a more detailed comparison, we translated this predicted rate into an occupancy in the first layer of the Belle II PXD detector.
For this we took into account the $20\,\mu$s read-out frame of the PXD and the active area of the first layer (8 ladders with dimensions given in Section 4). Since the prediction for SuperB was made for their vertex detector, which has a radius of 1.3 cm, we corrected the rate to account for the larger radius (1.4 cm) of the PXD at Belle II. The rate under these conditions then yields about

$$\begin{aligned} N_{tracks}^{SuperB} &= Rate \times t_{PXD} \times r_{corr} \times Area = \\ &= 10^7 \times (2 \times 10^{-5}) \times \frac{(1.3)^2}{(1.4)^2} \times 80 = 13800 \text{ tracks.} \end{aligned} \tag{5.1}$$

Here, $Rate$ is the rate for the two-photon process obtained from SuperB BDK simulation, t_{PXD} is the memory time of the pixel detector, r_{corr} is the radial correction to account for the different location of the vertex detectors at Belle II and Super B from the interaction point and the last term, $Area$, is the active area of the eight ladders in the fist PXD layer.

The result of this translation is also shown in Table 5.1. The $10\,\mathrm{MHz/cm^2}$ corresponds to about 13800 tracks per read-out frame in the PXD, which would lead to an occupancy of 1.3% in the first layer of the pixel detector consisting of about 3 Million pixels, under the assumption of 3 pixels per track. Such a high occupancy would be harmful for the PXD. This would mean that the pixel detector will be full of background hits, and hence it will be useless. Therefore, we decided to perform a measurement which would allow us to better constrain the cross section of the $\gamma\gamma$-process.

5.2 Method of measurement

The investigated three MC generators give rather consistent predictions concerning the amount of particles seen in the Belle/Belle II detector. Still, the $\gamma\gamma$-process has never been tested experimentally in this phase-space.
The $\gamma\gamma$-process produces charged particles with extremely small momenta. This makes a measurement of the contribution of this process to the total cross section rather difficult. It is not possible to trigger on these events nor is it likely that many tracks from charged particles produced in the $\gamma\gamma$-process are reconstructed.
Most particles reaching the tracking detectors have a momentum around $10\,\mathrm{MeV}$. Thus, they only produce one or two hits in the first couple of tracking layers. A track reconstruction is not possible for these tracks. Instead, we used a method that is based on the amount of activity seen in the relevant detectors. For this purpose we used Belle data collected during the dedicated QED experiments performed for this study. The three important ingredients to this method are discussed in the following.

5.2.1 Triggering on QED processes

Due to the soft energy spectrum of the $\gamma\gamma$-process it is not possible to setup a track or calorimeter trigger on the particles produced in the QED-interactions. It was therefore decided to use a random trigger, since it has the highest probability to be a "background only" trigger.
Because the $\gamma\gamma$-process has such a large cross section it constitutes a large fraction of background processes in Belle. Particles from this background are present in any event recorded by the Belle detector. However, due to the steep drop-off with increasing momentum, only very little detector hits are expected from this process. By choosing a random trigger for the QED studies, the probability of observing a physics event or another background event with higher energetic particles is greatly reduced compared to other triggers available in Belle. Thus, the relative contribution of QED events to the detector hits is most advantageous for a random trigger.
Nevertheless, with random triggers during the read-out time of $2\,\mu\mathrm{s}$ of the silicon vertex detector (SVD), only 1.2 tracks are expected to hit the first layer of the SVD based on the estimation from the KoralW Monte Carlo generator.

5.2.2 Hit multiplicities in the SVD

Since the particle spectrum of the $\gamma\gamma$-process is very soft, it is unlikely to find reconstructed particle tracks coming from this process. However, many particles are expected to travel to the silicon vertex detector and produce hits in particular in its first layer. Therefore a study of the hit multiplicities in the vertex detector gives us a possibility to determine the background contribution from the $\gamma\gamma$-process.
Before starting the measurements of the QED experiment the correlation between tracks, hit-multiplicities and cluster-multiplicities in the SVD was studied.
For events from a random trigger sample, a preselected Bhabha sample (containing Bhabha scattering events) and from a preselected multi-hadron physics sample the number of outgoing tracks is compared to the hit and cluster multiplicities in the first layer of the vertex detector.
In the random trigger sample, no reconstructed tracks were found in the events. The observed number of hits and clusters per event for one of the innermost layers of the SVD are shown in Figure 5.5. On average there are in each event 61 background hits in about 20 clusters. Since no particles are present in the event, these constitutes the constant background noise. Thus, they are background hits.
We have also taken data without beams to prove that the 61 hits come from luminosity. The hit distribution is given in Figure D.2 in Appendix D.0.2.
In the preselected Bhabha sample, slightly more hits are seen. In this sample exactly two reconstructed tracks are required. The hit and cluster distributions for the Bhabha sample are shown in Figure 5.6.

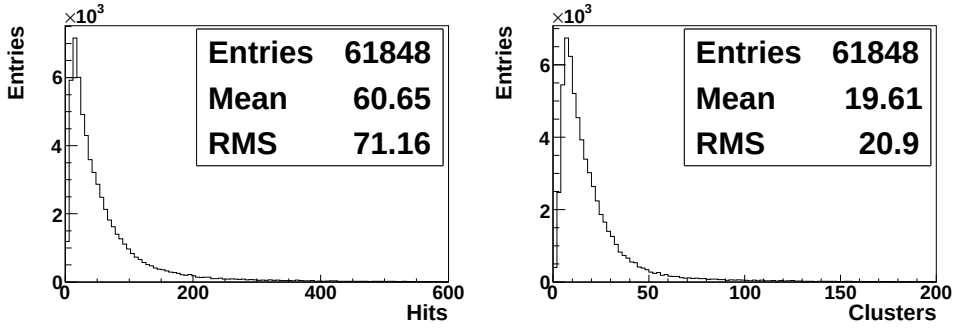

Figure 5.5: Hit (left) and cluster (right) multiplicity in the *rz*-plane in the first SVD layer for preselected zero track events of the random trigger sample.

For the Bhabha events we observed on average 65 hits and 22 clusters. These are 2 clusters with 2-3 hits more than for random events. Since there are exactly 2 tracks in these events, we conclude that each track produces a cluster with up to 3 hits.

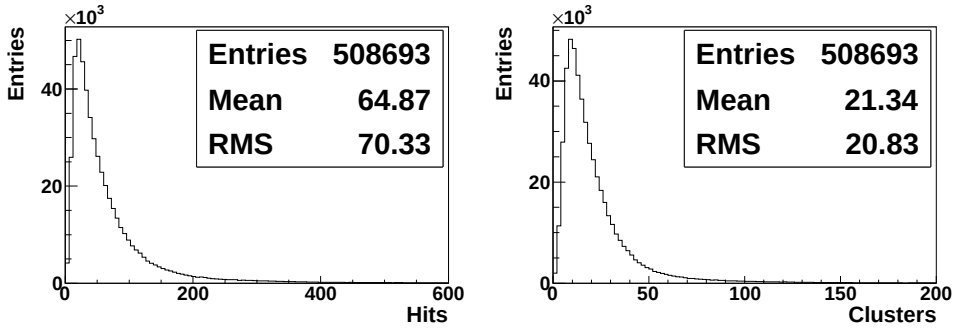

Figure 5.6: Hit (left) and cluster (right) multiplicity in the rz-plane in the first SVD layer from the Bhabha sample.

To confirm this assumption we looked at the multi-hadron sample. In the multi-hadron sample many more particles are present. On average about 10-12 reconstructed tracks are found, as seen in Figure 5.7. Accordingly, many more hits and clusters are seen in the first layer of the SVD, which is shown in Figure 5.8. A total of 92 hits and 29 clusters is observed.
The average number of tracks, hits and clusters per event for the three samples are summarized in Table 5.2. As can be seen, for the multi-hadron sample the simple assumption, that each track in the acceptance produces a cluster of up to 3 hits is also valid. This rough estimation was used in Section 5.1.1 to estimate occupancies related to the $\gamma\gamma$-process.

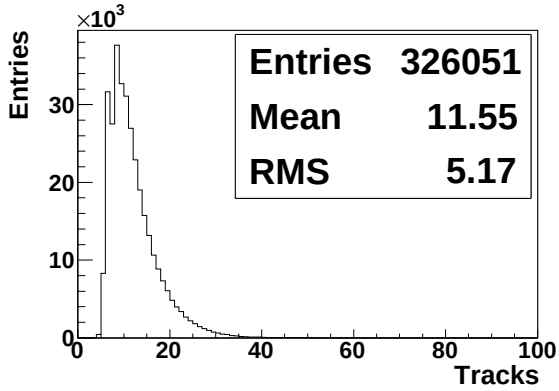

Figure 5.7: Reconstructed track multiplicity from the multi-hadron sample with $\int Ldt = 6.3\,(\text{fb})^{-1}$.

The numbers in Table 5.2 also show us, that it is possible to determine the average number of tracks crossing the detector only from the observed hits multiplicities. Due to the large number of background hits, this is not possible on the event by event basis. But by looking at large data samples, the average number of tracks crossing the

detector can be deduced from the average hit multiplicities.

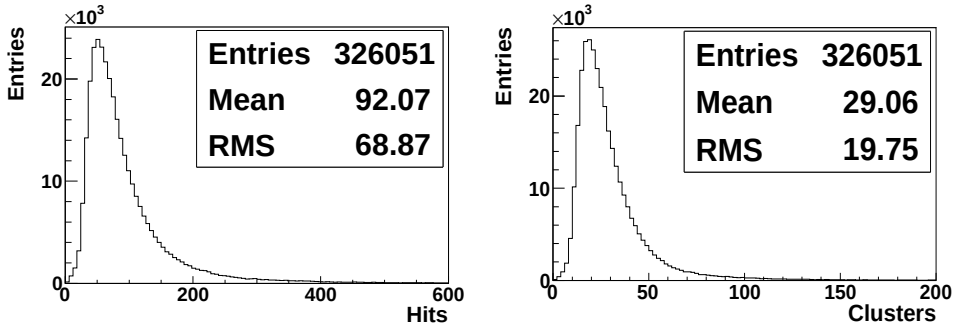

Figure 5.8: Hit (left) and cluster (right) multiplicity in the rz-plane in the first SVD layer from the multi-hadron sample.

Since a track reconstruction is not possible for the particles produced in the $\gamma\gamma$-process, we used these hit multiplicities to determine how many particles were seen in the first layer of the silicon vertex detector. To reduce the statistical uncertainty, large event samples of 500 000 events per measured point were used (in the following referred as runs).

Data Sample	Hits	Clusters	Tracks	Associated Hits/Track
Random Trigger	60.6	19.6	0	
Bhabha sample	64.9	21.3	2	2.1
Multi-hadron sample	92.1	29.1	11.5	2.7

Table 5.2: Correlation between hits and tracks in three different data samples.

Table 5.3 shows the expected number of tracks and hits in the SVD coming only from the $\gamma\gamma$-process. The estimated values for the expected number of tracks in the PXD from the KoralW Monte Carlo are corrected for the luminosity change between KEKB and SuperKEKB, the radius difference between the PXD and the SVD and their read-out time difference. Thus, the number of tracks and hits in the SVD are extracted. The same applies for the SuperB Monte Carlo.

Detector	Expected tracks at Belle/Belle II	Expected tracks at SuperB	Expected hits at Belle/Belle II	Expected hits at SuperB
PXD	2500	13800	7500	41400
SVD	1.2	6.7	3.7	20.3

Table 5.3: Expected number of tracks and hits per SVD frame.

If we take the estimation of the KoralW Monte Carlo generator, we would expect 3-4 hits in the SVD coming from the $\gamma\gamma$-background. It is clear, that this number is so small, compared to the average hit multiplicities from Table 5.2. Thus, additional means are needed to extract the background contribution from QED processes.
On the other hand, if the SuperB prediction is correct, we would see about 20 additional hits. This would be clearly visible in the data.

5.2.3 Luminosity variation

To extract a cross section for the $\gamma\gamma$-process or at least produce an upper limit which can be used for the occupancy estimation in Belle II, it was decided to vary the luminosity during the time of the measurement and observe the dependence of the detector activity.
This approach assumes that low-energetic QED processes are the main source of background in Belle and that in particular no other background source depends directly on the luminosity. Naturally, there is also machine background in Belle, such as the Touschek effect or beam-gas scattering. Therefore, it was decided to perform three different experiments, where the luminosity is varied in different ways, to be able to distinguish between background from the machine and luminosity dependent background. Since machine background mainly depends on the amount of particles in the beam, i.e. the beam currents, it was decided to change the luminosity also by varying other parameters.
The luminosity not only depends on the beam currents, but also on the two fractions of the bunch that actually intersect. This fraction can be changed by introducing a slight offset in one of the beams, thus reducing the area of intersection. Alternatively, a widening of one of the beams reduces the luminosity since the number of particles in the area of intersection is reduced for this beam. Both methods result in a reduced luminosity without reducing the machine background.
So to extract the background contribution of the $\gamma\gamma$-process the following method will be used: The luminosity of the beams will be varied using the three different methods described above. Starting from the maximal luminosity it will be decreased in several steps. For each step random trigger events are recorded. Then the hit multiplicity in

the SVD and in particular in the first layer of the SVD is studied as a function of the luminosity. This hit multiplicity should decrease with decreasing luminosity. Since no other background source is expected to depend directly on the luminosity, the decrease should be most pronounced in the first layer of the SVD, where it should be around 2 hits when going from a luminosity of $0\,(\mathrm{nb\,s})^{-1}$ to the maximum luminosity of $10\,(\mathrm{nb\,s})^{-1}$.
Since the particles from $\gamma\gamma$-process are not expected to hit the central drift chamber (CDC), the hit multiplicities of the CDC are not expected to show any dependence on the luminosity. This expectation should also be verified to confirm the absence of other luminosity dependent background sources.

5.3 Measurement setup

The measurement of the QED fraction to the cross section at Belle is based on an extraction of the hit multiplicities in the four layers of the silicon detector. From the dependence of the hit multiplicities on the instantaneous luminosity, the QED background can be extracted.

5.3.1 SVD hits

Since no tracking can be used, the analysis of the QED contribution is based on vertex detector hits. The four layers of the SVD have the following radii: 2.0 cm for the innermost layer and 4.35 cm, 7.0 cm and 8.88 cm for the other three layers, respectively. QED background is mainly expected in the first layer.
The SVD modules [81] have two orientations: $r\phi$ and rz. The $r\phi$-planes measure the ϕ coordinate of the outgoing track and the rz-planes measure the z coordinate. We look at the hits in the $r\phi$ and rz-planes of each layer independently. To obtain the hit multiplicities, the sum of all hits in one plane is used. For our measurements we averaged the hit multiplicities for all events taken at the same luminosity. Thus, for each layer we have two multiplicity values per luminosity setting, one from $r\phi$ and one from rz-plane.

5.3.2 Random trigger setup

In order to measure the QED fraction at Belle true random triggers are needed. The reason for this is that QED processes do not produce signal for triggering, but in true random triggers a contribution from QED is present.
The random triggers at Belle were studied for several data sets taken from different running periods of the detector.
The combined random trigger at Belle is setup from three signals: the "**Luminosity**" trigger and the "**Physics**" trigger which have a delayed signal on real triggers by a $100\,\mu$s and the "**Bunch0**" trigger that triggers at the same transition time of every first

bunch crossing.
To check the quality of the random trigger setup, the hit distributions in the different layers of the silicon vertex detector were plotted.

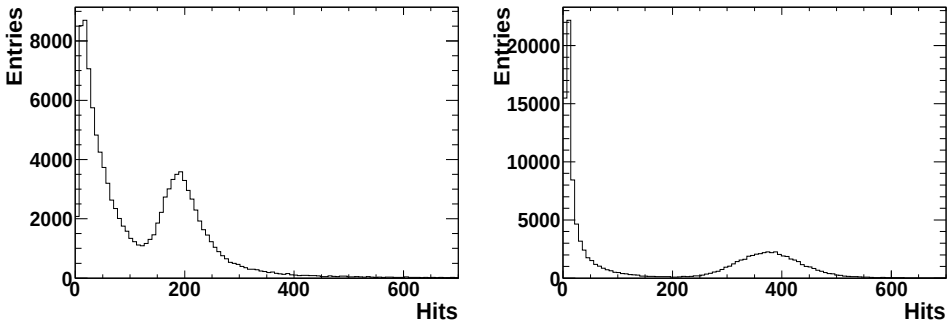

(a) Layer 1 (b) Layer 2

Figure 5.9: Hit distribution in the inner two layers of the SVD in the rz-plane.

Figure 5.9 shows the hit distribution for the rz-plane of the first and second SVD layer. One can see that the histograms not only consist of the typical falling spectrum of background hits, but show a distinct ”bump” for a higher number of hits. This ”bump” was observed in all layers of the vertex detector, in rz-planes and $r\phi$-planes alike and in all the data samples that were studied.
The comparison with physics data showed that the ”bump” does not have its origin in physics. Figure 5.10 shows hit multiplicity in the silicon detector for the inner two layers extracted by using the multi-hadron sample. No ”bump” structure can be seen, neither in the two histograms nor in the other layers of the SVD that we studied.

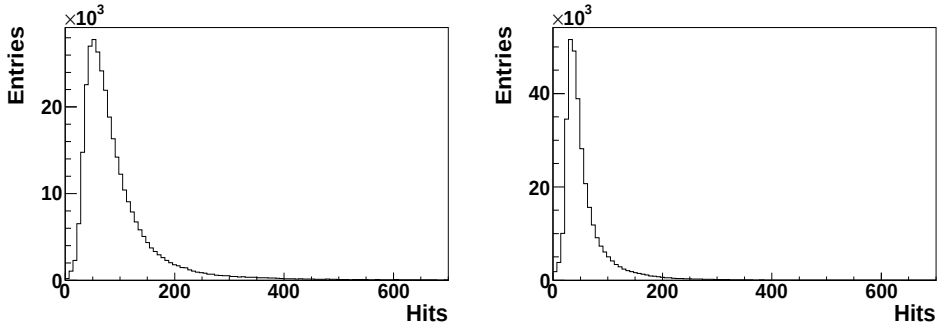

(a) Layer 1 (b) Layer 2

Figure 5.10: Hit distributions in the first two SVD layers (rz-planes) from the multi-hadron event sample.

Further investigation showed that the ”bump” is coming from the delayed ”**Physics**” and ”**Luminosity**” triggers. This is shown in Figure 5.11.

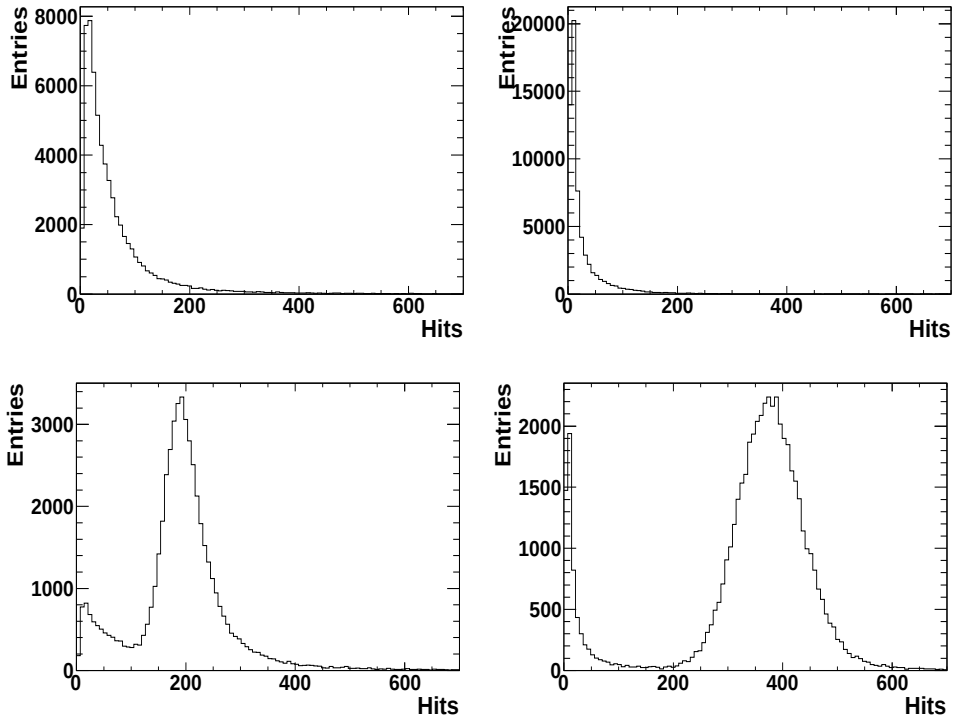

Figure 5.11: SVD hit multiplicities in rz-planes of the first (left) and second (right) layer for ”**Bunch0**” selection (top) and ”**Luminosity**” and ”**Physics**” selection (bottom) of the random trigger sample.

It shows the hit multiplicities in the first two layers of the SVD. The upper two plots are taken from the ”**Bunch0**” selection of a random trigger sample. Whereas the two plots below show the ”**Luminosity**” and ”**Physics**” selection from a random trigger sample. The ”bump” can only be seen in the lower two plots. From this strange observation about the random trigger events we concluded that there was a problem with the random triggered events in Belle. So, we looked for an alternative.

5.3.2.1 Real random triggers at Belle

Due to the fact that with the standard random trigger a problem was observed, we asked for and were provided with a pure random trigger. This was setup by the beam

crew at KEK and it was generated by a gate generator. Figure 5.12 shows that the SVD hit multiplicity in the first layer of the silicon detector does not have an additional component. The investigation of the outer three layers shows the same.
This proves that the new introduced trigger behaves as expected. Its trigger rate was 400 Hz. Using this trigger setup the experiments for the QED background extraction were done.

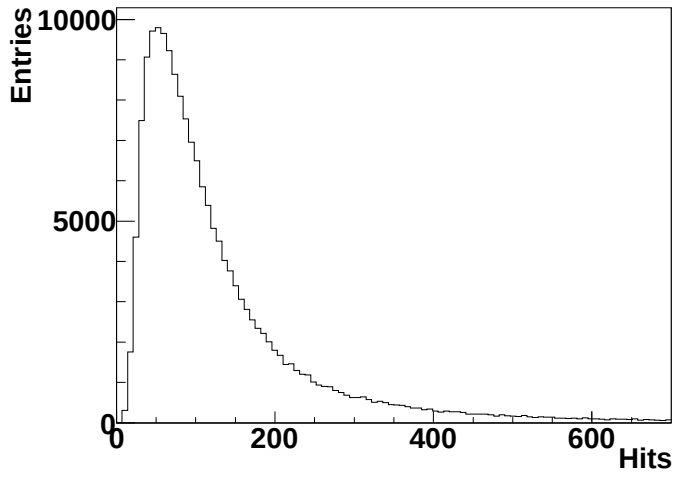

Figure 5.12: Hit multiplicity in the first SVD layer from one of the test runs with the random trigger used during the QED experiments.

5.3.2.2 Background levels for different experiments

In Figure 5.13 are shown the hit distributions in the first layer of the SVD for different data sets taken with the standard random trigger setup. These hit multiplicities are taken from the "**Bunch0**" selection from the random trigger sample. As it can be seen from these plots, the background levels change between data sets.
However, within the data set taken with the provided real random trigger the background remains unchanged. Figure 5.14 shows the hit distributions in the first layer of the vertex detector. These distributions are taken from a different running periods of the same data set.

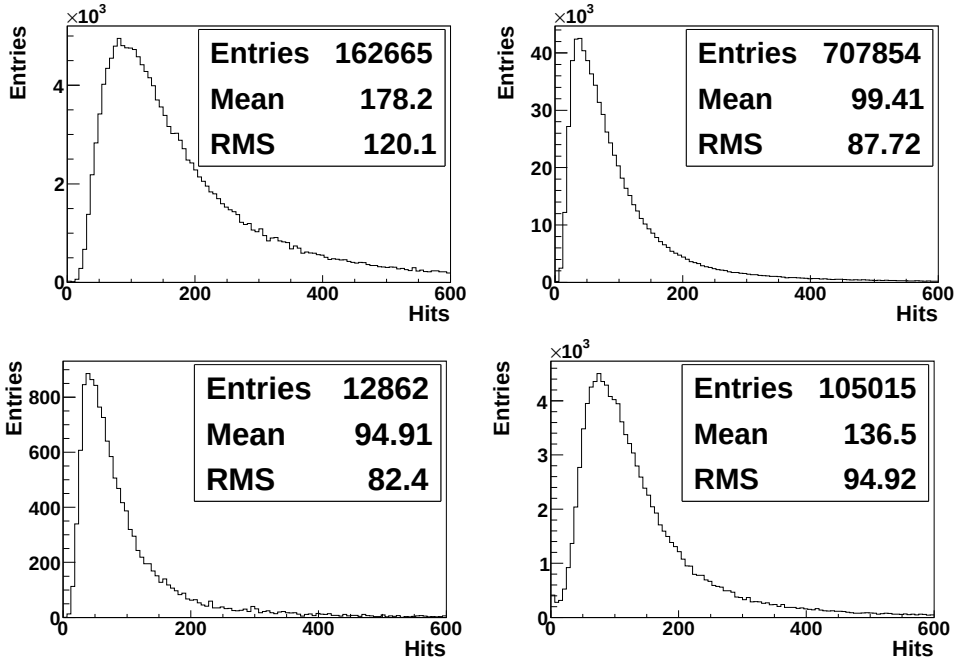

Figure 5.13: Hit distributions in the first SVD layer (rz-plane) obtained from different running periods of data taking with the pre-existing random triggers.

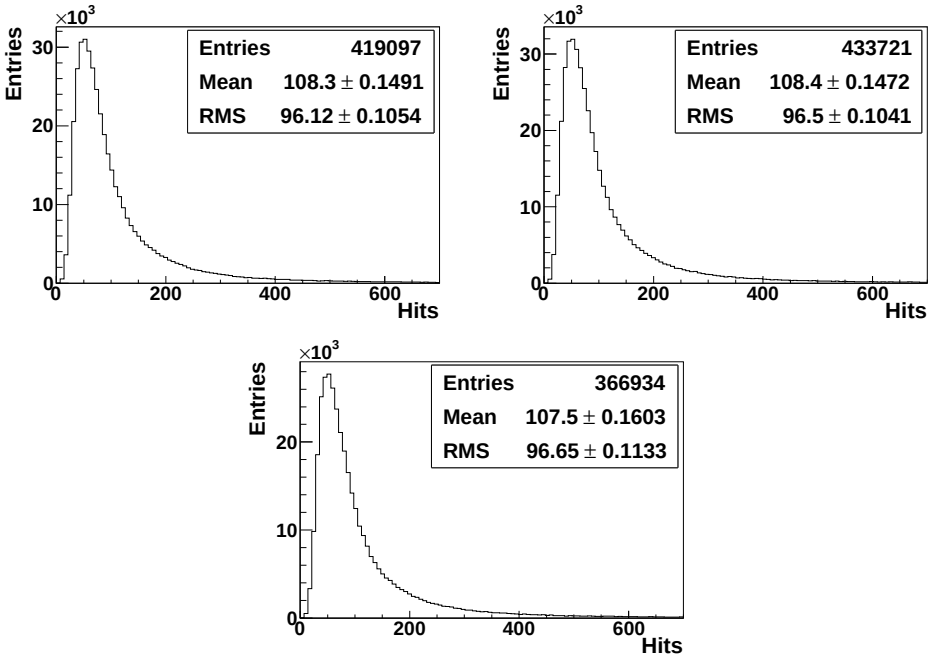

Figure 5.14: Hit distributions in the first SVD layer (rz-plane) obtained from a different running periods of data taking with the real random triggers.

5.3.3 Machine experiments for different luminosities

The basic idea for the QED experiments was to change luminosity and not too many beam parameters during data taking and extract the fraction of $\gamma\gamma$ QED background events. The luminosity was changed in three ways: widening the beam, introducing vertical a offset and reducing the current in one beam. Each method corresponds to one Belle experiment number (**A**, **B** or **C**), which is summarised in Table 5.4.
The data taking for all three experiments took aproximatelly 24 hours. More details concerning the QED background runs, such as beam currents, beam sizes, injection, etc. can be found under [82].
To compare the measurements from each of the three experiments, four luminosity-steps were chosen: $10, 8, 6, 4\,/\text{nbs}$. It was not possible to go lower in luminosity, because the beams were lost. The highest luminosity of $\sim 10\,/\text{nbs}$ is the standard Belle luminosity. At each luminosity step, one measurement point (run), with 500 000 random trigger events was taken. Afterwards, the observed hits per event were analysed and then averaged over the 500 000 events. This large number of events was essential for negligibly small statistical uncertainties.

Experiment	Run	L(/nbs)	t(s)
(**A**)	414	9.62	1025
	416	7.86	1081
	417	5.75	1091
	418	4.20	1141
	419	0.0	746
	420	0.0	233
(**B**)	401	9.71	1058
	403	7.59	1091
	408	6.08	1097
	409	3.71	1024
	411	5.97	1131
(**C**)	421	9.49	903
	422	9.39	900
	424	8.09	900
	425	7.04	900
	426	6.01	900
	427	4.81	430

Table 5.4: Overview of the runs taken in experiment 73. In this experiment the QED studies were done and the luminosity of the beam was changed. The luminosity was changed in three ways: In experiment (**A**) the beams were separated vertically, in experiment (**B**) there was a vertical increase of the beam size in the High Energy Ring and in experiment (**C**) the current in the beam was changed by stopping the injection.

5.4 Data analysis

The analysis presented in the following is based on the extracted hit multiplicities in the silicon vertex detctor. For the extraction of the two-photon QED background hits in the silicon detector we look in both orientations, rz and $r\phi$-plane independently, for each of the four vertex detector layers.

5.4.1 Hit multiplicities in the SVD

The analysis of the data collected during the QED experiments started by checking the hit spectra of the SVD layers. Two examples of these spectra are shown in Figure 5.15. The left histogram shows the hit multiplicities seen in the rz-plane of the first SVD layer during a high luminosity run of experiment A. The right histogram shows the hit multiplicity in the same plane for a lower luminosity run of experiment C.

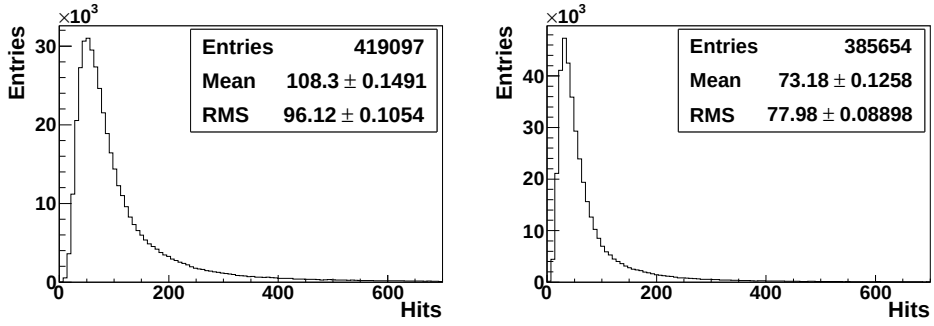

(a) exp.(**A**): L = 9.62 /nbs (b) exp.(**C**): L = 6.01 /nbs

Figure 5.15: Hit multiplicities in the rz-plane in the first layer of the SVD for experiment (A) (left) and experiment (C) (right) for different luminosities.

As expected both spectra show the typical shape for random trigger events without any additional components. We also checked the hit multiplicity distributions in the rϕ-planes and of the outer layers of the silicon vertex detector (see Figures in Appendix D.0.2). Also in the other SVD layers the hit distribution spectrum has the expected shape. Looking at all the data collected with the real random trigger we observed similar spectrum for the different runs, taken at different luminosity setting. Therefore, we are confident that the measurement setup, in particular the trigger and the noise levels in the vertex detector were stable during the time of the data taking.
During the whole data taking we monitored the background levels not only of the silicon vertex detector, but also the background behavior of the central drift chamber. In contrary to our initial assumption, we observed a strong dependence of the background levels in the SVD and the CDC on the beam luminosity. This was quite unexpected since particles from QED background processes do not reach the

central drift chamber, while other background sources apparent in the drift chamber were not expected to depend on the luminosity. Looking at the statistic boxes of the two histograms in Figure 5.15 one can see, that there is a significant difference between the mean hit multiplicity in the left histogram ($L = 10\,(\text{nbs})^{-1}$) and the right histogram ($L = 6\,(\text{nbs})^{-1}$). This strong dependence on the luminosity is even more apparent when looking at the mean values from all runs and luminosities of the QED experiment which are given in Table 5.5. Similarly large differences were also seen when looking at the other layers of the silicon vertex detector, which are also shown in the Table 5.5.
In addition, strong changes of the background activity in the central drift chamber, with the changes in luminosity were also seen. In Figure 5.16 (a), the drift chamber current activity as a function of luminosity is shown. One can clearly see the strong variations of the current which depends on the luminosity. Figure 5.16 (b) shows how the mean hit multiplicity in the central drift chamber changes as a function of the luminosity. Table 5.6 summarizes the results from these observations.

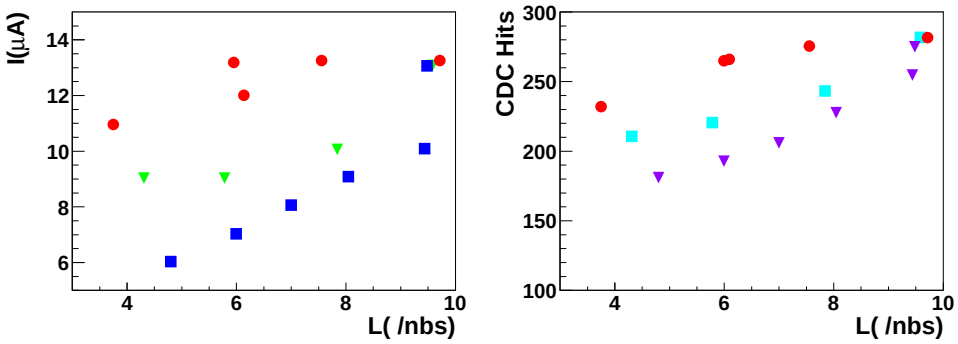

(a) CDC current (b) CDC hit multiplicity

Figure 5.16: The activity of the Central Drift Chamber. The CDC current as a function of luminosity (left) for the three QED experiments (A(green triangles), B(red circles) and C (blue squares)). The CDC hit multiplicity as a function of luminosity (right) for the three QED experiments (A (light blue squares), B (red circles) and C (purple triangles)).

It is clear from these observations, that this background could not be related to QED processes. Particles from the QED background are too soft to produce hits in the drift chamber. This had to be a so-far unknown background component which also strongly depends on the luminosity changes. Since we observed different trends during the three different machine tunings (experiments A, B, C), this background component is directly related to the machine operation itself.

(a) Experiment A

rz-plane						
SVD	9.62 /nbs	7.86 /nbs	5.75 /nbs	4.30 /nbs	0.0 /nbs	0.0 /nbs
1	108.3±0.15	92.03±0.13	81.98±0.12	76.61±0.12	123.5±0.23	71.03±0.27
2	48.48±0.07	42.92±0.06	39.76±0.06	38.14±0.06	59.82±0.11	37.43±0.13
3	44.22±0.06	39.00±0.06	36.21±0.05	35.13±0.05	54.15±0.09	35.10±0.11
4	38.95±0.06	34.08±0.05	31.58±0.04	30.63±0.04	48.28±0.08	31.20±0.10
$r\phi$-plane						
1	103.7±0.14	87.44±0.13	77.03±0.12	71.5±0.11	115.7±0.21	64.59±0.26
2	49.05±0.09	42.37±0.08	38.64±0.07	36.78±0.07	60.98±0.13	36.16±0.15
3	37.97±0.06	33.54±0.05	31.74±0.05	30.72±0.04	47.58±0.08	30.61±0.10
4	38.01±0.05	33.14±0.04	30.83±0.04	29.83±0.04	47.51±0.08	30.24±0.09

(b) Experiment B

rz-plane					
SVD	9.71 /nbs	7.59 /nbs	6.08 /nbs	3.71 /nbs	5.97 /nbs
1	108.4±0.15	103.2±0.14	98.69±0.14	86.22±0.14	99.75±0.14
2	48.68±0.07	47.06±0.07	46.00±0.07	41.91±0.06	46.53±0.07
3	44.53±0.06	43.69±0.06	42.98±0.07	38.91±0.06	42.95±0.06
4	39.18±0.06	38.30±0.05	37.58±0.05	33.79±0.05	38.24±0.05
$r\phi$-plane					
1	103.7±0.14	98.01±0.14	92.98±0.13	79.83±0.13	93.82±0.13
2	49.22±0.08	47.54±0.08	46.11±0.08	41.16±0.08	46.55±0.08
3	38.29±0.06	38.65±0.05	37.96±0.05	34.04±0.05	36.68±0.05
4	38.23±0.05	37.54±0.05	36.98±0.05	33.19±0.04	37.14±0.05

(c) Experiment C

rz-plane						
SVD	9.49 /nbs	9.39 /nbs	8.09 /nbs	7.04 /nbs	6.01 /nbs	4.80 /nbs
1	107.5±0.16	100.5±0.15	89.01±0.14	79.87±0.13	73.18±0.12	67.19±0.18
2	48.24±0.08	45.11±0.07	40.77±0.07	37.25±0.06	34.89±0.06	32.94±0.08
3	43.35±0.07	40.12±0.06	36.54±0.06	33.55±0.05	31.42±0.05	30.24±0.07
4	38.30±0.06	35.37±0.05	31.86±0.05	29.11±0.04	27.40±0.04	26.15±0.06
$r\phi$-plane						
1	102.9±0.15	96.15±0.14	84.96±0.13	75.91±0.13	69.25±0.12	63.12±0.17
2	48.92±0.09	45.62±0.09	40.60±0.08	36.72±0.07	33.92±0.07	31.76±0.10
3	37.32±0.06	35.31±0.05	32.28±0.05	29.59±0.05	27.80±0.04	26.72±0.07
4	37.49±0.06	34.82±0.05	31.41±0.04	28.63±0.04	26.85±0.04	25.54±0.06

Table 5.5: SVD hit multiplicity as a function of luminosity in the four layers of the silicon detector in both, rz and $r\phi$-planes.

Experiment	$L(/nbs)$	I(μA)	Hits
(**A**)	9.62	13	280.190
	7.86	10	242.790
	5.75	9	220.930
	4.20	9	210.430
(**B**)	9.71	13	279.680
	7.59	13	273.150
	6.08	12	264.750
	3.71	11	231.020
	5.97	13	264.670
(**C**)	9.49	13	274.320
	9.39	10	254.950
	8.09	9	227.860
	7.04	8	206.590
	6.01	7	192.770
	4.81	6	181.770

Table 5.6: The corresponding luminosity, CDC current and the total CDC hit multiplicity of the runs taken in experiment 73. In this experiment the QED studies were done and the luminosity of the beam was changed. The luminosity was changed in three ways: In experiment (**A**) the beams were separated vertically, in experiment (**B**) there was a vertical increase of the beam size in the High Energy Ring and in experiment (**C**) the current in the beam was changed by stopping the injection.

For the measurement of the QED background contribution, we needed to correct for the effect of this additional background component. It was our plan to extract the contribution from QED background from the different mean hit multiplicities observed for two runs with different luminosity. However, due to the additional background not only the QED was responsible for the observed change. Therefore, we corrected for the additional background component using the information about the change of background level in the drift chamber.
After the correction we could compare the corrected mean hit multiplicities measured in runs with less than nominal luminosity, to the measurements of runs of the same series (A, B or C) with the nominal luminosity of $10\,(\mathrm{nbs})^{-1}$. The observed decrease of the corrected mean hit multiplicity in the central drift chamber could then be extrapolated to zero luminosity. The difference between the extrapolated value for zero luminosity and the corrected hits at maximum luminosity was then taken to be the contribution from the QED background.

5.4.2 Correcting for the change in background activity in the CDC

To correct for the additional luminosity-dependent background the luminosity dependence of the drift chamber activity is used. For this, measurements of the currents from

the drift chamber and the hit multiplicities were studied.

5.4.3 A CDC background measurement using the measured CDC currents

To extract the detector activity during data taking, the online monitoring of the currents of the central drift chamber were used. However we observed on these monitors that the drift chamber current was quite unstable and showed large variation over time. These fluctuations of the current in the drift chamber appear in all three experiments.

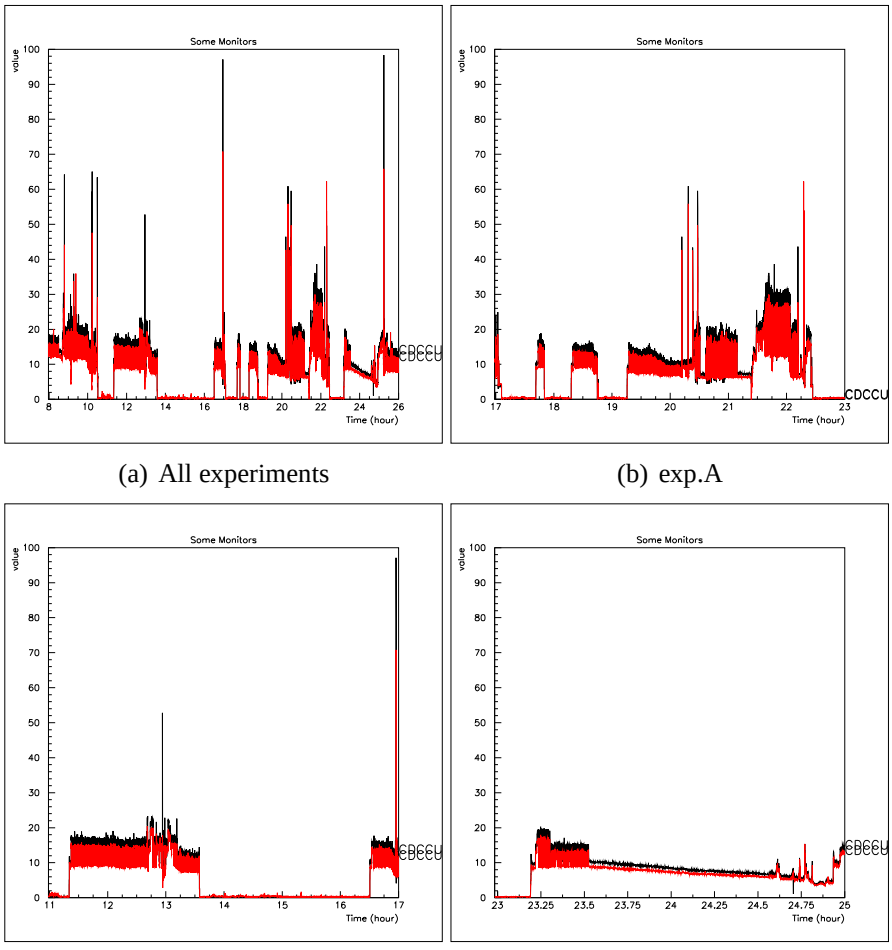

(a) All experiments (b) exp.A

(c) exp.B (d) exp.C

Figure 5.17: CDC current during data taking of the three QED experiments.

In Figure 5.17 one can see the CDC current behavior during the data taking time of the QED experiments. The time is represented in hours. The subsections with $I^{CDC} = 0$

correspond to the time needed to setup the beams between two runs.
To improve the reliability of this approach using the drift chamber current information, we tried to remove the data taking periods which had large fluctuations in the CDC current. However, it was discovered, that these fluctuations occur every $25-30\,\mathrm{s}$, as seen in Figure 5.18. According to the machine experts they could be related to the beam injection. This made a removal of the time periods with large fluctuations impossible. As a consequence, we decided not to use the central drift chamber current information in our analysis.

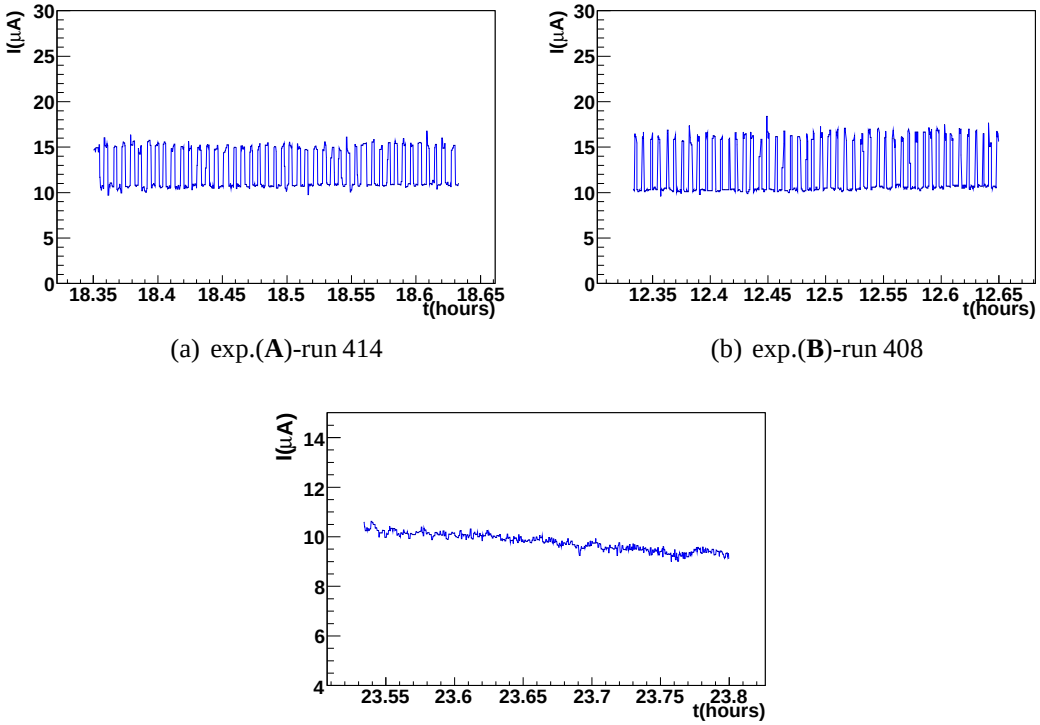

(a) exp.(**A**)-run 414

(b) exp.(**B**)-run 408

(c) exp.(**C**)-run422

Figure 5.18: CDC current during different running periods of the three QED experiments.

5.4.4 Measuring the CDC background with the observed hit multiplicities

As it was seen in Section 5.4.3, Figure 5.16 (b) shows that the hit multiplicities seen in the central drift chamber depend on the luminosity. Since this luminosity-dependence is not due to QED processes we need to correct for it.
The central drift chamber at Belle consists of 50 layers [83]. Figure 5.19, shows the hit multiplicity in each of the 50 CDC layers, for the three QED experiments at

standard luminosity, $L \sim 10\,/\text{nbs}$. As one can see, the three plots are in a very nice agreement. The total hit multiplicity of the drift chamber, shown in Figure 5.16 (b), which in the following will be used to correct the measurements obtained from the vertex detector, is the sum of the 50 multiplicities.

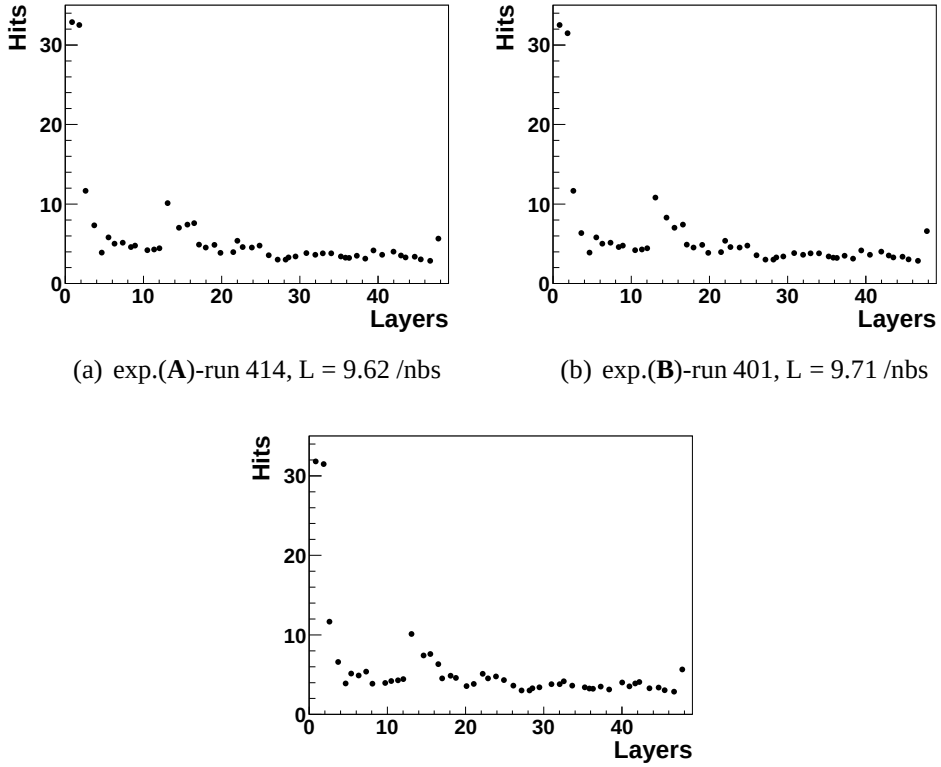

(a) exp.(**A**)-run 414, L = 9.62 /nbs

(b) exp.(**B**)-run 401, L = 9.71 /nbs

(c) exp.(**C**)-run421, L = 9.49 /nbs

Figure 5.19: Average number of hits per event in each of the 50 layers of the central drift chamber (CDC).

For the correction a reference luminosity L_{max} is chosen. The hit multiplicities obtained from the layers of the silicon vertex detector are then corrected for the additional luminosity-dependence using

$$N^{SVD}_{hits\_corr}(L_i) = N^{SVD}(L_i) \times \frac{N^{CDC}(L_{max})}{N^{CDC}(L_i)}, \tag{5.2}$$

where $N^{SVD}_{hits\_corr}(L_i)$ is the corrected SVD hit multiplicity, $N^{SVD}(L_i)$ is the SVD hit multiplicity measured for luminosity L_i, $N^{CDC}(L_{max})$ is the CDC hit multiplicity at reference luminosity and $N^{CDC}(L_i)$ is the CDC hit multiplicity at luminosity L_i.
The reference luminosity is the highest luminosity value in experiments (A) and (B),

but in experiment (C) a lower luminosity is chosen as a reference point, because a huge drop was observed when going from maximum luminosity to the luminosity of $9.39\,/\mathrm{nbs}$.
The effect of the correction using the CDC hit multiplicity can be seen in Figure 5.20 (b), where the corrected vertex detector hit multiplicities as a function of luminosity are shown. Compared to Figure 5.20 (a), the SVD hit multiplicities show a much smaller dependence on the luminosity.

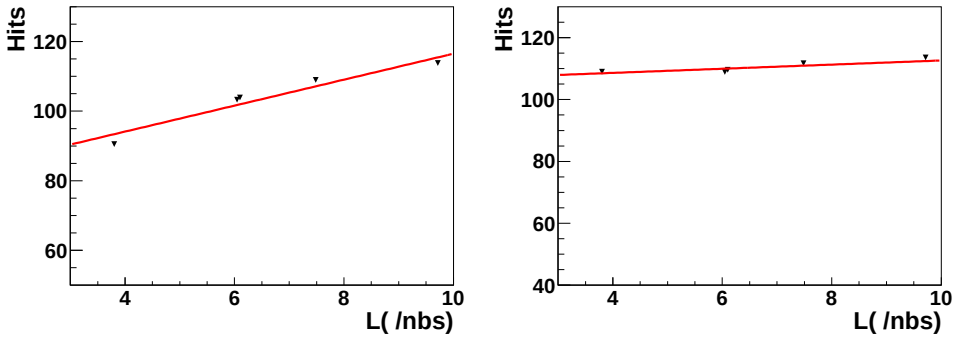

Figure 5.20: Comparison between hit multiplicities in the first SVD layer in rz-plane as a function of luminosity before (left) and after (right) applied correction using the CDC activity in experiment B.

From the extrapolation of the fitted line in Figure 5.20 (b), we can estimate that in the first layer of the vertex detector, 10-15 hits are due to background processes that are only seen in the SVD. According to our initial assumption this is the QED background. At the same time the outer three layers of the SVD show weaker trends compared to the first one (see Figure D.5 in the Appendix D.0.3). This confirms our expectation that at larger radii the presence of the QED background is smaller.
Histograms in Figure 5.21 show the extracted QED contribution corrected by using the CDC activity. Each entry in these histograms corresponds to the hit increase for maximum luminosity, extrapolated from two corrected SVD measurements. Since the highest luminosity is taken as a reference there are 6 (8) measurements per layer in experiments A (B, C). As you can see, the extrapolated values are distributed either around 0 hits or around 15 hits. At first it was not clear to us where the component with large contribution is coming from.
We investigated all four layers of the silicon vertex detector and discovered that the larger component comes from the first SVD layer only. This is shown in Figure 5.22. The peak for 0 hits contribution is coming from the outer three layers, as shown in Figure 5.23.

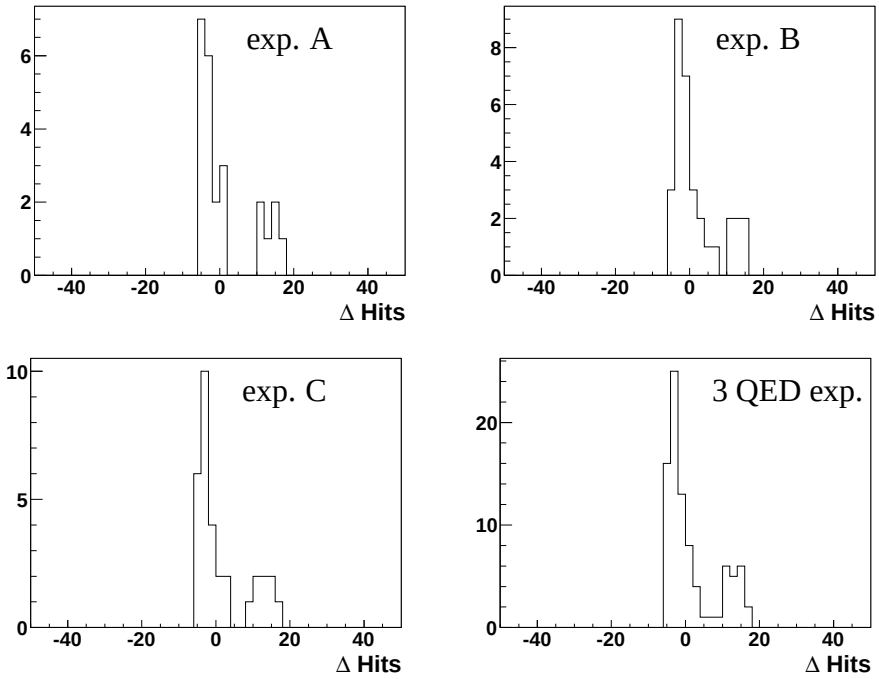

Figure 5.21: The extracted QED contribution from all four layers of the SVD in the three QED experiments investigated separately and together.

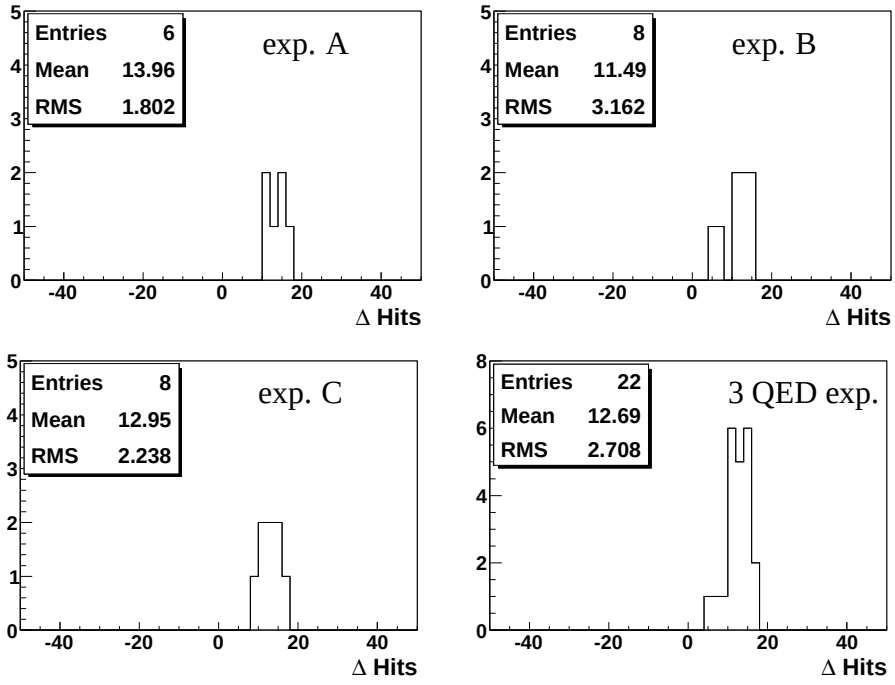

Figure 5.22: The extracted QED contribution in the 1st SVD layer from experiments A, B and C and from the three QED experiments in total.

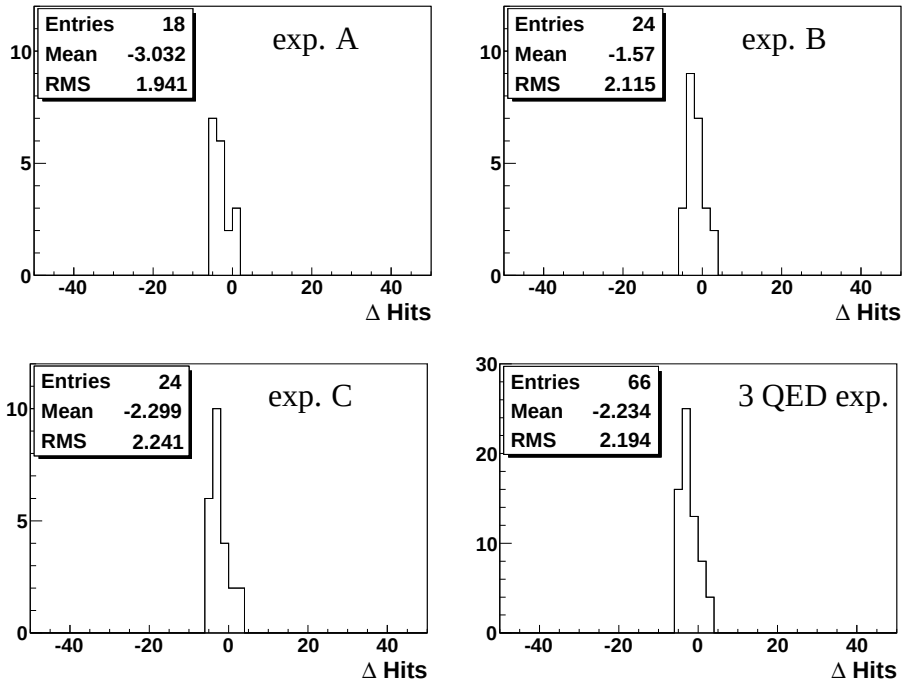

Figure 5.23: The extracted QED contribution in the outer three SVD layers from experiment A , B and C and the extracted QED contribution in the 2nd-4th layer of the SVD in total from the three QED experiments.

5.4.5 Systematics taken using different subsets of CDC layers

The correction on the drift chamber activity represents one of the larger systematic uncertainties of the measurement. Therefore, we investigated how the result depends on the exact choice of the correction factor. For this we recalculated the correction factors using different subsets of the layers from the drift chamber.
In a first step we divided the 50 layers of the central drift chamber in five subsets of 10 drift chamber layers and recalculated the correction factors. Table 5.7 shows the resulting values for the QED hit contribution in the first layer of the silicon vertex detector in both, rz and $r\phi$-planes, calculated using the five different subsets of CDC layers for the correction. Whereas, the QED background contribution in the separate three outer layers of the SVD and the total contribution from QED in the three outer layers taken together, using the same five different subsets of CDC layers for the correction is shown in Table 5.8.
As a next step, we reduced the number of drift chamber layers used in the correction factor by 10 in each step. Again, the resulting QED hit contributions in the SVD are shown in Tables 5.9 and 5.10 for the first layer of the silicon vertex detector and its remaining three layers taken together, respectively. As it can be seen, the results in the four tables are consistent with each other and prove the reliability of the CDC hit correction method.

(a) 1st SVD layer *rz*-plane

CDC layers	exp.(**A**)	exp.(**B**)	exp.(**C**)	All exp.
1 - 50	15.66±0.47	13.65±1.89	13.86±2.20	14.27±1.96
1 - 10	20.96±1.90	16.41±2.08	25.76±0.71	21.05±4.32
10 - 20	6.85±2.89	13.97±2.56	1.73±5.96	7.58±6.71
20 - 30	13.83±0.52	11.56±1.36	6.08±3.24	10.19±3.87
30 - 40	16.07±1.15	10.21±1.31	7.96±1.29	10.99±3.49
40 - 50	14.57±0.63	9.90±1.55	7.89±0.96	10.45±2.90

(b) 1st SVD layer *r*ϕ-plane

CDC layers	exp.(**A**)	exp.(**B**)	exp.(**C**)	All exp.
1 - 50	12.27±0.73	9.32±2.66	12.04±1.88	11.11±2.42
1 - 10	17.95±2.31	12.30±2.84	24.72±0.61	18.35±5.71
10 - 20	2.84±2.71	9.67±3.40	-0.87±5.82	3.97±6.26
20 - 30	10.31±0.35	7.08±2	3.75±2.96	6.75±3.38
30 - 40	12.71±1.51	5.63±2.02	5.74±0.92	7.60±3.49
40 - 50	11.10±0.95	5.30±2.33	5.67±0.55	7.02±2.94

Table 5.7: QED background contribution in the 1st SVD layer in the *rz*-plane (a) and in the *r*ϕ-plane (b), determined using the subset of CDC layers indicated in the first column as correction factors.

(a) 2nd SVD layer

CDC layers	exp.(**A**)	exp.(**B**)	exp.(**C**)	All exp.
1 - 50	-2.07±2.66	0.38±1.74	-0.32±2.45	-0.54±2.48
1 - 10	0.54±2.65	1.72±1.79	5.44±2.35	2.75±3.07
10 - 20	-6.39±3.18	0.52±2.06	-6.17±3.30	-3.80±4.35
20 - 30	-2.96±2.72	-0.64±1.47	-4.09±2.63	-2.52±2.75
30 - 40	-1.87±2.65	-1.29±1.49	-3.20±2.45	-2.14±2.36
40 - 50	-2.61±2.66	-1.44±1.64	-3.23±2.44	-2.41±2.38

(b) 3rd SVD layer

CDC layers	exp.(**A**)	exp.(**B**)	exp.(**C**)	All exp.
1 - 50	-4.55±0.55	-3.13±1.75	-4.48±0.53	-4.01±1.32
1 - 10	-2.31±1.03	-1.01±1.16	0.45±0.54	1.18±1.76
10 - 20	-8.27±1.01	-3.00±1.83	-9.48±1.84	-6.79±3.34
20 - 30	-5.32±0.45	-4.00±1.64	-7.71±0.81	-5.71±1.96
30 - 40	-4.39±0.76	-4.58±1.69	-6.96±0.49	-5.39±1.64
40 - 50	-5.02±0.60	-4.71±1.74	-6.99±0.52	-5.62±1.54

(c) 4th SVD layer

CDC layers	exp.(**A**)	exp.(**B**)	exp.(**C**)	All exp.
1 - 50	-2.48±0.63	-1.96±1.00	-2.09±0.25	-2.15±0.73
1 - 10	-0.55±1.15	-0.88±1.02	2.41±0.66	0.44±1.77
10 - 20	-5.89±0.56	-1.84±1.25	-6.65±1.23	-4.70±2.44
20 - 30	-3.19±0.40	-2.77±0.86	-5.04±0.41	-3.71±1.19
30 - 40	-2.32±0.91	-3.30±0.82	-4.35±0.60	-3.42±1.12
40 - 50	-2.91±0.73	-3.42±0.91	-4.38±0.71	-3.63±0.99

(d) 2nd-4th SVD layer

CDC layers	exp.(**A**)	exp.(**B**)	exp.(**C**)	All exp.
1 - 50	-3.03±1.94	-1.57±2.12	-2.30±2.24	-2.23±2.19
1 - 10	-0.73±2.13	-0.37±2.21	2.77±2.51	0.67±2.79
10 - 20	-6.85±2.20	-1.44±2.28	-7.43±2.72	-5.19±3.69
20 - 30	-3.82±1.93	-2.45±1.95	-5.61±2.22	-3.98±2.45
30 - 40	-2.86±2.00	-3.06±1.93	-4.83±2.16	-3.65±2.23
40 - 50	-3.51±1.95	-3.19±2.00	-4.87±2.17	-3.89±2.18

Table 5.8: QED background contribution in the 2nd (a), 3rd (b) and in the 4th SVD layer (c), as well as the total QED background contribution in the outer three layers of the SVD (d), determined using the subset of CDC layers indicated in the first column as correction factors.

(a) 1st SVD layer, *rz*-plane

CDC layers	exp.(**A**)	exp.(**B**)	exp.(**C**)	All exp.
1 - 50	15.66±0.47	13.65±1.89	13.86±2.20	14.27±1.96
10 - 50	12.02±0.86	11.82±1.78	5.36±3.28	9.52±3.90
20 - 50	14.78±0.51	10.62±1.37	7.25±1.88	10.53±3.30
30 - 50	15.34±0.89	10.06±1.42	7.93±1.11	10.72±3.19
40 - 50	14.57±0.63	9.91±1.55	7.89±0.96	10.45±2.90

(b) 1st SVD layer $r\phi$-plane

CDC layers	exp.(**A**)	exp.(**B**)	exp.(**C**)	All exp.
1 - 50	12.27±0.73	9.32±2.66	12.04±1.88	11.11±2.42
10 - 50	8.38±0.63	7.35±2.55	2.98±2.98	6.04±3.35
20 - 50	11.33±0.80	6.07±2.09	4.99±1.50	7.11±3.08
30 - 50	11.92±1.24	5.47±2.17	5.71±0.71	7.31±3.21
40 - 50	11.10±0.95	5.3±2.33	5.67±0.55	7.02±2.94

Table 5.9: QED background contribution in the 1st SVD layer in the *rz*-plane (a) and in the $r\phi$-plane (b), determined using the subset of CDC layers indicated in the first column as correction factors.

(a) 2nd SVD layer

CDC layers	exp.(**A**)	exp.(**B**)	exp.(**C**)	All exp.
1 - 50	-2.07±2.66	0.38±1.74	-0.32±2.45	-0.54±2.48
10 - 50	-6.47±1.21	-0.52±1.71	-4.44±2.62	-2.85±2.97
20 - 50	-2.50±2.66	-1.09±1.52	-3.53±2.46	-2.37±2.46
30 - 50	-2.23±2.65	-1.37±1.56	-3.22±2.44	-2.28±2.36
40 - 50	-2.60±2.65	-1.44±1.64	-3.23±2.44	-2.41±2.38

(b) 3rd SVD layer

CDC layers	exp.(**A**)	exp.(**B**)	exp.(**C**)	All exp.
1 - 50	-4.55±0.55	-3.13±1.75	-4.48±0.53	-4.01±1.32
10 - 50	-6.09±0.45	-3.90±1.72	-8.01±0.83	-5.99±2.11
20 - 50	-4.93±0.56	-4.40±1.68	-7.24±0.45	-5.58±1.68
30 - 50	-4.70±0.68	-4.64±1.71	-6.98±0.49	-5.51±1.59
40 - 50	-5.02±0.60	-4.71±1.74	-6.99±0.52	-5.62±1.54

(c) 4th SVD layer

CDC layers	exp.(**A**)	exp.(**B**)	exp.(**C**)	All exp.
1 - 50	-2.48±0.63	-1.96±1.00	-2.09±0.25	-2.15±0.73
10 - 50	-3.89±0.32	-2.68±0.99	-5.31±0.35	-3.97±1.30
20 - 50	-2.82±0.66	-3.14±0.86	-4.61±0.41	-3.59±1.03
30 - 50	-2.61±0.82	-3.36±0.86	-4.36±0.65	-3.52±1.05
40 - 50	-2.91±0.73	-3.42±0.91	-4.38±0.71	-3.63±0.99

(d) 2nd-4th SVD layer

CDC layers	exp.(**A**)	exp.(**B**)	exp.(**C**)	All exp.
1 - 50	-3.03±1.94	-1.57±2.12	-2.30±2.24	-2.23±2.19
10 - 50	-4.61±1.93	-2.37±2.06	-5.92±2.21	4.27±2.58
20 - 50	-3.42±1.94	-2.88±1.95	-5.13±2.14	-3.84±2.25
30 - 50	-3.18±1.97	-3.12±1.96	-4.85±2.16	-3.77±2.19
40 - 50	-3.51±1.95	-3.19±2.00	-4.87±2.17	-3.89±2.18

Table 5.10: QED background contribution in the 2nd (a), 3rd (b) and in the 4th SVD layer (c), as well as the total QED background contribution in the outer three layers of the SVD (d), determined using the subset of CDC layers indicated in the first column as correction factors.

5.5 Full detector simulation of KoralW events and comparison with the data

So far, the simple estimation of the expected background rate in the silicon vertex detector was based on the number of generated tracks and the assumption that each track produces up to three hits in the SVD. To improve the knowledge of the expectation, we decided to do a full Monte Carlo simulation.

5.5.1 The full detector simulation

For this we simulated KoralW events merging in one detector event all interactions corresponding to one read-out frame at $L = 10\,/\mathrm{nbs}$. These merged events are then fed into the standard Belle analysis software framework-BASF.
Figures 5.24 and 5.25 show the hit distribution per read-out frame.

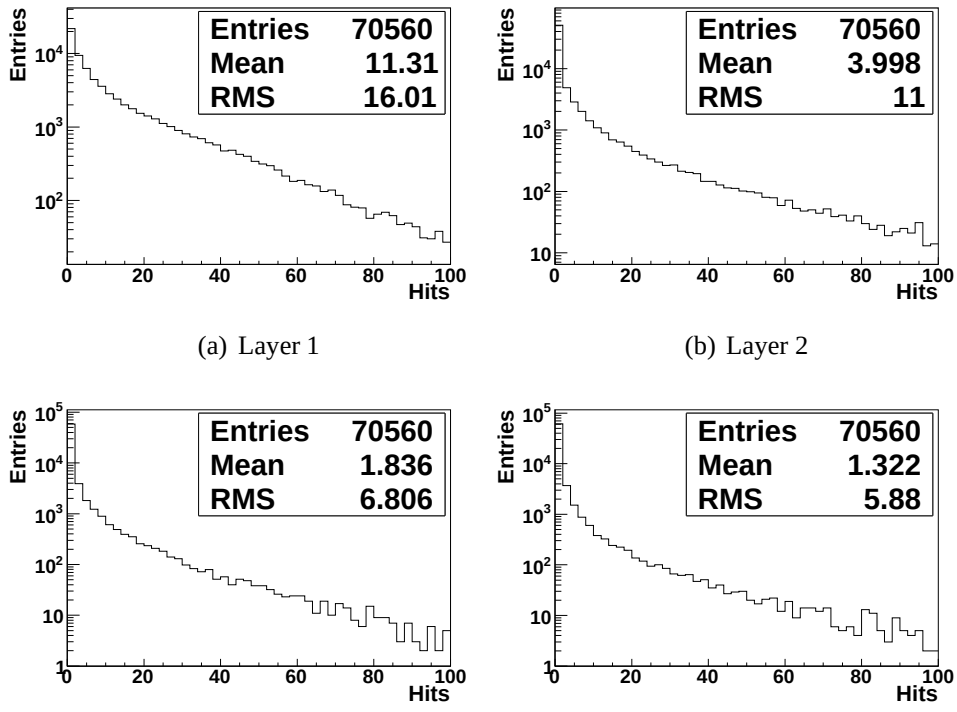

(a) Layer 1 (b) Layer 2

(c) Layer 3 (d) Layer 4

Figure 5.24: SVD hit multiplicities in the rz-plane of the four SVD layers from the full KoralW simulation.

Since, here only the QED process is considered, the observed hit multiplicities are significantly smaller than what is shown in Figure 5.15 and Table 5.5. As one can see,

there is a clear difference in the multiplicities of the four layers. The number of hits in the first layer of the silicon vertex detector is significantly larger then in the outer three layers.

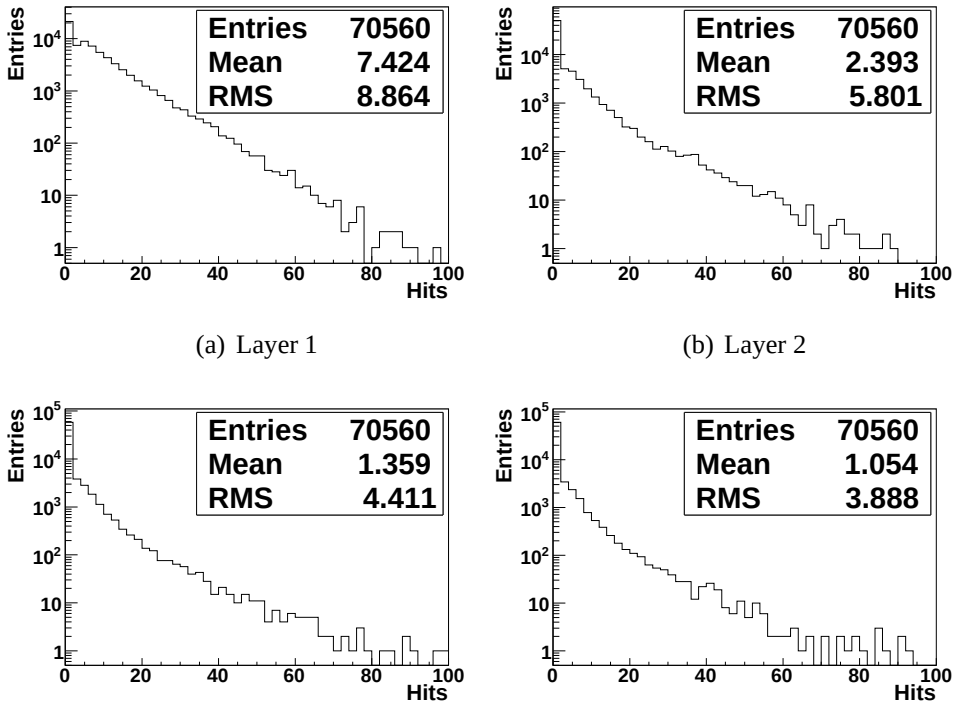

(a) Layer 1 (b) Layer 2

(c) Layer 3 (d) Layer 4

Figure 5.25: SVD hit multiplicities in the $r\phi$-plane of the four SVD layers from the full KoralW simulation.

This seems to be an explanation why also in the data we see more hits coming from QED events in the innermost layer compared to the other three layers. To understand the origin of this difference in hits we use the event display.

5.5.2 Event display of KoralW events

Using the event display we discovered that in many QED events, so-called low momentum ”curlers” appear. These low-momentum tracks are only able to reach the first layer of the silicon vertex detector and have too little P_t to reach the second one. Instead, they go back and produce multiple hits in the innermost layer of the vertex detector. That is the reason why a larger amount of hits is measured in the first SVD layer.
An example is shown in Figure 5.26. The event shows one outgoing track that is curling around SVD layer 1 producing multiple hits. The hits in the strip-detector modules

are shown by the black lines. The trajectory of the outgoing electron is shown in blue, while the dashed purple line indicates a photon. Additional events with ”curlers” are also shown in Figure 5.27.

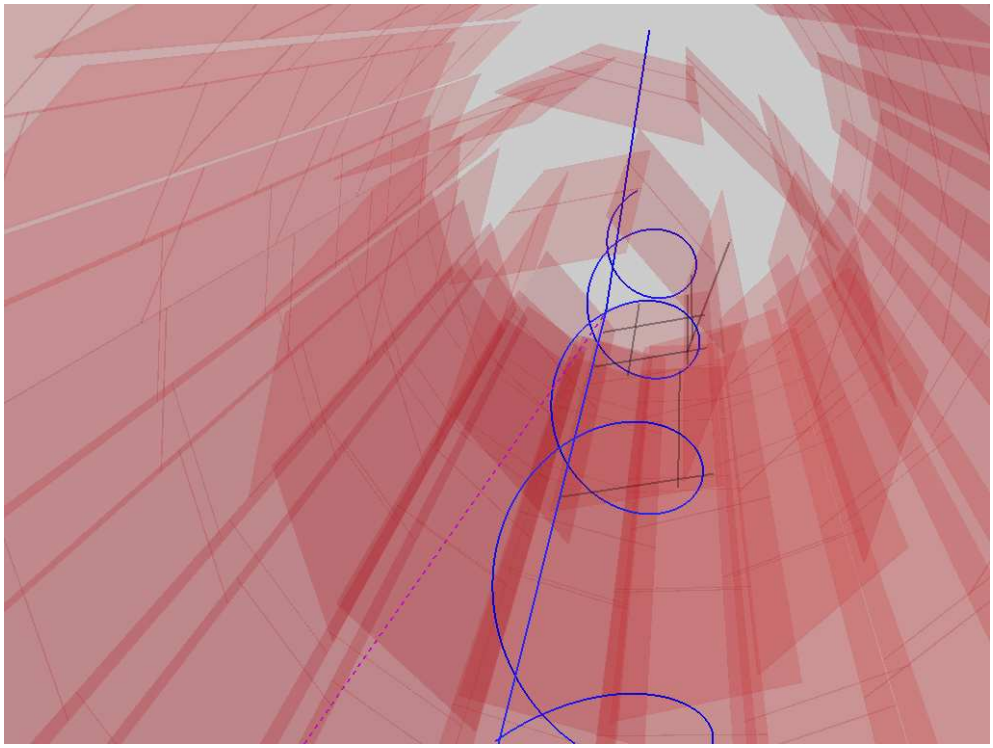

Figure 5.26: Event display of the two-photon KoralW events in the SVD.

5.5.3 Comparison between Monte Carlo and data

After doing the full simulation, we confirmed that the observed QED hit rates in the four silicon vertex detector layers are in a good agreement with the expectation from Monte Carlo simulations. From the Monte Carlo simulations we expect on average 10 hits from QED in the innermost layer of the SVD, and 0-3 hits in the more distant layers. This is also seen in the data (see Figures 5.22 and 5.23).
From the event display we learned that our naive assumption of 3 hits per track has to be scaled up significantly.
Table 5.11 compares the measured hit multiplicities in the silicon vertex detector in all four layers, with the Monte Carlo expectations. In this table for KoralW we used the results for the hit multiplicities from the full simulation. For the purpose of this comparison we scaled up the SuperB prediction to account for the larger number of hits per track, using the 5.5 factor difference between the KoralW and SuperB BDK Monte Carlo generator estimations (see Section 5.1.1). Comparing the Monte Carlo prediction and the measurement in Table 5.11, we can clearly see that the

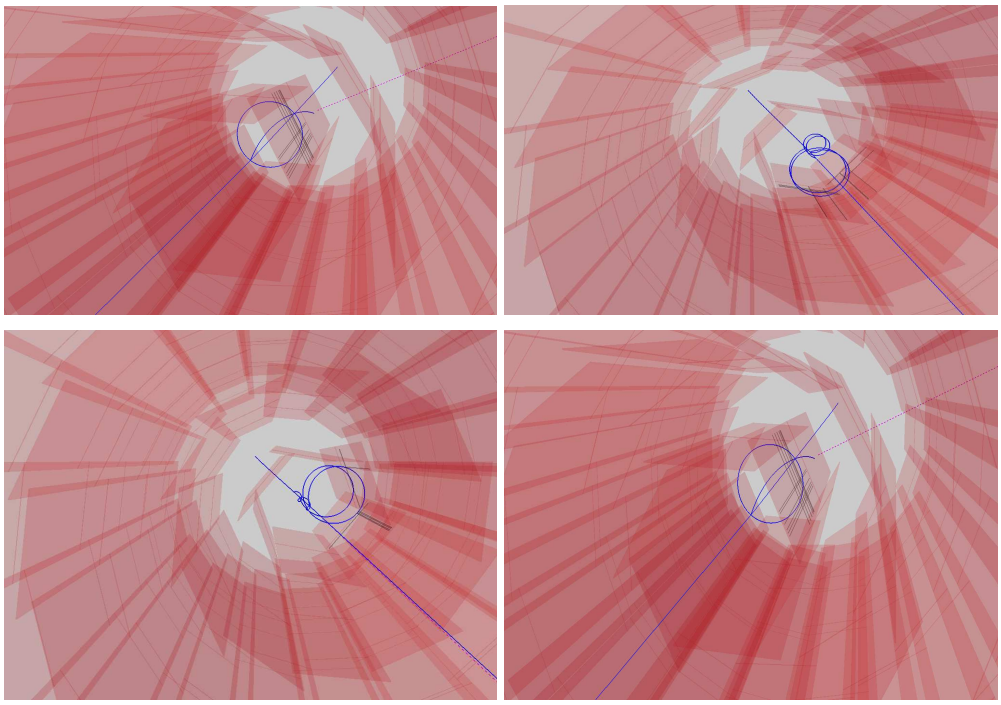

Figure 5.27: Event displays of two-photon events simulated using the full KoralW simulation.

measurements exclude the predictions made by the SuperB collaboration.

Experiment	SVD layers	Hits	QED hits	KoralW	SuperB(BDK)
Belle	1	~ 100	13.3 ± 2.6	11.31	62.2
	2 - 4	~ 45	-2.9 ± 2.1	2.38	13.1
Belle II	Occupancy (1st PXD)		$(0.8 \pm 0.2)\,\%$	0.7%	4.0%

Table 5.11: Comparison between data and Monte Carlo.

Thus, we can use the KoralW prediction to estimate the QED background occupancy in the pixel detector for Belle II. Taking into account the difference in the radial distance between the silicon vertex detector at Belle and the pixel detector at Belle II, the difference in the read-out time, the difference in the instantaneous luminosity and the different geometry of the new pixel detector itself [84][14], as indicated in Table 5.12, we get an expected occupancy of

Experiment	$r[cm]$	$t[\mu s]$	$L\,[1/\text{nbs}]$
Belle	2	2	10
Belle II	1.4	20	1000

Table 5.12: Radius of the first layer of the inner detector and its read-out time.

$$\begin{aligned} occupancy[1stPXDlayer] &= \frac{N_{hits}^{1st} \times r_{corr} \times t_{corr} \times L_{corr}}{N_{pixels}^{1st}} = \\ &= \frac{11.31 \times (\frac{2.0}{1.4})^2 \times \frac{20}{2} \times \frac{1000}{10}}{3 \times 10^6} = 0.7\% \end{aligned} \tag{5.3}$$

from the full KoralW simulation and an occupancy of $(0.8 \pm 0.2)\,\%$ from the QED measurements. Here, N_{hits} is the average hit multiplicity obtained in the first SVD layer, r_{corr} accounts for the radial difference between the two detectors, t_{corr} and L_{corr} account for the difference in the read-out time and in luminosity, respectively, while N_{pixels}^{1st} is the overall amount of pixels in the first layer of the pixel detector. As one can see these results are in agreement and the value obtained for the occupancy in the innermost layer of the pixel detector is clearly below the limiting occupancy of 2-3%. Thus, we conclude that the low-momentum QED background will not be a danger for the operation of the pixel detector.

Chapter 6

Conclusion

In this thesis, two separate studies are presented: the first measurement of the branching fraction of the decay $B^0 \to \psi(2S)\pi^0$ with the Belle detector and the estimation of the QED background for the pixel detector of the planned Belle II experiment.
For the measurement of the $B^0 \to \psi(2S)\pi^0$ branching fraction the complete data set of 772 million $B\bar{B}$ pairs was used. We extracted the branching fraction using an extended unbinned maximum likelihood fit and obtained a value of

$$\mathcal{B}(B^0 \to \psi(2S)\pi^0) = (1.07 \pm 0.23 \pm 0.08) \times 10^{-5},$$

where the first is the statistical error and the second is the systematic uncertainty. According to this result the extracted signal yield is about 80 events, which is unfortunately insufficient to perform the time-dependent analysis to extract the CP violating parameters. The systematic error on the branching fraction is mostly due to uncertainties on efficiencies, which are not important for the CP violation measurements. For the time-dependent measurements the systematic uncertainty due to the vertexing is the most prominent contribution. Therefore, with increased statistics and improved vertex reconstruction, we would be able to obtain precise measurement of the mixing-induced and direct CP violation parameters. The decay $B^0 \to \psi(2S)\pi^0$ is a $b \to c\bar{c}d$ transition that occurs either through a tree or through a penguin diagram. For a tree dominating diagram, we expect the mixing-induced and direct CP violation parameters to be consistent with the measurement from $B \to J/\psi K_S$, which is a $b \to c\bar{c}s$ transition. However, if there is a significant penguin contribution or other substantial contributions, precision measurements of time-dependent CP asymmetry of this channel, may reveal values of the CP parameters that differ from the Standard Model expectations. Therefore, measurements of CP asymmetries in the $b \to c\bar{c}d$ transitions such as $B^0 \to \psi(2S)\pi^0$ are important in identifying whether or not the Standard Model provides a complete description of the CP violation phenomena in the B meson system.
In order to increase massively the statistics, the KEKB accelerator is being upgraded to SuperKEKB whose target luminosity will be $8 \times 10^{35}\,\mathrm{cm}^{-2}\mathrm{s}^{-1}$, which is a factor of

40 improvement compared to KEKB. However, the increase of luminosity means also an increase of the background levels.
This fact is the subject of the second study of this thesis: the estimation of the low momentum QED background from the reaction $e^+e^- \to e^+e^-e^+e^-$. These low momentum secondary electrons and positrons mostly affect the new pixel vertex detector, which is the innermost part of the upgraded Belle detector. It can work properly with a maximal occupancy of 3 %.
The contribution from the low momentum QED background was estimated by performing dedicated experiments at KEK, shortly before KEKB was closed. From the data we took we estimated an occupancy in the innermost layer of the pixel detector of $(0.8 \pm 0.2)\%$, which is far below the operational limit of 3%. The experiments showed higher occupancy in the innermost layer of the vertex detector compared to the more distant layers. This was due to the low momentum curling tracks which may cross a few times the planes of the silicon vertex detector. This observation was cross-checked with a full detector simulation that confirmed our experiments results. The estimated occupancy for the innermost layer of the pixel detector using MC simulation was found to be 0.7%, which is consistent with the measurements obtained from the data. These results imply a safe operation of the PXD, since the contribution from the other background sources is expected to be below 1%.

Appendix A

Parameterization Functions

A.1 Polynomials

Polynomials are very useful mathematical tools and because of their simple definition, they can be calculated on computer systems and represent various functions. They also can be differentiated and integrated quite easily. For the fitting purposes two kinds of polynomials were used.

A.2 Chebyshev Polynomials

The Chebyshev polynomials are set of orthogonal polynomials which are defined over the interval [-1,1]. The recursive formulation of these polynomials that enables simple calculation of their higher orders is given by

$$C_{i+1}(x) = 2xC_i(x) - C_{i-1}(x). \tag{A.1}$$

The first few Chebyshev polynomials of a first kind are given as

$$\begin{aligned}
C_0(x) &= 1 \\
C_1(x) &= x \\
C_2(x) &= 2x^2 - 1 \\
C_3(x) &= 4x^3 - 3x \\
C_4(x) &= 8x^4 - 8x^2 + 1 \\
C_5(x) &= 16x^5 - 20x^3 + 5x \\
C_6(x) &= 32x^6 - 48x^4 + 18x^2 - 1 \\
C_7(x) &= 64x^7 - 112x^5 + 56x^3 - 7x \\
C_6(x) &= 128x^8 - 256x^6 + 160x^4 - 32x^2 + 1 \\
C_7(x) &= 256x^9 - 576x^7 + 432x^5 - 120x^3 + 9x
\end{aligned} \tag{A.2}$$

A.3 Bernstein Polynomials

The Bernstein polynomials of degree n are defined as

$$B_{i,n}(x) = \binom{n}{i} x^i (1-x)^{n-i} \tag{A.3}$$

for $i = 0, 1, ..., n$, where

$$\binom{n}{i} = \frac{n!}{i!(n-i)!} \tag{A.4}$$

The Bernstein polynomials of degree 1 are given by

$$\begin{aligned} B_{0,1}(x) &= 1-x \\ B_{1,1}(x) &= x \end{aligned} \tag{A.5}$$

The Bernstein polynomials of degree 2 are given by

$$\begin{aligned} B_{0,2}(x) &= (1-x)^2 \\ B_{1,2}(x) &= 2x(1-x) \\ B_{2,2}(x) &= x^2 \end{aligned} \tag{A.6}$$

The Bernstein polynomials of degree 3 are given by

$$\begin{aligned} B_{0,3}(x) &= (1-x)^3 \\ B_{1,3}(x) &= 3x(1-x)^2 \\ B_{2,3}(x) &= 3x^2(1-x) \\ B_{3,3}(x) &= x^3 \end{aligned} \tag{A.7}$$

The advantage of the Bernstein polynomials is that they all are defined positive, namely, Bernstein polynomials of degree n, are non-negative over the interval [0,1].

Appendix B

Signal MC Model Dependent Parameters of M_{BC}

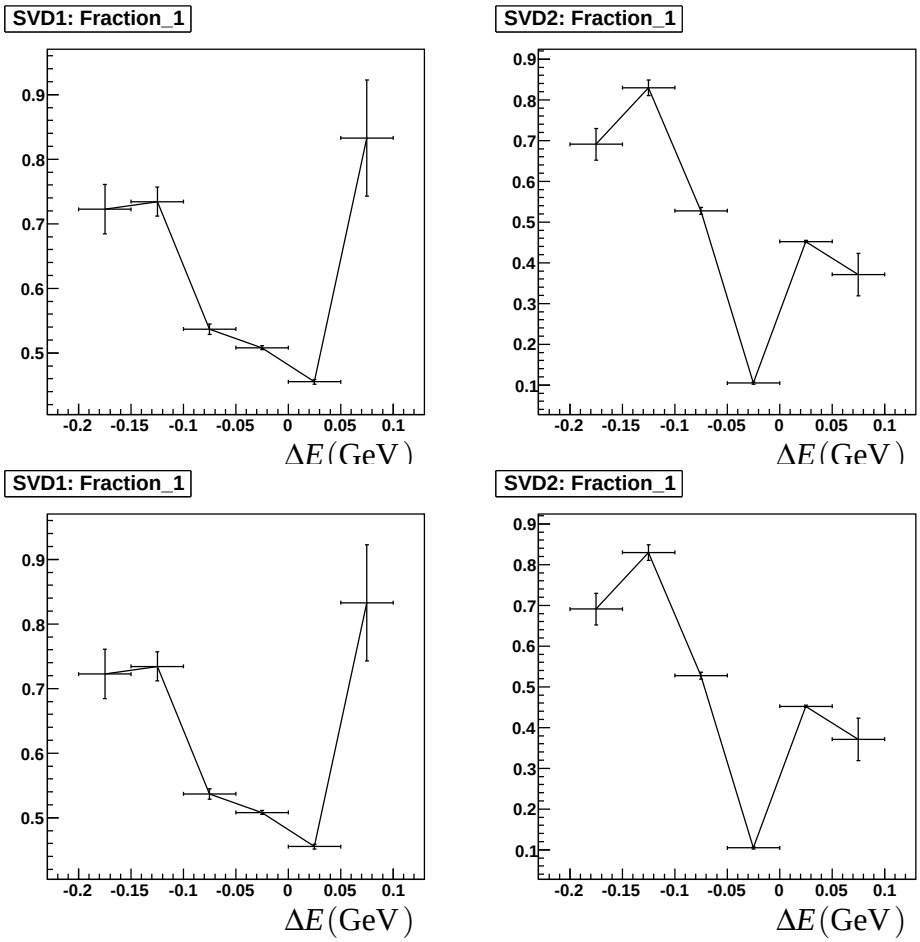

Figure B.1: The plot above shows the mean value of the 1st Bifurcated Gaussian for SVD1 (left) and SVD2 (right) in slices of ΔE, while the plot below shows the mean value of the 2nd Bifurcated Gaussian for SVD1 (left) and SVD2 (right) in slices of ΔE.

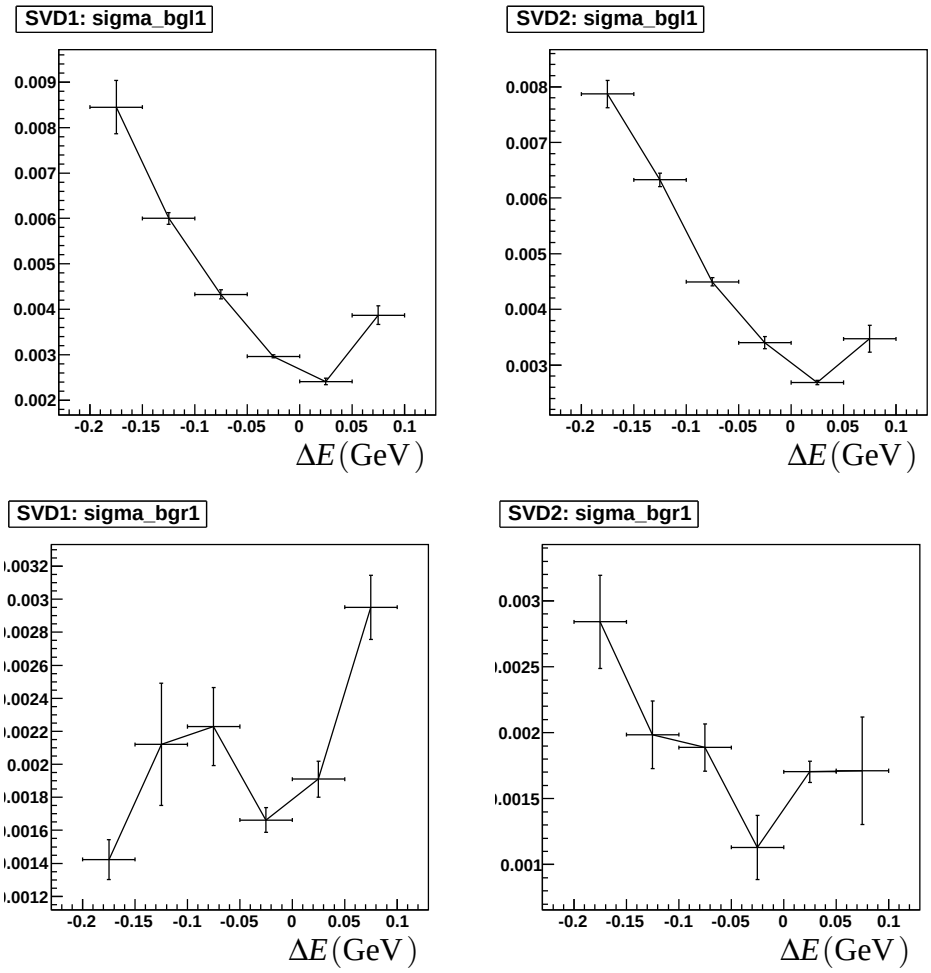

Figure B.2: The plots above show the width on the left side of the maximum value of the 1st Bifurcated Gaussian for SVD1 (left) and SVD2 (right) in slices of ΔE. The plots below show the same but for the the width on the left side of the maximum value of the Bifurcated Gaussian.

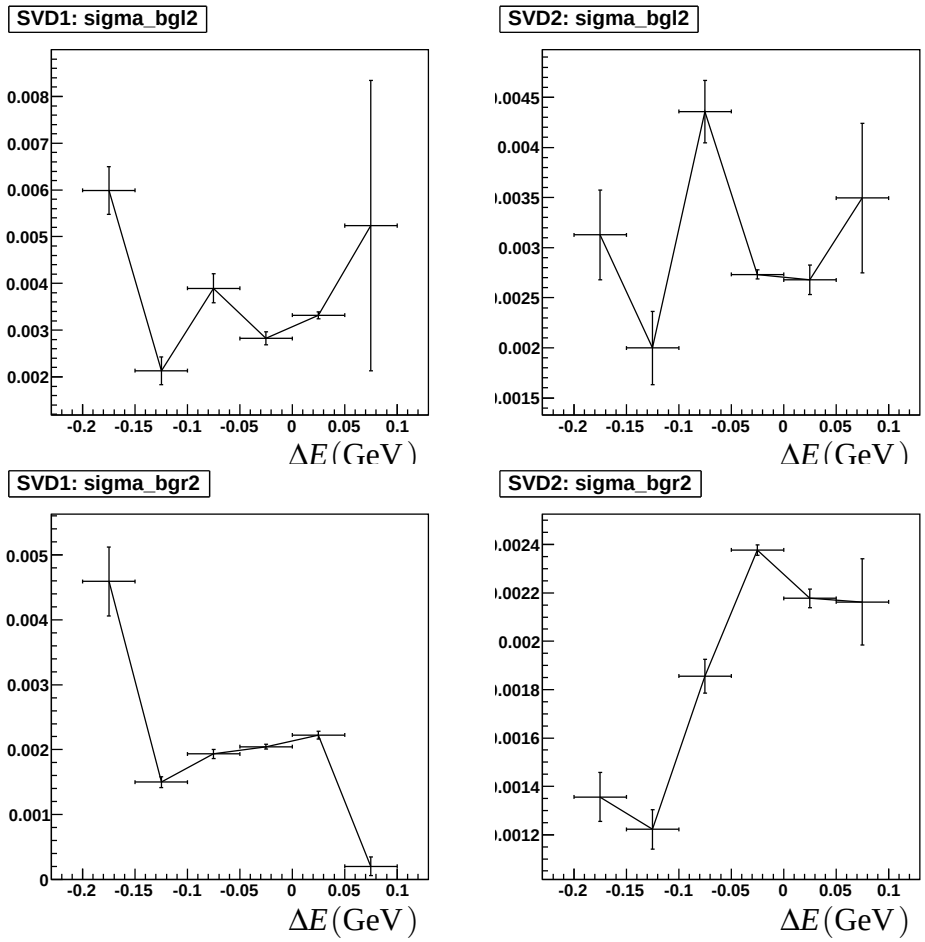

Figure B.3: The plots above show the width on the left side of the maximum value of the 2nd Bifurcated Gaussian for SVD1 (left) and SVD2 (right) in slices of ΔE. The plots below show the same but for the the width on the left side of the maximum value of the Bifurcated Gaussian.

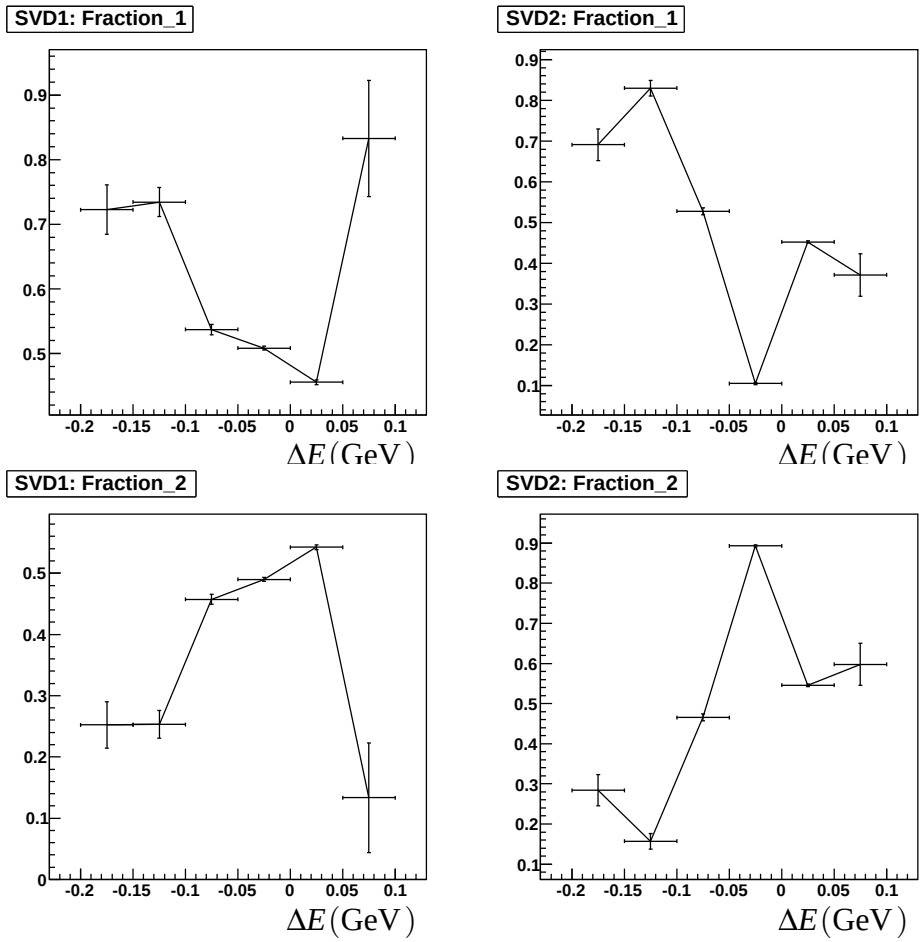

Figure B.4: The two fractions for each of the Bifurcated Gaussians are shown from top to bottom and for SVD1 and SVD2 from left to right.

Appendix C

M_{BC} in slices of ΔE

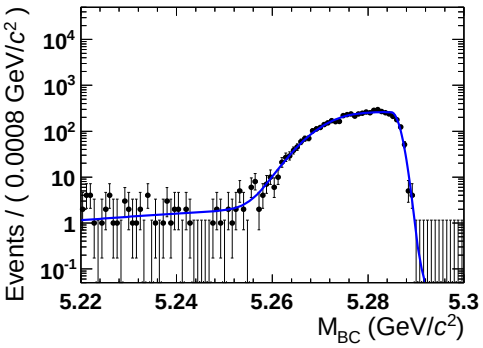

(a) $-0.2\,\mathrm{GeV} \leq \Delta E < -0.15\,\mathrm{GeV}$

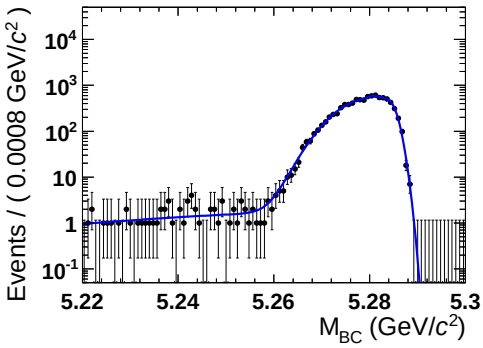

(b) $-0.15\,\mathrm{GeV} \leq \Delta E < -0.1\,\mathrm{GeV}$

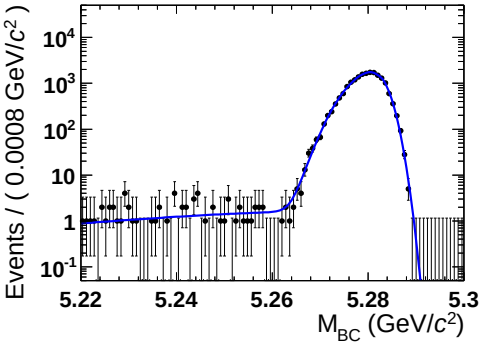

(c) $-0.1\,\mathrm{GeV} \leq \Delta E < -0.05\,\mathrm{GeV}$

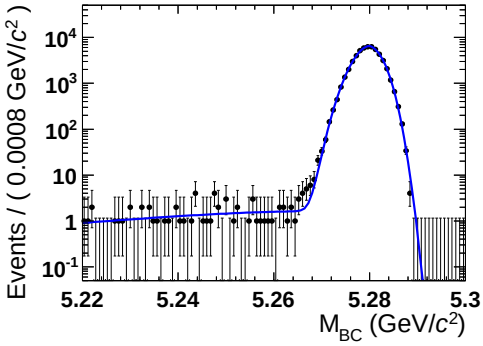

(d) $-0.05\,\mathrm{GeV} \leq \Delta E < 0.\,\mathrm{GeV}$

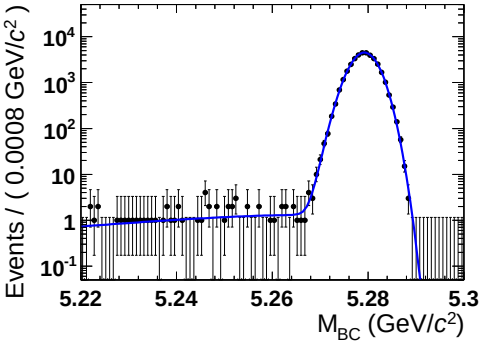

(e) $0.\,\mathrm{GeV} \leq \Delta E < 0.05\,\mathrm{GeV}$

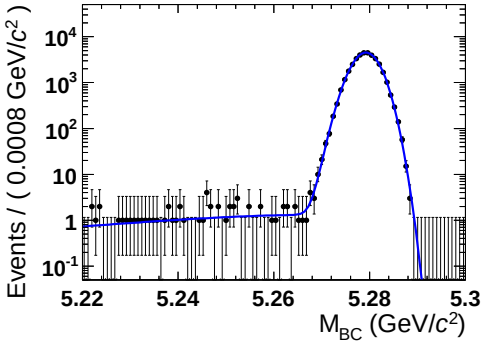

(f) $0.05\,\mathrm{GeV} \leq \Delta E \leq 0.1\,\mathrm{GeV}$

Figure C.1: Fitted M_{BC} distributions in slices of ΔE for SVD1.

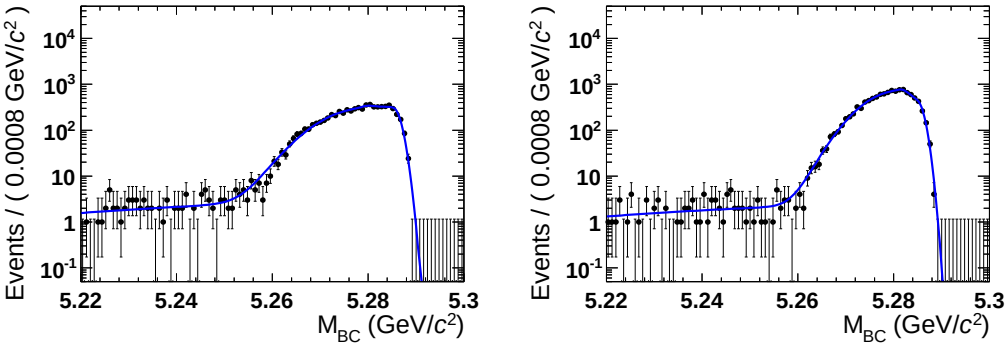

(a) $-0.2\,\mathrm{GeV} \leq \Delta E < -0.15\,\mathrm{GeV}$

(b) $-0.15\,\mathrm{GeV} \leq \Delta E < -0.1\,\mathrm{GeV}$

(c) $-0.1\,\mathrm{GeV} \leq \Delta E < -0.05\,\mathrm{GeV}$

(d) $-0.05\,\mathrm{GeV} \leq \Delta E < 0.\,\mathrm{GeV}$

(e) $0.\,\mathrm{GeV} \leq \Delta E < 0.05\,\mathrm{GeV}$

(f) $0.05\,\mathrm{GeV} \leq \Delta E \leq 0.1\,\mathrm{GeV}$

Figure C.2: Fitted M_{BC} distributions in slices of ΔE for SVD2.

Appendix D

QED study

D.0.1 Monte Carlo Generators

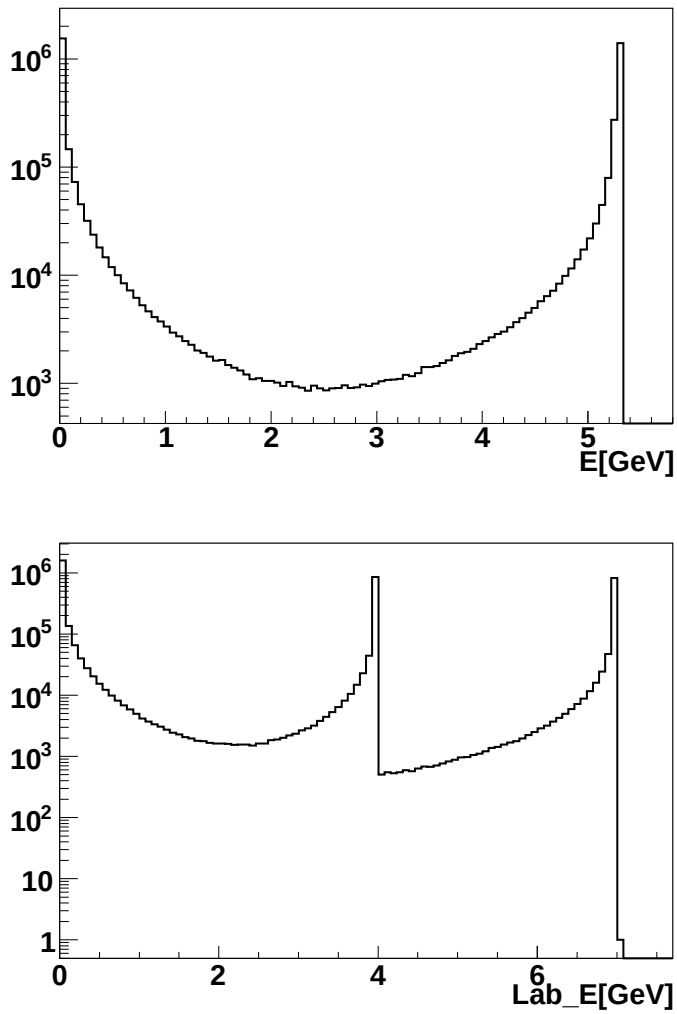

Figure D.1: Energy spectrum of the electron in the center-of-mass system (top) and after the Lorentz boost (bottom) extracted using the BDK Monte Carlo generator.

D.0.2 Hit Multiplicities in the SVD

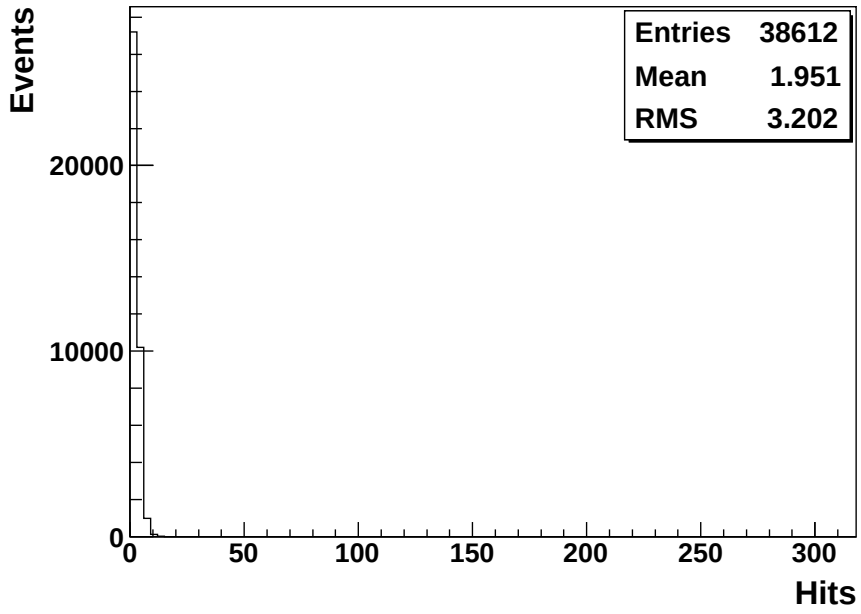

Figure D.2: Hit multiplicities in the rz-plane in the first layer of the Silicon Vertex Detector (SVD) for data taken when the beams were turned off.

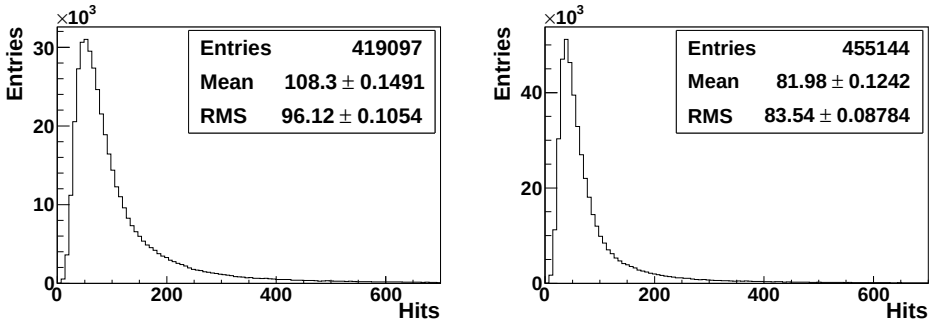

(a) exp.(**A**): L = 9.62 /nbs

(b) exp.(**A**): L = 5.75 /nbs

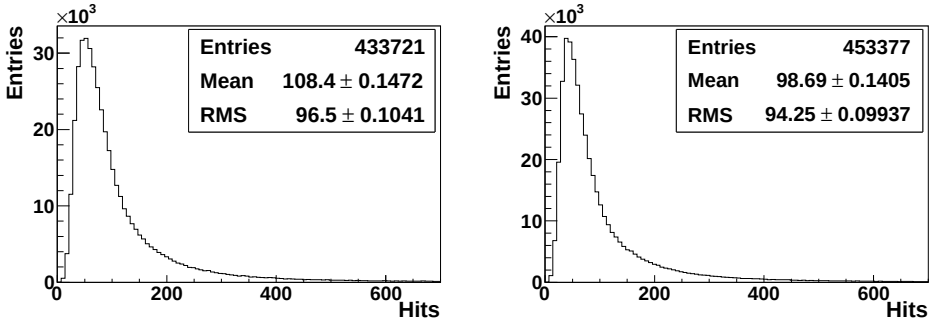

(c) exp.(**B**): L = 9.71 /nbs

(d) exp.(**B**): L = 6.08 /nbs

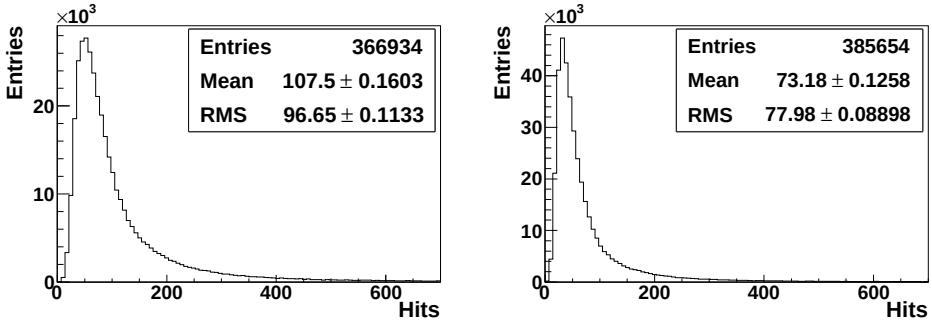

(e) exp.(**C**): L = 9.49 /nbs

(f) exp.(**C**): L = 6.01 /nbs

Figure D.3: Hit multiplicities in the *rz*-plane in the first layer of the Silicon Vertex Detector (SVD) of experiment (A)-(top), experiment (B)-(middle), experiment (C)-(bottom) for different luminosities.

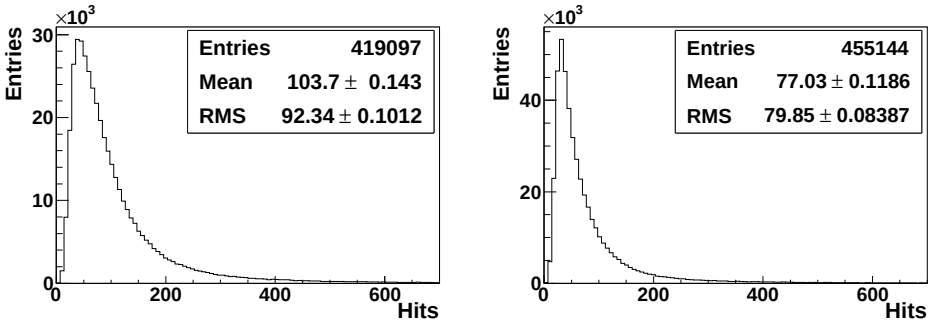

(a) exp.(**A**): L = 9.62 /nbs

(b) exp.(**A**): L = 5.75 /nbs

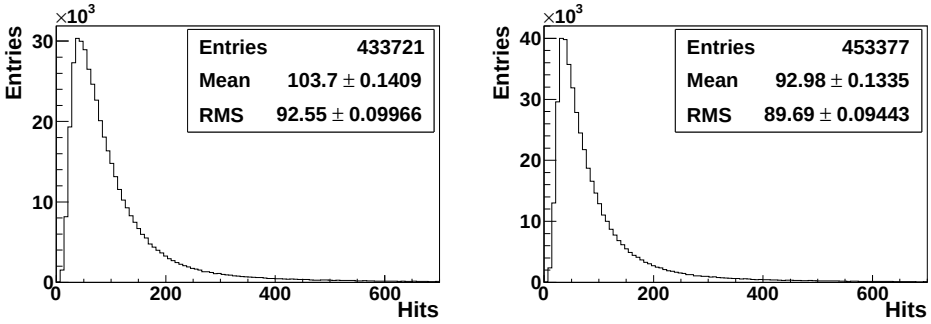

(c) exp.(**B**): L = 9.71 /nbs

(d) exp.(**B**): L = 6.08 /nbs

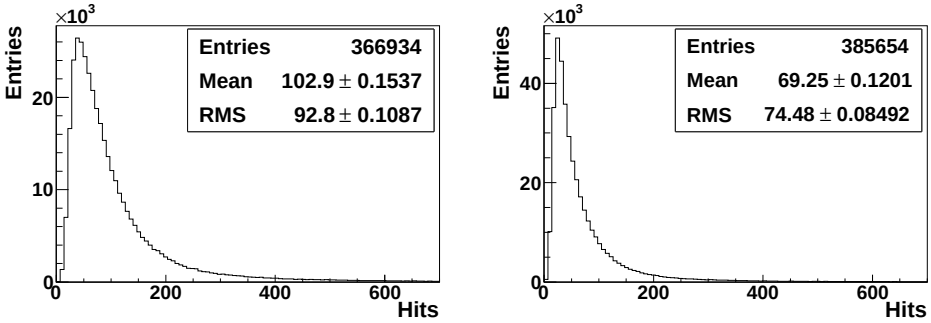

(e) exp.(**C**): L = 9.49 /nbs

(f) exp.(**C**): L = 6.01 /nbs

Figure D.4: Hit multiplicities in the $r\phi$-plane in the first layer of the Silicon Vertex Detector (SVD) of experiment (A)-(top), experiment (B)-(middle), experiment (C)-(bottom) for different luminosities.

D.0.3 Correcting for the Background Change using the CDC activity

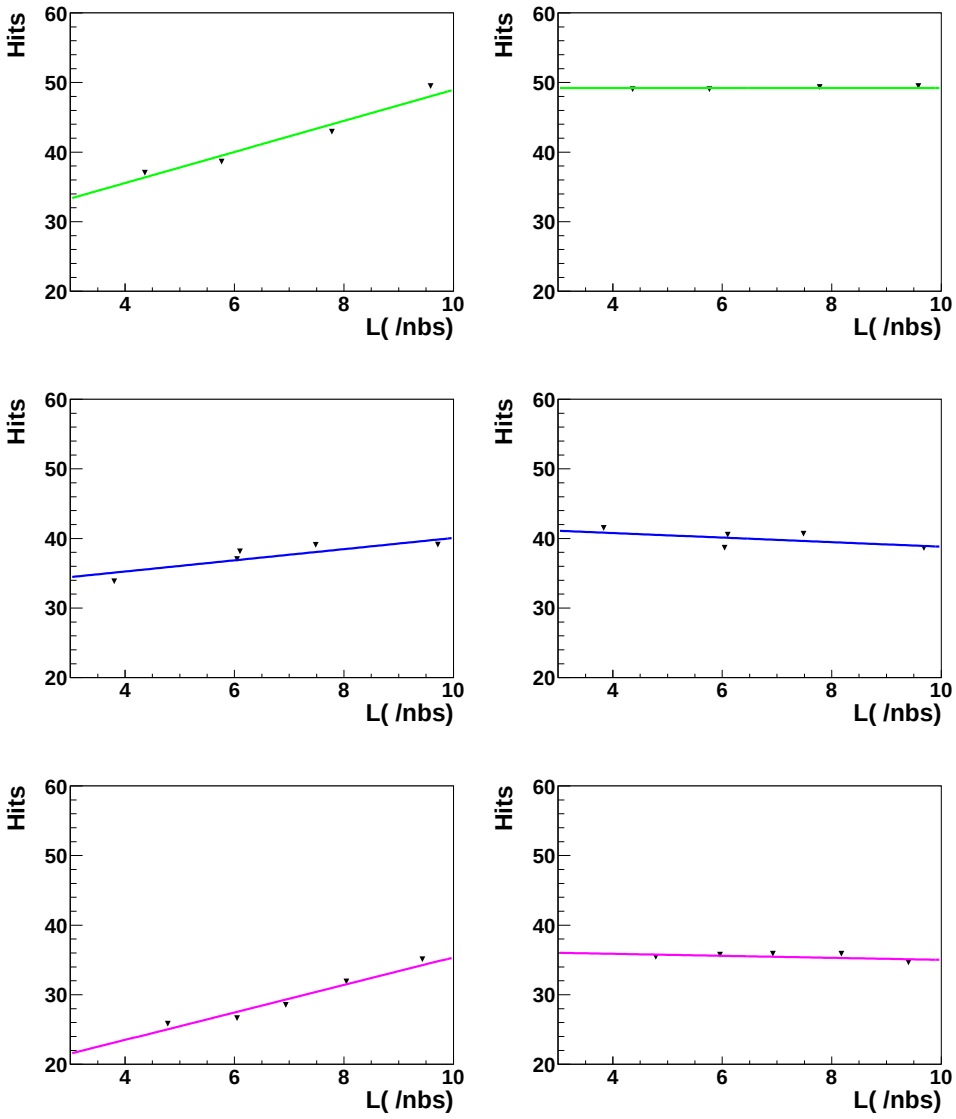

Figure D.5: Hit multiplicities as a function of luminosity before (left) and after (right) applied correction using the CDC activity in the $r\phi$ plane. The plots show the hit multiplicities in the second (top), third (middle) and fourth (bottom) SVD layer for the three QED experiments (A), (B) and (C) from top to bottom, respectively.

List of Figures

List of Tables

Bibliography

[1] J. H. Christenson, J. W. Cronin, V. L. Fitch, and R. Turlay. ***Evidence for the*** 2π ***Decay of the*** K_2^0 ***Meson***. Physical Review Letters, **13**:138–140, (1964). doi:10.1103/PhysRevLett.13.138.

[2] M. Bargiotti, A. Bertin, M. Bruschi, et al. ***Present knowledge of the Cabibbo-Kobayahsi-Maskawa matrix***. Riv.Nuovo Cim., **23N3:1**, (2000). arXiv: 0001293.

[3] L. Canetti, M. Drewes, and M. Shaposhnikov. ***Matter and Antimatter in the Universe***. New J. Phys., **14:095012**, (2012). doi:10.1088/1367-2630/14/9/095012.

[4] A. Hutton. ***PEP-II: an Asymmetric B Factory Based on PEP***. IEEE, **1**:84–86, (1991). doi:10.1109/PAC.1991.164208.

[5] F. Takasaki. ***Status of KEKB accelerator and detector, BELLE***. Int.J.Mod.Phys.A, **15S1**:12–21.

[6] The BaBar Collaboration. ***The BABAR Detector***. Nuclear Instruments and Methods in Physics Research Section A: Accelerators, Spectrometers, Detectors and Associated Equipment, **479**:1–116.

[7] A. Abashian et al. ***The Belle detector***. Nuclear Instruments and Methods in Physics Research Section A: Accelerators, Spectrometers, Detectors and Associated Equipment, **479**:117–232, (2002). doi:10.1016/S0168-9002(01)02013-7.

[8] A. Abashian et al. ***Measurement of the CP Violation Parameter*** $sin2\phi_1$ ***in*** B_d^0 ***Meson Decays***. Physical Review Letters, **86**:2509–2514, (2001). doi:10.1103/PhysRevLett.86.2509.

[9] K. Abe et al. ***Observation of Large CP Violation in the Neutral Meson System***. Phys.Rev.Lett., **87:091802**, (2001). doi:10.1103/PhysRevLett.87.091802.

[10] K. Abe et al. ***Observation of Mixing-induced CP Violation in the Neutral Meson System***. Physical Review D, **66:032007**, (2002). doi:10.1103/PhysRevD.66.032007.

[11] K. Abe et al. ***Improved Measurement of Mixing-induced CP Violation in the Neutral Meson System***. Physical Review D, **66:071102**, (2002). doi:10.1103/PhysRevD.66.071102.

[12] B. Aubert et al. ***Measurement of CP-violating asymmetries in B^0 decays to CP eigenstates***. Physical Review Letters, **86**:2515–2522, (2001). doi:10.1103/PhysRevLett.86.2515.

[13] B. Aubert et al. ***Observation of CP violation in the B^0 meson system***. Physical Review Letters, **87:091801**, (2001). doi:10.1103/PhysRevLett.87.091801.

[14] ***Belle II Technical Design Report***. (2010). arXiv: 1011.0352v1.

[15] C.S. Wu et al. ***Experimental Test of Parity Conservation in Beta Decay***. Phys. Rev., **105**:1413–1415, (1957). doi:10.1103/PhysRev.105.1413.

[16] D. Griffiths. ***Introduction to Elementary Particles***. Wiley-VCH; 2nd edition, New York, USA, 2008. ISBN 3527406018.

[17] H. Burkhardt et al. ***First evidence for direct CP violation***. Physics Letters B, **206**:169–176, (1988). doi:10.1016/0370-2693(88)91282-8.

[18] A. Carbone. ***A search for time-integrated CP violation in $D^0 \to h^+h^-$ decays***. arXiv: 1210.8257.

[19] T. Aaltonen et al. ***Measurement of the difference of CP-violating asymmetries in $D^0 \to K^+K^-$ and $D^0 \to \pi^+\pi^-$ decays at CDF***. arXiv: 1207.2158.

[20] T. Aaltonen et al. ***Measurements of Direct CP Violating Asymmetries in Charmless Decays of Strange Bottom Mesons and Bottom Baryons***. Physical Review Letters, **106:181802**, (2011). doi:10.1103/PhysRevLett.106.181802.

[21] I. J. R. Aitchison and A. J. G. Hey. ***Gauge Theories in Particle Physics***. Adam Hilger Ltd, Bristol, England, 1982. ISBN 0-85274-534-6.

[22] F. Halzen and A. D. Martin. ***Quarks and Leptons: An Introductory Course in Modern Particle Physics***. Wiley, New York, USA, 1984. ISBN 0-471-88741-2.

[23] S.M. Bilenky and J. Hošek. ***Glashow-Weinberg-Salam theory of electroweak interactions and the neutral currents***. Physics Reports, **90**:73–157, (1982). doi:10.1016/0370-1573(82)90016-3.

[24] S. L. Glashow, J. Iliopoulos, and L. Maiani. ***Weak Interactions with Lepton-Hadron Symmetry***. Physical Review D, **2**:1285–1292, (1970). doi:10.1103/PhysRevD.2.1285.

[25] L. L. Chau and W. Y. Keung. ***Comments on the Parameterization of the Kobayashi-Maskawa Matrix***. Physical Review Letters, **53**:1802–1805, (1984). doi:10.1103/PhysRevLett.53.1802.

[26] L. Wolfenstein. ***Parameterization of the Kobayashi-Maskawa Matrix***. Physical Review Letters, **51**:1945–1947, (1983). doi:10.1103/PhysRevLett.51.1945.

[27] J. Beringer et al. ***Review of Particle Physics (Particle Data Group)***. Physical Review D, **86**:010001, (2012). doi:10.1103/PhysRevD.86.010001.

[28] T. Browder et al. ***On the Physics Case of a Super Flavor Factory***. Journal of High Energy Physics, (2008). doi:10.1088/1126-6708/2008/02/110.

[29] J. Beringer et al. ***(Particle Data Group)***. Physical Review D, **86**:010001, (2012) and 2013 partial update for the 2014 edition.

[30] N. Cabibbo. ***Unitary Symmetry and Leptonic Decays***. Physical Review Letters, **10**:531–533, (1963). doi:10.1103/PhysRevLett.10.531.

[31] I.I. Bigi and A.I. Sanda. ***CP Violation***. Cambridge University Press, 2009. ISBN 9780521847940.

[32] M. Gell-Mann and A. Pais. ***Behavior of Neutral Particles under Charge Conjugation***. Physical Review D, **97**:1387–1389, (1955).

[33] K. Abe et al. ***Improved measurement of CP-violating parameters*** $sin2\phi_1$ ***and*** $|\lambda|$***, B meson lifetimes, and*** $B^0 - \bar{B}^0$ ***mixing parameter*** Δm_d. Physical Review D, **71**, (2005). doi:10.1103/PhysRevD.71.072003.

[34] B. Aubert et al. ***Improved Measurement of CP Asymmetries in*** $B^0 \to (cc)K^{(*)0}$ ***Decays***. arXiv: 0607107.

[35] S. Kurokawa and E. Kikutani. ***Overview of the KEKB accelerators***. Nuclear Instruments and Methods in Physics Research Section A: Accelerators, Spectrometers, Detectors and Associated Equipment, **499**:1–7, (2003). doi:10.1016/S0168-9002(02)01771-0.

[36] K. Akai et al. ***RF systems for the KEK B-factory***. Nuclear Instruments and Methods in Physics Research Section A: Accelerators, Spectrometers, Detectors and Associated Equipment, **499**:45–65, (2003). doi:10.1016/S0168-9002(02)01773-4.

[37] K. Hosoyama et al. ***Development of the KEKB Superconducting Crab Cavity***. In *Proceedings of the 11th European Particle Accelerators Conference (EPAC08)*. Genoa, Italy, 2008.

[38] H. Aihara. ***The Belle Silicon Vertex Detector***. Nuclear Instruments and Methods in Physics Research Section A: Accelerators, Spectrometers, Detectors and Associated Equipment, **466**:268–274, (2001). doi:10.1016/S0168-9002(01)00538-1.

[39] H. Aihara et al. ***Belle SVD2 Vertex Detector***. Nuclear Instruments and Methods in Physics Research Section A: Accelerators, Spectrometers, Detectors and Associated Equipment, **568**:269–273, (2006). doi:10.1016/j.nima.2006.05.281.

[40] M. Tomoto et al. ***Z-trigger system with the BELLE Central Drift Chamber***. Nuclear Instruments and Methods in Physics Research Section A: Accelerators, Spectrometers, Detectors and Associated Equipment, **447**:416–423, (2000). doi:10.1016/S0168-9002(99)01075-X.

[41] H. Hirano et al. ***A high-resolution cylindrical drift chamber for the KEK B factory***. Nuclear Instruments and Methods in Physics Research Section A: Accelerators, Spectrometers, Detectors and Associated Equipment, **455**:294–304, (2000). doi:10.1016/S0168-9002(00)00513-1.

[42] U. Shoji. ***The BELLE central drift chamber***. Nuclear Instruments and Methods in Physics Research Section A: Accelerators, Spectrometers, Detectors and Associated Equipment, **379**:421–423, (1996). doi:10.1016/0168-9002(96)00555-4.

[43] T. Sumiyoshi et al. ***Silica aerogel Cherenkov counter for the KEK B-factory***. Nuclear Instruments and Methods in Physics Research Section A: Accelerators, Spectrometers, Detectors and Associated Equipment, **433**:358–391, (1999). doi:10.1016/S0168-9002(99)00460-X.

[44] I. Adachi et al. ***Study of a threshold Cherenkov counter based on silica aerogels with low refractive indices***. Nuclear Instruments and Methods in Physics Research Section A: Accelerators, Spectrometers, Detectors and Associated Equipment, **355**:390–398, (1995). doi:10.1016/0168-9002(94)01119-2.

[45] T. Sumiyoshi et al. ***Silica aerogels in high energy physics***. Journal of Non-Crystalline Solids, **225**:369–374, (1998). doi:10.1016/S0022-3093(98)00057-X.

[46] S. K. Sahu et al. ***Measurement of radiation damage on a silica areogel Cherenkov radiator*** . Nuclear Instruments and Methods in Physics Research Section A: Accelerators, Spectrometers, Detectors and Associated Equipment, **382**:441–446, (1996). doi:10.1016/S0168-9002(96)00768-1.

[47] H. Kichimi et al. ***The BELLE TOF system***. Nuclear Instruments and Methods in Physics Research Section A: Accelerators, Spectrometers, Detectors and Associated Equipment, **453**:315–320, (2000). doi:10.1016/S0168-9002(00)00651-3.

[48] K. Hanagaki. ***Status of electron identification***, May (2000). BELLE Internal Note 312, accessible by Belle members only.

[49] H. C. Huang. ***Performance of a small angle BGO calorimeter at Belle***. In *Proceedings of the 10th International Conference on Calorimetry in Particle Physics*, pages 161–166. Pasadena, California, USA, March 2002.

[50] Y. Makida, K. Aoki, Y. Doi, J. Haba, M. Kawai, Y. Kondo, A. Yamamoto, and H. Yamaoka. ***Performance of a Superconducting Solenoid Magnet for BELLE Detector in KEK B-factory***. IEEE Transactions on Applied Superconductivity, **9**:475–478, June (1999). doi:10.1109/77.783338.

[51] K. Abe et al. ***Performance of the endcap RPC for the BELLE at KEK***. Nuclear Since Symposium, IEEE, **1**:855–859, (1997). doi:10.1109/NSSMIC.1997.672716.

[52] A. Abashian et al. ***The K_L/μ detector subsystem for the BELLE experiment at the KEK B-factory***. Nuclear Instruments and Methods in Physics Research Section A: Accelerators, Spectrometers, Detectors and Associated Equipment, **449**:112–124, (2000). doi:10.1016/S0168-9002(99)01383-2.

[53] Y. Hoshi, M. Sanpei, T. Nagamine, S. Narita, M. Yamaga, A. Yamaguchi, and K. Abe. ***Nonflammable gas mixture for RPC***, (1997). BELLE Internal Note 185, accessible by Belle members only.

[54] T. E. Browder and K. Honscheid. ***B mesons***. Progress in Particle and Nuclear Physics, **35**:81–219, (1995). doi:http://dx.doi.org/10.1016/0146-6410(95)00042-H.

[55] D.J. Lange. ***The EvtGen particle decay simulation package***. Nuclear Instruments and Methods in Physics Research Section A: Accelerators, Spectrometers, Detectors and Associated Equipment, **462**:152–155, (2001). doi:10.1016/S0168-9002(01)00089-4.

[56] R. Brun et al. ***GEANT 3.21.*** Report No., **CERN DD/EE/84-1**, (1984).

[57] C. J. Fox and S. Wolfram. ***Observables for the Analysis of the Event Shapes in the e^+e^- Annihilation and Other Processes***. Physical Review Letters, **41**: 1581–1585, (1978). doi:10.1103/PhysRevLett.41.1581.

[58] H. Albrecht et al. ***Search for hadronic $b \to u$ decays***. Physics Review Letters B, **241**:278–282, (1990). doi:10.1016/0370-2693(90)91293-K.

[59] S. E. Lee and K. Miyabayashi. ***Improved measurement of time-dependent CP violation in $B^0 \to J/\psi\pi^0$ decays***, July (2007). BELLE Internal Note 957, accessible by Belle members only.

[60] B. Casey. ***Hadron B***. BELLE Internal Note 390, accessible by Belle members only.

[61] S.W. Lin, P. Chang, and H.C. Huang. ***Update of π^0 Systematics Using Inclusive*** $\eta(78/\text{fb})$, (2003). BELLE Internal Note 645, accessible by Belle members only.

[62] P. Koppenburg. ***A Measurement of the Track Finding Efficiency Using Partially Reconstructed*** D^* ***Decays***, (2003). BELLE Internal Note 621, accessible by Belle members only.

[63] S. Nishida. ***Study of Kaon and Pion Identification Using Inclusive*** D^* ***Sample***, (2005). BELLE Internal Note 779, accessible by Belle members only.

[64] L. Hinz, C. Jacoby, J. Wicht, and E. Nakano. ***Lepton efficiency and systematic error for experiments 21 to 27***, (2004). BELLE Internal Note 777, accessible by Belle members only.

[65] L. Hinz. ***Lepton ID efficiency correction and systematic error***, (2006). BELLE Internal Note 954, accessible by Belle members only.

[66] M.C. Chang. ***Observation of the decay*** $B^0 \to J/\psi\eta$, (2007). BELLE Internal Note 884, accessible by Belle members only.

[67] T. Aushev et al. ***Status and prospects of SuperKEKB collider and Belle II experiment***. (2012). arXiv: 1201.1248.

[68] T. Kuhr et al. ***Status of SuperKEKB and Belle II***. (2011). arXiv: 1101.1916.

[69] S. Rummel, L. Andricek, H.-G. Moser, and R. Richter. ***Intrinsic properties of DEPFET active pixel sensors***. Journal of Instrumentation, **4**, March (2009). doi:10.1088/1748-0221/4/03/P03003.

[70] I. Adachi et al. ***sBelle Design Study Report***. Technical report, 2008.

[71] ***Belle II Technical Design Report***. Technical report, 2010.

[72] J. Haba. ***Beam Background in the Belle Detector***, (1999). BELLE Internal Note 277, accessible by Belle members only.

[73] A. Bozek, S.K. Sahu, H. Ozaki, and S. Uno. ***Simulation Study of Beam-backgrounds on Silicon Vertex Detector at KEK B-Factory***, (1997). BELLE Internal Note 174, accessible by Belle members only.

[74] S.K. Sahu. ***A Generator for Studies of Background due to Beam-Gas Interactive at KEK B-Factory***, (1997). BELLE Internal Note 172, accessible by Belle members only.

[75] T. Browder, S. Olsen, S.K. Swain, and H. Yamamoto. ***Synchrotron Radiation Background Simulation Study for Belle***, (2007). BELLE Internal Note 361, accessible by Belle members only.

[76] K. Kanazawa, Y. Ohnishi, Y. Nakayama, C. Kiesling, S. Koblitz, et al. ***Beam Background Simulation for SuperKEKB/Belle-II***. In *Proceedings of IPAC2011*, volume C1109094, pages 3700–3702. San Sebastian, Spain, 2011.

[77] F. A. Berends, P. H. Daverfeldt, and R. Kleiss. ***Monte Carlo Simulation of Two-Photon Processes II: Complete Lowest Order Calculations for Four-Lepton Production Processes in Electron-Positron Collisions***. Computer Physics Communications, **40**:285–307, (1986). doi:10.1016/0010-4655(86)90115-3.

[78] S. Jadach, W. Placzek, M. Skrzypek, B.F.L. Ward, and Z. Was. ***The Monte Carlo Program KoralW version 1.51 and The Concurrent Monte Carlo KoralW and YFSWW3 With All Background Graphs and First Order Corrections to W Pair Production***. Computer Physics Communications, **140**:475–512, (2001). doi:10.1016/S0010-4655(01)00296-X.

[79] A. Denner, S. Dittmaier, M. Roth, and D. Wackeroth. ***RacoonWW 1.3: A Monte Carlo Program for Four-Fermion Production at e^+e^- Colliders***. Computer Physics Communications., **153**:462–507, (2003). doi:10.1016/S0010-4655(03)00205-4.

[80] W. Wittmer et al. ***Status of the Super-B factory design***. In *Proceedings of the DPF-2011 Conference*. Providence, Rhode Island, USA, August 2011.

[81] H. Ozaki. ***Naming and Numbering Conventions etc. in SVD***, (1996). BELLE Internal Note 137, accessible by Belle members only.

[82] `http://belle.kek.jp/secured/runinfo/runsum/exp73/`. Online run summaries web page accessible by Belle members only.

[83] S. Uno. ***The BELLE Central Drift Chamber***. Nuclear Instruments and Methods in Physics Research Section A: Accelerators, Spectrometers, Detectors and Associated Equipment, **A 379**:421–423, (1996). doi:10.1016/0168-9002(96)00555-4.

[84] F. Simon. ***DEPFET Vertex Detectors: Status and Plans***. (2010). arXiv: 1007.0428.

Acknowledgements

First of all I would like to express my deepest gratitude and appreciation to Prof. Dr. Christian Kiesling for giving me an opportunity to work in the Belle group at MPI, for his unselfish support and interest in my work, for his constant guidance and continuous enlightening discussions about various physics topics.

The success of this work I also owe to my everyday supervisors, Jeremy Dalseno and Luigi Li Gioi. To Jeremy Dalseno for introducing me to the analysis techniques and to Luigi Li Gioi for his interest and experience in all aspects of the analysis and his dedication to Belle physics. Both of them provided an guideline which was of an invaluable importance in realizing this work. To Luigi Li Gioi I am especially grateful for taking time for a detailed proof reading of this thesis.

For a friendly atmosphere, very pleasant to work in, I thank my colleagues from the Belle group: Martin Ritter, Kolja Prothmann, Andreas Moll. I especially thank Martin Ritter for solving any kind of computing problems.

For the rich scientific program of the experiment and the pleasant working atmosphere I would like to thank the colleagues from the Belle/Belle II collaboration.

A heartfelt thanks goes to Ana Behrendt who encouraged me to choose High Energy Physics for my PhD and move to Germany to start at MPI.

There are not enough words to express my feelings for my family. Words of warmest gratitude belong to my parents and my sister Tanja who are making my life worth living. Their believe in me made me to persuade my dream. They have been and still are standing by my side in my best and my worst days. They have lifted me up when I felt down, especially during the difficulties of past months. Their patience, support, understanding and love had followed me everywhere and I would not have been, what I am today without them.

Last but not least, Goran thank you for all the encouragement, patience and love you gave me trough my path here.